Ink-Jet Printing of Multi-Phase Formulations

ASHLEY STEPHEN JOHNS

Ink-Jet Printing of Multi-Phase Formulations

A thesis submitted in partial fulfilment of the requirements for the degree of Doctor of Philosophy at the University of Durham by

Ashley Stephen Johns

Department of Chemistry

Durham University

June 2017

Abstract

Ink-jet formulations are tailored for specific applications to give high performance in storage, during jetting, as drops impact the substrate and during evaporation; high performance of the final product is also targeted. This thesis explores the ink-jet printing of multi-phase formulations and their potential applications.

First, phase-separating inks were investigated. Formulations based upon binary mixtures of partially miscible liquids were explored: the minor component in suitable formulations was present initially below its miscibility limit and increased in concentration during evaporation until the mixture passed the binodal. Aqueous solutions of di(propylene glycol) methyl ether acetate (DPGMEA) phase separated after jetting: the new oil-rich phase formed at the contact line where evaporative flux is greatest. Phase-selective patterning was demonstrated using sodium oxalate and benzoic acid, which partitioned into opposite phases. Decane-in-methanol solutions phase separated throughout the drop but the high volatility of methanol did not allow composition gradients to equilibrate; phase selective patterning is not possible for this mixture. A quantitative criterion for the observation of phase separation during evaporation was developed and may be calculated from reference data.

Second, the delivery of high-molecular-weight (MW) polymers via emulsions was investigated. The ink-jet printing of high-(MW) polymers in solution is non-trivial: first, concentrated solutions are too viscous for print heads. Second, high strain rates during printing causes chain degradation. Third, high strain rates cause polymers to undergo the coil-stretch transition and introduce non-Newtonian jetting dynamics: long-lived elastic filaments develop that delay drop breakoff and decelerate the main drop. Emulsions shield polymers from high strain rates during printing through the interfacial tension and Gibbs elasticity of the dispersed phase droplets; strain occurs only in the polymer-free continuous phase. The optimised model formulation contained 3.8 %wt polystyrene (M_n = 419 kDa) overall; polystyrene was dissolved in methyl benzoate and dispersed throughout an aqueous solution of sodium dodecylsulphate. During evaporation on the substrate, the dispersed phase coalesced to give an even polystyrene deposit with the shape of a spherical cap. The emulsion increased the maximum printable concentration of the polymer by a factor of 15 and long-lived elastic filaments were not formed during jetting. A variety of discontinuous phase solvents were trialled: nozzle clogging was more frequent with toluene and anisole, whilst diethyl phthalate did not evaporate on the substrate. A neutrally buoyant discontinuous phase is advantageous.

Contents

Publication List

Aspects of this thesis have been circulated in the following articles:

A. S. Johns and C. D. Bain, in *Proceedings of NIP31: The 31st International Conference on Digital Printing Technologies and Digital Fabrication 2015*, Society for Imaging Science and Technology, Springfield, VA, 2015, pp. 476–480.

A. S. Johns and C. D. Bain, in *Proceedings of NIP32: The 32nd International Conference on Digital Printing Technologies and Printing for Fabrication 2016*, Society for Imaging Science and Technology, Springfield, VA, 2016, pp. 275–280.

A. S. Johns and C. D. Bain, *ACS Appl. Mater. Interfaces*, 2017, **9**, 22918–22926.

Copyright

Dedication

During my studies I have been well looked after by many thoughtful and caring people. The kindness so freely shown has enabled me to thrive here, and I shall look back fondly on my time Durham. I thank Mum, Dad, Kirsty, Shaun and Gran for their steadfast love and support. I thank my past and present housemates (Babs, Silvers, Coatesy, Moxy, JP, Doddsy and Philip) for day-by-day companionship and good times. I am grateful to my Christchurch family for sharing life and for never ceasing to speak the truth in love. I thank my supervisor Colin for being a constant source of encouragement. I have always appreciated the support and assistance offered by the wider group.

Throughout my studies, I have put my work into context using Scripture. When dealing with microlitre and picolitre droplets, I recall Isaiah 40v15, which teaches the LORD's greatness:

Behold, the nations are like a drop from a bucket, and are accounted as the dust on the scales; behold, he takes up the coastlands like fine dust.

When contending with difficult problems or scientific subtleties, I recall Isaiah 55v8−9, which teaches the LORD's wisdom:

For my thoughts are not your thoughts, neither are your ways my ways, declares the LORD. For as the heavens are higher than the earth, so are my ways higher than your ways and my thoughts than your thoughts.

Though completing a PhD represents a significant achievement, I gladly divert all glory away from myself and lay the crown at the feet of my Lord and Saviour, Jesus Christ.

1 An Introduction to Ink-Jet Printing Technology and Formulation

Traditional printing methodologies operate by transferring media from a master pattern onto the desired substrate when the two are pressed into contact.[1] Consequently, when the design requires any modification, the master pattern must be physically altered in order for the change to be brought into effect. Though a trivial example, the common childhood activity of potato stamping illustrates well the limitations of traditional printing methods: were the child to have finished stamping squares and wished to move onto stars, a person skilled with a knife would be required to whittle a new master pattern from a new potato.

Ink-jet printers operate by depositing patterns without making direct contact with the substrate, in stark contrast with traditional methods. Print heads are mounted above the substrate and generate streams of picolitre droplets. Devices deliver the fluid to the surface in a controlled and repeatable manner to build up patterns drop by drop. Precise control over all aspects of ink-jet printing allows high-resolution arrays to be achieved with little variation between print runs.

Ink-jet technology has a number of advantages versus traditional methods: first, it offers superior flexibility because a physical master pattern is not required. Instead, the design is contained in a digital file that is electronically communicated to the device. Reconfiguring ink-jet printers in the event that a small alteration to the design were desired is thus no harder than depositing an entirely different pattern. Second, it is non-contact so can be implemented when the substrate is fragile, rough, textured or non-planar; printing onto non-solid substrates or powders is also possible. Third, ink-jet printing can be used to pattern a diverse range of fluids, provided their properties meet the requirements of the print head. Fourth, ink-jet devices are versatile; they can be designed and physically arranged to perform complex, multi-step manufacturing processes.[1]

This section is organised as follows: first, the working principle of common ink-jet techniques is given (Section 1.1). Second, important characteristics of ink-jet formulations are discussed (Section 1.2). Third, a brief survey of the application of ink-jet technology is made (Section 1.3). Fourth, the motivation for this thesis is provided, along with an outline of the rest of the document (Section 1.4).

1.1 Ink-Jet Printing Technology

An early patent for a device that bears resemblance to an ink-jet printer was filed by Lord William Kelvin[2] in 1870 for a machine capable of automatically recording telegraph messages by marking a paper feed with ink. Commercial ink-jet printers are a more recent phenomenon and have been developed since the 1960s and 1970s.[3–5] Whilst applications were initially limited to depositing low-resolution bar codes and postal addresses,[1] the technology is now ubiquitous in homes and offices for printing text and graphics onto paper. Modern-day systems largely divide into two categories: continuous ink-jet (CIJ) and drop-on-demand (DOD) ink-jet printers. This section introduces the principles of operation for CIJ and DOD systems.

1.1.1 Continuous Jetting Systems

CIJ systems operate by drawing a liquid from a reservoir and propelling it out of a nozzle to form a liquid jet moving through air. The Rayleigh-Plateau instability causes the jet to break into a series of discrete drops which are deposited on the substrate if no further intervention is made. The quality of CIJ printing relies upon the production of regularly-sized drops at consistent intervals. Methods to exercise control over jet break up have been developed, as well as means to selecting which drops are allowed to impact the substrate.[6] Drops produced in CIJ systems typically have velocities >10 m s^{-1}, with generation frequencies >100 kHz.[1,7]

Sweet[3] designed a system where the nozzle orifice is vibrated at a specific frequency to generate a stream drops at consistent intervals and with regular size (Fig. 1.1a). The purpose of the vibration is to ensure that the disturbance that eventually leads to jet break-up is initiated in a controlled manner. The stream of drops passes through an electrode that assigns a drop-specific charge. Drops are then directed to the correct location on the substrate by a deflection field. A gutter is positioned below the ink stream so that undesired drops can be recycled and thus not mark the paper feed.

Hertz[8] constructed a machine that utilises electrodes in a different way to dictate whether a drop reaches the substrate or not (Fig. 1.1b). A drop stream is produced by the Plateau-Rayleigh instability and passes through a variable-voltage ring electrode close to the point of jet break-up. Drops that are required for the pattern are not imparted any charge by the ring electrode and are allowed to fall unimpeded to the substrate. If a particular drop is not required, a high charge is imparted to it by the ring electrode, causing it to explode. The particles in the resulting spray all bear a charge of the same sign so that

they repel one-another orthogonally to the jet direction. The spray is intercepted by further electrodes and thus not make a mark on the surface.

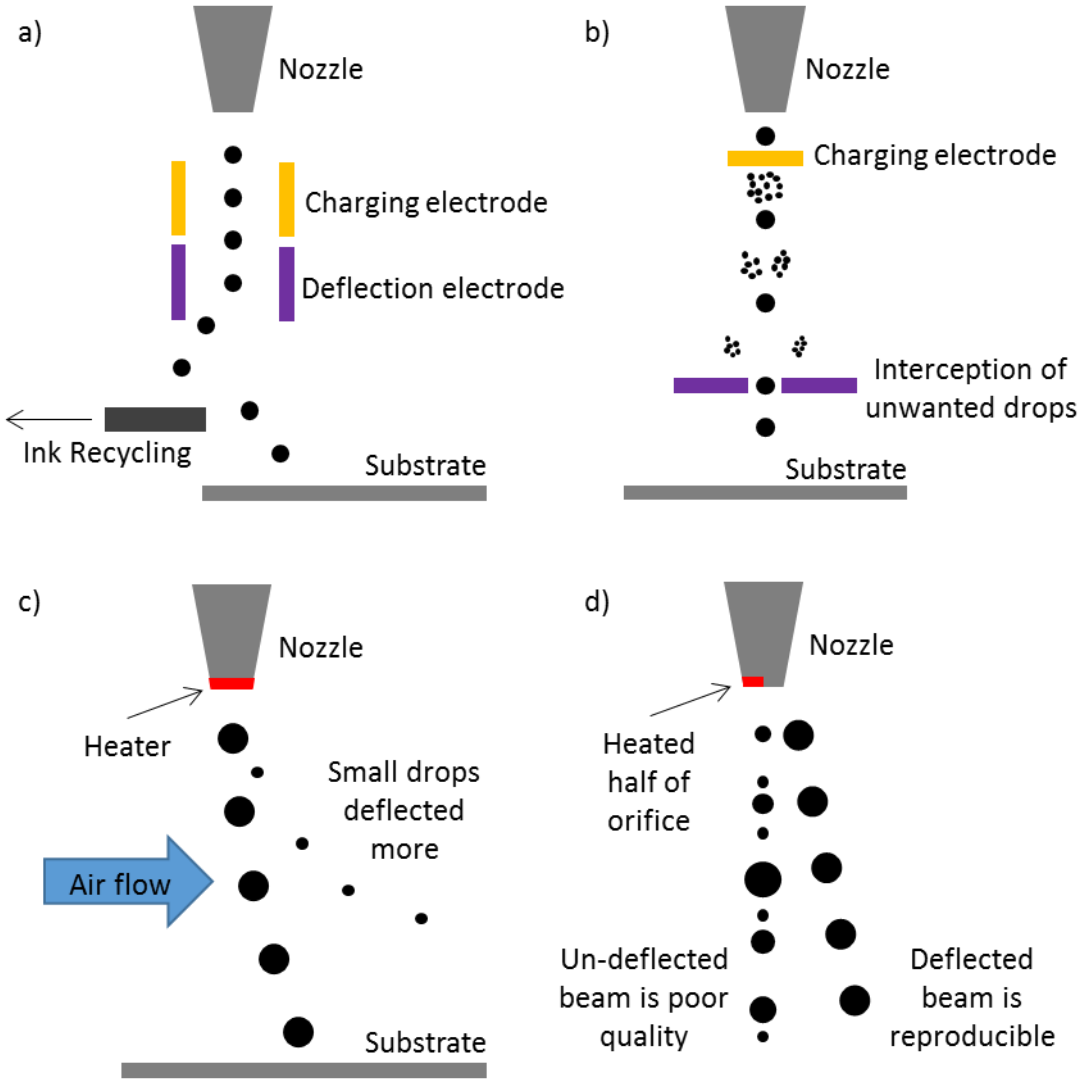

Figure 1.1. Schematic diagrams of the operating principles behind some continuous ink-jet printing methods discussed in the text. (a) The device designed by Sweet[3] where drops are charged by an electrode and deflected either to the substrate or the ink-recycling facility. (b) The device designed by Hertz[8] where required drops fall straight to the substrate and unwanted drops are exploded by excessive charge and intercepted. (c) The STREAM method[9] where heat modulation controls drop size and airflow removes smaller drops. (d) Controlled heating of an element encircling half of the nozzle orifice produces a reproducible deflected beam.[10]

The Sweet[3] and Hertz[8] methodologies both require charging and deflector electrodes whose bulk limits application. Recently, Kodak[9] developed STREAM by taking advantage of advances in electronics to install heating elements around the nozzle orifice (Fig. 1.1c) The Marangoni instability is exploited to control drop size: a pulse of heat is applied to the fluid as it exits the nozzle so that the temperature varies along the

jet, causing surface tension gradients; the warmer regions exhibit a lower surface tension and the colder regions a higher surface tension. The jet necks where the fluid is hotter and balloons where colder, leading to break-up. The volume of each drop is dictated by the length of the heat pulse and, when an air flow is introduced from the side, larger drops deviate less from their direction of travel than smaller ones. Small drops are directed away from the substrate and into an ink-recycling facility, so that drop selection occurs on a size basis.

A novel technique, developed by Chwalek *et al.*,[10] is distinct from the above methods because it deflects the fluid jet before it has broken into drops (Fig. 1.1d). The device possesses a heating element which encircles half the nozzle orifice and is subjected to voltage pulses; the jet is therefore asymmetrically heated. The apparatus produces a deflected beam of regular drops using three effects: first, the heated side of the jet has a lower surface tension than the unheated side so that a Marangoni stress bends the stream towards the latter. Second, a difference in curvature on both sides of the nozzle is driven by the surface tension gradient, deflecting the jet towards the cooler side. Third, the heated side has a lower viscosity than the unheated side, giving a pressure gradient that supports the first two effects. The deflected beam is a controlled and reproducible ink-jet.

1.1.2 Drop-on-Demand Jetting Systems

Drop-on-demand (DOD) jetting techniques only produce drops when required, unlike in CIJ systems which must have means for selecting a sub-set of those produced. Drops generated by DOD devices typically have velocities <10 m s^{-1} and drop generation frequencies <50 kHz;[6] both metrics are lower than for CIJ systems.

A common type of DOD ink-jet system, patented by Zoltan[4] in 1972, uses a piezoelectric transducer to squeeze a single drop from the nozzle (Fig. 1.2a). The nozzle orifice is sufficiently small that the fluid surface tension alone prevents liquid escape and the ink feed is under little or no static pressure. A cylindrical transducer surrounds the fluid chamber and contracts when an electrical signal is applied. Ink is rapidly displaced and is able to overcome the surface tension at the orifice to release a drop. Liquid in the chamber is replenished from an attached reservoir. Kyser and Sears[5] developed a similar device where a transducer plate forms a wall of the fluid chamber and the electrical signal causes it to bend inwards (Fig. 1.2b).

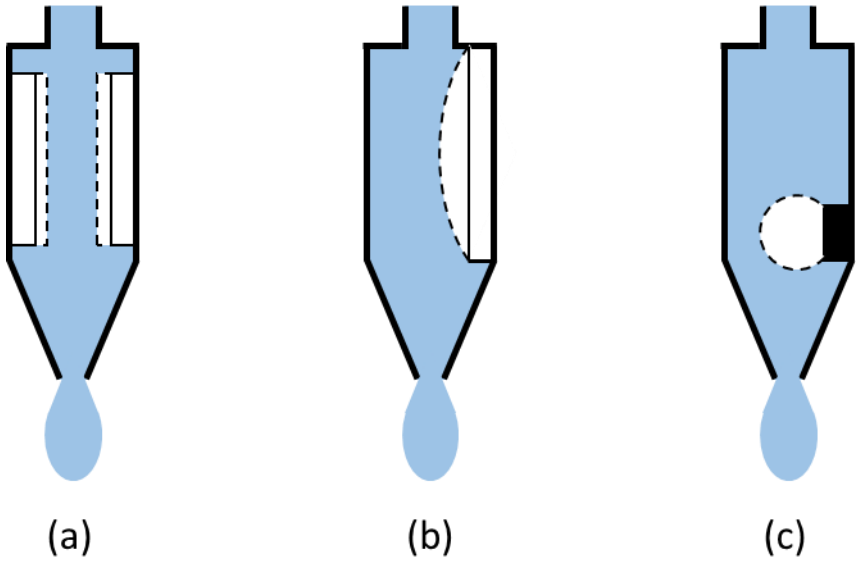

Figure 1.2. Schematic diagrams of the operating principles behind some drop-on-demand ink-jet printing methods discussed in the text. (a) The device designed by Zoltan[4] where a piezoelectric jacket contracts from initial volume (solid lines) to final volume (dashed lines) to eject a drop. (b) The device designed by Kyser and Sears[5] where a piezoelectric wall bends from its initial position (solid line) to final position (dashed line) to eject a drop. (c) The thermal drop-on-demand device where a bubble generated by the heater causes drop ejection.[11–13]

The waveform used to actuate the transducer in a piezoelectric DOD print head can be varied in order to modify the size of the drops being ejected.[6] Large drops relative to the orifice can be generated by applying a series of square waves but the production of small drops is more challenging. Chen and Basaran[14] investigated how the shape of the waveform affected drop generation in a print head with a cylindrical piezoelectric element. Three waveforms were trialled: the first was a square wave (Fig. 1.3a), which caused asymmetric drop ejection and the production of satellite droplets. Satellites are undesired additional drops, typically much smaller than the primary drop. The second was a bipolar waveform that was initially negative (Fig. 1.3b). The transducer first expands and draws ink back into the nozzle and then contracts to eject a drop. Drops were generated axisymmetrically, with reduced satellite formation versus the simple square wave. The third waveform trialled was a negative-positive-negative W-shaped pulse sequence (Fig. 1.3c). The mode of operation is the same as for the bipolar waveform, except that an additional negative pulse acts to withdraw the ink before full droplet formation. The drops generated had radii of approximately half the orifice radius.

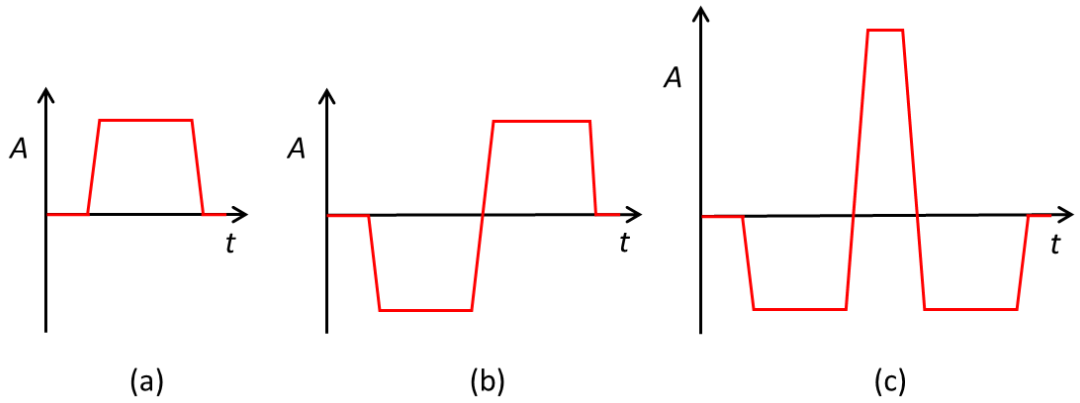

Figure 1.3. Schematic diagrams of amplitude *A* against time *t* for waveforms that can be used to actuate a piezoelectric transducer located in a drop-on-demand print head. (a) A monopolar waveform. (b) A bipolar waveform, which draws the fluid further inside the chamber before squeezing it out. (c) A W-shaped waveform, which behaves the same as a bipolar waveform but snaps the fluid back during drop formation to reduce drop volume.

Gan and co-workers[15] systematically investigated the variables of the three waveforms types. For a simple square wave, drop volume increased with amplitude linearly and for water, a 5-fold reduction in drop volume was achieved with a W-shaped waveform versus a monopolar waveform. Riefler and Wriedt[16] demonstrated that a drop with a 4-µm radius can be printed from a nozzle with a 40-µm diameter if a non-standard and freely-adjustable waveform is implemented.

Thermal ink-jet (TIJ) printing is the other standard actuation method implemented in DOD ink-jet print heads.[6] TIJ devices place heating elements in close proximity to the ink chamber at a position upstream from the nozzle orifice.[11–13] When a controlled heat pulse is supplied, the fluid close to the heater vaporises and expands (Fig. 1.2c). Consequently, the pressure in the chamber increases and a volume of ink is ejected from the orifice; the fluid in the chamber is replenished from the reservoir. TIJ print heads are able to produce drops of differing size: devices can have a line of heaters along the chamber so that changing the number activated changes the vapour volume and hence the drop volume.[12]

The choice of which of the various continuous and DOD ink-jet techniques to implement in a particular scenario depends largely on the specifics of the application. Typically CIJ ejects drops at higher velocities than DOD methods; CIJ systems are thus able to have a larger distance between the nozzle and substrate, which is advantageous for non-planar substrates.[7] However, piezoelectric and thermal DOD print heads do not require drop selection systems which often take the form of bulky electrodes; thus DOD devices are can be placed in closer proximity to the substrate.[6] Further, DOD printing

only exposes the fluid to the print head environment once, whilst ink recycling is commonplace when continuous ink jets are employed. Applications where sensitive or degradable fluids are deposited are therefore better served by DOD jetting. Piezoelectric devices are particularly favourable for sensitive fluids since samples are not subjected to heat, as in TIJ.

1.2 Ink-Jet Formulation

This section introduces important factors when designing ink-jet formulations. First, physical fluid properties are discussed and second, wider design considerations are noted.

1.2.1 Fluid Properties of Ink-jet Formulations

Fluids that are suitable for DOD ink-jet printing possess physical properties that exist within certain bounds. The Reynolds number *Re* is the ratio of inertial forces to viscous forces:

$$Re = \frac{v\rho d}{\eta}, \tag{1.1}$$

where v is the drop velocity, ρ is the fluid density, η is the fluid viscosity and d is the orifice diameter. The Weber number *We* quantifies the magnitude of inertial forces to surface forces:

$$We = \frac{v^2\rho d}{\gamma}, \tag{1.2}$$

where γ is the surface tension. The Ohnesorge number *Oh* eliminates inertial forces, giving the balance between viscous and surface forces:

$$Oh = \frac{\sqrt{We}}{Re} = \frac{\eta}{\sqrt{\gamma\rho d}}. \tag{1.3}$$

Defining $Z = 1/Oh$, Reis and Derby[17] suggest that printable fluids have $1 \leq Z \leq 10$, whilst Jang *et al.*[18] suggest $4 \leq Z \leq 14$. In both cases, the lower limit corresponds to failure of the drop to detach from the orifice due to viscous dissipation of the impulse from the print head. The upper limit, on the other hand, corresponds to the point where satellites begin to be generated.

The liquid-air surface tension of the fluid presents an additional barrier to drop formation; the kinetic energy imparted to the ink must be sufficient to overcome surface forces. Duineveld *et al.*[19] considered the pressure generated by the inertia of the drops required to overcome the Laplace pressure at the orifice to give the minimum fluid velocity $v_{\min}$ as

$$v_{\min} = \left(\frac{4\gamma}{\rho d}\right)^{1/2}. \tag{1.4}$$

Consequently, $We > 4$ for the fluid to have sufficient energy to overcome surface forces.

Fluid properties upon arrival of jetted drops at the substrate are also an important consideration when designing ink-jet formulations. It is unfavourable for high-resolution applications for drops to splash when they impact the surface. The onset of splashing for impact upon a planar surface is given by[20]

$$Re^{5/4}Oh = 50\,. \tag{1.5}$$

Together, the criteria $1 \leq Z \leq 10$, We > 4 and $Re^{5/4}Oh$ produce a range of fluid properties which are conducive to effective ink-jet printing, as displayed in Figure 1.4.

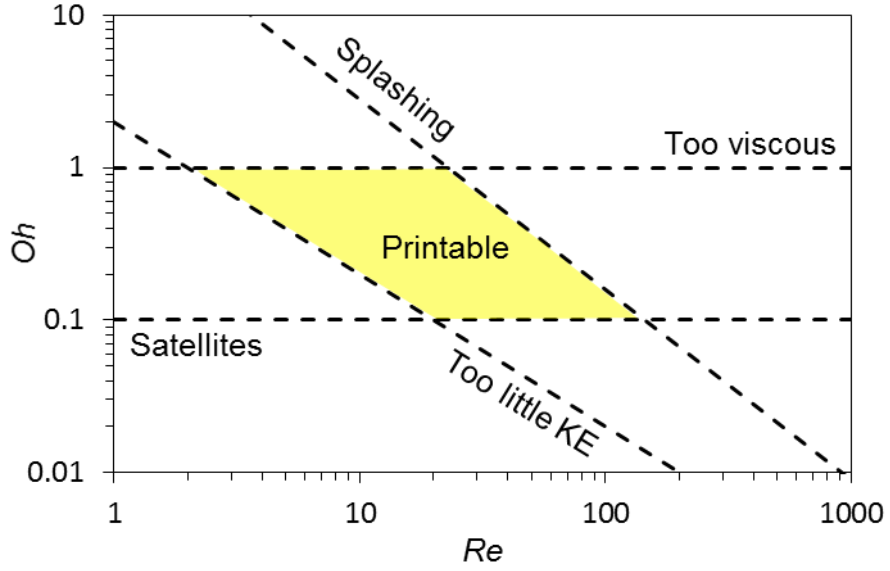

Figure 1.4. Fluids possessing physical properties embodied by the yellow region are printable; explanations for the dashed lines are given in the text. *Re* is the Reynolds number and *Oh* is the Ohnesorge number.[20]

1.2.2 Ink-Jet Formulation Design[21]

Considerable care is taken when designing ink-jet formulations. Not only must the fluid possess the correct balance of viscous and surface forces for effective printing, but it must also meet the wider criteria required by the process: first, the ink must be stable so that it does not degrade between formulation and printing. Second, it must be chemically inert towards the print system, so that damage is not caused to the hardware. Third, the fluid must flow effectively throughout the apparatus and wet the surfaces thereof to guard against the development of air bubbles. Fourth, the ink should give a stable meniscus at the nozzle orifice; it must not be susceptible to flooding of the nozzle faceplate due to the failure to sustain the weight of the fluid column in the print head or due to favourable wetting properties. Fifth, jetting should be stable for long periods to avoid printed defects due to misfires. Sixth, the fluid should have the correct interaction with the substrate to realise the desired pattern; wetting, spreading and absorption behaviour should be considered, as well as the drying dynamics. Seventh, the final deposit should meet the requirements of the intended use of the pattern; deposit connectivity, topology, morphology and functionality should be optimised.

Ink-jet formulations are therefore highly specialised for application, comprising many components to achieve optimal patterning. Plotting of text and graphics onto paper

is the most ubiquitous application of ink-jet technology and exemplifies well the complexity of formulations. The bulk of aqueous inks is water (60 – 90 %wt) and for colour, a pigment or dye is required (<10 %wt). In addition a number of other additives are included: a co-solvent optimises the viscosity and raises the solubility of dyes; surfactants influence the wetting properties of the fluid and the degree of penetration into the substrate; biocides improve the longevity of formulations by inhibiting biological growth; buffers stabilise the pH at the optimal level; defoamers inhibit bubble growth; binders improve adhesion of the deposit to the substrate; charging agents facilitate the assignment of drop-specific charges during CIJ; and initiators allow ultra-violet curing on the substrate.

1.3 Applications of Ink-Jet Printing

Ink-jet print heads are tolerant of a wide variety of fluid properties. Consequently, ink-jet formulations can be designed to incorporate a broad range of materials, facilitating the fabrication of diverse products.[22,23] Common functional materials delivered to substrates from print heads include metals, polymers and ceramics. Metals can be deposited on substrates in a molten state,[24] as a nanoparticle suspension[25] or as a degradable salt in solution;[26] silver nanoparticle deposits have been sintered to produce conductive tracks[25] and microelectromechanical systems can be built up from nanoparticle layers.[27] Polymers can be delivered as a hot wax[28] or in solution; ink-jet printing has been used to deposit doped polymers in organic light-emitting devices[29] and to generate large organic photovoltaic films for use in solar cells.[30] Ceramics can be delivered as nanoparticles, which when pyrolysed can give three-dimensional structures.[31]

Ink-jet technology may also be used as part of complex manufacturing processes. Three examples are given: first, Costa and Hutchings[32] demonstrated that ink-jet printing can be used to mask substrates prior to etching; a solvent-based polymer ink was deposited onto steel that was subsequently etched with acid to pattern the metal surface. Second, ink-jet printed drops can act as the etchant: de Gans *et al*.[33] jetted solvent drops onto a polystyrene film so that material in the film re-distributed to leave holes where drops impacted. Third, inverse ink-jet printing is possible: Jahn *et al*.[34] deposited an array of ink-jet printed drops and applied a layer of immiscible polymer on top, which after solidification left cavities in the polymer film.

1.4 Thesis Motivation and Outline

Ink-jet fluids are tailored for specific applications to give high performance in storage, during jetting, as drops impact the substrate and during evaporation; high performance of the final product is also targeted. The motivation for this thesis is to further explore formulation design. The aim is to develop novel formulation strategies that facilitate new applications of ink-jet printing or enhance the viability of existing applications. Two particular avenues of investigation are pursued in this thesis: first, the design and application of inks that are formulated as a single phase but separate during evaporation on the substrate. Second, the feasibility of using emulsion formulations to overcome the limitations of jetting high-molecular-weight polymers in solution.

This thesis is organised as follows: in Chapter 2, the instrumentation and procedures used during practical investigations are detailed; in Chapter 3, the investigation into phase-separating fluids is presented and discussed; in Chapter 4, the investigation into the use of emulsions as a means for delivering high-molecular-weight polymers is presented and discussed; in Chapter 5, the concluding remarks are made.

2 Instrumentation and Procedures

The key equipment implemented in the collection of results in this thesis are outlined in this chapter, along with a description of common procedures. First, methods of preparing substrates are detailed. Second, an overview of the rig used to print and image drops is given. Third, image processing routines are presented. Last, a description of the methods used to determine contact angles and surface and interfacial tensions are provided. Significant deviations from the procedures or experimental arrays recorded here are noted alongside the affected results in the subsequent chapters.

2.1 Substrate Preparation

Glass coverslips were square (width 22 mm, thickness 0.13 − 0.16 mm) or circular (diameter 16 mm, thickness 0.13 – 0.17 mm) geometries. The coverslips can be used with very little treatment, especially if trace particulates on the surface are beneficial for inducing pinning of the drop contact line, were it desired. A short period of bath sonication in ethanol (AR grade, 2 min), with solvent removed under an argon or nitrogen flow, removed particulates on the surface and was sufficient for exploratory trials. A more rigorous cleaning procedure was used to ensure a more repeatable cleanliness. The substrates were placed in a PTFE beaker (60 mL) and bath sonicated in ethanol (AR grade) for 5 min. They were then rinsed with pure water (Milli-Q) and as much fluid as possible was decanted from the beaker. Chromosulphric acid, BIC, (*Merck Millipore*, ≥92% H_2SO_4, ≥1.3% CrO_3) was then added so that the coverslips were entirely submerged and left covered. The use of a PTFE beaker ensures the BIC does not act upon the walls and heat the vessel. After 30 min, the BIC was decanted out of the beaker and the substrates were rinsed well in pure water, before being dried under a flow of argon or nitrogen. The substrates were stored in covered petri dishes. Pure water drops (Milli-Q) formed a contact angle of 4 ± 1° on substrates manufactured in this manner.

Glass coverslips with a hydrophobic coating were also manufactured and implemented as printing substrates. They are useful in cases where the jetted fluids ordinarily wet glass surfaces or, as a result of low surface tension, do not form spherical caps under ink-jet impact conditions. The procedure used for hydrophobising substrates was as follows. Glass coverslips were washed with acetone and ethanol, placed in a bath sonicator in 2-%wt alkaline detergent solution (*Decon Laboratories*, Decon90) for 2 hours, rinsed in water (Milli-Q) and dried at 130° for >1 hour. Hexamethyldisilazane (*Alfa Aesar*, >98%) was deposited on the surface by vapour deposition in a vacuum desiccator

overnight. The coated substrates were rinsed in water, dried under an argon flow and stored in a covered petri dish. The contact angle for pure water was 75 ± 2°.

2.2 A Rig for Visualising Ink-Jet Printed Drops

Two rigs were employed. The first was initially designed and constructed by Dr. E. Talbot,[35] though improvements have since been made by the author, and the second was constructed in conjunction with Miss. B. Kazmierski. The purpose of the rigs is to allow ink-jet printed drops to be visualised during the jetting and drying processes. They each comprise a complete printing system, arrays of lenses and mirrors, illumination sources, high-speed cameras and a PC unit. Both rigs have similar design, capability and operation. The first rig was used for the majority of the experiments reported in subsequent chapters and a description is provided below.

2.2.1 Ink-Jet Printing System

Figure 2.1 displays a schematic diagram of the ink-jet printing system. Liquid was supplied to the print head (*MicroFab*, MJ-ABP-01) from an air-tight reservoir, comprising a 7-mL glass vial and custom PTFE cap. The container was connected to the nozzle via a length of fluorinated ethylene propylene tubing (i.d. = 1.6 mm) submerged at one end in the fluid, a microfluidic junction (*OmniFit*) and a length of PTFE tubing (i.d. = 1.27 mm) connected to the print head inlet. Early experiments made use of silicone tubing (i.d. = 1 mm) but was replaced with the PTFE tubing to ensure no plasticisers leached into the formulation. The application of an overpressure using the syringe allowed fluid to be pushed to the print head. Fluid was kept at the orifice by surface tension, so the height of the fluid column above the print head and the magnitude of the overpressure

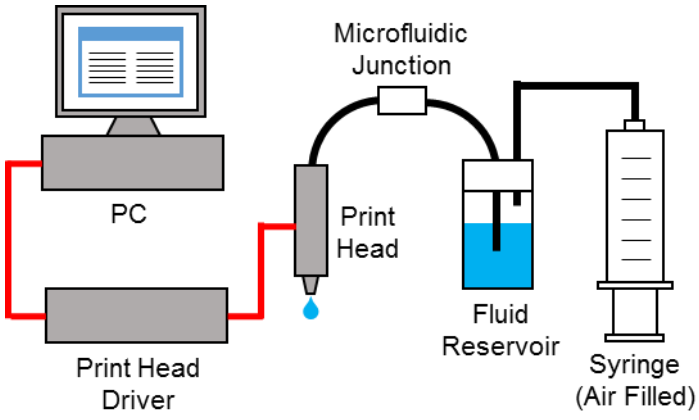

Figure 2.1. Schematic diagram of the ink-jet printing system. An overpressure resulting from compression of the air in the syringe supplies the print head with fluid from the reservoir. The print head is actuated with a driver controlled by a PC.

were controlled to ensure that the nozzle plate did not flood.

The print head was connected to a driver (MicroFab, CT-M3-02 JetDrive III Controller) that was controlled by software (*MicroFab*, JetServer v1.03.05) on the PC. The print head is compatible with a wide range of fluids including aqueous, organic and aromatic solvents, as well as formulations containing biological, electrical, polymeric and particulate materials.[36] It can be operated in the temperature range 20 − 70° and with fluids that have viscosities of 3 – 20 mPa s, surface tensions of 20 – 70 mN m^{-1} and a pH in the range 2 – 11. The print head is constructed using a glass tube that tapers down at one end to an orifice of diameter 50 μm, which functions as the nozzle (Fig. 2.2).[37] The other end is connected to the fluid supply. The print-head produces drops using a piezoelectric mechanism, through a cylindrical lead zirconate titanate (PZT) element with radial poling that is bonded to a portion of the glass tube. The inner and outer surfaces of the PZT element are electrodes, with the electrode on the inner surface wrapping around onto the outer surface to make it accessible. Both electrodes are connected to wires that receive electrical input from the driver. The device is cased in a metallic body and the nozzle has a degree of protection from damage provided by metal appendages on the casing.

Drops were ejected from the nozzle when the print head was actuated by the driver. The driver can induce the printing of a single drop on demand or a continuous stream of drops at a specified frequency. The outer electrode in the print head is grounded and any voltages were applied by the driver to the inner electrode, generating an electrical field across the PZT element.[37] Application of a positive voltage to the inner electrode

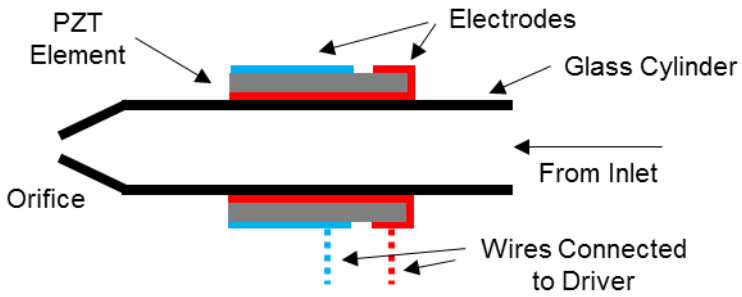

Figure 2.2. Schematic diagram showing a cross-section through the dispensing element for a *MicroFab* MJ-ABP-01 print head. A glass cylinder is connected to the fluid supply at one end and narrows to the orifice at the other. A cylindrical lead zirconate titanate (PZT) element is bonded to the glass. The element changes shape under voltages applied to the electrodes by the driver, resulting in the ejection of drops from the orifice.

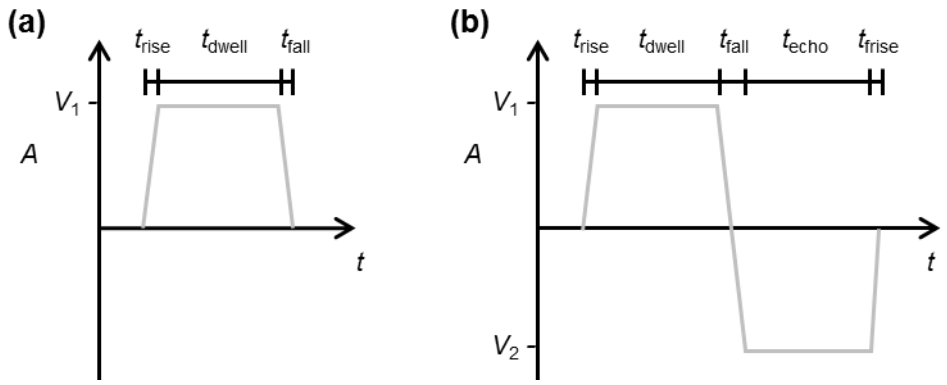

Figure 2.3. The amplitude A over time t for (a) a unipolar and (b) a bipolar waveform, appropriate for actuating the print head. A unipolar waveform is characterised by a voltage V_1, rise time t_{rise}, dwell time t_{dwell} and a fall time t_{fall}. A bipolar waveform is additionally characterised by a second voltage V_2, an echo time t_{echo} and a final rise time t_{frise}.

causes the element to expand radially and contract axially, whilst a negative voltage causes it to contract radially and expand axially, as a result of its radial poling. The glass tube deforms with the element, since the two are bonded.

The actuation signal, or waveform, was defined using the software on the PC, with either unipolar or bipolar signals possible (Fig. 2.3). A unipolar waveform is characterised by a voltage V_1, rise time t_{rise}, dwell time t_{dwell} and a fall time t_{fall}. A bipolar waveform is additionally characterised by a second voltage V_2, an echo time t_{echo} and a final rise time t_{frise}. Considering the unipolar waveform first, the element expands during t_{rise} so that an expansion wave propagates in both directions along the tube. The perturbation is reflected as a compression wave at the supply end back towards the orifice, resulting in the ejection of a drop. The shape of the element is held constant during t_{dwell} and contracts over t_{fall}. If t_{dwell} is timed to end as the reflected compression wave passes, a larger and faster drop can be printed. The principle behind a bipolar waveform is identical, except the additional element modulation is designed to cancel out residual oscillations in the glass tube so that the fluid in the system returns to rest more quickly.[38] A symmetrical bipolar waveform was implemented in the printing trials in the subsequent chapters, typically characterised by t_{rise} = 3 μs, t_{dwell} = 25 μs, t_{fall} = 6 μs, t_{echo} = 25 μs and t_{frise} = 3 μs. A lower voltage threshold V_{min} exists below which viscous and surface forces prevent drop detachment.[38] Above the threshold, drops are ejected and drop volume and velocity are linear with V_1. The amplitude of the waveforms were varied to ensure the ejection of a single drop with minimal satellites, with the appropriate value of V_1 found just above V_{min}.

2.2.2 Imaging the Jetting Process

Figure 2.4 shows the experimental arrangement for imaging the jetting dynamics at the nozzle. The orifice was backlit using an LED (*Beaglehole Instruments*, 455 nm). A video recording corresponding to a single print head actuation was collected using a high-speed camera (*Photron*, FASTCAM SA4) with a telescopic lens (*LaVision*, 12x Zoom Lens). The camera CCD has an array of 1024 × 1024 pixels and has a maximum frame-recording rate of 500×10^3 frames per second (fps) on a region of interest of 128 by 16 pixels. Software on the PC (*Photron*, PFV v3.3.8) was used to control the camera, allowing recording parameters such as the area of the CCD to be used, the shutter speed and the frame rate to be defined. The software contained a manual trigger to start recordings. The camera trigger output was connected to the print head driver master trigger so that initiating a recording on the camera also resulted in the ejection of a drop from the nozzle. The software was also the means for visualising and saving the video output.

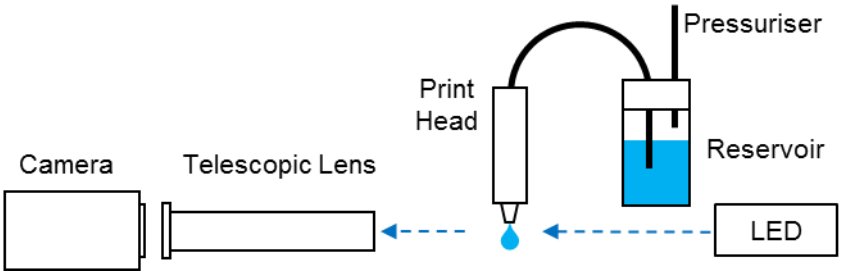

Figure 2.4. Schematic diagram of the rig used to image the formation and detachment of drops at the print head orifice. The system was illuminated by an LED and recorded using a high-speed camera.

2.2.3 Imaging Drops on the Substrate

Figure 2.5 shows the experimental arrangement for imaging the drying dynamics of drops on the substrate. The rig is capable of collecting images of the drop from the side and from underneath. Imaging from the side allows drop height, diameter and contact angle as function of time to be investigated, whilst imaging from below allows internal drop drying dynamics to be probed.

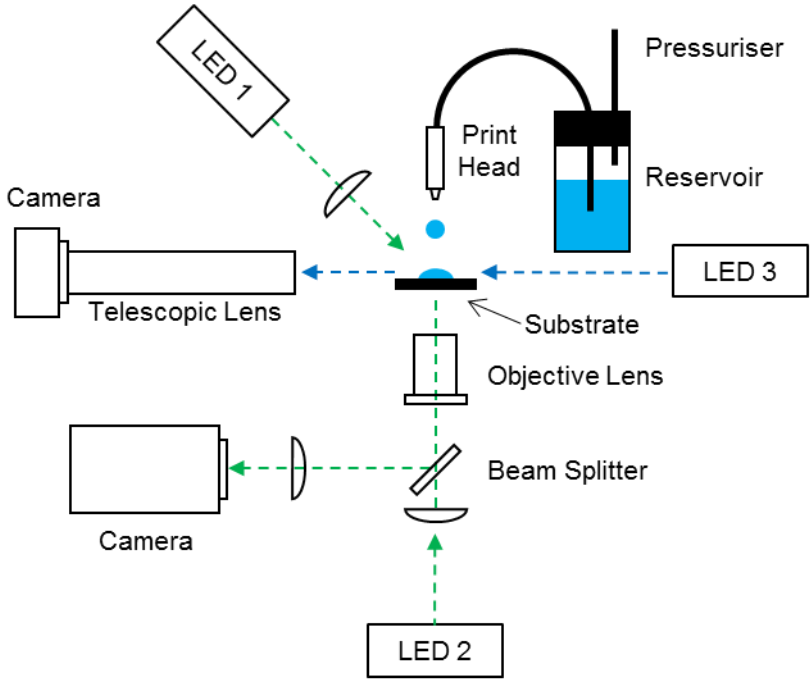

Figure 2.5. Schematic diagram of the rig used to image the drying process of jetted drops on a substrate. Three LEDs were implemented to allow recording to take place on two high-speed cameras simultaneously from the side and from below. Unlabelled components in the path of the lights are plano-convex spherical lenses.

2.2.3.1 Imaging Printed Drops from Below

To record the view of printed drops from underneath, two complementary methods of illumination were employed, to allow both dark- and bright-field imaging. Dark-field images were obtained using a collimated LED (Thorlabs, 505 nm, LED 1) mounted obliquely to the substrate (~20° from the plane of the substrate) with a lens condensing the light down to a focused spot. Refraction of the light from LED 1 through the drop is depicted in Figure 2.6. The path of the light was such that light did not pass directly through the drop or the glass substrate into the objective lens held below. Illumination with LED 1 was not uniform for drops with high contact angles: only the side of the drop facing the source exposed to incident light whilst the side facing away is in shadow (see Fig 2.6). However, drops with low contact angles were fully illuminated. Discontinuities in the refractive index such as suspended particulate material scattered light, of which an amount was directed towards the objective. Only the parts of interfaces and surfaces not in shadow to LED 1 were visible. Typical images captured using dark-field illumination are shown in Figure 2.7 for (a) particles on a substrate and (b) a printed drop of an emulsion of toluene and SDS solution. The particles are strongly scattering and their centres are readily discerned against the black background (Fig. 2.7a). In Figure 2.7b, only the left edges of the main drop and suspended droplets are visible since that

corresponds to the face exposed to incident light from LED 1. The positions of the suspended drops are better indicated than the drop footprint, due to the small size of the former. The drop footprint was generally poorly resolved using dark-field illumination.

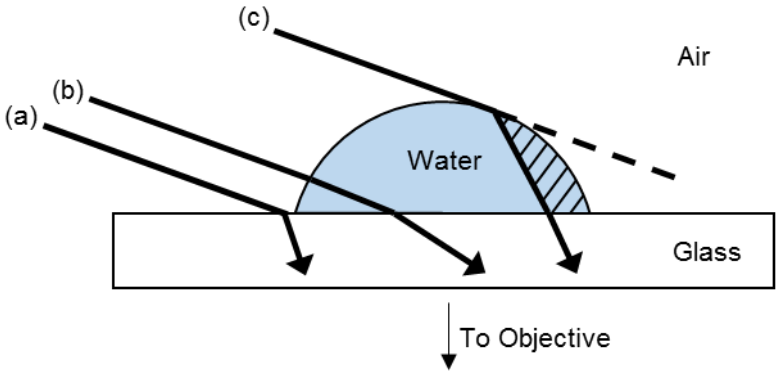

Figure 2.6. Schematic diagram of the path of incident light from LED 1 through a drop of water with a contact angle of 75° on a glass substrate. (a) Light incident on the substrate. (b) Light incident at the drop surface closest to LED 1. (c) Light incident at the tangent to the drop surface. In all three cases, light is not refracted onto the normal of the lower glass-air surface and is consequently not passed to the objective lens mounted below. The shaded portion of the drop has no light from LED 1 passing through it so that particulate material would not scatter within the region.

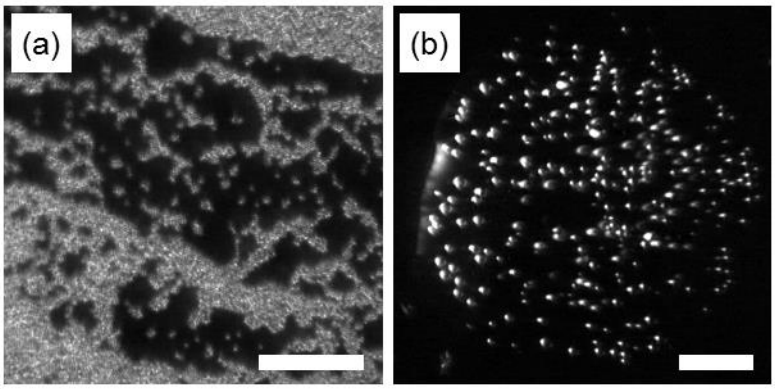

Figure 2.7. Images collected on the printing rig using dark-field illumination (LED 1 only). (a) Polystyrene particles with a diameter of 1 μm deposited onto a glass substrate. (b) A drop of an emulsion of toluene (φ_v = 0.1) and 4 mM SDS jetted using a symmetrical bipolar waveform of amplitude 30 V and deposited onto an untreated substrate. Scale bars are 30 μm.

Drops were also illuminated by a second collimated LED (Thorlabs, 505 nm, LED 2, Fig. 2.5). Light from the source was passed through the rear aperture of the objective lens and onto the underside of the sample, where it reflected from the upper substrate surface and the underside of any species on the substrate back towards the objective; light reflected from the lower substrate surface was not in the focal plane. Illumination with LED 2 was suited to the tracking of phase boundaries like larger suspended droplets or the contact line. Figure 2.8 displays typical images collected for (a) particles on a

substrate and (b) a printed water drop. The particles have a much lower contrast relative to the substrate and their centres are harder to observe than when using LED 1 (compare Figs. 2.7a and 2.8a). The light from LED 2 was orthogonal to the plane of the substrate so that the entire drop footprint was evenly illuminated (Fig. 2.8b), unlike in the case for LED 1 where part of the drop was in shadow (compare Figs. 2.7b and 2.8b).

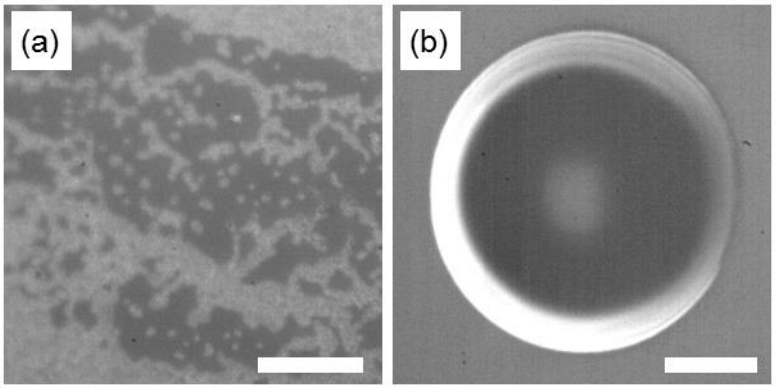

Figure 2.8. Images collected on the printing rig using LED 2 only. (a) Polystyrene particles with a diameter of 1 μm deposited onto a glass substrate. (b) A drop of water jetted using a symmetrical bipolar waveform of amplitude 30 V and deposited onto a substrate hydrophobised with hexamethyldisilazane. Scale bars are 30 μm.

The strengths of illumination with LED 1 and 2 are complementary and when both were employed simultaneously, complex drying dynamics were effectively visualised. LED 2 highlighted the shape of the drop footprint and the extent of large structures, whilst LED 1 highlighted edges and made smaller species and details easy to track; suspended particles were best imaged with illumination from LED 1 since they are strongly scattering, giving a strong contrast relative to the black background.

Images from underneath were collected with the objective lens mounted below the substrate. The centrelines of the print head, drop and objective lens were aligned, with the upper surface of the substrate in the focal plane of lens. The lens (*Olympus*, 50×) is semi-apochromatic, has a numerical aperture of 0.50 and has a working distance of 10.6 mm. The objective is infinity corrected and was imaged onto the CCD of a high-speed camera (*Photron*, FASTCAM APX RS) with a plano-convex spherical lens. The camera CCD has an array of 1024 × 1024 pixels and has a maximum frame-recording rate of 360 × 10^3 fps. The control software and triggering regime was the same as that described above in Section 2.2.2.

2.2.3.2 Imaging Printed Drops from the Side

To view a drop on the substrate from the side, a very similar set up to that described above in Section 2.2.2 is employed (Fig. 2.5). The drop was silhouetted against a collimated LED (*Beaglehole Instruments*, 455 nm) and images were recorded with a high-speed camera (*Optronis*, CR450x3) equipped with a telescopic lens (*LaVision*, 12x Zoom Lens). The camera has a maximum frame rate of 1×10^4 fps and a CCD with an array of 1024 × 1024 pixels. Software on the PC (*Optronis*, TimeBench v2.6.10.937) was used to control the camera, allowing the recording frame rate, shutter speed and area of the CCD to be used to be defined. The software contained a manual trigger to initiate recordings. The camera trigger output was connected to the master trigger on the print head driver so that initiating a recording also caused a drop to be ejected onto the substrate from the print head. A typical image of an ink-jet printed drop captured from the side is displayed in Figure 2.9. The cusps mark the position of the contact line and mark the separation between the drop and its reflection.

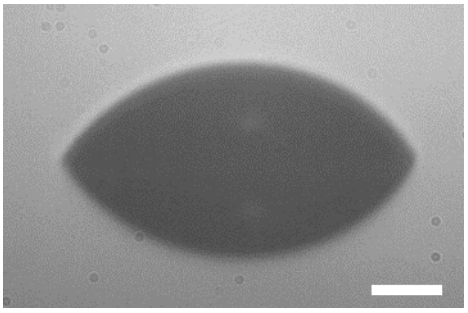

Figure 2.9. A drop of an aqueous 6-%wt butanol solution imaged from the side using the printing rig. The drop was jetted using a symmetrical bipolar waveform of amplitude 30 V onto a substrate hydrophobised with hexamethyldisilazane.

2.2.3.3 Imaging Printed Drops from Below and from the Side Simultaneously

Drops were imaged from the side and from underneath simultaneously when it was desirable to consider internal drying dynamics alongside changes in drop geometry and size. The triggering regime was modified so that the print head driver and *Optronis* high-speed camera were triggered from the *Photron* high-speed camera. All images were calibrated against an array of dots of known size and spacing (*LaVision*, Micro Calibration Plate).

2.3 Image Processing

The MATLAB script used to extract the drop geometry from side-view video footage was written by Dr. L. Yang. The core function of the program is to detect the edge of drops, fit a circular arc and extract the drop height, radius and contact angle. Edge detection is performed by importing a greyscale image as a matrix and using a Sobel operator to detect the rate of change of pixel greyscale along each image row and column. For the simple case where a series of white pixels butt against a series of black pixels, the edge is perfectly sharp, so that the differential greyscale will only show an integer value at the edge and be zero everywhere else (Fig. 2.10a). A more realistic scenario would see the transition from white to black take place via a region of pixels of intermediate greyscale, giving uncertainty as to the exact location of the edge (Fig. 2.10b). A plot of differential greyscale against pixel number now shows a peak with a finite width. If the edge is assumed to appear where the greyscale gradient is steepest, the edge is located at the peak maximum. For each row and column, the edge is taken to be at the location of the first maximum reached when scanning inwards from the image boundaries. A threshold value below which any maxima are disregarded as noise is a required input of the program and can be varied to improve results. The algorithm returns a series of points that correspond to the edge. The equation in Cartesian coordinates for a circle of radius R, centred at (a,b) is

$$R^2 = (x-a)^2 + (y-b)^2. \tag{2.1}$$

The circular arc that best fits the edge is then found using the linearised equation for a circle:

$$x = a \pm \sqrt{(y-b)^2 - R^2}. \tag{2.2}$$

To operate the program, the user imports a calibration image recorded at the time of experiment. The image comprises an array of dots of known size. The field of view is cropped so that only one dot is visible, so that the program can fit a circle in order to isolate its diameter in pixels. Input of the dot diameter gives the calibration factor. Next, the video recording of a drying drop is imported. The camera is triggered before the drop arrives on the substrate so that the first frame is empty. The first frame can then be considered a background and subtracted from all subsequent images. The removal of the background simplifies the images so that the only pixels that do not appear white are those that correspond to the drop. Edge detection is thus more reliable. The other user inputs are the noise threshold and the frame rate; the drop baseline is manually identified from the cusps marking the place where the drop and its reflection meet. The drop contact angle as a function of time is calculated from the tangent to the fitted circular arc at the baseline.

The drop height h and radius r are calculated from the arc relative to the baseline, and assuming the drop is axisymmetric, its volume V can then be calculated using the spherical cap relationship.

$$V = \frac{1}{6}\pi h(3r^2 + h^2). \tag{2.3}$$

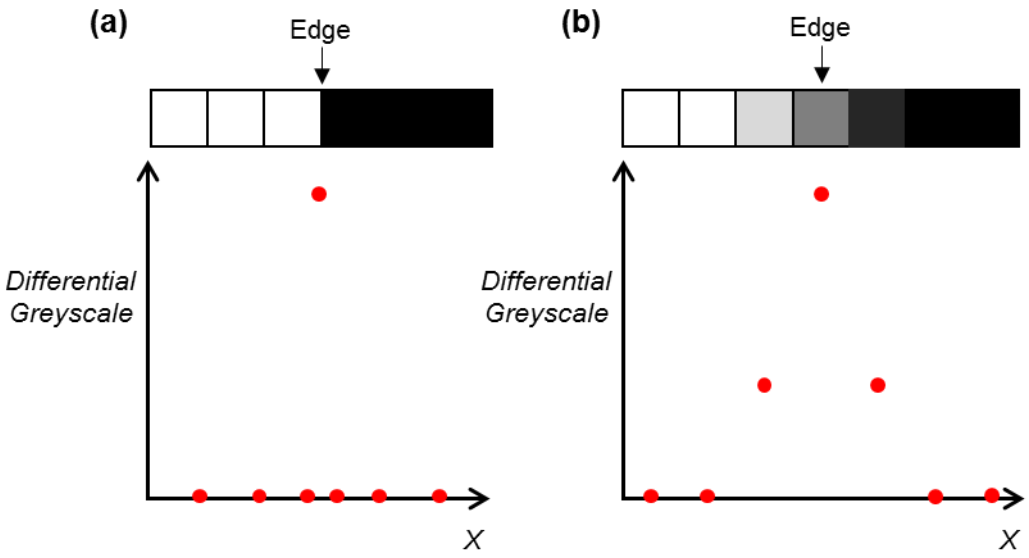

Figure 2.10. Differential greyscale against pixel number X for (a) perfectly sharp edge and (b) a less-sharp edge.

2.4 Pendant Drop Tensiometry and Contact Angle Measurements

The instrument used to measure contact angles and interfacial tensions (*First Ten Ångstroms*, FTÅ200) is schematically displayed in Figure 2.11. It features a translation stage, a mechanical syringe pump, an LED backlight, a telescopic lens and a camera (*Watec*, Wat-902B). The instrument is controlled from software (*First Ten Ångstroms*, Fta32 v2.0) on a PC that allowed the camera feed to be visualised, the syringe dispenser to be actuated, image capture and analysis routines to be run.

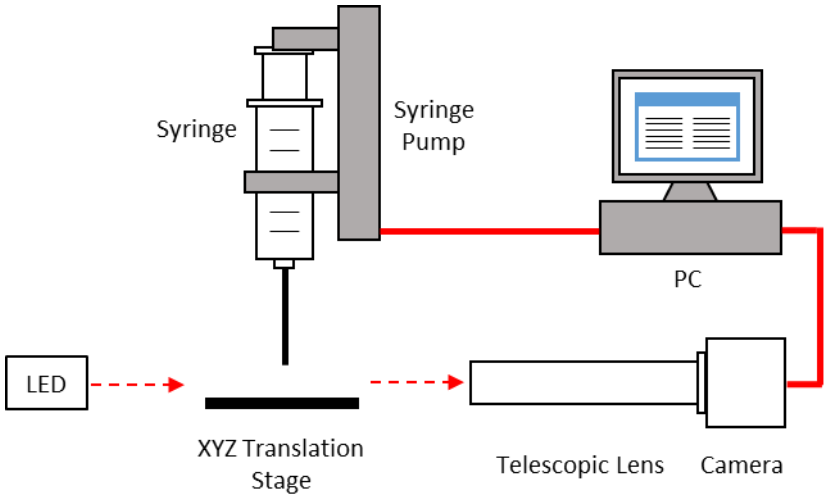

Figure 2.11. Schematic diagram of the instrument used to measure contact angles and interfacial tensions (*First Ten Ångstroms*, FTÅ200). A syringe is suspended in a mechanical pump above an XYZ translation stage. Fluids either suspended from the needle or dispensed onto a surface are illuminated by an LED and images are collected by a camera. The equipment is controlled from a PC.

2.4.1 Surface and Interfacial Tension Measurements

The surface and interfacial tensions of solutions and liquid mixtures were measured by pendant drop tensiometry. Mixtures and solutions were prepared by mass using an analytical balance in volumetric flasks. The glassware had been bath sonicated in dilute alkaline detergent solution for >30 min (*Decon Laboratories*, Decon90), rinsed with water (Milli-Q) and dried in an oven. Where the liquid-air surface tension was of interest, samples were decanted into cuvettes and an air bubble was formed at the tip of a J-shaped needle fitted onto an air-filled syringe mounted in the mechanical dispenser (Fig. 2.12a). Where a liquid-liquid interfacial tension was of interest, the syringe was filled with the fluid of lower density so that the drop was buoyant. The syringe, needle and cuvettes were cleaned in the same manner as the glassware used to make the samples. The cell was positioned on the tensiometer in front of LED backlight such that the camera viewed the bubble or drop as a silhouette. The focus was optimised through the software by maximising the greyscale gradient over the bubble/drop edge. Typically, videos were

recorded for 2 – 5 s at 10 fps to ensure the surface or interfacial tension was not changing over time. Images were calibrated in situ using a 3-mm sphere.

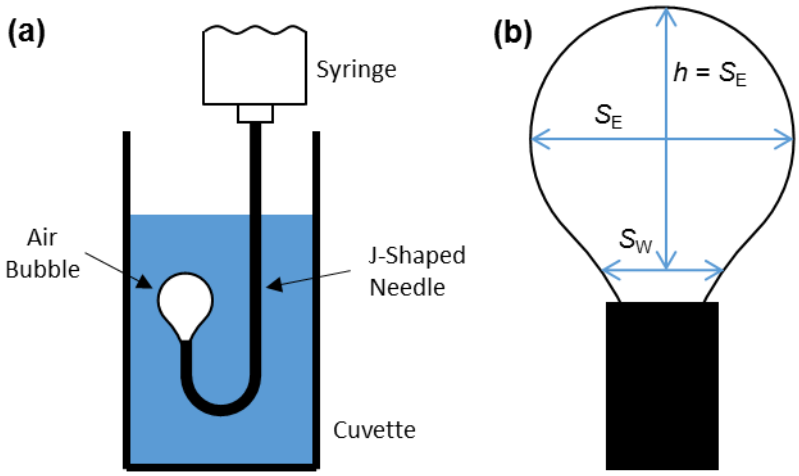

Figure 2.12. (a) Schematic diagram of the arrangement used to measure air-liquid surface tensions. A cuvette is partially filled with the target liquid. Air is dispensed from the syringe through a J-shaped needle and a bubble forms at the tip. The syringe can be filled with a liquid to allow liquid-liquid interfacial tensions to be measured. (b) The key bubble dimensions used to extract the surface or interfacial tensions from images using the Bashforth-Adams method. S_E is the maximum diameter of the drop. S_W is the diameter at a distance h from the apex equal to S_E.

Surface and interfacial tensions were extracted from captured images using the Fta32 software. The software runs an edge detection routine and then solves the Young-Laplace equation numerically. The Laplace pressure Δp of the pendant drop or bubble is defined according to

$$\Delta p = \gamma \left(\frac{1}{R_1} + \frac{1}{R_2} \right), \tag{2.4}$$

where γ is the surface or interfacial tension and R_1 and R_2 are the radii of curvature. A pendant drop can be assumed axisymmetric and thus the hydrostatic pressure can be written as

$$\Delta p = \Delta \rho g h, \tag{2.5}$$

where $\Delta \rho$ is the difference in density between the drop or bubble and the surrounding media, g is the acceleration due to gravity and h is the height in the drop; h is measured from the drop apex. The combination of equations (2.4) and (2.5) gives the Laplace-Young equation:[39]

$$\Delta \rho g h = \gamma \left(\frac{1}{R_1} + \frac{1}{R_2} \right). \tag{2.6}$$

Fluid densities were measured using a pycnometer of volume = 1.004 ± 0.004 mL. The image size is defined by the calibration factor. The software solves the Laplace-Young equation for γ numerically using the user inputs according to the Bashforth-Adams

method.[40] The principle behind the Bashforth-Adams technique is that a form factor that describes the drop or bubble geometry is compared against reference tables to determine γ. The maximum diameter of the drop or bubble S_E is found from the curves that describe the edge (Fig. 2.12b). Measuring from the apex, the diameter at which the height h is equal to S_E is denoted S_W. Padday[41] has produced a reference table against which the surface or interfacial tension can be found using the values of S_W/S_E and $\Delta\rho$.

The air bubble or liquid drop formed at the tip of the J-shaped needle must be sufficiently large that the shape is influenced by both gravitational and capillary forces. The relative magnitudes of the surface and gravitational forces are quantified using the Bond number *Bo*:

$$Bo = \frac{\Delta\rho g h_0 r_0}{\gamma}, \tag{2.7}$$

where $\Delta\rho$ is the difference in density between the drop/bubble and the surrounding liquid, g is the acceleration due to gravity, h_0 is the distance between the needle and the drop/bubble apex, r_0 is the equatorial radius and γ is the surface/interfacial tension. For an air bubble of volume ~7 μL suspended in a liquid with γ = 30 mN m^{-1}, $\Delta\rho$ ~ 1000 kg m^{-3}, h_0 ~ 3 mm and r_0 ~ 1 mm. Consequently, *Bo* ~ 1 and both gravitational and surface forces influence the bubble shape. Similarly, for a liquid drop of volume 35 μL suspended in an immiscible liquid with γ = 3 mN m^{-1}, $\Delta\rho$ ~ 30 kg m^{-3}, h_0 ~ 5 mm and r_0 ~ 2 mm, *Bo* ~ 1.

2.4.2 Contact Angle Measurements

Contact angle measurements for sessile drops of solutions or liquid mixtures were carried out using the FTÅ200 instrument. Solutions and liquid mixtures were deposited from a syringe equipped with a straight blunt needle onto hydrophobic and hydrophilic substrates prepared as per Section 2.1; the needle was withdrawn from the drops before measurements were taken. Liquid sample and glassware preparation was conducted in the manner above in Section 2.4.1. The contact angles for pure water were measured in the open. For a liquid mixture containing volatile components, the composition of the drop would be subject to change due to evaporation were the measurement conducted in the open. To mitigate, the substrate was housed in a covered cuvette with a needle inlet and suspended above a tissue soaked in the sample in order to saturate the environment with the sample vapour, thus preventing evaporation (Fig. 2.13a). Where a liquid-liquid-solid contact angle was of interest, the substrate was submerged in a covered cuvette of the fluid of lower density and a syringe was used to deposit a drop of the denser liquid.

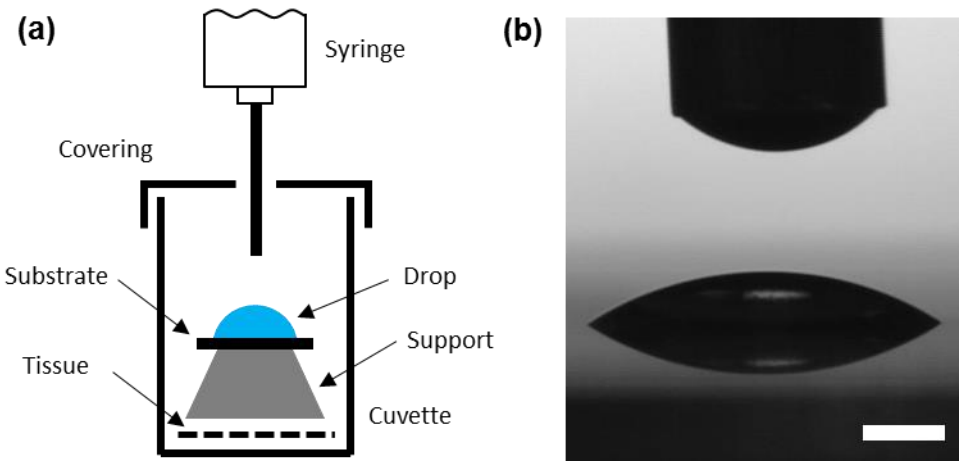

Figure 2.13. (a) Schematic diagram of the arrangement used to measure the contact angles of liquid mixtures with volatile components. A covered cuvette has a substrate supported above a tissue soaked in the target liquid. A drop is placed on the substrate using the syringe. (b) An image of a water drop on a glass substrate hydrophobised with hexamethyldisilazane, with the needle tip in view. The scale bar is 0.5 mm.

In all cases, the syringe-substrate assembly was positioned on the tensiometer translation stage in front of the LED backlight and in view of the camera and telescopic lens. The substrate was tilted by a few degrees along the LED-camera axis so that the cusps that mark the points at which the drop and its reflection meet would be visible (Fig. 2.13b). Sessile drops were created by pressing a small amount of fluid out of the syringe needle and then raising the substrate using the translation stage to extract the pendant drop. Video footage of the sessile drop formation was typically carried out at 10 fps for 2 – 5 s after transfer in order to track the contact angle over time. For drops that formed immediate and constant contact angles, single images were sufficient.

Contact angles were extracted using the Fta32 software. The user is able to define the drop baseline using the cusps that show the points at which the drop and its reflection meet. The program can then fit a circular arc across the whole drop surface or, if the drop is distorted, it can perform a non-spherical fit to both contact points in turn. The equations that describe the drop edge and the baseline are then solved for their intersections and the equation for the drop edge is differentiated at the intersection to find the gradient.[40] The contact angle then follows from basic trigonometry, taking into account any baseline tilt.

The influence of gravitational forces upon the drop shape may be estimated using the bond number (Equation (2.7)); for a sessile drop r_0 is the contact line radius and h_0 is the apex height. When measuring solid-liquid-vapour contact angles, drop volumes were < 1 μL. For a 0.5 μL drop with $\Delta\rho$ = 1000 kg m^{-3}, r_0 = 0.7 mm, h_0 = 0.5 mm and γ = 30 mN m^{-1}, *Bo* ~ 0.1 and gravitational forces do not influence the drop shape. When

measuring liquid-liquid-solid contact angles, it was more difficult to extract drops from the needle than in air; drops were as small as possible to minimise the effect of gravity on drop shape. For a 15 μL drop with $\Delta\rho$ = 30 kg m^{-3}, r_0 = 2.5 mm, h_0 = 2.7 mm and γ = 3 mN m^{-1}, *Bo* ~ 0.7; gravitational forces are smaller in magnitude than interfacial forces.

3 The Ink-Jet Printing of Fluids that Phase Separate on the Substrate

Ink-jet formulations are highly tailored so that desired properties are manifested at every stage of a process. Effective design requires a detailed knowledge of fluid dynamics and of the chemical, physical and rheological properties of the materials implemented. The nature of formulations therefore differ widely depending on their requirements. For graphics applications, pigments are often delivered as aqueous dispersions with additives incorporated to stabilize the particles, modify the viscosity, control spreading behaviour on the substrate, reduce the occurrence of bubbles and prevent jetting failure after an idle period.[42] Once a drop arrives on the substrate, control over drying dynamics and deposit morphology can be exerted. Collection of solids at the drop periphery under convective flow[43] can be prevented using additives to generate surface tension gradients that give rise to internal flows.[44] Strategies for controlling particulate migration using formulation rheology have been demonstrated.[45]

When designing functional inks, the overall miscibility of all the components is an important consideration and solvent mixtures are often used to optimize the solubility of active ingredients. Such mixtures are chosen to be fully miscible. Many pairs of liquids are, however, only partially miscible and exist as one phase only over a limited range of compositions. If the minor component were to be present at a concentration above its solubility limit, a second phase rich in that species would form. This chapter presents an investigation into the behaviour of an ink-jet formulation of a partially miscible solvent pair deliberately chosen so that phase separation occurred during evaporation of a droplet on a substrate. The aim is to discover if phase separation influences the way a drop dries and whether it could provide an interesting control mechanism for deposit morphology.

This chapter is organised as follows: first, physical aspects of multi-phase systems and manipulations thereof are discussed (Section 3.1). Second, fundamentals of the wetting and spreading of surfaces by a liquid are presented (Section 3.2). Third, an overview of the evaporative dynamics of sessile droplets is given (Section 3.3). Fourth, a criterion for observing phase separation in ink-jet scenarios is developed and potential applications are postulated (Section 3.4). Fifth, printing trials with the butanol-water system are presented and the criterion for separation is refined (Section 3.5). Sixth, a wide range of aqueous systems are screened for formulations with the propensity to separate during evaporation (Section 3.6). Seventh, an account of printing trials with the

DPGMEA-water system is presented (Section 3.7), including patterning trials with solutes (Section 3.8). Eighth, a non-aqueous phase-separating formulation is investigated (Section 3.9) and ninth, phase separation in jetted polymer-salt solutions is explored (Section 3.10). Last, a summary of the investigation is given (Section 3.11).

3.1 Physical Aspects of Multi-Phase Systems

This section describes systems with multiple phases. First, illustrative phase diagrams are presented, along with their interpretation. Second, a description of the kinetics of phase separation is given.

3.1.1 Phase Diagrams[46]

Phase diagrams are a powerful way of rationalising the physical changes to a system as external conditions are varied. Figure 3.1 displays a typical temperature-composition phase diagram at constant pressure for formulations comprising partially miscible liquids A and B showing regular solution behaviour. It may be used to illustrate how phase-separation can be realised in an ink-jet formulation containing partially miscible liquids. The diagram has a one-phase region (P = 1), corresponding to a single liquid phase, and a two-phase region (P = 2), corresponding to two liquid phases in equilibrium. Consider a formulation with the composition marked at point (a): the proportion of liquid B present is below the solubility limit so that the system is a single phase, rich in A.

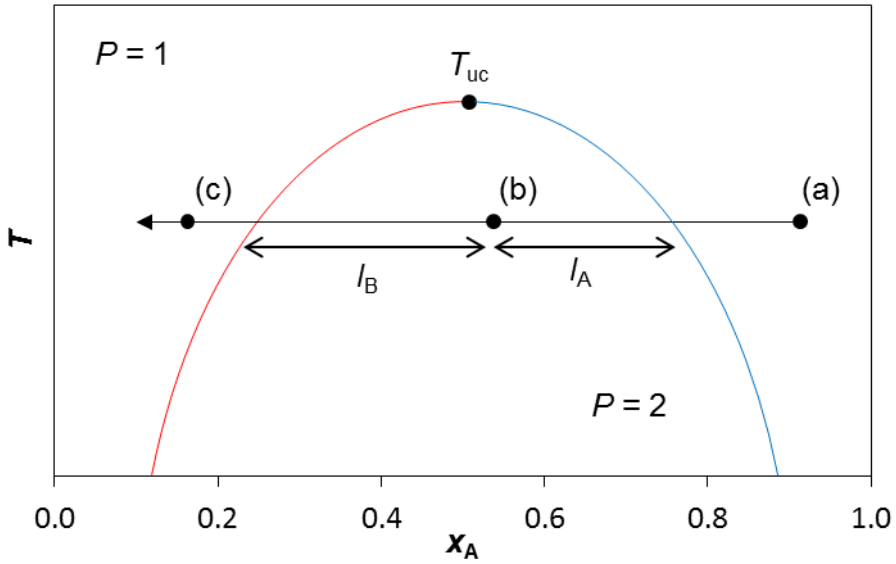

Figure 3.1. A typical liquid-liquid phase diagram for a binary mixture of A and B showing regular solution behaviour, as a function of temperature T and mole fraction of A, x_A. In the two-phase region, the blue line gives the composition of the phase rich in A and the red line gives the composition of the phase rich in B. T_{uc} is the upper critical solution temperature.

If a formulation were printed with the conditions marked by point (a) and evaporation at constant temperature were to occur such that the mole fraction of liquid B increased, the mixture may pass into the two-phase region: at point (b), liquid B has increased in concentration and surpassed its solubility limit. The system now exists in a

phase-separated state. The compositions of the two phases in equilibrium are given by the termini of the tie line and their relative proportions are given by the lever rule:

$$n_A l_A = n_B l_B \,. \tag{3.1}$$

where n_A and n_B are the number of moles of the phases rich in A and B respectively, and l_A and l_B are lengths on the tie line. In the two-phase region at fixed temperature and pressure, as the global composition changes, the relative proportions of the two phases may change, but the compositions are fixed.

If evaporation were to continue such that the formulation were to continue to be enriched with liquid B, the mixture may pass into the one-phase region of the diagram again: at point (c) the fraction of liquid B has become so large that the proportion of liquid A is below its solubility limit in B. Consequently, a single phase, rich in B, is formed.

The mutual solubility limits of A and B increase with temperature so that the two-phase region occupies an increasingly small mole fraction range. The phase boundaries for the phase rich in A and the phase rich in B converge at higher temperatures to a point known as the upper critical solution temperature T_{uc} (Fig. 3.1), above which the system forms a single phase at all compositions. When designing a phase-separating formulation, the components must be below T_{uc} under drying conditions else separation cannot be observed. For example, methanol and pentane mixtures have T_{uc} = 287 K,[47] so that mixtures are fully miscible under ambient conditions of T = 293 K.

3.1.2 Kinetics of Phase Separation[48]

The stability of a mixture of partially miscible liquids A and B towards phase separation depends on the composition. Assuming the mixture may be described as being regular in character, the variation of the free energy of mixing, $\Delta_{mix}G^{reg}$, with composition at temperature T is typified by Figure 3.2a. Outside of the miscibility range of liquids A and B, the phase compositions that minimise the free energy is given by the co-tangent to $\Delta_{mix}G^{reg}$; these compositions are marked *a* and *b*. As the temperature is raised, the entropic contribution to $\Delta_{mix}G^{reg}$ increases so that compositions *a* and *b* converge (Fig. 3.2b). When the upper-critical solution temperature T_{uc} reached, the entropy of mixing becomes large enough to eliminate the minima caused by the enthalpy of mixing. Tracing the compositions corresponding to *a* and *b* as a function of temperature gives the binodal boundary. Compositions in the range $0 < x_A < a$ and $b < x_A < 1$ are stable with respect to phase separation. Also marked on Figure 3.2a are the inflexion points *c* and *d*, which also converge to the same point as *a* and *b* when T_{uc} is reached (Fig. 3.2b). Tracing the compositions corresponding to *c* and *d* as a function of temperature gives the spinodal

boundary. Compositions in the range $a < x_A < c$ and $d < x_A < b$ are metastable with respect to phase separation, whilst compositions in the range $c < x_A < d$ are unstable with respect to phase separation.

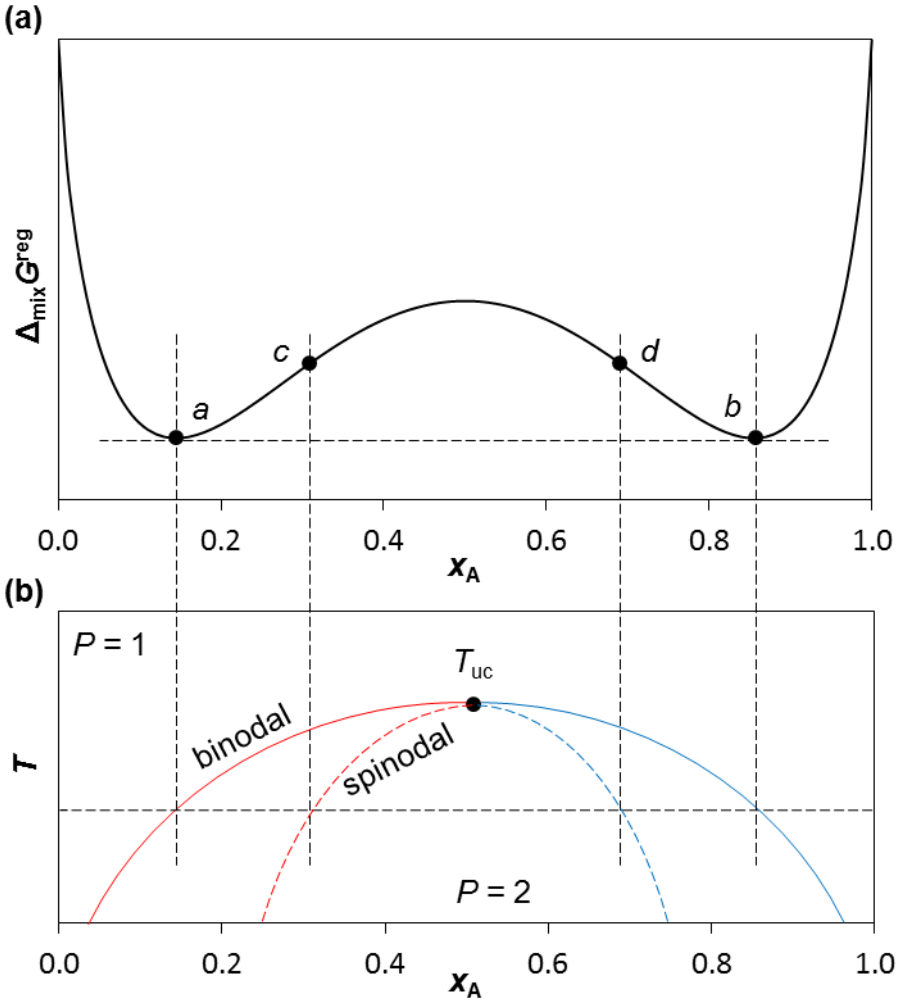

Figure 3.2. (a) The Gibbs free energy of mixing for a regular binary mixture, $\Delta_{mix}G^{reg}$, against the mole fraction of component A, x_A, characteristic for $\beta > 2$. (b) A liquid-liquid phase diagram for a binary mixture of A and B, as a function of temperature T and mole fraction of A, x_A. The solid lines are the binodal boundaries and mark the two phase region. The dashed lines mark the spinodal boundaries. In the two phase region, the blue line gives the composition of the phase rich in A and the red line gives the composition of the phase rich in B. T_{uc} is the upper critical solution temperature.

The mode of phase separation observed when a liquid B is present in liquid A at concentrations above the miscibility limit depends on the initial composition. Compositions that are unstable with respect to miscibility ($c < x_A < d$) undergo phase separation by spinodal decomposition. The curvature of the free energy of mixing between c and d is negative, so that small fluctuations in composition decrease the free energy. Consequently, the process has no energy barrier and occurs spontaneously. The local composition in the mixture changes continuously with time and tends towards

compositions at *a* and *b* where free energy in minimised. Since composition change is continuous, the interfaces between the two phases are initially diffuse, but become more defined with time. The lack of barrier to spinodal decomposition in the unstable part of the phase diagram means that separation happens throughout the whole of the sample simultaneously, leading to a bicontinuous morphology for solids or viscous liquids.

The mechanism for phase separation for compositions in the metastable region ($a < x_A < c$ and $d < x_A < b$) is different because the curvature of the free energy of mixing is positive. Small fluctuations in composition therefore have the effect of raising the free energy, so that it is favourable for the system to return to homogeneity. The free energy of a system in the range $a < x_A < c$ is reduced if a large fluctuation in composition results in a phase that is close to composition *b*. Metastable compositions therefore phase separate through a nucleation and growth process. Classic nucleation theory states that the change in free energy $\Delta_{nuc}G$ on forming a droplet of a new phase of *n* molecules is given by

$$\Delta_{\mathrm{nuc}}G = \frac{4}{3}\pi r^3 \Delta_{\mathrm{demix}}G_{\mathrm{v}} + 4\pi r^2 \gamma_{\mathrm{AB}}\,, \tag{3.2}$$

where $\Delta_{demix}G_v$ is the free energy change of moving from a homogenous state to a phase separated state *per unit volume*, *r* is the radius of the cluster and γ_{AB} is the interfacial tension between the two phases. The first term is the free energy released by nucleating a new phase and is negative, whilst the second term is the free energy penalty of creating the new interface and is positive. The second term is dominant below a critical radius r_c, so that it is unfavourable for small droplets to grow. If, however, the nucleus survives long enough to grow larger than r_c, then it is energetically favourable for it to grow. Phase separation therefore requires large composition fluctuations and the growth of critical nuclei; hence the system is metastable towards separation. The critical radius is given by

$$r_{\mathrm{c}} = -\frac{2\gamma_{\mathrm{AB}}}{\Delta_{\mathrm{demix}}G_{\mathrm{v}}}\,. \tag{3.3}$$

The rate of formation of critical nuclei may be estimated using Arrhenius-style dynamics. The random seeding of the second phase leads to isolated droplets of the second phase that are unevenly distributed across the system, in a marked difference to spinodal decomposition.

The principles of phase separation kinetics may be applied to an ink-jet scenario. Were a formulation of partially miscible liquids A and B with $x_A > b$ (see Fig 3.2) jetted onto a substrate, the drop would initially be a single phase. Were component B to increase in concentration during evaporation, the formulation would eventually pass through the

binodal; the formulation would then be metastable and separation could occur through nucleation and growth of the second phase. Depending on nucleation sites and the rate of evaporation, separation might not occur until the formulation passes through the spinodal, at which point there is no barrier to separation.

3.2 Fundamentals of the Wetting of Surfaces by Fluid

Section 3.1 considered the thermodynamic origins of phase separation and the manipulation of multi-phase systems. This section describes basic models of the wetting and spreading of fluids on, first, liquid surfaces and, second, solid surfaces. The equilibrium morphology of liquid drops at rest on surfaces depend partly on the associated surface and gravitational forces; the models presented will apply to scenarios where the gravitational forces can be neglected so that fluid lenses adopt spherical cap geometries in the absence of contact line pinning.

3.2.1 The Wetting of Liquid Surfaces by Liquids

A drop of liquid B placed on the surface of liquid A may either spread to cover the surface (Fig. 3.3a), partially wet as a lens (Fig. 3.3b) or pseudo-partially wet as a thin film with excess liquid forming a lens (Fig. 3.3c).[49,50]

The short-range forces that govern the propensity of a lens of liquid B to spread over liquid A are displayed in Figure 3.4a. The spreading coefficient $S_{B/A}$ is defined as

$$S_{B/A} = \gamma_{AV} - (\gamma_{BV} + \gamma_{AB}) , \tag{3.4}$$

where γ_{AV} is the surface tension of liquid A, γ_{BV} is the surface tension of liquid B and γ_{AB} is the interfacial tension between liquids A and B. A criterion for complete wetting ($\theta_1 = \theta_2 = 0$) of liquid A by liquid B is $S_{B/A} > 0$, whilst for $S_{B/A} < 0$, liquid B remains as a lens.

$S_{B/A}$ cannot be greater than zero at equilibrium, since liquid A is in the presence of the vapour of both A and B, and liquid A would condense a film of B onto its surface. The initial spreading coefficient, however, where liquid A is only in equilibrium with vapour A and liquid B is only in equilibrium with vapour B, can be positive. Once in contact, liquids A and B become mutually saturated, changing the surface and interfacial tensions from those for pure A and B.[51] The equilibrium value of the spreading coefficient therefore differs from the initial value.

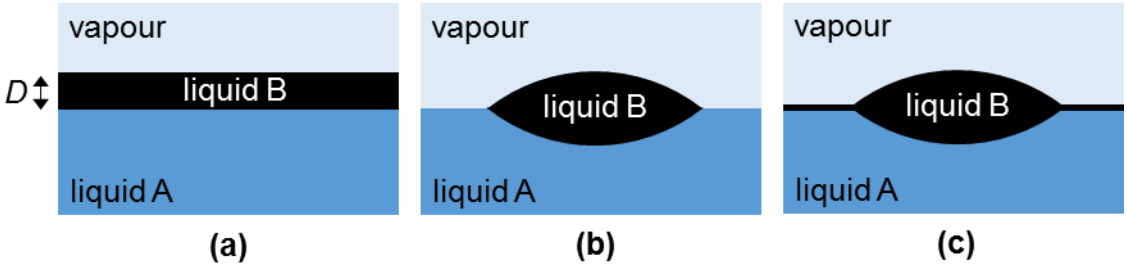

Figure 3.3. The different modes of wetting by liquid B on liquid A. (a) Complete wetting: liquid B spreads over liquid A. (b) Partial wetting: liquid B forms a lens on the surface of liquid A. (c) Pseudo-partial wetting: liquid B forms a monolayer over the surface of liquid A and the remaining fluid forms a lens.

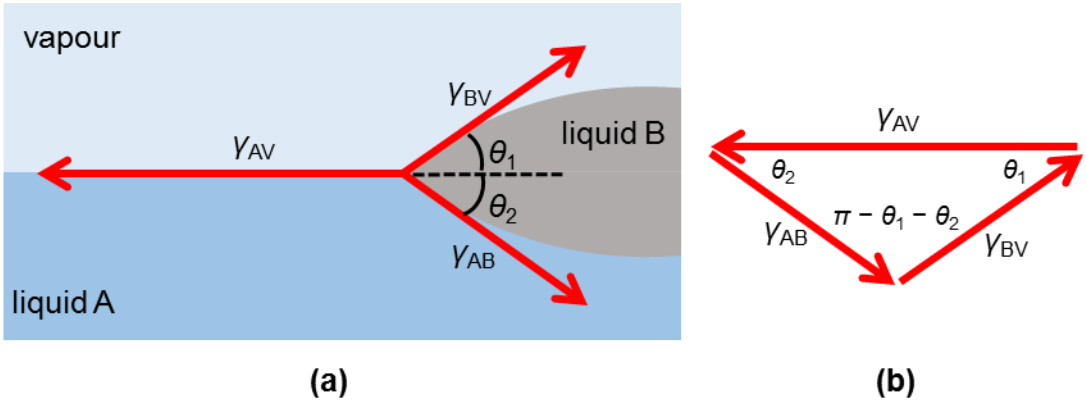

Figure 3.4. (a) The equilibrium contact angles of liquid B resting as a lens on liquid A. (b) There is no net force at the contact line so the surface and interfacial forces can be rearranged into a Neumann triangle.

The long-range forces also have an impact on the propensity for liquid B to spread over liquid A. Consider a film of liquid B of thickness D on liquid A in air (Fig. 3.3a). The interfacial free energy $F(D)$ per unit area is given by

$$F(D) = \gamma_{AB} + \gamma_{BV} - \frac{A_H}{12\pi D^2}, \tag{3.5}$$

where A_H is the Hamaker constant. The last term in the equation represents the effect of the long-range van der Waals forces between liquid A and the vapour phase, which act via the film of liquid B. The Hamaker constant is a function of the dielectric properties of all three phases, and can either be positive or negative. For phases 1 and 2 interacting across medium 3, if $A_{H,132} > 0$ the free energy reduces as the film thins, whilst if $A_{H,132} < 0$ the free energy reduces as the film thickens.[49,50]

Liftshitz theory allows Hamaker constants to be calculated from the static dielectric constants ε_1, ε_2 and ε_3 of the three phases and their dielectric constants at imaginary frequencies.[52] Assuming all three phases have the same main electronic UV absorption frequency ν_e (typically ~3×10^{15} s^{-1}), a simplified expression for $A_{H,132}$ may be written in terms of the refractive indices n_1, n_2 and n_3 at visible wavelengths:

$$A_H = A_{H,\nu=0} + A_{H,\nu>0} \tag{3.6}$$

$$A_H \approx \frac{3}{4}kT\left(\frac{\varepsilon_1 - \varepsilon_3}{\varepsilon_1 + \varepsilon_3}\right)\left(\frac{\varepsilon_2 - \varepsilon_3}{\varepsilon_2 + \varepsilon_3}\right) + \frac{3h\nu_e}{8\sqrt{2}} \frac{(n_1{}^2 - n_3{}^2)(n_2{}^2 - n_3{}^2)}{(n_1{}^2 + n_3{}^2)^{0.5}(n_2{}^2 + n_3{}^2)^{0.5}\{(n_1{}^2 + n_3{}^2)^{0.5} + (n_2{}^2 + n_3{}^2)^{0.5}\}}. \tag{3.7}$$

For oil on water, A_H is usually positive.

Throughout preceding analysis, the line tension has been neglected. The line tension τ is the energy per unit length associated with the three-phase contact line; it can have a positive or negative value and is predicted to have a magnitude of 10^{-11} – 10^{-12} N.[53] The line tension can be included in Equation (3.8):

$$\cos\theta_1 = \frac{\gamma_{AV} - \gamma_{AB}\cos\theta_2}{\gamma_{BV}} - \frac{\tau}{\gamma_{BV} r_0}, \tag{3.8}$$

where r_0 is the radius of the lens. For a drop with $r_0 = 10^{-4}$ m and $\gamma_{BV} = 10^{-2}$ N m^{-1}, the last term in the above equation is ~10^{-5}. It is therefore reasonable to neglect the line tension when analysing ink-jet printed drops.

The wetting behaviour of liquid B on liquid A, then, depends on both the short- and long-range forces (Eq. (3.5)). Since $S_{B/A}$ and A_H can both be greater than or less than zero, there exist four different combinations of the two and sketches of $F(D)$ for each is displayed in Figure 3.5. The four combinations have a common limit of $F(D) \rightarrow (\gamma_{AB} + \gamma_{BV})$ as $D \rightarrow \infty$. Equation (3.5) breaks down if the system no longer resembles a liquid covered by a film of finite thickness. Consequently, short range forces dominate as $D \rightarrow 0$ so that $F(D) \rightarrow \gamma_{AV}$.[50]

When $S_{B/A} < 0$, the minimum in $F(D)$ occurs as $D = 0$ for both $A_H > 0$ and $A_H < 0$ (Figs. 3.5a and 3.5b).[50] The result in both cases is partial wetting: a lens is formed. The drop shape would be determined by the balance of gravitational and surface forces and for small drops where the Bond number $Bo << 1$, the latter are of much larger magnitude the former. Neglecting gravitational forces, the lens adopts a configuration as displayed in Figure 3.4a. The net force at the three-phase contact line at equilibrium is zero.[51] The contact angles of liquid B above and below the surface of A are therefore given by

$$\gamma_{AV} = \gamma_{BV}\cos\theta_1 + \gamma_{AB}\cos\theta_2 . \tag{3.9}$$

Since at equilibrium the net force at the contact line is zero, the three surface tensions may be treated as vectors and arranged end to end into Neumann's triangle (Fig. 3.4b). If all three surface tensions are known, angles θ_1 and θ_2 may thus be computed using the cosine rule: for a triangle with sides of length a, b and c, with opposite angles A, B and C respectively,

$$a^2 = b^2 + c^2 - 2bc\cos A . \tag{3.10}$$

When $S_{B/A} > 0$ and $A_H > 0$ (Fig 3.5c), the free energy is minimised at a finite value of D. A thin film of liquid B therefore spreads over the surface of liquid A until that thickness is achieved; the excess liquid forms lenses (Fig. 3.3c).[50] The thin film has a molecular thickness[49] since the strength of the dispersion interaction decays with D: short-range forces become dominant at both $D \rightarrow 0$ and $D \rightarrow \infty$.

Finally, when $S_{B/A} > 0$ and $A_H < 0$ (Fig 3.5d), the free energy is minimised as the film thickens. Consequently liquid B spreads to cover the surface of liquid A.[50]

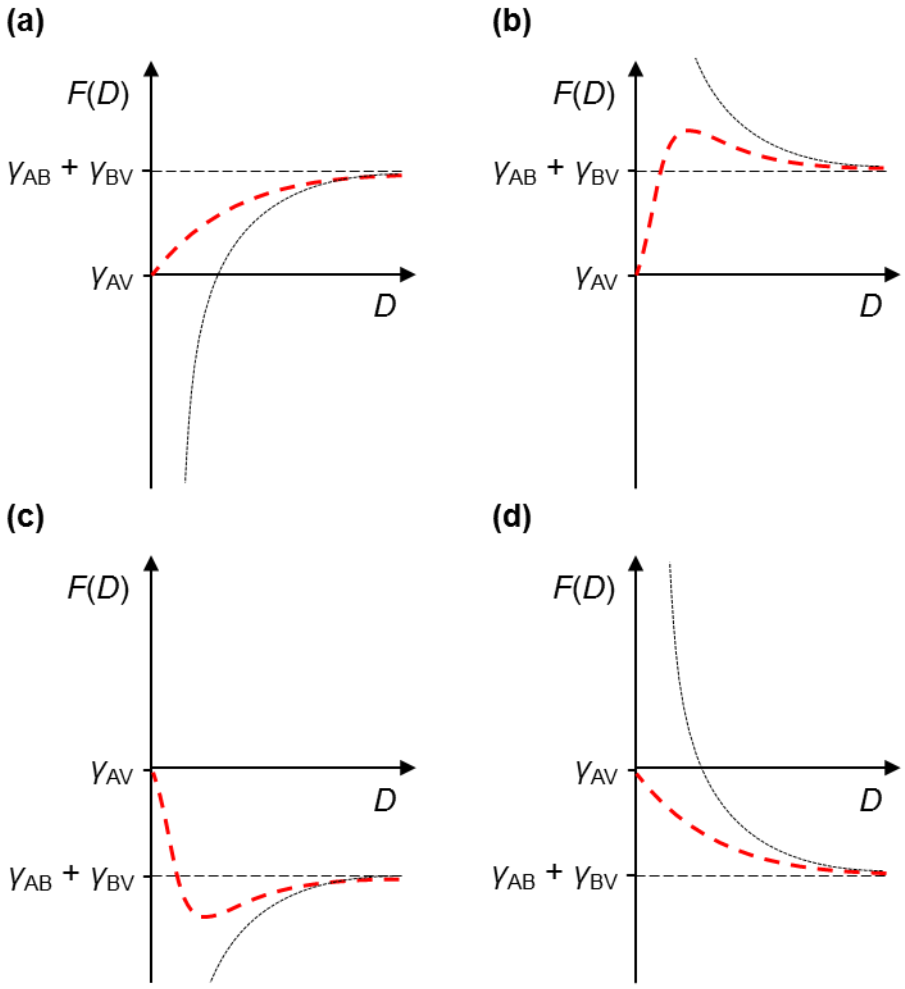

Figure 3.5. (– – –)Sketches of Equation (3.5) for (a) $S_{A/B} < 0$, $A > 0$, (b) $S_{A/B} < 0$, $A < 0$, (c) $S_{A/B} > 0$, $A > 0$ and (d) $S_{A/B} > 0$, $A < 0$. (– – –) $\gamma_{AB} + \gamma_{BV}$. (·····) Sketch of $-A_H/12\pi D^2$.

The wetting and spreading of an ink-jet printed drop undergoing phase separation is complex. Considering the limit of low *Pe* (see Section 3.4.2), compositions of the phases are uniform so that both phases are mutually saturated; surface and interfacial tensions that relate to the pure components are therefore not useful for calculating $S_{B/A}$ or resolving liquid-liquid-vapour contact angles. The wetting and spreading behaviour of the new phase depends upon $S_{B/A}$ and A_H: the new phase may spread over the surface of the drop or collect into a lens, with or without a thin layer over the surface.

3.2.2 The Wetting of Solid Surfaces by Liquids[51]

The wetting behaviour of a liquid on a solid is in many ways analogous to that of a liquid wetting another liquid, except that the normal force is not balanced at the contact line. Using the letters S, L and V to represent the solid, liquid and vapour phases respectively, the spreading ratio for a liquid on a solid $S_{L/S}$ at equilibrium is given by[51]

$$S_{L/S} = \gamma_{SV} - (\gamma_{LV} + \gamma_{SL})\,. \tag{3.11}$$

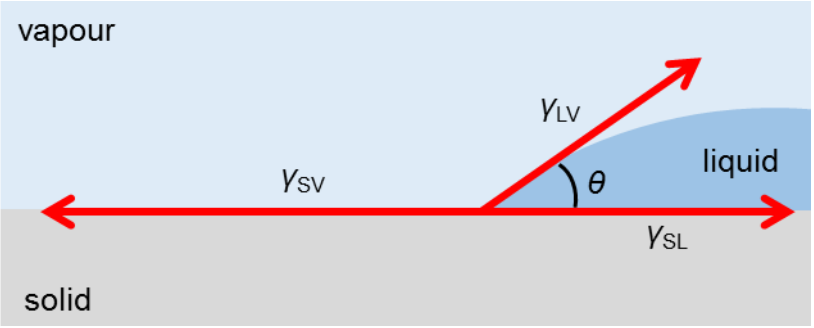

Figure 3.6. The equilibrium contact angle of a liquid resting as a lens on a solid.

Here, γ_{SV} refers to the surface tension of the solid with an adsorbed film of molecules originally from the liquid phase, since the solid is in equilibrium with the liquid vapour. If $S_{L/S} > 0$ and $A < 0$, the liquid will spread over the surface of the solid and form a zero contact angle; the liquid is consequently said to "wet" the solid.[50] As before, the equilibrium value of $S_{L/S}$ cannot be greater than zero since γ_{SV} refers to a solid with a condensed film of liquid on the surface. If $S_{L/S} > 0$ and $A > 0$, there is pseudo-partial wetting. If $S_{L/S} < 0$, the fluid does not spread but remains as a drop with a contact angle θ (Fig. 3.6). At equilibrium, there is no net force at the three-phase line so the forces may be related to one another through the Young equation:[51]

$$\gamma_{SV} = \gamma_{SL} + \gamma_{LV} \cos\theta \, . \tag{3.12}$$

If $0 < \theta < 180°$, the liquid is said to partially wet the surface.

The Young equation may also be applied for a solid-liquid contact angle when the system is submerged in a second liquid, as opposed to a vapour phase. This scenario is anticipated during the phase separation of an ink-jet formulation during evaporation: were the two phases to be in contact with each other and the substrate, a solid-liquid-liquid contact angle would be present.

When a drop is at equilibrium on a uniform planar surface orthogonal to the direction of gravity, the contact angle is equal at all points around the contact line. If the surface were tilted, however, the contact angles may differ along the direction of the slope (Fig. 3.7). The contact angle θ_a on the side of the drop that advances is greater than the equilibrium angle, whilst the contact angle θ_r on the side that recedes is lower than the equilibrium angle. The maximum difference between θ_a and θ_r before the drop moves is the contact angle hysteresis. The hysteresis results from the drop contact line achieving a metastable state so that equilibrium geometry is not obtained. Hysteresis can be caused, for example, by heterogeneous and rough surfaces.

A heterogeneous surface is not uniform with respect to chemical identity or structure, with each region type giving a characteristic equilibrium contact angle. The

Cassie-Baxter equation predicts the contact angle θ_{CB} for a surface comprising regions S1 and S2 according to

$$\cos\theta_{CB} = f_1 \cos\theta_1 + f_2 \cos\theta_2 \,, \tag{3.13}$$

where f_1 and f_2 are the respective fractions of the surface covered regions of S1 and S2, and θ_1 and θ_2 are the respective equilibrium contact angles of regions of S1 and S2. The fluid at the contact line shows a greater affinity for the regions that give rise to the lower contact angle. Observed hysteresis may therefore result from energy barriers that must be surmounted in order for the contact line to pass over regions of lower wettability in order to reach preferred sites.[51]

A rough surface has a greater actual surface area than the projected surface area. The roughness r is quantified through the ratio of the projected to the actual surface areas. Invoking the Young equation, the contact angle θ_{rough} on a rough surface may be written in terms of the angle θ_{planar} observed for a chemically identical planar surface:

$$\cos\theta_{rough} = r\cos\theta_{planar} \,. \tag{3.14}$$

Thus surface roughness lowers the contact angle for $\theta_{planar} < 90°$, but raises it for $\theta_{planar} > 90°$. Hysteresis on rough surfaces origins from metastable geometries originating from energy barriers to movement of the contact line over topographical features.[51]

In ink-jet scenarios, contact angle hysteresis may also be caused by the presence of particulates on the substrate or solid content in the fluid.[54] The additional solid is able to pin mechanically the contact line, increasing the advancing contact angle and reducing the receding contact angle. The final size of the deposition pattern is thus strongly influenced by the fixing of the contact line by solids early in the drying process. Additionally, hysteresis produces uncertainty in contact angle measurements: the drop may occupy shapes with angles intermediate between θ_r and θ_a.

The wettability of surfaces may be altered by changing the surface chemistry. For example, a substrate may be made more hydrophilic through the addition of oxygen-based polar groups,[55] whilst it may be made more hydrophobic through fluorination.[56]

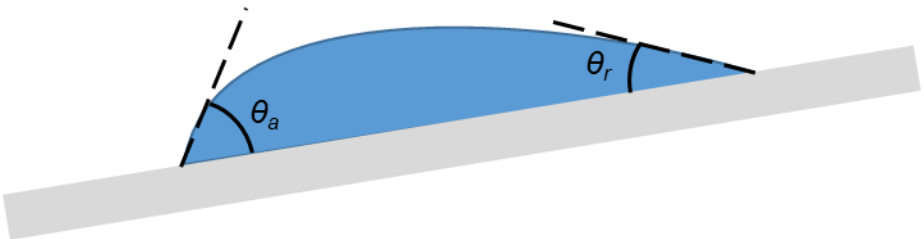

Figure 3.7. Contact angle hysteresis. θ_a is the advancing contact angle and θ_r is the receding contact angle.

3.3 Evaporation Dynamics of Sessile Droplets

The aim of this investigation is to explore the potential for novel applications of phase-separating fluids. The basic requirement is that the fluid must be formulated as a single phase, but separate as compositions change dynamically during evaporation. This section focusses on the evaporative dynamics of sessile droplets: first, the simplified case of single-solvent drops are considered. Second, the impact of surface tension gradients are discussed. Third, strategies for mitigating against outward capillary flow are presented.

3.3.1 Evaporation of Single-Solvent Sessile Drops

A drop at rest on a substrate assumes the shape of a spherical cap provided gravitational forces do not have a significant impact. For an ink-jet printed drop ($r_0 \sim 60$ μm, $h_0 \sim 50$ μm) gravitational forces do not impact the drop shape since $Bo \ll 1$ (Equation (2.7)).

During evaporation, any internal flows could in principle deform the drop shape. The relative magnitudes of viscous and surface forces is given by the Capillary number *Ca*:

$$Ca = \frac{\eta u}{\gamma}, \tag{3.15}$$

where η is the fluid viscosity and u is the velocity of internal flows. For an ink-jet printed droplet comprising a single low-viscosity solvent, $Ca \ll 1$. Models of evaporation for single-solvent drops based on a spherical cap geometry are therefore relevant to ink-jet scenarios.[57]

For an evaporating sessile drop, vapour transport away from the surface may occur either ballistically[58] or diffusively,[43,59] depending on the value of the Knudsen number:

$$Kn = \frac{\lambda}{r_0}, \tag{3.16}$$

where λ is the mean free path length of the vapour. Ballistic vapour transport occurs for $Kn > 1$, meaning that molecules rapidly move away from the surface and there is little chance of them re-condensing;[57] for water drops under ambient conditions ballistic evaporation typically requires $r_0 < 100$ nm. In contrast, if $Kn < 1$, molecules move away from the surface diffusively provided a concentration gradient exists; diffusion-limited evaporation has been observed for ink-jet printed drops.[60]

For a diffusion-limited drop that is isothermal with its surroundings, the average change in mass over time during evaporation is given by[61]

$$-\frac{dm}{dt} \approx \pi r_0 D_{\mathrm{vap}} (1 - H) \rho_{\mathrm{vap}} (0.27\theta^2 + 1.30), \tag{3.17}$$

where D_{vap} is the diffusion coefficient of the vapour, H is the relative vapour pressure (the relative humidity for water), θ is the drop contact angle and ρ_{vap} is the partial density of the vapour at the drop surface; ρ_{vap} at atmospheric pressure may be calculated from the vapour pressure p_{vap} using the perfect gas equation of state:[62]

$$p_{\mathrm{vap}} = \frac{\rho_{\mathrm{vap}} RT}{M}, \tag{3.18}$$

where M the molecular molar mass. The rate of change of mass with time is thus linear for drops with pinned contact lines (constant r_0) and small contact angles (so that $0.27\theta^2 << 1.30$). The total drying time t_f of the droplet may be estimated from

$$t_{\mathrm{f}} = \rho_{\mathrm{l}} V_{\mathrm{drop}} \left(\frac{dm}{dt}\right)^{-1}, \tag{3.19}$$

where ρ_l is the liquid density and V_{drop} is the initial volume of the drop. Similarly, the average mass flux per unit contact area J_{av} is given by

$$J_{\mathrm{av}} = \frac{dm}{dt}(\pi r_0{}^2)^{-1}. \tag{3.20}$$

The evaporative flux is not equal over the entire drop surface unless $\theta = 90°$. For a drop with $\theta = 90°$, the fluid adopts a hemispherical shape. Taking a cross section, the circle to which the arc corresponds has its centre at the substrate. Consequently, if sectors of equal central angles are drawn and extrapolated outside the drop surface, the entire

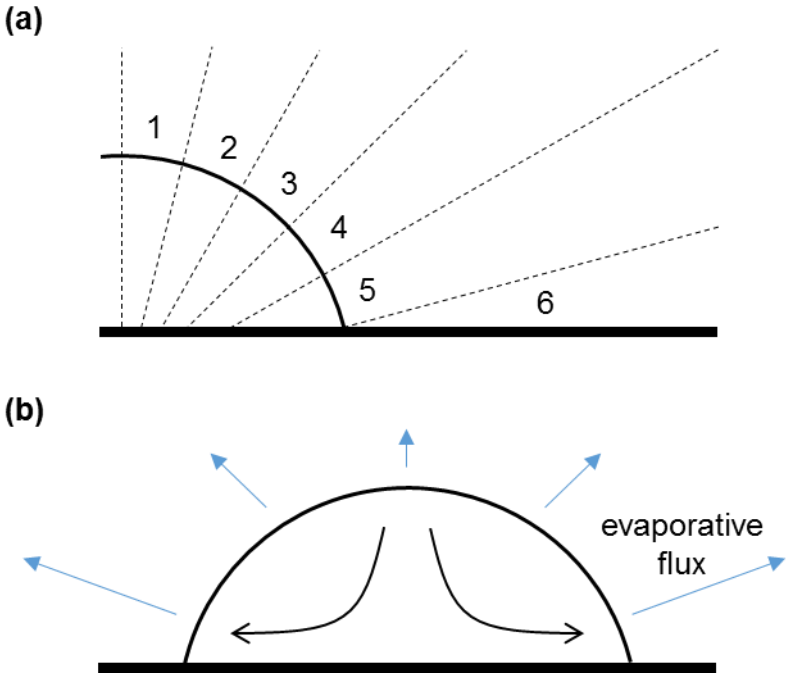

Figure 3.8. (a) A cross section through a spherical cap. The dashed lines extrapolate to the centre of the circle traced out by the drop surface and represent equal sectors. (b) Qualitative sketch of the magnitude of evaporative flux (blue arrows) at different parts of the drop surface. The black arrows show the outward radial flow that occurs if the contact line is pinned.

cross-sectional area of the atmosphere is contained; evaporative flux is therefore equal across the whole drop surface.[57]

For drops where $\theta \neq 90°$, the flux is not equal across the whole surface.[57] Taking the case where $\theta < 90°$ first and repeating the procedure carried out for the hemispherical drop, the entire cross-sectional area of the atmosphere is not contained in extrapolated sectors (Fig. 3.8a); additional volume is present at the contact line that is not associated with a surface sector (sector 6). Molecules evaporating from the sector at the contact line (sector 5) are able diffuse into sector 6, raising the concentration gradient at the surface and strongly increasing the local evaporation rate. Additionally, evaporation is enhanced (but by a smaller degree) in sector 4 since molecules are able to diffuse into sector 5 due to the lower vapour concentration in the latter. Repeating the logic for sectors 3 – 1 yields the result that the evaporative flux is largest close to the contact line and smallest at the apex (Fig. 3.8b). The evaporative flux $J(r, \theta)$ from the droplet surface may be approximated by[61]

$$J(r,\theta) = J_0(\theta)\left(1 - \left(\frac{r}{r_0}\right)^2\right)^{-\lambda}, \tag{3.21}$$

where r is the radial distance from the centre of the drop, λ is given by

$$\lambda(\theta) = 0.5 - \frac{\theta}{\pi} \tag{3.22}$$

and $J_0(\theta)$ is

$$J_0(\theta) = \frac{\rho_{\text{vap}}(1-H)}{r_0}\left(\frac{(8\pi - 4)(\theta - \pi/2)^2}{\pi^3} + 1\right). \tag{3.23}$$

The divergence in evaporative flux at the contact line to infinity given by Equation (3.21) is unphysical and one transport process must be rate limiting. The high flux implies that molecules that have evaporated are unlikely to re-condense onto the drop. The evaporation at the contact line may therefore be modelled as ballistic at distances from the surface lower than the mean free path of the vapour.

Were $\theta > 90°$, the trend in evaporative flux is reversed versus the case for $\theta < 90°$: now sectors close to the contact line are restricted by the presence of the substrate, leading to enhanced flux at the apex relative to the contact line.[57]

The enhanced evaporative flux at the contact line relative to the apex for $\theta < 90°$ gives rise to flows inside the drop if the contact line is pinned at its original location. If greater mass loss is occurring at the contact line than the apex, but the contact line is fixed, the loss of volume must be reflected in the decreasing height of the drop and a decreasing contact angle. The change in vertical distance of each point on the surface is

therefore greatest at the apex, but smallest at the contact line. There is thus a mismatch between where net loss of volume is manifested (at the apex) and where evaporative flux is greatest (at the contact line). A pinned drop with $\theta < 90°$, must therefore have an internal flow to meet the constraints. The flow is an outward radial flow, sometimes termed capillary flow.[43]

The evaporation of real drops cannot be assumed isothermal. The transfer of molecules from the liquid to the vapour phase is an endothermic process since enthalpies of vapourisation are positive. Evaporative cooling has the effect of retarding the rate of mass loss and increasing the drying time.[63] Additional thermal energy may be supplied from the substrate if it is a good thermal conductor, limiting the impact of evaporative cooling. Some substrates, like PTFE, are thermal insulators and evaporative cooling is likely to be observed. All printing experiments presented in this thesis were conducted onto glass substrates for which the thermal conductivity κ_S is 1.5 W m^{-1} K^{-1} at 298 K so evaporative cooling is less significant than for PTFE (κ_S = 0.25 W m^{-1} K^{-1})[64,65].

3.3.2 Marangoni Flows in Sessile Droplets

Surfaces at equilibrium have identical surface tensions at all points and, in the absence of external agitation, the fluid remains at rest. If, however, the surface tension is non-identical at all points, gradients in the surface tension exist. The imbalance in the surface tension results in a force that acts along the gradient, moving fluid in the direction of increasing surface tension; flows of this type are termed Marangoni flows. The velocity v of the flow may be determined from

$$\frac{d\gamma}{d\hat{t}} = -\eta \frac{dv}{d\hat{n}}, \tag{3.24}$$

where $\hat{t}$ and $\hat{n}$ are unit vectors that are tangential and normal to the surface, respectively. Marangoni flows act to reduce the overall free energy of the surface by increasing the surface area occupied by regions of lower surface energy, and diminishing those of higher surface energy. Marangoni flows can be driven by gradients in surface tension caused by temperature and composition gradients. For a droplet on a substrate, surface tension gradients give rise to Marangoni flows that cause re-circulating cells to develop; the directionality of the re-circulation depends on the relative magnitudes of contributions from a variety of sources.[57]

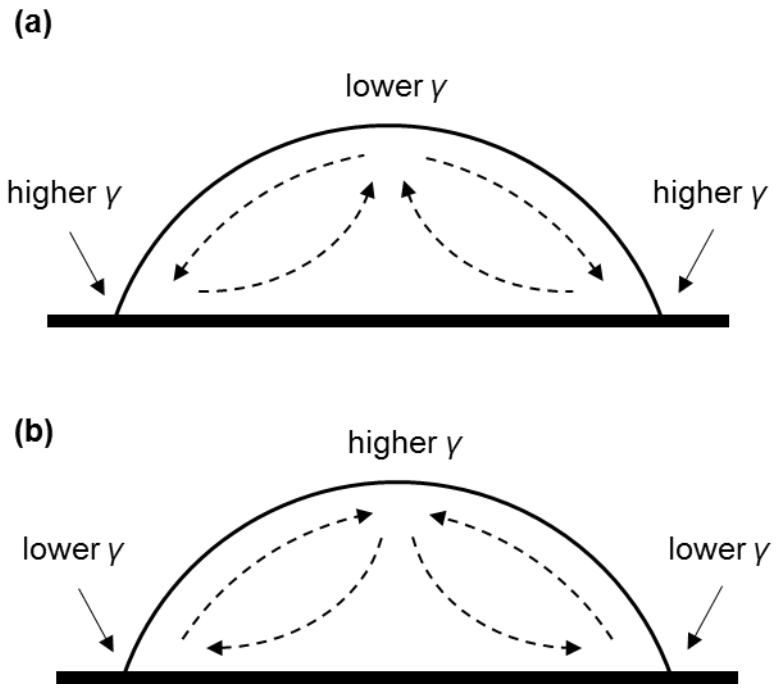

Figure 3.9. Cross sections through sessile drops with surface tension gradients; the resulting internal Marangoni flows are marked. (a) The contact line has a higher surface tension than the apex. (b) The apex has a higher surface tension than the contact line.

Marangoni flows in evaporating droplets can be driven by thermal gradients at the drop surface.[66,67] The first source of thermal gradients is non-uniform evaporative cooling. The regions of the drop that experience the highest evaporative flux also experience evaporative cooling to the largest extent.[67] For drops with spherical cap geometries and $\theta < 90°$, evaporative flux is highest at the contact line, resulting in a cooling of the contact line relative to the drop apex. Since the surface tension of liquids increase as temperature decreases, evaporative cooling leads to a Marangoni flow from the apex to the contact line and re-circulating cells that move inwards near the base of the drop (Fig 3.9a). The second source of thermal gradients in an evaporating drop is caused by the non-uniform transfer of heat from the substrate to the fluid in the drop. The surface close to the contact line of the drop has a smaller vertical distance to the substrate than that of the apex. Consequently, the heat lost to evaporative cooling is more rapidly replaced at the contact line than at the apex. The situation can therefore arise where the contact line has a higher temperature and lower surface tension than the apex, leading to a Marangoni flow along the surface from the former to the latter (Fig 3.9b); the direction of the fluid near the base of the drop in the re-circulating flow is radially outward.

Both non-uniform evaporative cooling and non-uniform heat conduction path length contribute to the thermal gradients, with the relative magnitudes determining the directionality of the re-circulating cells. The ratio of the thermal conductivity of the

substrate κ_S to the thermal conductivity of the liquid κ_L defines the relative conductivity κ_R:

$$\kappa_R = \frac{\kappa_S}{\kappa_L}. \tag{3.25}$$

For $\kappa_R > 2$, the heat conduction path length is the dominant contribution and the Marangoni flow along the drop surface moves from the contact line to the apex. In contrast, for $\kappa_R < 1.45$, the evaporative cooling is the dominant contribution and the Marangoni flow along the drop surface moves from the apex to the contact line. At intermediate values of κ_R, the direction of the flow depends on the contact angle, with conduction path length dominating above a critical angle and evaporative cooling dominating below a critical angle.[67] Most of the formulations trialled in this thesis are aqueous based and printed onto glass substrates. For water at 298 K, κ_L = 0.6 W m^{-1} K^{-1},[64] so κ_R = 2.4; conduction path length is expected to be dominant in determining thermal gradients and Marangoni flows are expected to move from the contact line to the apex.

Marangoni flows in evaporating drops may also be driven by surface tension gradients caused by composition gradients in the fluid. Composition gradients can develop due to unequal volatility of components in fluid mixtures. For a drop with $\theta <$ 90°, the enhanced evaporative flux at the contact line leads to a local depletion of the more volatile component relative to the apex. In fluid mixtures, the surface tension is dependent on the relative proportions of the components. If the more volatile component also has the lower surface tension, then the contact line has a higher surface tension than the apex, leading to a Marangoni flow along the surface from the latter to the former (Fig 3.9a). In contrast, should the more volatile component have the higher surface tension, the apex develops the higher surface tension, so that the Marangoni flow runs in the reverse direction (from the contact line to the apex, Fig 3.9b).[68]

Composition-driven Marangoni flows have also been observed in surfactant solutions. Still *et al.*[44] tracked internal flows in SDS solutions using suspended polystyrene spheres. The transport of SDS to the contact line by the outward radial flow led to a local increase in concentration in surfactant. The surface tension at the contact line was therefore lowered relative to that of the apex, leading to a Marangoni flow from the former to the latter (Fig 3.9b). The particles were therefore observed to become trapped in re-circulatory eddies.

3.3.3 Influence of Drying Dynamics on Deposit Morphology

The outward radial flow in single-solvent sessile drops is caused by the non-uniform evaporative flux profile over the surface. The flow occurs provided a number of conditions are met: first, the drop must have adopted the shape of a spherical cap. Second, the contact angle must be less than 90°. Third, the contact line must be pinned. When particulates are suspended in a single-solvent sessile drop and these conditions are met, the particulates are transported to the contact line by the convective flow, whereupon they are deposited. The resulting deposit is therefore a concentrated ring, with the centre heavily depleted of solid. The formation of deposits with a ring morphology under outward convective flow is termed "the coffee ring effect"; the deposits are often referred to as "ring stains". The terminology derives its name from the frequently-observed transport of fine coffee grounds to the edge of coffee drops and spills, resulting in deposits with dark outer edges.[43]

The deposition of ring stains is generally disadvantageous for applications and a more even distribution of material over the drop contact area is desirable. Strategies for eliminating the coffee ring effect centre on breaking the conditions required to drive the outward convective flow. The first strategy to avoid the coffee ring effect is to prevent contact line pinning. If the contact line is not pinned, then the loss of volume at the contact line can be reflected by a decrease in the radius, and not the height as in the pinned case. The contact line might be prevented from pinning through the induced motion of the contact line using electrowetting.[69]

The second strategy to avoid the coffee ring effect is to prevent enhanced evaporative flux at the contact line.[57] If the differential in the evaporative flux at different parts of the surface can be reduced, there is no need for transport of fluid to the contact line from the apex and capillary flow ceases. The modification of the evaporative flux profile has been achieved by controlling the diffusion of vapour from the drop surface. If the drop were placed in a closed volume with a hole to the atmosphere directly above the drop, control is exerted over the diffusion path of the vapour. The diffusion path of vapour evaporating from the contact line is limited by the walls of the container, but the vapour from the apex is able to pass through the hole to the atmosphere. The evaporative flux is therefore enhanced at the apex and counteracts the effect of additional diffusion volume at the contact line. The principle has been demonstrated to limit the development of ring stains, and can be significant enough to reverse the direction of the flow to give a central deposit.[70]

The third strategy for mitigating the coffee ring effect is to alter the internal flow profile of the evaporating drop. The discussion in Section 3.3.2 detailed how surface tension gradients can be created on the drop surface that are able to drive Marangoni flows. The Marangoni flows lead to re-circulating cells that move particles back towards the centre of the drop once they reach the contact line.[68] Consequently, particulates can be prevented from depositing at the contact line whilst the Marangoni flow persists. The collection of particulates in the centre of the drop due to the addition of surfactants,[44] the non-uniform evaporation of binary solvents[68] and thermal effects[71] have all been demonstrated. In the case of binary solvents, the Marangoni flow ceases when the more volatile component is exhausted. Once the drop becomes a single component, coffee-ring flow commences and begins to transport particulates to the contact line.[68] Depletion flocculation and incorporation of fluids with a yield stress have been used as strategies to fix the particles in a central spot in the drop to mitigate against convective flow after the cessation of Marangoni flows.[72] Park and Moon obtained even layers of particles across the drop footprint with binary solvent mixtures.[73]

3.4 Phase Separation as a Potential Tool for Formulation Design

Sections 3.1 − 3.3 outlined the thermodynamics of phase separation, fundamentals of wetting and spreading of fluids and the dynamics of evaporating droplets. This section draws upon the background knowledge in order to identify the key requirements for designing phase-separating ink-jet formulations. Basic separation dynamics are predicted and avenues for novel application are suggested.

3.4.1 The Criterion for a Printed Droplet to Phase Separate

For a mixture to phase separate when printed, the components must be partially miscible. The formulation should be in a single phase during printing, with the minor component present at a concentration close to its solubility limit. If the major component is the more volatile, the drying drop would be enriched in the minor component until the local composition passed through the binodal and phase separation occurred. For a spherical cap with a contact angle less than 90°, the evaporative flux is greatest at the contact line.[43] The fluid composition is therefore expected to change the fastest at the drop periphery, so that any second phase would form first at the drop contact line. Consequently, the relative evaporation rates of the components is of first importance for the phase separation to be realised: the minor component must have a longer lifetime on the substrate than the major component, so that the former is able to increase in concentration until it supersaturates. If the reverse were true, the initial concentration of the minor component would prove to be the maximum and the solute would remain solvated for the duration of the drying process.

The rate of evaporation for a spherical cap of material A, r_A, is proportional to its vapour pressure p_A and its diffusion coefficient in air, D_A:[61]

$$r_A \propto p_A D_A. \tag{3.26}$$

For water, the relative humidity, *RH*, must also be taken into account:

$$r_w \propto p_w D_w (1 - RH). \tag{3.27}$$

For evaporation into stagnant air, the proportionality coefficient depends on the drop radius and contact angle (Eq. (3.17)), but is independent of the component if *r* is expressed in terms of moles. For a liquid-liquid mixture of major component A and minor component B, the situation where B increases in concentration until it supersaturates is given by

$$\frac{r_B}{x_B} < \frac{r_A}{x_A}, \tag{3.28}$$

or $r_B x_A < r_A x_B$, where r is expressed in molar terms. Conversely, if $r_B x_A > r_A x_B$, the concentration of B decreases with time and the drop remains as a single phase throughout drying. Therefore defining κ as

$$\kappa = \frac{r_A x_B}{r_B x_A}, \tag{3.29}$$

the quantitative criterion for the observation of phase separation is $\kappa > 1$.

3.4.2 Potential Applications of Phase Separating Ink-Jet Formulations

Developing ink-jet printed formulations that phase separate during evaporation gives rise to new possibilities for application. The obvious application is patterning control. Phase separation is expected first at the contact line so that an annular ring rich in the minor component develops. Were two solutes present in the original formulation such that each partitioned favourably into opposite phases, they could be deposited as concentric circles. Thus phase-separating formulations have the potential to facilitate control over patterning on a microscopic level. One could imagine the deposition of arrays of hydrophobic or hydrophilic rings, or conductive tracks with insulating material running down the outside.

Alternatively, the new phase B might not remain as annular ring but could completely undercut the major phase A, so that the former maximized its contact with the substrate. For undercutting to occur, the minor phase would need to have superior wetting affinity of the substrate versus the major phase: the criterion for undercutting is $S_{A/B/S} > 0$ ($\gamma_{AS} > \gamma_{AB} + \gamma_{BS}$) and $A_{H,\,A/B/S} < 0$. Undercutting could allow a particulate or solvated material present in the major phase to aggregate before adhesion to the surface.

A second potential application of phase separation at the contact line is control over the evaporation dynamics. In a pinned single-solvent drop ($\theta < 90°$) evaporative flux is greatest at the contact line, leading to an outward radial flow that gives rise to deposits possessing ring-stain morphologies.[43] Were the newly-formed minor phase in a phase-separating drop to remain as an annular ring, there is the possibility of disrupting the outward convective flow. At equilibrium, the vapour pressure of a component must be the same in each of the liquid phases in contact. During evaporation, the major component must therefore diffuse into the phase rich in the minor component to maintain a constant vapour pressure of the major component over the drop surface. Were diffusion through the minor liquid phase to become evaporation-limiting, as opposed to diffusion in the vapour,[43] a change in behaviour from outward convective flow might be expected. Thus phase-separating drops may provide a mechanism to disrupt the coffee-ring effect.

For phase-selective patterning to be realised, the solutes must have sufficient time to partition into the correct phase before drying is complete. The Péclet number *Pe* measures the speed of advective transport against the speed of diffusive transport:

$$Pe = \frac{r_0 v}{D_{\mathrm{BA}}}, \tag{3.30}$$

where r_0 is the initial drop height, v is the surface velocity at the apex and D_{BA} is the liquid diffusion coefficient of solute B in solvent A. For a drop of water of volume 330 pL ink-jet printed onto a hydrophobic substrate, $r_0 = 6 \times 10^{-5}$ m and $v = 1 \times 10^{-5}$ m s^{-1}; $D_{\mathrm{AB}} \sim 10^{-9}$ m^2 s^{-1}.[74] Thus $Pe \sim 0.6$. As $Pe < 1$, diffusive transport is dominant over advective transport and the solutes can be expected to partition before evaporation is complete. For smaller drops or less volatile solvents *Pe* would be smaller. For bulky solutes or for more volatile solvents, *Pe* might be greater than unity and concentration gradients would be observed.

3.5 Butanol and Water Mixtures

The first system to be investigated for phase separation upon deposition was butanol-water. This section is organised as follows: first, the rationale behind identifying the system for trial is outlined. Second, experimental details are presented. Third, a physical model of expected separation behaviour based upon physical data is constructed. Fourth, printing results are presented. Fifth, the criterion κ for phase separation given in Section 3.4.1 is discussed and refined.

3.5.1 Rationale

In an ideal binary solution, the vapour pressure of a component, p_A, is calculated from the vapour pressure of the pure liquid, p_A^*, according to Raoult's law:

$$p_A = x_A p_A^* . \tag{3.31}$$

The vapour pressures of pure water and *n*-butanol are 3.14 kPa and 0.93 kPa at 298 K, respectively.[64] Butanol has a mole fraction of 0.02 at saturation.[75] At 298 K, the diffusion coefficients for water and butanol in air are 2.5×10^{-5} and 0.9×10^{-5} m^2 s^{-1}, respectively.[76,77] Assuming ideal vapour pressures and that $RH = 0.4$, then from Eq. (3.29) $\kappa^{raoult} = 5.6 >> 1$, suggesting that water–butanol mixtures would be a good candidate for a mixture that phase separates during evaporation.

Hereafter, the following nomenclature will be used to describe a phase-separating butanol-water mixture: *butanol-rich phase* for a water solution in butanol, comprising > 50 %vol butanol; *water-rich phase* for a butanol solution in water, comprising > 50 %vol water; *saturated* to indicate the minor component is present at its miscibility limit.

3.5.2 Experimental Details and Procedures

Butan-1-ol (*Fisher*, AR) and water (Milli-Q) were used as received. The mutual solubilities of these materials were determined by adding drops of the minor component to the major component until saturation was achieved. Fluids were contained in 10-mL volumetric flasks and bath sonicated between the addition of drops of the minor component. Saturation was defined as being the point at which markings on paper were fully obscured due to the cloudiness of the mixture (path length ~3 cm). Butanol reached saturation in water at 7.6 %wt and water reached saturation in butanol at 20.2 %wt. The temperature was 294 K. The mutual solubilities are in close agreement with recommended values at 293 K: 7.7 %wt for butanol in water and 20 %wt for water in butanol.[75]

Predictions of equilibrium contact angles and wetting behaviour require the surface tensions of aqueous butanol solutions and water solutions in butanol to be known,

as well as the interfacial tension between the two saturated solutions. The surface and interfacial tensions were measured by pendent drop tensiometry using the equipment and procedures described in Section 2.4. The solution densities were measured across the full range of miscibility and were found to be linear in composition:

$$\rho = \rho_A{}^* + k[\mathrm{B}]\,, \tag{3.32}$$

where ρ is the density of the solution, ρ_A* is the density of major component A, [B] is the concentration of minor component B and k is a constant. The values of the constants ρ_A* and k and associated uncertainties were determined by linear regression and are given in Table 3.1. Figure 3.10 shows the surface tensions in air of butanol- and water-rich liquids over the range of miscibility at 296 K. The surface tension between air and water-rich liquids, γ_{WA}, decreases from that of pure water as the solute increases in concentration, with a decreasing rate of change (Fig. 3.10a). The value at saturation, $\gamma_{WA}{}^{sat}$, is taken to be 24.13 ± 0.07 mN m^{-1} as observed for the 7.6 %wt butanol solution. In contrast, the surface tension in air of butanol-rich liquids, γ_{BA}, is independent of water concentration (Fig. 3.10b). The value at saturation, $\gamma_{BA}{}^{sat}$, is 23.30 ± 0.05 mN m^{-1}, as for the 20.1 %wt solution. The interfacial tension between a 7.6 %wt butanol solution and a 20.1 %wt water solution, $\gamma_{WB}{}^{sat}$, was measured at 1.618 ± 0.006 mN m^{-1}.

Contact angles of the saturated solutions were measured on a glass substrate hydrophobised with hexamethyldisilazane (Section 2.1) using the procedures outlined in Section 2.4.2. Measurements of the contact angle were made using the tensiometer imaging system. A 20.1 %wt water solution on the substrate in air had a contact angle, $\theta_{BA}{}^{sat}$, of 8 ± 1°. A 7.6 %wt butanol solution on the substrate in air had a contact angle of 41 ± 2°. A 7.6 %wt butanol solution on the substrate and submerged in a 20.1 %wt water solution (in butanol) had a measured contact angle of 117 ± 2°.

TABLE 3.1. The constants and standard errors obtained from a linear least-squares fitting routine for the densities of water and butanol mixtures as a function of composition at T = 295 K.

Major Component A	Minor Component B	ρ_A* / (g mL^{-1})	k / [g mL^{-1} (%wt)$^{-1}$]
Water	Butanol	0.9923 ± 0.0003	−0.00147 ± 0.00006
Butanol	Water	0.8030 ± 0.0002	0.00186 ± 0.00002

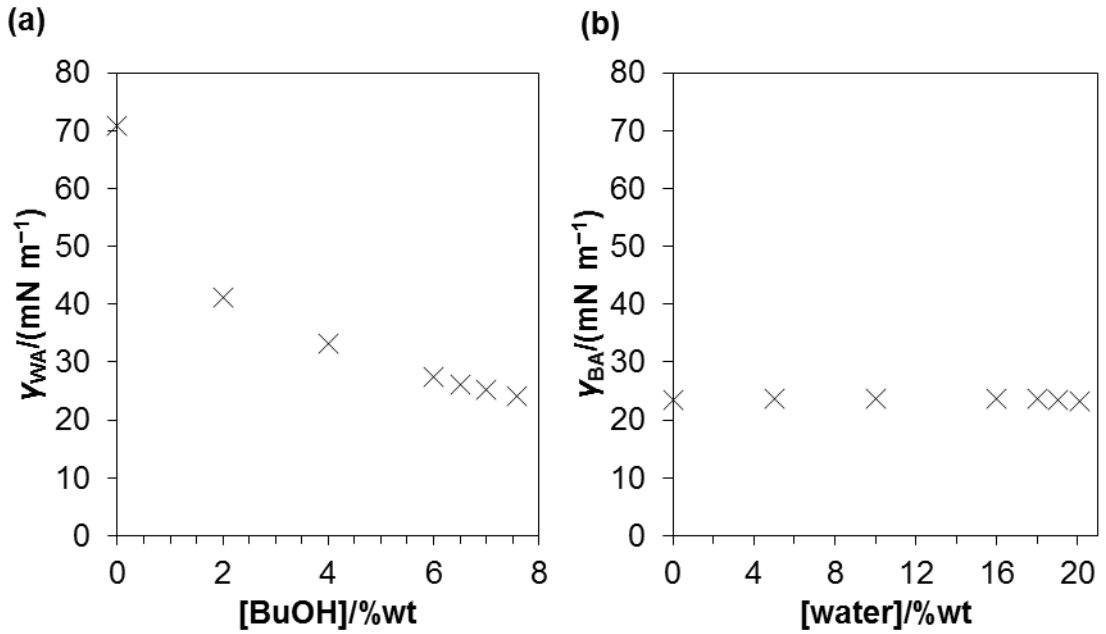

Figure 3.10. (a) The surface tension in air of aqueous solutions of butanol, γ_{WA}, up to the miscibility limit, at 296 K. (b) The surface tension in air of butanol solutions of water, γ_{BA}, up to the miscibility limit, at 296 K.

3.5.3 Expected Separation Behaviour

For a spherical cap with a contact angle of less than 90°, evaporative flux is greatest at the contact line.[43] Were an aqueous solution of butanol to phase separate upon deposition from an ink-jet print head, it would be expected that the butanol-rich phase would form at the contact line because that is where composition is changing the fastest. A physical model of how the butanol-rich and water-rich phases would behave in contact can be deduced using physical data. The equilibrium spreading coefficient, $S_{B/W}$, for a butanol-rich liquid resting on a water-rich liquid in air is defined in terms of the surface and interfacial tensions according to

$$S_{B/W} = \gamma_{WA} - (\gamma_{WB} + \gamma_{BA})\,. \tag{3.33}$$

If both liquids are mutually saturated and using γ_{WA}^{sat} = 24.13 ± 0.07 mN m^{-1}, γ_{BA}^{sat} = 23.30 ± 0.05 mN m^{-1} and γ_{WB}^{sat} = 1.618 ± 0.006 mN m^{-1}, $S_{B/W}$ = −0.788 ± 0.004 mN m^{-1}.

A negative value of $S_{B/W}$ indicates that the oil will not wet the aqueous surface thermodynamically. A saturated butanol-rich liquid will therefore form a lens when resting on a saturate water-rich liquid in air (Section 3.2.1). The lens will possess specific contact angles above and below the air-water surface in order that no net force is present at the three-phase contact line (Fig. 3.11a). The angles at the three-phase contact line are readily calculated from Neumann's triangle (Fig. 3.11b) by solving the following simultaneous equations produced using the cosine rule (Eq. (3.10)):

$$\gamma_{WB}{}^2 = \gamma_{WA}{}^2 + \gamma_{BA}{}^2 - 2\gamma_{WA}\gamma_{BA}\cos\theta_1 \ ; \tag{3.34}$$

$$\gamma_{BA}{}^2 = \gamma_{WA}{}^2 + \gamma_{WB}{}^2 - 2\gamma_{WA}\gamma_{WB}\cos\theta_2 \ ; \tag{3.35}$$

$$\theta_3 = \pi - \theta_1 - \theta_2 \ . \tag{3.36}$$

The angles at the three-phase contact line are displayed in in Figure 3.11c.

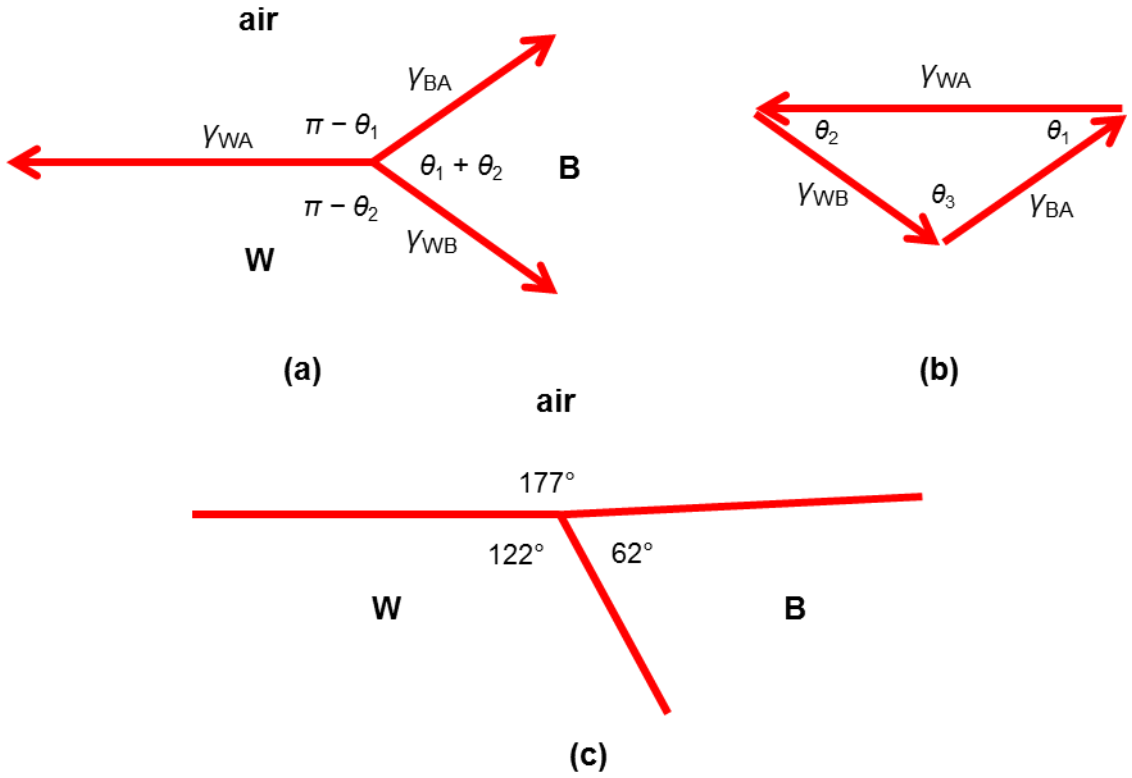

Figure 3.11. (a) The force balance at the three-phase contact line for a lens of water-saturated butanol (B) on butanol-saturated water (W) in air. The arrow lengths are not to scale to aid clarity. (b) Neumann triangle. (c) The equilibrium angles at 296 K. Due to rounding, the angles do not sum to 360°.

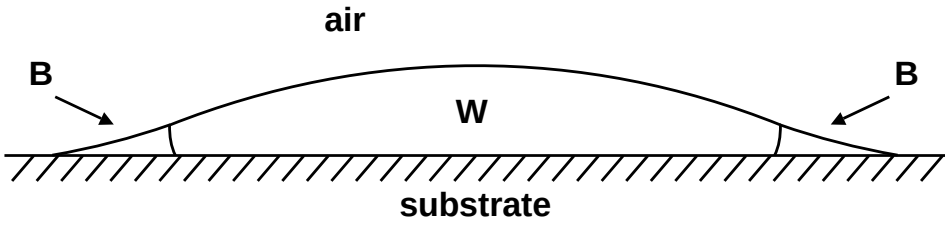

Figure 3.12. Geometry of a butanol-saturated water (W) drop with a water-saturated butanol phase (B) at the contact line. The model is based on measured surface and interfacial tensions (T = 296 K) and contact angles on a hydrophobized substrate (T = 295 K).

The geometry of an annular ring of the butanol-rich phase at the contact line of a drop of water-rich phase, can be predicted by resolving forces at the three 3-phase contacts: (1) the butanol-rich liquid on the substrate in air has a contact angle of 8°; (2) the water-rich phase on the substrate and submerged in the butanol rich phase has a measured contact angle of 117°; (3) the calculated angles for the liquid-liquid-air contact

line are shown in Figure 3.11c. The sum of internal angles for the butanol-rich phase is 133°, significantly less than the 180° required for the interfaces to be straight. The interfaces must, therefore, be curved. The Laplace pressure is given by

$$\Delta p = \frac{2\gamma}{R_{ij}}. \tag{3.37}$$

where Δp is the difference in pressure on either side of an interface and R_{ij} is the radius of curvature. The sign of the curvature is determined when passing from the phase *i* to phase *j*.

When the second phase is just forming, its height *h* is small compared with the height of the drop *H*. Since the angles are independent of the volume of the phase, the radii of curvature are proportional to *h* and Δp is inversely proportional to *h*. Hence when $h << H$, the Laplace pressure of the new phase forming at the contact line is of much larger magnitude than that of the major phase. Consequently, the Laplace pressure of the water-rich phase may be neglected when determining the shape of the annular ring. Then, for the butanol-rich phase, the Laplace pressure across both interfaces is equal:

$$\frac{{\gamma_{\mathrm{BA}}}^{\mathrm{sat}}}{{R_{\mathrm{BA}}}^{\mathrm{sat}}} = \frac{{\gamma_{\mathrm{BW}}}^{\mathrm{sat}}}{{R_{\mathrm{BW}}}^{\mathrm{sat}}}. \tag{3.38}$$

The ratio between the two radii of curvature, ${R_{\mathrm{BA}}}^{\mathrm{sat}} : {R_{\mathrm{BW}}}^{\mathrm{sat}}$, is 14.6 : 1 and would appear as in Figure 3.12. Both of the boundaries along the butanol-rich phase are concave, allowing the sum of the three internal angles to sum to less than 180°, whilst both of the boundaries along the water-rich phase are convex. The geometry in Figure 3.12 shows that the butanol-rich phase would not undercut the water-rich phase completely.

The accuracy of the surface/interfacial tension and contact angle measurements, and therefore the accuracy of Figure 3.12, may be examined by checking the self-consistency of the data. The forces at the contact line for the butanol-rich phase in air, the water-rich phase in the butanol-rich phase and the water-rich phase in air, each on a hydrophobised substrate, are shown in Figure 3.13. The force balances are:

$${\gamma_{\mathrm{SA}}}^{\mathrm{sat}} = {\gamma_{\mathrm{SB}}}^{\mathrm{sat}} + {\gamma_{\mathrm{BA}}}^{\mathrm{sat}} \cos {\theta_{\mathrm{BA}}}^{\mathrm{sat}} \; ; \tag{3.39}$$

$${\gamma_{\mathrm{SW}}}^{\mathrm{sat}} = {\gamma_{\mathrm{SB}}}^{\mathrm{sat}} + {\gamma_{\mathrm{WB}}}^{\mathrm{sat}} \cos\left(\pi - {\theta_{\mathrm{WB}}}^{\mathrm{sat}}\right) \; ; \tag{3.40}$$

$${\gamma_{\mathrm{SA}}}^{\mathrm{sat}} = {\gamma_{\mathrm{SW}}}^{\mathrm{sat}} + {\gamma_{\mathrm{WA}}}^{\mathrm{sat}} \cos {\theta_{\mathrm{WA}}}^{\mathrm{sat}}. \tag{3.41}$$

Subtracting (3.40) from (3.39) gives

$${\gamma_{\mathrm{SA}}}^{\mathrm{sat}} - {\gamma_{\mathrm{SW}}}^{\mathrm{sat}} = {\gamma_{\mathrm{BA}}}^{\mathrm{sat}} \cos {\theta_{\mathrm{BA}}}^{\mathrm{sat}} - {\gamma_{\mathrm{WB}}}^{\mathrm{sat}} \cos\left(\pi - {\theta_{\mathrm{WB}}}^{\mathrm{sat}}\right) \tag{3.42}$$

and (3.41) may be rearranged into

$${\gamma_{\mathrm{SA}}}^{\mathrm{sat}} - {\gamma_{\mathrm{SW}}}^{\mathrm{sat}} = {\gamma_{\mathrm{WA}}}^{\mathrm{sat}} \cos {\theta_{\mathrm{WA}}}^{\mathrm{sat}}. \tag{3.43}$$

Equating (3.42) and (3.43) and solving for θ_{WA}^{sat} gives $\theta_{WA}^{sat} = 22°$. The measured value was 41 ± 3°.

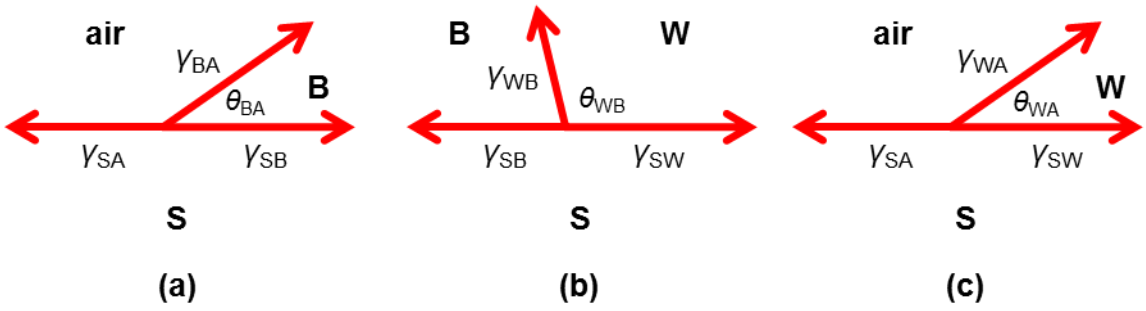

Figure 3.13. The force balance at various three-phase contact lines. The phase are water-saturated butanol (B), butanol-saturated water (W), the substrate (S) and air.

The error is unlikely to enter through equation (3.39) since γ_{BA} was invariant over the entire miscibility range (Fig. 3.10b) and cos θ_{BA}^{sat} varies little for small changes in small angles. The error may enter through Equation (3.40): cos ($\pi - \theta_{WB}^{sat}$) changes by ~20% over the uncertainty range in the value of θ_{WB}^{sat}. However, propagating a 2° error in θ_{WB}^{sat} only changes the calculated value of θ_{WA}^{sat} by < 1°. More likely, the inconsistency in the measurements derives from contact angle hysteresis: the contact angle adopted on a substrate may be between θ_r and θ_a.

Another possible source of the inconsistency in the data is composition change in the liquid used to measure θ_{WA}^{sat}: though care was taken to conduct measurements in vapour saturated with butanol, butanol evaporation at the needle tip may have occurred before deposition onto the substrate. The surface tension of butanol solutions is very sensitive to concentration (Fig. 3.10a), so it is possible that a change in composition during contact angle measurement led to a value of θ_{WA}^{sat} that is larger than the equilibrium value.

3.5.4 Experimental Results

Ink-jet printing is a method for depositing fluid onto a surface in the absence of direct contact between the apparatus that forms a pattern and the substrate. Suitable substrates may possess a wide variety of textures, geometries, mechanical strengths and other characteristics. The printing experiments were conducted onto glass substrates for a few reasons: first, glass is transparent so that drying drops can be viewed from underneath, allowing internal processes and suspended species to be tracked. The inherent geometrical restriction in ink-jet printing is that the print head is mounted directly opposite the substrate, thus blocking the view from above the drop. Second, a glass substrate is

homogeneous and has a low roughness, so that formulation characteristics are probed in the simplest possible scenario: the isolation and explanation of dynamics is thus easier. Printing repeatability is also ensured, provided substrates are clean. Third, the properties of glass substrates are readily tuned by treating the surface, allowing the degree to which the drop pins and the contact angle to be controlled. Modification of the substrate may facilitate wetting or beading as desired.

When a 6 %wt butanol solution was printed onto a hydrophobised substrate no phase separation was observed, as shown in Figure 3.14; the bright rings are optical artefacts.

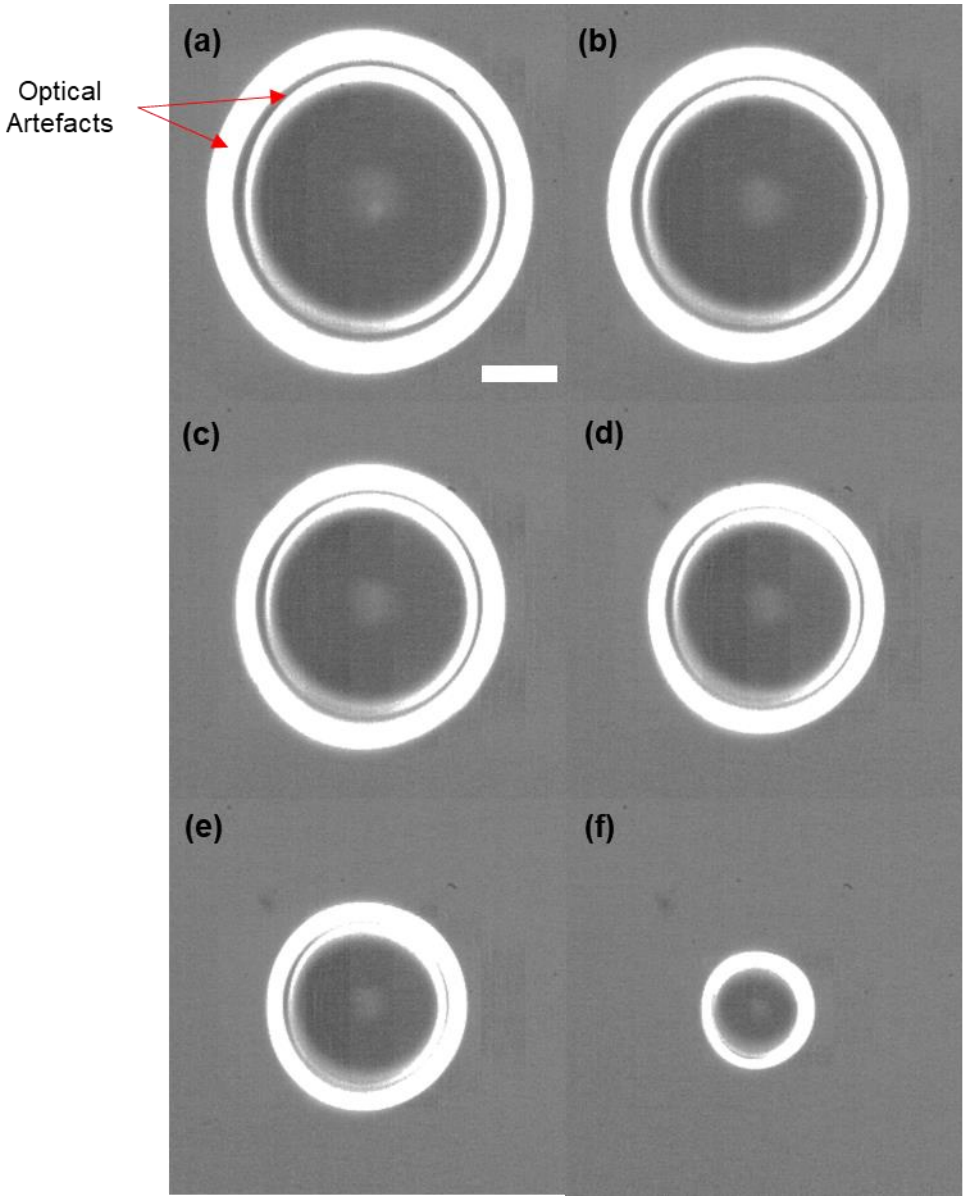

Figure 3.14. A drop of 6 %wt butanol solution viewed from underneath. Images were captured (a) 8 ms, (b) 1.0 s, (c) 2.0 s, (d) 3.0 s, (e) 4.0 s and (f) 5.5 s after deposition onto a hydrophobised substrate. The drop was jetted with a symmetrical bipolar waveform with a drive voltage of 30 V. The scale bar is 20 μm.

The presence and directionality of any internal flows during the drying process was discerned by seeding a 6 %wt butanol solution with 0.05 %wt polystyrene particles of diameter 1 μm. After deposition, a flow was initially present that moved radially inwards along the base of the drop and along the liquid-air surface from the apex to the contact line (Fig. 3.15). This behaviour is a Marangoni flow and is indicative of a surface tension gradient along the liquid-air surface (see Section 3.3.2).[44,73] The direction of movement of the particles showed that the drop apex had a lower surface tension than the contact line, such that fluid was "pulled" from the former to the latter.[44] For an aqueous butanol solution, the surface tension increases towards the pure value for water as the concentration of the solute decreases (Fig 3.10a). The printed drop was therefore deficient in butanol at the contact line relative to the apex and the local concentration of butanol was determined by the evaporative flux profile (Fig. 3.15). Consequently, butanol was evaporating too quickly for phase separation to be observed. After 1.86 s, the Marangoni flows ceased and the particles began an outward radial migration, commonly referred to as coffee-ring flow.[43]

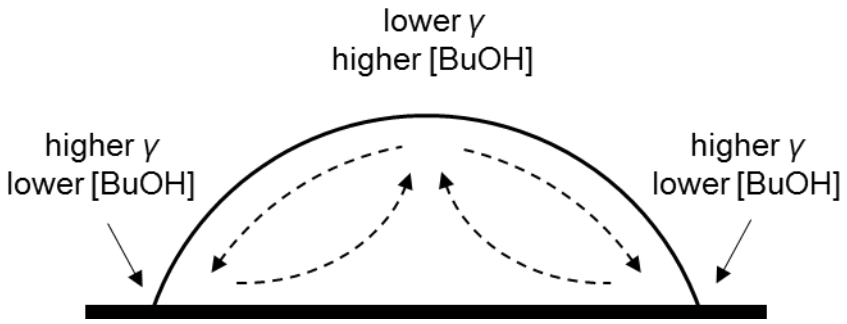

Figure 3.15. The internal flows observed in an evaporating drop of a 6 %wt butanol solution.

The above analysis is further supported using information extracted from images of the same drying drop, but captured from the side. The changes in volume over time for a 6 %wt butanol solution and for pure water are plotted in figures 3.16 and 3.17. The water drop shows a linear reduction in volume over time over the first 3 s, after which the rate slows slightly. For the butanol solution, the Marangoni flows ceased at t = 1.86 s. After t = 1.86 s, the rate of volume decrease in the drop of butanol solution matches that for the pure water: for 2 s < t < 3 s, both evaporate at 60.2 ± 0.4 pL s^{-1}. Thus, butanol fully evaporated before this period. Before t = 1.86 s, however, the evaporation rate of the butanol solution shows a small deviation from linearity: the rate of loss decreases before accelerating to resume the prior trend. Similarly, the contact angle does not vary smoothly during the same period: the rate of increase accelerates before decelerating. Since contact angle is an input into the calculation of the volume of the sessile drop, the

trend in volume over the period would be produced if the contact angle were over-estimated and then under-estimated. As the contact angle is changing rapidly over the period, it is likely that the deviations in contact angle, and therefore volume, are caused by inaccuracies in the edge fitting routine. Marangoni flows are also known to distort drop shapes from spherical cap geometries.[78]

The contact angle during drying for the 6 %wt butanol solution and for pure water are also plotted in Figures 3.16 and 3.17. The water drop maintained an approximately constant contact angle (70 − 80° over the first 4.5 s) throughout evaporation and volume loss was reflected in the recession of the contact line; it dried in constant-angle mode. Similarly, the contact line did not for pin for the butanol solution, but the contact angle behaviour differed to that of water: for the butanol solution, it increased over time and reached a maximum of 77° at around t = 2 s, just after the point at which the Marangoni flows stopped. Increasing surface tension is consistent with increasing contact angle and with decreasing butanol concentration (Fig. 3.10a). The convergence of the contact angle of the drop of butanol solution upon that of water, at the point of the cessation of Marangoni flows, further demonstrates that butanol completely evaporated early in the lifetime of the drop.

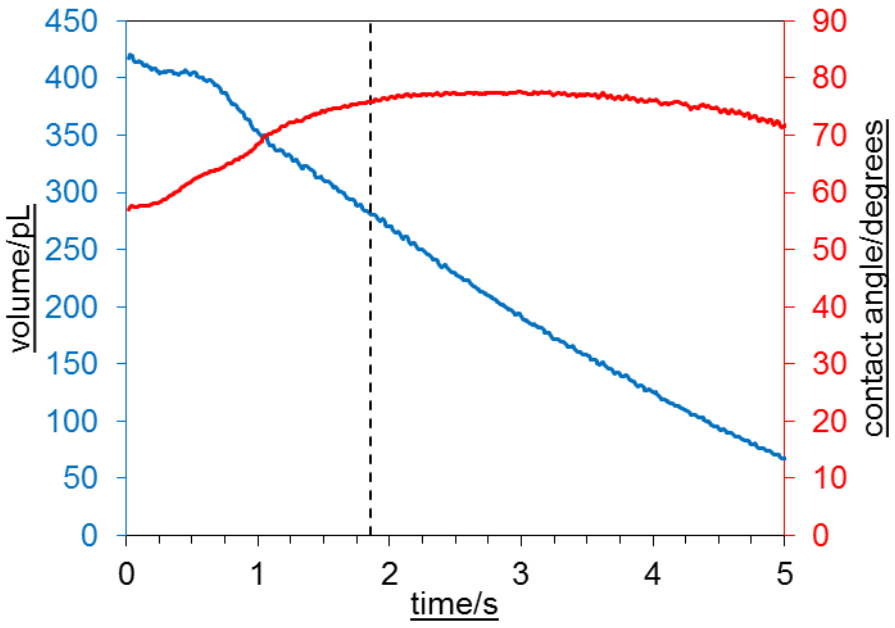

Figure 3.16. The drop volume (blue) and contact angle (red) of a 6 %wt butanol solution with 0.05 %wt polystyrene particles over time. Marangoni flows ceased after 1.86 s (black dashed line). The drop was jetted with a symmetrical bipolar waveform with a drive voltage of 30 V.

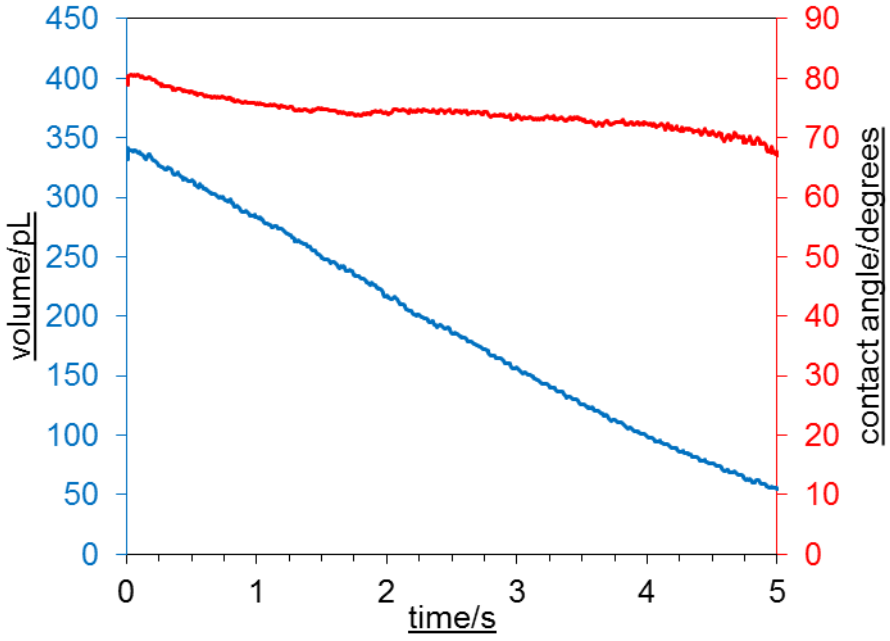

Figure 3.17. The drop volume (blue) and contact angle (red) of water with 0.05 %wt polystyrene particles over time. The drop was jetted with a symmetrical bipolar waveform with a drive voltage of 30 V.

3.5.5 Non-Ideality of Aqueous Butanol Solutions

The saturated solution of butanol does not phase separate under ink-jet printing conditions due to the non-ideality of the component vapour pressures. The component vapour pressures show major deviations from Raoult's law (Fig. 3.18).[79] At phase coexistence the water-rich phase has a minimum x_{water} = 0.98 and the butanol-rich phase has a maximum x_{water} = 0.51.[75] Since the two phases coexist at equilibrium, each component must have the same vapour pressure in both phases.

The vapour pressure of butanol in aqueous solution is better described by Henry's law

$$p_A = x_A H_A, \tag{3.44}$$

where H_A is the Henry constant (Fig. 3.18). The Henry constant for butanol in water at 298 K is 44.8 kPa[64], giving a butanol vapour pressure in the saturated solution of 0.90 kPa; the measured value from the literature is 0.65 kPa.[79] The vapour pressure of butanol is therefore modelled much more accurately by Henry's law than Raoult's law: the former gives an error of a factor of 1.4 whilst the latter gives an error of a factor of 50. The vapour pressure of water in a saturated butanol solution is 3.1 kPa, barely deviating from the pure liquid value.[79]

The aim is to use a single value κ (Eq. (3.29)) to screen mixtures for phase separation. Therefore, κ should be calculated from readily available data. Using the Henry law vapour pressure for butanol, taking the vapour pressure of water to be unchanged

from the pure liquid value and RH = 0.4, κ^{henry} = 0.08. A value less than unity indicates phase separation will not be observed. If a second phase were to form, it would evaporate more quickly than the water-rich phase. The value of κ^{henry} is a good indicator of whether phase separation is expected and explains the behaviour of the aqueous butanol solutions. In general, where the value of the Henry constant is not readily available for a solute in a particular solvent, the pure liquid vapour pressures may be used as an estimate of the partial vapour pressure in the saturated mixtures. In the case of water and butanol, this approximation would barely deviate from the value of κ^{henry}.

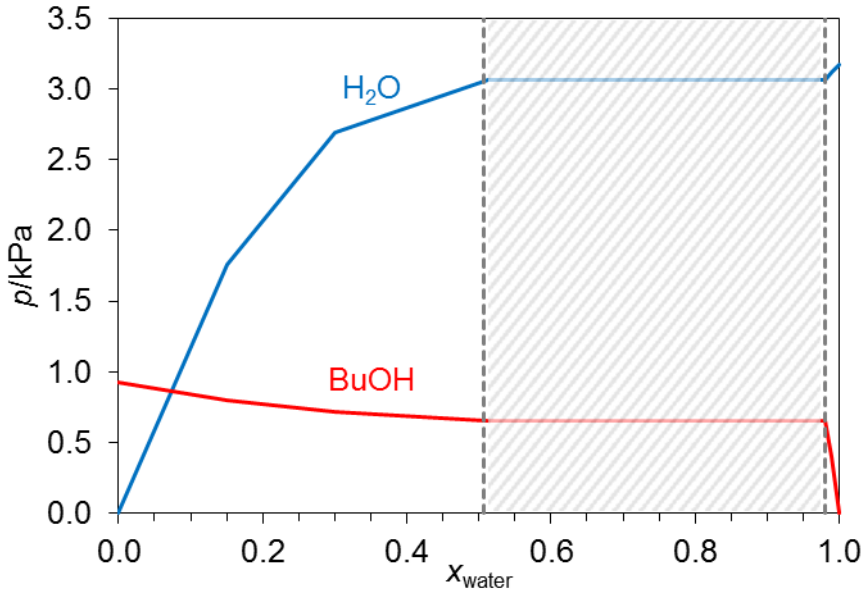

Figure 3.18. The vapour pressures p of water (blue) and butanol (red) in binary solution, as a function of the mole fraction of water, x_{water} at 298 K.[79] The shaded area between the dashed grey lines represents the two-phase region.

3.6 Screening for Aqueous Phase-Separating Mixtures

A binary solution that would phase separate upon printing will have $\kappa^{henry} > 1$. In order to identify a mixture that will phase separate, a wide series of liquids that have partial miscibility with water at room temperatures have been screened using this criterion and recorded in Table 3.2. Water has been assumed to have the same vapour pressure in the mixtures as in pure water. The search focussed on materials that have an aqueous solubility of the same order as butanol, so that any phase that separated out would have an appreciable volume. The value of H_A was then considered, with better candidates having a value lower than that of butanol. None of candidates 1−11 will produce aqueous formulations that phase separate under printing conditions because $\kappa^{henry} \leq 1$. They have the correct solubility characteristics but their vapour pressure in solution at the solubility limit is too high. *m*-Cresol is borderline but is excluded from further investigation on account of its toxicity. The remaining entries in Table 3.2 (12−24) are glycol ether derivatives, which provide more viable candidates for components of phase-separating formulations under evaporation. The increased molecular size has the dual effect of lowering the vapour pressure at ambient temperatures and lowering D_A so that some have $\kappa^{henry} > 1$. The great majority of the glycol ethers tabulated are expected to supersaturate during the evaporation of a binary aqueous solution. Some of them, however, have such low vapour pressures that complete evaporation would not be achieved on a practical timescale. Dipropylene glycol methyl ether acetate (DPGMEA) and dipropylene glycol *n*-propyl ether have the highest vapour pressures of the viable glycol ether candidates and thus appear to be the most suitable. The structure of DPGMEA is given in Figure 3.19a.

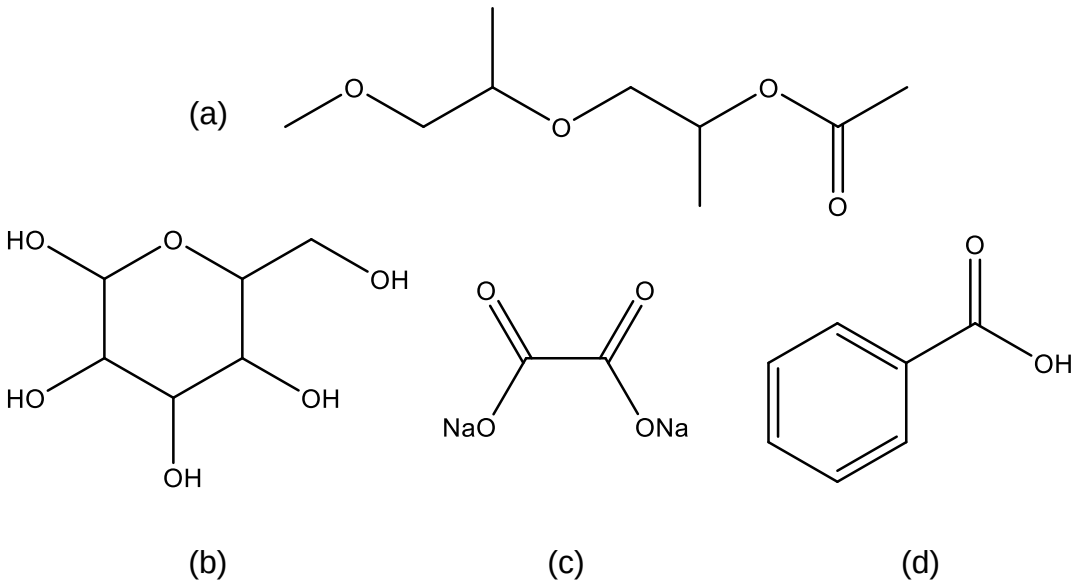

Figure 3.19. The chemical structures of (a) DPGMEA, (b) D-(+)-glucose, (c) sodium oxalate and (d) benzoic acid.

TABLE 3.2. Physical data at 298 K relating to a series of potential components for formulating aqueous phase-separating fluids under evaporation and an assessment of their viability.

	A	Solubility/ %wt[a]	$x_{A,lim}$	H_A/ kPa[b]	$p_{A,lim}$/ kPa	D_A/ (10^{-5} m^2 s^{-1})[c]	κ^{henry}	Viable?
1	*n*-Butanol	7.5	0.0192	44.8	0.862	0.90	0.08	N
2	Acetic Anhydride	15.0	0.0300	24.2	0.726	0.86	0.16	N
3	Isobutyric Acid	20.0	0.0486	4.96	0.241	0.87	0.77	N
4	Furfural	7.9	0.0158	18.2	0.289	0.89	0.20	N
5	Acetylacetone	10.0	0.0196	25.3	0.497	0.81	0.16	N
6	Aniline	3.4	0.0068	9.52	0.064	0.85	0.39	N
7	Cyclohexanol	3.8	0.0071	14.2	0.100	0.81	0.28	N
8	Isovaleric Acid	4.1	0.0075	7.90	0.059	0.79	0.51	N
9	Valeric Acid	2.4	0.0043	7.50	0.032	0.79	0.54	N
10	*m*-Cresol	2.2	0.0037	4.06	0.015	0.78	1.01	N
11	Butyl Acetate	0.7	0.0011	2347	2.490	0.73	0.002	N
12	Propylene Glycol Methyl Ether Acetate	16.0	0.0253	24.1	0.609	0.70	0.19	N
13	Dipropylene Glycol Methyl Ether Acetate	16.0	0.0177	1.16	0.021	0.57	4.86	Y
14	Dipropylene Glycol *n*-Propyl Ether	19.6	0.0243	1.15	0.028	0.58	4.91	Y
15	Propylene Glycol *n*-Butyl Ether	5.5	0.0079	22.0	0.173	0.66	0.22	N
16	Dipropylene Glycol *n*-Butyl Ether	4.5	0.0044	2.16	0.010	0.55	2.69	Y
17	Tripropylene Glycol *n*-Butyl Ether	4.5	0.0034	0.23	0.001	0.48	28.7	Y
18	Propylene Glycol Phenyl Ether	1.0	0.0012	2.55	0.003	0.65	1.91	Y
19	Propylene Glycol Diacetate	7.4	0.0089	0.80	0.007	0.65	6.12	Y
20	Dipropylene Glycol Dimethyl Ether	35.0	0.0564	0.07	0.004	0.61	77.3	Y
21	Diethylene Glycol Hexyl Ether	2.0	0.0019	0.10	0.0002	0.55	59.5	Y
22	Diethylene Glycol *n*-Butyl Ether Acetate	4.0	0.0037	0.20	0.001	0.55	29.0	Y
23	Ethylene Glycol *n*-Butyl Ether Acetate	1.6	0.0018	31.3	0.057	0.62	0.16	N
24	Ethylene Glycol Phenyl Ether	2.5	0.0033	1.14	0.004	0.66	4.24	Y

a: [1−11],[64] [12−24].[80] *b*: [1−10],[64] [11, 19, 21−23],[81] [12−18, 20, 24].[82] *c*: [1−24].[76,77]

3.7 DPGMEA and Water Mixtures

In the last section it was established that a DPGMEA-water mixture possesses the correct material properties for κ^{henry} to be greater than unity and is therefore expected to show phase separation upon jetting. This section presents an account of the investigation into the separation behaviour of water-DPGMEA formulations. First, physical data pertaining to the system is provided. Second, a physical model of expected separation behaviour based upon physical data is constructed. Third, results of printing on hydrophobic and hydrophilic substrates are presented.

Hereafter, the following nomenclature will be used to describe a phase separating butanol-water mixture: *DPGMEA-rich phase* for a water solution in DPGMEA, comprising > 50 %vol DPGMEA; *water-rich phase* for a DPGMEA solution in water, comprising > 50 %vol water; *saturated* to indicate the minor component is present at its miscibility limit.

3.7.1 Experimental Details and Procedures

Dipropylene glycol methyl ether acetate, DPGMEA, (*Sigma-Aldrich*, 99%) and water (Milli-Q) were used as received. The mutual solubilities of these materials were determined according to the procedure outlined in Section 3.5.2. DPGMEA reached saturation in water at 16.6 %wt and water reached saturation in DPGMEA at 5.1 %wt. The temperature was 296 K.

Predictions of equilibrium contact angles and wetting behaviour require the surface tensions of aqueous DPGMEA solutions and water solutions in DPGMEA to be known, as well as the interfacial tension between the two saturated solutions. The surface and interfacial tensions were measured by pendent drop tensiometry using the equipment and procedures described in Section 2.4. The solution densities were measured across the full range of miscibility and were found to be linear in composition. The data was fitted by linear regression to Eq. (3.32) and the values of the constants ρ_A* and k are given in Table 3.3.

TABLE 3.3. The constants and standard errors obtained from a linear least-squares fitting routine for the densities of water and DPGMEA mixtures as a function of composition.

Major Component A	Minor Component B	ρ_A* / (g mL^{-1})	k / [g mL^{-1} (%wt)$^{-1}$]
Water	DPGMEA	0.9930 ± 0.0003	0.00060 ± 0.00002
DPGMEA	Water	0.9701 ± 0.0001	0.00141 ± 0.00004

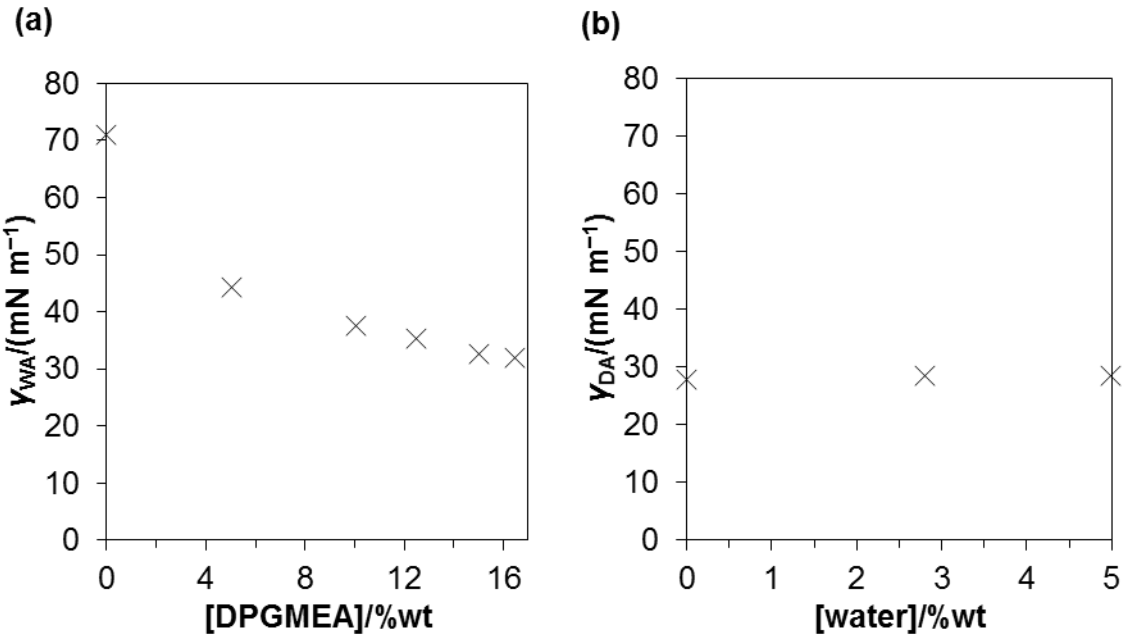

Figure 3.20. (a) The surface tension in air of aqueous solutions of DPGMEA, γ_{WA}, up to the miscibility limit, at 296 K. (b) The surface tension in air of DPGMEA solutions of water, $\gamma_{DA,}$ up to the miscibility limit, at 294 K.

Figure 3.20 shows the surface tensions in air of DPGMEA- and water-rich liquids over the range of miscibility. The value at saturation, γ_{WA}^{sat}, is measured to be 31.9 ± 0.2 mN m^{-1}. The surface tension in air of DPGMEA-rich liquids, γ_{DA}, is independent of water concentration (Fig. 3.20b) with a value of 28.43 ± 0.06 mN m^{-1}, which is used for γ_{DA}^{sat}. The interfacial tension between a 16.5 %wt DPGMEA solution and a 5.0 %wt water solution, γ_{WD}^{sat}, was measured at 3.15 ± 0.02 mN m^{-1} at 295 K.

The surface and interfacial tensions quoted above were measured from water and DPGMEA solutions that were just below saturation, though droplets of the second phase were suspended in the cuvette when air bubbles were formed at the J-shaped needle. To check the validity of the measurements, they were repeated with both phases in contact in the cuvette. The results were γ_{WA}^{sat} = 32.6 ± 0.2 mN m^{-1}, γ_{DA}^{sat} = 28.71 ± 0.06 mN m^{-1} and γ_{DW}^{sat} = 3.13 ± 0.02 mN m^{-1} at 295 K. The values of γ_{DA}^{sat} and γ_{DW}^{sat} are very similar to the first set of experiments. The repeated value of γ_{WA}^{sat} is 0.7 mN m^{-1} higher than before but the drop shape may have been distorted by oil-rich phase that wetted the J-shaped needle as it penetrated the upper oil-rich layer to reach the lower water-rich layer.

Contact angles of the saturated solutions were measured on glass substrates made hydrophobic with hexamethyldisilazane or hydrophilic by treatment with BIC (Section 2.1). Measurements of the contact angle were made using the tensiometer imaging system using the procedures are outlined in Section 2.4.2. The results are recorded in Table 3.4

with the associated standard deviations. The saturated DPGMEA-rich liquids form a low contact angle of only a few degrees on both the hydrophobic and hydrophilic substrates. In contrast, the saturated water-rich liquids show significantly different wetting behaviour depending on the substrate: a few degrees on a hydrophilic substrate but a much higher 32° on a hydrophobic substrate. When a drop of saturated DPGMEA solution with $r \sim$ 1.5 mm was placed on a hydrophilic substrate, a DPGMEA-rich annulus formed. The contact angle of the DPGMEA-rich phase on the water-rich phase was < 4°.

TABLE 3.4. Contact angles at 295 K for saturated mixtures of water and DPGMEA on hydrophobic and hydrophilic substrates in various media.

Drop Minor Component	Drop Major Component	Medium	θ_{sat}(Hydrophobic)/ degrees	θ_{sat}(Hydrophilic)/ degrees
Water	DPGMEA	Air	7 ± 1	7 ± 1
DPGMEA	Water	Air	31 ± 1	6 ± 1
DPGMEA	Water	Water-Saturated DPGMEA	113 ± 1	22 ± 1

3.7.2 Expected Separation Behaviour

The geometry of a two-phase DPGMEA-water mixture is predicted using the principles that guided the evaluation of the butanol-water system in Section 3.5.3. Phase separation is expected first at the contact line. If both the DPGMEA-rich and water-rich phases are mutually saturated and using γ_{WA}^{sat} = 31.9 ± 0.2 mN m^{-1}, γ_{DA}^{sat} = 28.43 ± 0.06 mN m^{-1} and γ_{WD}^{sat} = 3.15 ± 0.02 mN m^{-1}, the spreading ratio $S_{D/W}$ = +0.300 ± 0.003 mN m^{-1} (see Section 3.2.1) using the first set of measurements. With the second set of measurements, $S_{D/W}$ = +0.710 ± 0.004 mN m^{-1}. A positive value of $S_{D/W}$ indicates that the oil-rich phase spreads over the surface of the water-rich phase thermodynamically.

The sign of the Hamaker constant dictates whether the DPGMEA-rich phase spreads or pseudo-partially wets (Section 3.2.1). The Hamaker constant may be estimated using Equation (3.7). The refractive indices and static dielectric constants of the saturated liquid phases have not been measured; the values pure water and DPGMEA will be used as an approximation since it is the sign of A_H that is important. Using the dielectric constants ε_{air} = 1, ε_{water} = 80 and ε_{DPGMEA} = 11 and the refractive indices n_{air} = 1, n_{water} = 1.33 and n_{DPGMEA} = 1.42, $A_H \sim +0.9 \pm 10^{-20}$ J.[83] If $S_{D/W} > 0$ and $A_H > 0$, pseudo-partial wetting is anticipated. Thin films of the DPGMEA-rich phase will spread over the surface

of the evaporating drop and the excess fluid should collect into a bulk geometry based upon the short-range surface forces. The presence of a thin film of the oil-rich phase in a phase-separating drop should allow the oil-rich phase to be transported to the apex more easily under buoyancy.

The best-estimate values of $S_{D/W}$ calculated from the measured contact angles and surface/interfacial tensions are unphysical. At equilibrium, the following inequality must hold:

$$\gamma_{DA}{}^{sat} + \gamma_{WD}{}^{sat} - \frac{A_H}{12\pi D^2} \geq \gamma_{WA}{}^{sat} . \tag{3.45}$$

Equation (3.45) may be rearranged into

$$-\frac{A_H}{12\pi D^2} \geq S_{D/W} . \tag{3.46}$$

Since $A_H \sim +10^{-20}$ J and D is a molecular length scale ($\sim 10^{-10}$ m), $S_{D/W} \leq -0.3$ mN m^{-1}. The value calculated from the experiments ($S_{D/W} = +0.300$ mN m^{-1}) does not agree with this analysis since it is greater than zero.

The self-consistency of the contact angles and surface/interfacial tensions reported in Section 3.7.1 can be checked in the same manner as for the butanol-water system (see Section 3.5.3) using

$$\begin{aligned} \gamma_{DA}{}^{sat} \cos\theta_{DA}{}^{sat} - \gamma_{WD}{}^{sat} \cos\left(\pi - \theta_{WD}{}^{sat}\right) \\ = \gamma_{WA}{}^{sat} \cos\theta_{WA}{}^{sat} . \end{aligned} \tag{3.47}$$

Solving for $\theta_{WA}{}^{sat}$ on the hydrophobic substrate gives $\theta_{WA}{}^{sat} = 32°$, which is almost identical to the measured value of 31 ± 1°. The data relating to the system on the hydrophobic substrate are therefore self-consistent. Similarly, solving for $\theta_{WA}{}^{sat}$ on the hydrophilic substrate gives $\theta_{WA}{}^{sat} = 12°$, which is slightly larger than the measured value of 6 ± 1°. The discrepancy corresponds to an error in cos $\theta_{WA}{}^{sat}$ of < 2%, so the data relating to the system on the hydrophilic substrate are also self-consistent. There is therefore no obvious inconsistency to explain the unphysical value of $S_{D/W}$. The reason for the unphysical value of $S_{D/W}$ remains unclear.

3.7.3 Experimental Results

Jetting experiments with DPGMEA solutions were carried out on both hydrophobic and hydrophilic substrates, giving different phase separation behaviour. Substrate preparation procedures are detailed in Section 2.1. Note that during printing trials, the substrates prepared with BIC showed very similar printing dynamics to those prepared by washing in *iso*-propanol or acetone: Figure 3.21 shows snapshots of the same formulation on both substrates prepared with acetone (a) and the full BIC procedure (b). The reason why

behaviour is so similar is that both remove particulate material from the surface, but neither causes chemical change. The only difference is that there is a higher degree of centrosymmetry when using substrates prepared with BIC as the surface possesses fewer pinning sites on account of the more aggressive treatment. During the printing trials discussed in Sections 3.7 and 3.8, drying dynamics observed on substrates prepared using BIC, acetone and iso-propanol are all therefore directly compared.

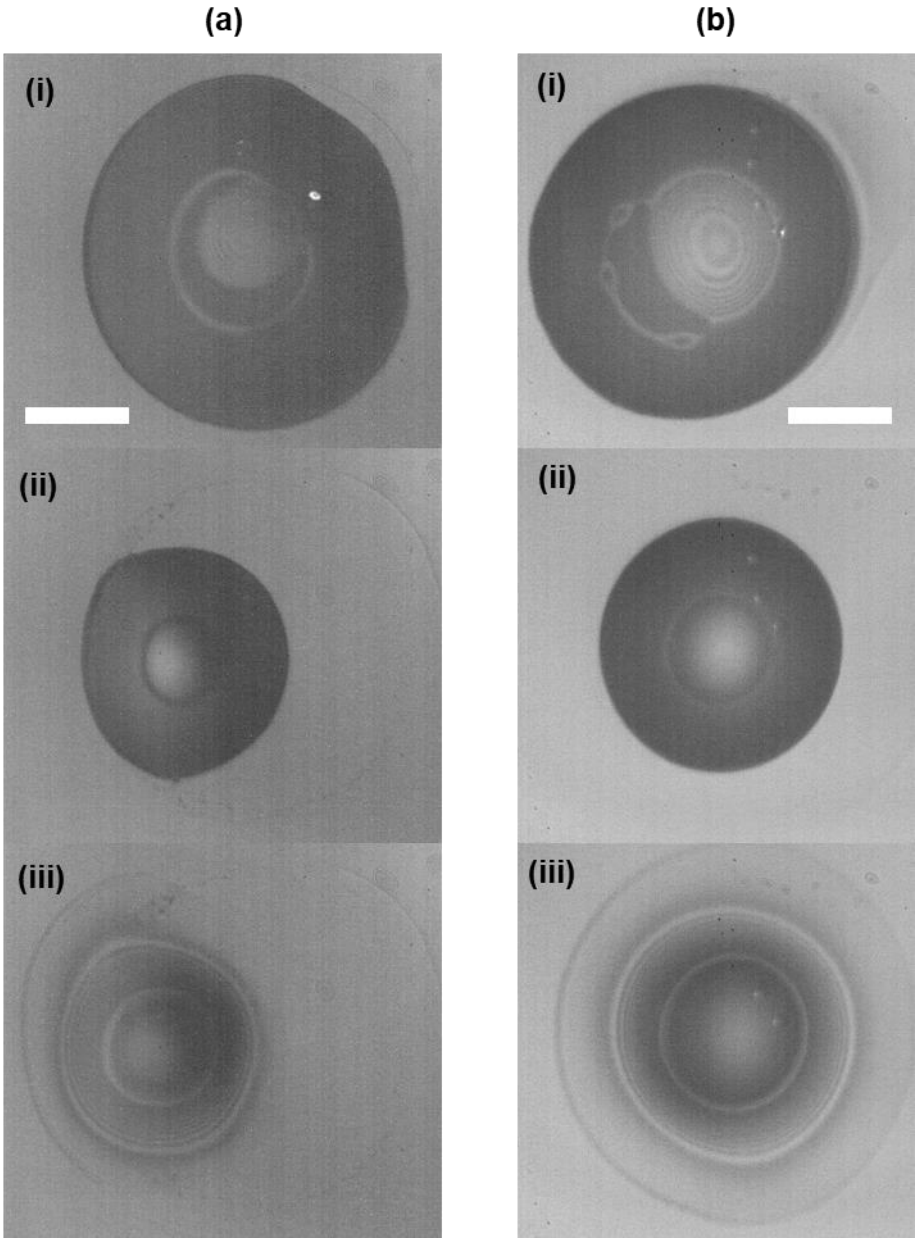

Figure 3.21. Drops of an aqueous solution containing 1.4 %wt sodium oxalate, 0.7 %wt benzoic acid and 3.8 %wt DPGMEA drying on (a) a substrate washed in acetone and (b) a substrate cleaned in BIC. (a) Images were captured (i) 6 ms, (ii) 0.7 s and (iii) 1.2 s after deposition. (b) Images were captured (i) 0.1 s, (ii) 0.9 s and (iii) 1.5 s after deposition. The drops were jetted with a symmetrical bipolar waveform with a drive voltage of 30 V. The scale bars are 30 μm.

3.7.3.1 Jetting onto Hydrophobic Substrates

An aqueous 15.1 %wt DPGMEA solution is close to the miscibility limit and printing trials were conducted with this solution onto a hydrophobised substrate. In contrast to the butanol solution, the DPGMEA solution did phase separate upon deposition onto the substrate. Figure 3.22 displays images of the drying process viewed from underneath and Figure 3.23 shows the change in volume and contact angle over time. The drop initially forms a spherical cap on the substrate and is a single phase (Fig. 3.22a); the bright ring at the contact line is an optical artefact arising from reflection of illumination from LED 2 into the camera (see Fig. 2.5). Over the first 0.2 s of drying the contact line remains pinned and the volume loss is reflected in the decreasing contact angle (Fig. 3.23). At t = 0.23 s, a second phase appears at the contact line (red dots in Fig. 3.22c) and is marked by a reduction in the rate of contact angle decrease (Fig. 3.23). The phase boundary moves radially inwards (Figs. 3.22d−e) until t = 3.0 s, when only one phase remains (Fig. 3.22f) and the volume and contact angle become constant (Fig 3.23). The volume of the liquid remaining after t = 3.0 s is 16 pL out of the initial 115 pL, representing 14% of the original volume, matching the initial proportion of DPGMEA (ρ = 0.97 g mL^{-1}) present in the formulation. DPGMEA has therefore increased in concentration at the contact line due to relatively rapid water evaporation and the local composition has passed through the binodal, leading to phase separation. The phase boundary has then moved inwards as more water evaporates until only DPGMEA remains on the substrate.

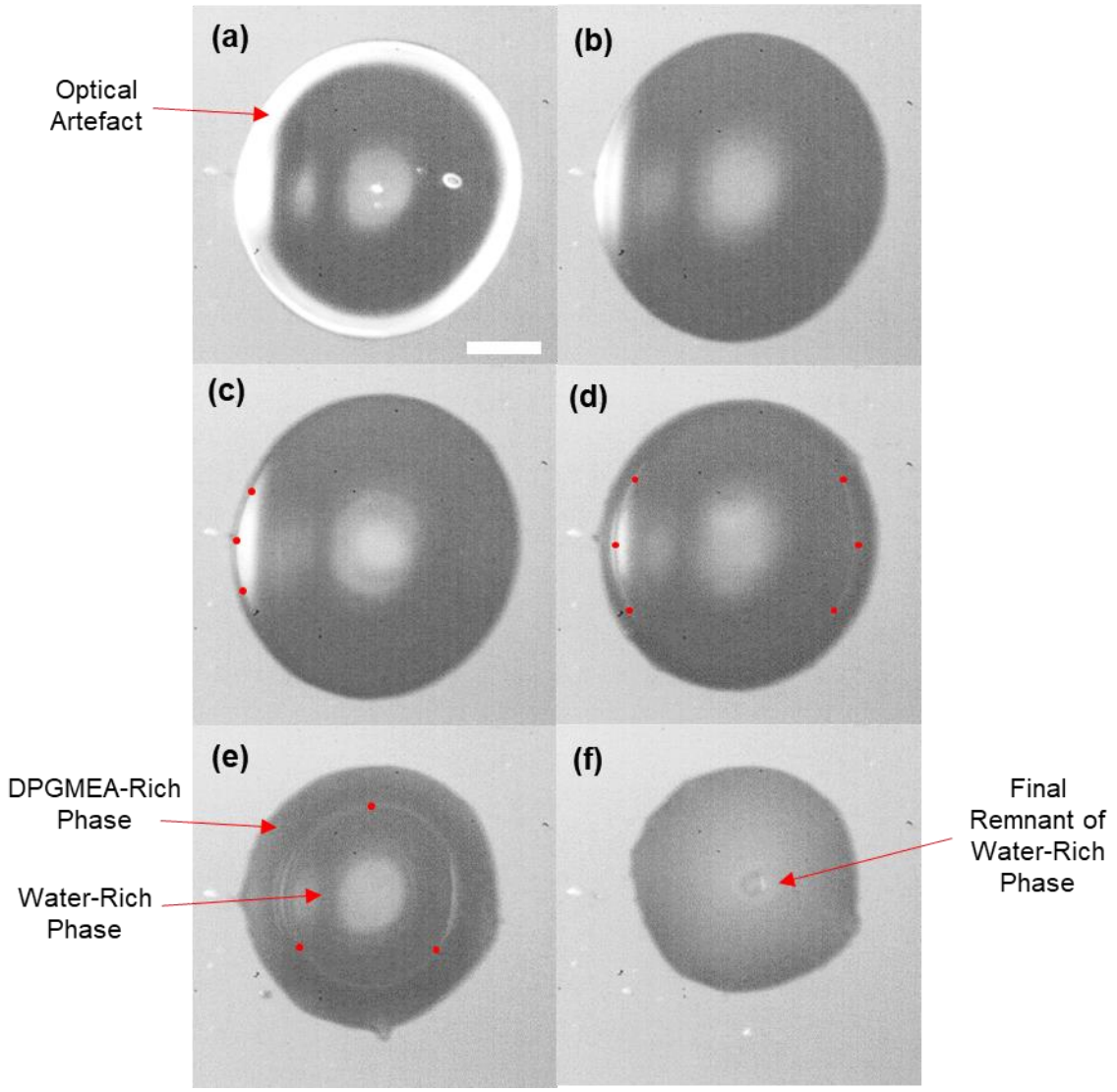

Figure 3.22. A drop of 15.1 %wt DPGMEA solution viewed from underneath. Images were captured (a) 8 ms, (b) 0.20 s, (c) 0.40 s, (d) 0.80 s, (e) 1.60 s and (f) 3.00 s after deposition onto a hydrophobised substrate. The drop was jetted with a symmetrical bipolar waveform with a drive voltage of 30 V. Red dots mark the interfacial boundary between the water-rich and DPGMEA-rich phases. The scale bar is 30 μm.

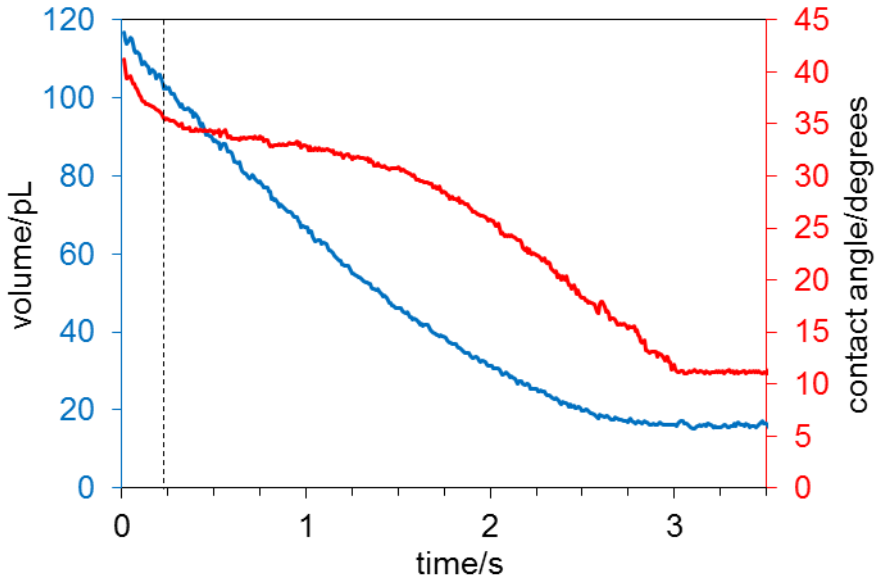

Figure 3.23. The drop volume (blue) and contact angle (red) of a 15.1 %wt DPGMEA solution over time. The vertical dashed line marks the time at which the second phase is first visible. Data for the same drop as displayed in Figure 3.22. The drop was jetted with a symmetrical bipolar waveform with a drive voltage of 30 V.

Throughout evaporation, complex interference patterns are observed at the centre of the drop. The patterns are consistent with the expectation that the oil-rich phase pseudo-partially wets the water-rich phase. For some drops, the film may collect into a lens, but it is unclear from the footage. The thin oil-rich film over the surface increases the rate of transport of the new phase to the apex under buoyancy.

The observation of phase separation for a 15.1%wt DPGMEA solution (where $\kappa^{henry} > 1$) but the single-phase evaporation scheme observed for a 6 %wt butanol solution (where $\kappa^{henry} < 1$) indicates that κ^{henry} is a useful criterion for determining whether phase separation is likely to occur for a particular mixture. The separation that occurred during the evaporation of a 15.1 %wt DPGMEA solution resulted in a DPGMEA-rich phase that did not evaporate on an appreciable timescale (Fig. 3.23, $t > 3$ s) leaving stagnant fluid on the substrate. The longevity of the oil is disadvantageous for application since any patterning control of a hypothetical particle or solute may be lost if the pattern is not strongly adhered to the substrate. The impact of the remaining DPGMEA after complete loss of the water would be reduced if the initial solution was of lower oil concentration.

When a 1.2 %wt DPGMEA solution was jetted onto a hydrophobised substrate phase separation occurred in a manner similar to that observed for the 15.1 %wt solution. Figure 3.24 displays images of the drying process viewed from underneath and Figure 3.25 shows the change in volume and contact angle over time. The drop formed a

spherical cap and was a single phase (Fig. 3.24a); the bright ring at the contact line is an optical artefact. Initial drying dynamics are the same as has been observed for pure water: volume loss is linear in time and the drop has a contact angle of ~70° (Fig. 3.25 *cf.* Fig 3.17). Given the low concentration of DPGMEA in the formulation, the surface tension is ~60 mN m^{-1} (Fig. 3.20a) giving a much higher contact angle than the ~40° observed for the near-saturated 15.1 %wt solution (Fig. 3.23). The contact angle reduces as water evaporates and the concentration of the ether acetate increases. At t = 3.9 s, a second phase rich in DPGMEA forms at the contact line (red dots in Fig. 3.24d) and the interfacial boundary moves radially inwards as water continues to evaporate (Fig. 3.24e) until only the ether acetate remains (Fig. 3.24f). Thus phase separation can be achieved even with the addition of only a small amount of the partially miscible component.

As was observed for the 15.1 %wt DPGMEA solution, complex interference patterns were visible at the centre of the drop after the second phase began to separate; the patterns are not visible before t = 3.9 s. Complex interference patterns are consistent with the presence of a thin film. The thin film must be immiscible with the major water-rich phase which it contacts, else they would coalesce. The patterns therefore indicate the presence of a thin film rich in the only other component: DPGMEA. A thin oil-rich film must have spread over the water-rich phase, as expected for a pseudo-partially wetting system.

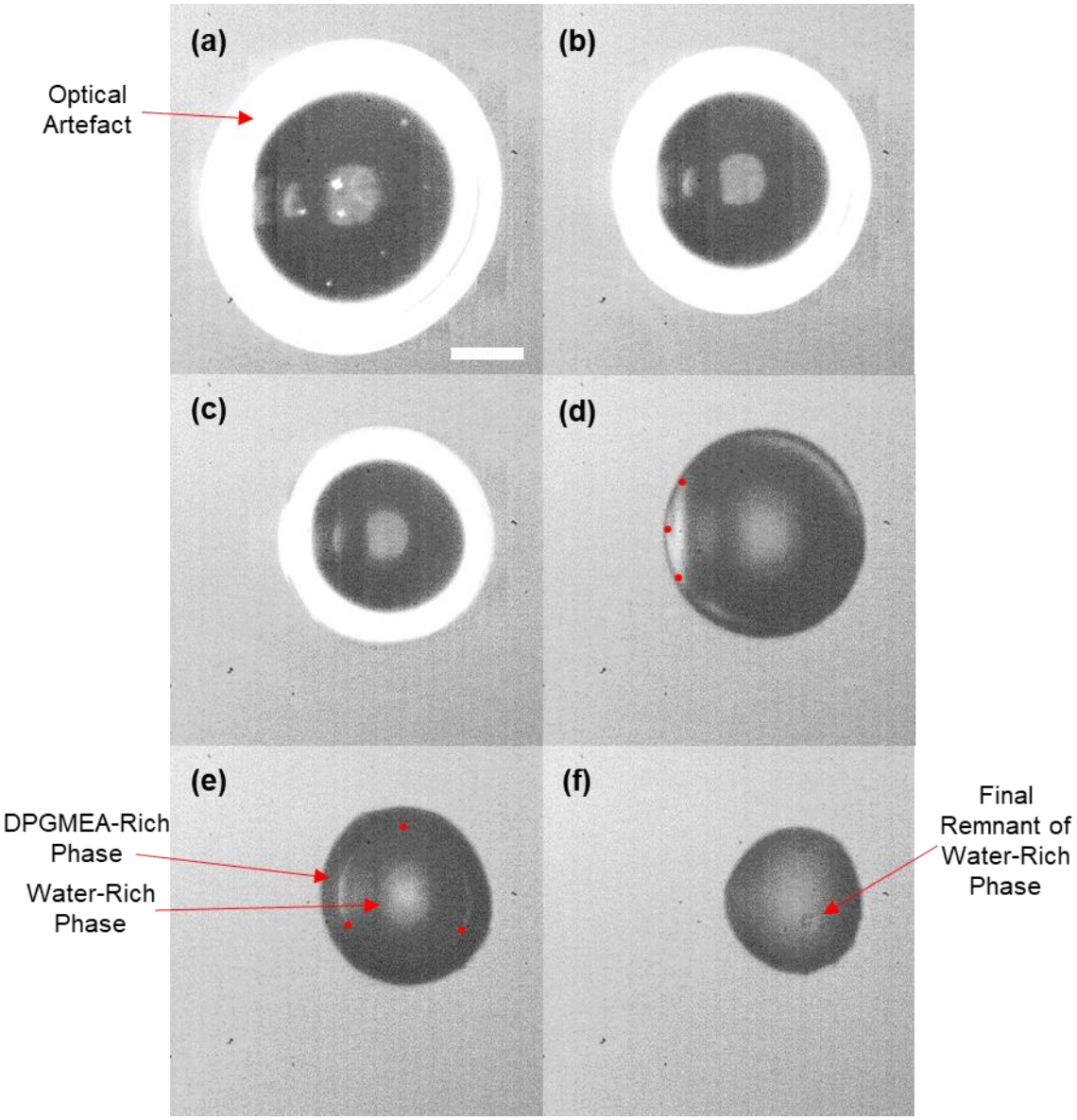

Figure 3.24. A drop of 1.2 %wt DPGMEA solution viewed from underneath. Images were captured (a) 8 ms, (b) 1.6 s, (c) 3.2 s, (d) 3.9 s, (e) 4.4 s and (f) 5.2 s after deposition onto a hydrophobised substrate. The drop was jetted with a symmetrical bipolar waveform with a drive voltage of 30 V. Red dots mark the interfacial boundary between the water-rich and DPGMEA-rich phases. The scale bar is 30 μm.

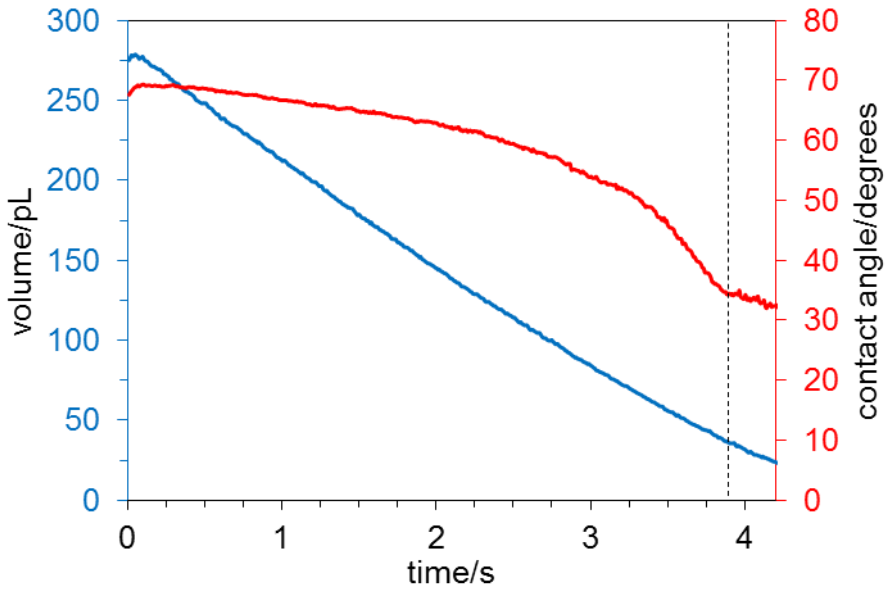

Figure 3.25. The drop volume (blue) and contact angle (red) of a 1.2 %wt DPGMEA solution over time. The vertical dashed line marks the time at which the second phase is first visible. Data for the same drop as displayed in Figure 3.24. The drop was jetted with a symmetrical bipolar waveform with a drive voltage of 30 V.

3.7.3.2 Jetting onto Hydrophilic Substrates

The dynamics of phase separation on a hydrophilic substrate differed from those observed on a hydrophobic substrate. The dynamics when drying takes place on a hydrophilic substrate (treated with BIC) are exemplified in Figure 3.26 for a 3.9 %wt DPGMEA solution. The micrographs are more complicated in appearance than their counterparts in Figures 3.22 and 3.24 due to the visibility of Newton rings. The observation of Newton rings indicates the drop is adopting a much lower contact angle than was observed on the hydrophobic substrate, as expected from the contact angles observed for water (Section 2.1) and for the saturated water-rich liquid (Table 3.4). The drop arrives at the substrate as a single phase and forms a uniform footprint (Fig. 3.26a). At $t \sim 0.25$ s, DPGMEA supersaturates at the contact line and the interfacial boundary moves radially inwards (red dots in Figs 3.26c−e), in common with the dynamics on a hydrophobic substrate (*cf.* Figs. 3.22e and 3.24e). After complete evaporation of the water, a thin film of DPGMEA remains (Fig. 3.26f).

A lens of the DPGMEA-rich phase is visible at the upper surface of the water-rich phase (yellow dots in Figs. 3.26b−e). The lens initially forms centrally (Fig 3.26b) and originates from a thin film on the drop surface that contracts. It is not stationary during drying, migrating close to the interfacial boundary (Figs. 3.26c−e), before merging with the oil annulus at late times.

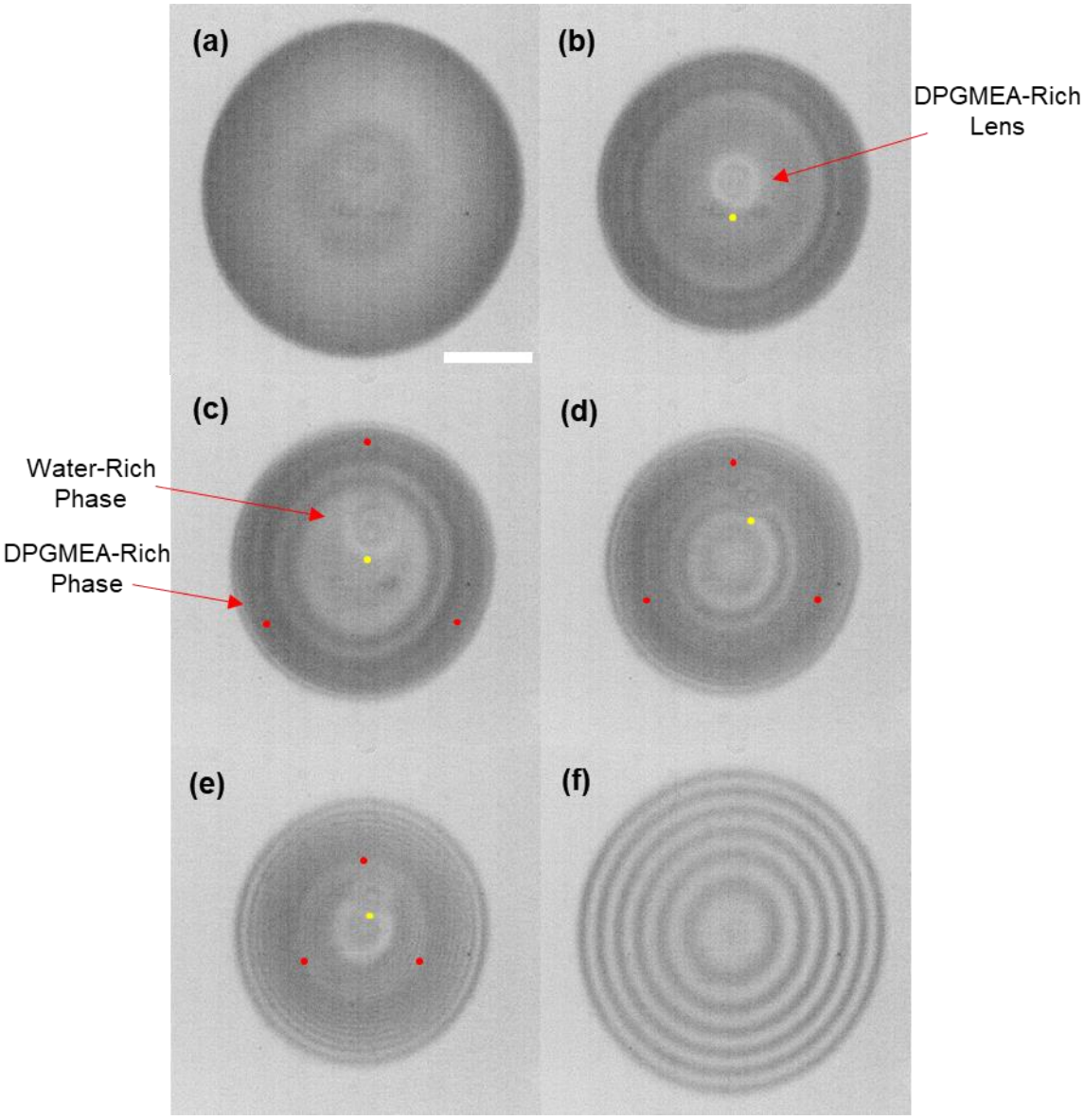

Figure 3.26. A drop of 3.9 %wt DPGMEA solution viewed from underneath. Images were captured (a) 0.10 s, (b) 0.28 s, (c) 0.33 s, (d) 0.43 s, (e) 0.53 s and (f) 0.77 s after deposition onto a substrate cleaned in BIC. The red dots mark the interfacial boundary between the water-rich and DPGMEA-rich phases. A DPGMEA-rich lens on the drop surface is marked by a yellow dot slightly below the feature. The drop was jetted with a symmetrical bipolar waveform with a drive voltage of 15 V. The scale bar is 30 μm.

For thin-film interference, the difference in thickness Δd between bright fringes or between dark fringes is a function of the refractive index n of the film and the wavelength λ of the illuminating light:

$$\Delta d = \frac{\lambda}{2n}. \tag{3.48}$$

As λ = 505 nm and n ~1.4 for DPGMEA,[83] Δd = 0.18 μm. In Figure 3.26e, the DPGMEA-rich phase therefore has a contact angle of ~3.2°, whilst in Figure 3.26f, the contact angle is ~1.7°. Since the DPGMEA film is still spreading in Figure 3.26f, it is likely the thermodynamic value of θ = 0.

3.7.4 Discussion

The first iteration of the criterion for phase separation (κ^{raoult}) assumed ideal vapour pressures in binary mixtures and falsely indicated that a butanol-water mixture would phase separate during evaporation. The origin of the failure of κ^{raoult} was that vapour pressures in mixtures of partially miscible liquids are highly non-ideal, with the vapour pressure at saturation of butanol equal to 70% of the value for pure butanol despite a mole fraction of 2%.[79]

The criterion κ^{henry} assumes the vapour pressure of the minor component may be modelled according to Henry's law and that the vapour pressure of the major component may be approximated to the value for the pure component. The criterion κ^{henry} correctly indicated that butanol-water mixtures do not phase separate during evaporation. It also allowed a wide range of aqueous candidate mixtures to be screened from literature data, resulting in the identification of glycol ethers as suitable materials for aqueous phase-separating formulations; practical jetting trials with DPGMEA-water mixtures showed that the system does indeed separate during evaporation.

κ^{henry} is a useful tool for formulation design: positively, κ^{henry} allows those seeking to develop other phase-separating formulations to screen candidate solvents efficiently; negatively, κ^{henry} allows those who wish to design formulations that remain a single phase throughout evaporation to screen out formulations with the propensity to separate during evaporation at an earlier stage in the design process and before practical trials commence. The strength of κ^{henry} as a metric is that it makes use of readily available physical data (gas-phase diffusion coefficients, the solubility limit, pure component vapour pressures and the Henry constant for the minor component); whether or not a system will separate on the substrate can thus be determined from reference data alone.

Water-based formulations were designed that phase separated on the substrate after deposition from the print head: 15.1 %wt, 3.9 %wt and 1.2 %wt DPGMEA solutions. The formulations have a number of attractive features for practical application: first, the majority of the vapour generated during evaporation is water, which is non-toxic. Second, the system does not rely on expensive solvents; water is ubiquitous and inexpensive. Third, separation was observed for a formulation that was not close to the binodal at formulation, allowing the timing of phase separation to be controlled until after water had begun to evaporate. Fourth, separation was observed when the minor component was present initially as a small proportion of the total fluid; thus for phase separation to be observed, only small quantities of co-solvent need be included in the original formulation.

The behaviour of the DPGMEA-water mixtures that most limits application is the longevity of the DPGMEA on the substrate after complete evaporation of water. Ink-jet printing is generally used as a means of fine patterning of solids and a long-lived oleic liquid on the substrate is not conducive to attaining dry deposits. For the DPGMEA-water formulations to be useful, the substrate would need to be passed under a heating element to drive off the excess oil. The persistence of the oil is also detrimental since any selective patterning could be compromised by wetting of the deposit originating from the aqueous phase by the oil (see Section 3.8.2). Faster evaporation would be achieved if the co-solvent to water had a similar solubility but higher volatility than DPGMEA. The screening of solvents carried out in Section 3.6 shows that it is difficult to find a liquid with the correct properties. Considering Table 3.2, a solvent with a structure intermediate between propylene glycol methyl ether acetate and dipropylene glycol methyl ether acetate might be suitable to water-based formulations that phase separate after jetting.

The mode of phase separation in the DPGMEA-water mixtures was largely as expected: the second phase formed at the contact line where evaporative flux was greatest and composition changed the most rapidly. The result was a ring of a phase rich in DPGMEA at the contact line surrounding a water-rich phase. The observations match those of a recent publication by Tan *et al.*,[84] which was published shortly after aspects of the present work (based on Sections 3.4 − 3.7) were submitted as a conference paper to *Printing for Fabrication 2016*.[85] Tan *et al*.[84] deposited 0.7-μL drops of *Ouzo* (37.3 wt% water, 61.1 %wt ethanol and 1.7 %wt anise oil) from a syringe onto a hydrophobised glass surface to give a sessile drop approximately 2 mm in diameter. The evaporation dynamics passed through four stages. First, the drop adopted a spherical cap and ethanol evaporated preferentially to water, with the composition changing fastest at the contact line; Marangoni flows were observed (see Fig 3.9a). Second, the reduction in concentration of ethanol at the contact line lowered the solubility of the anise oil, leading to the nucleation of a second phase; droplets were dispersed throughout the aqueous phase by the Marangoni flows and began to collect as a ring at the contact line. Third, complete ethanol evaporation left the aqueous phase resting on a ring of the oleic phase. Fourth, a continuous anise oil drop with a spherical cap geometry remained after complete water evaporation; water completely evaporated ~13 min after deposition. In the present work on DPGMEA-water mixtures, recirculating droplets were not observed since ethanol was not included, but otherwise drying dynamics followed the same pattern. Tan *et al.*[84] imaged the drying Ouzo drop from the side when the oil ring was present and geometries

equivalent to those that had been anticipated for the butanol-water mixture (see Fig 3.12) were observed.

3.8 Solute Patterning with DPGMEA and Water Mixtures

In the last section it was established that mixtures of partially miscible liquids can be formulated as a single phase, but the phase separate during evaporation. Aspects of the separation dynamics, like the appearance of the second phase at the contact line, were independent of the substrate. In this section, the possibility of using phase separation as a deposit patterning tool for ink-jet printing will be explored.

3.8.1 Glucose as the Solute

A pair of solutes needed to be identified which will favourably partition into opposite phases. The first candidate for the species expected to partition into the water-rich phase was D-(+)-glucose (*Sigma-Aldrich*, ≥99.5%); see Figure 3.19b for the structure. Glucose has a reported aqueous solubility of 0.9 g mL^{-1} at 298 K,[86] whilst the solubility of glucose in DPGMEA is low, with solid still visible at a concentration of 0.3 %wt. The inclusion of glucose into DPGMEA-water mixtures decreased the solubility of the DPGMEA: a formulation comprising 20 %wt glucose, 12 % DPGMEA and 68 %wt water exists as two phases, despite the 16.6 %wt solubility of DPGMEA in pure water. A formulation comprising 21 %wt glucose, 4 %wt DPGMEA and 75 %wt water existed as one phase.

Glucose deposits were not obtained during printing trials with glucose-DPGMEA-water mixtures. The evaporation dynamics are exemplified in Figure 3.27 for a formulation comprising 2.0 %wt glucose, 1.2 %wt DPGMEA and 96.8 %wt water printed onto a hydrophobic substrate; the bright ring close to the contact line in each micrograph is an optical artefact. At $t \sim 0.5$ s, a second phase rich in DPGMEA forms at the contact line and is visible in Figure 3.27c−e. The rate of evaporation appears to slow as the volume of the drop decreases and the drop has a very similar contact area with the substrate for 1.6 s < t < 4.0 s (compare Figs 3.27e−f). Complete evaporation of the drop was not observed, nor the precipitation of the glucose. To investigate whether the DPGMEA was the cause of incomplete evaporation, a simple 2.0 %wt glucose solution was ink-jet printed onto a hydrophobic substrate. The drop volume stabilised after the loss of the majority of the water and no glucose precipitated from solution, as had been observed for the comparable formulation containing DPGMEA.

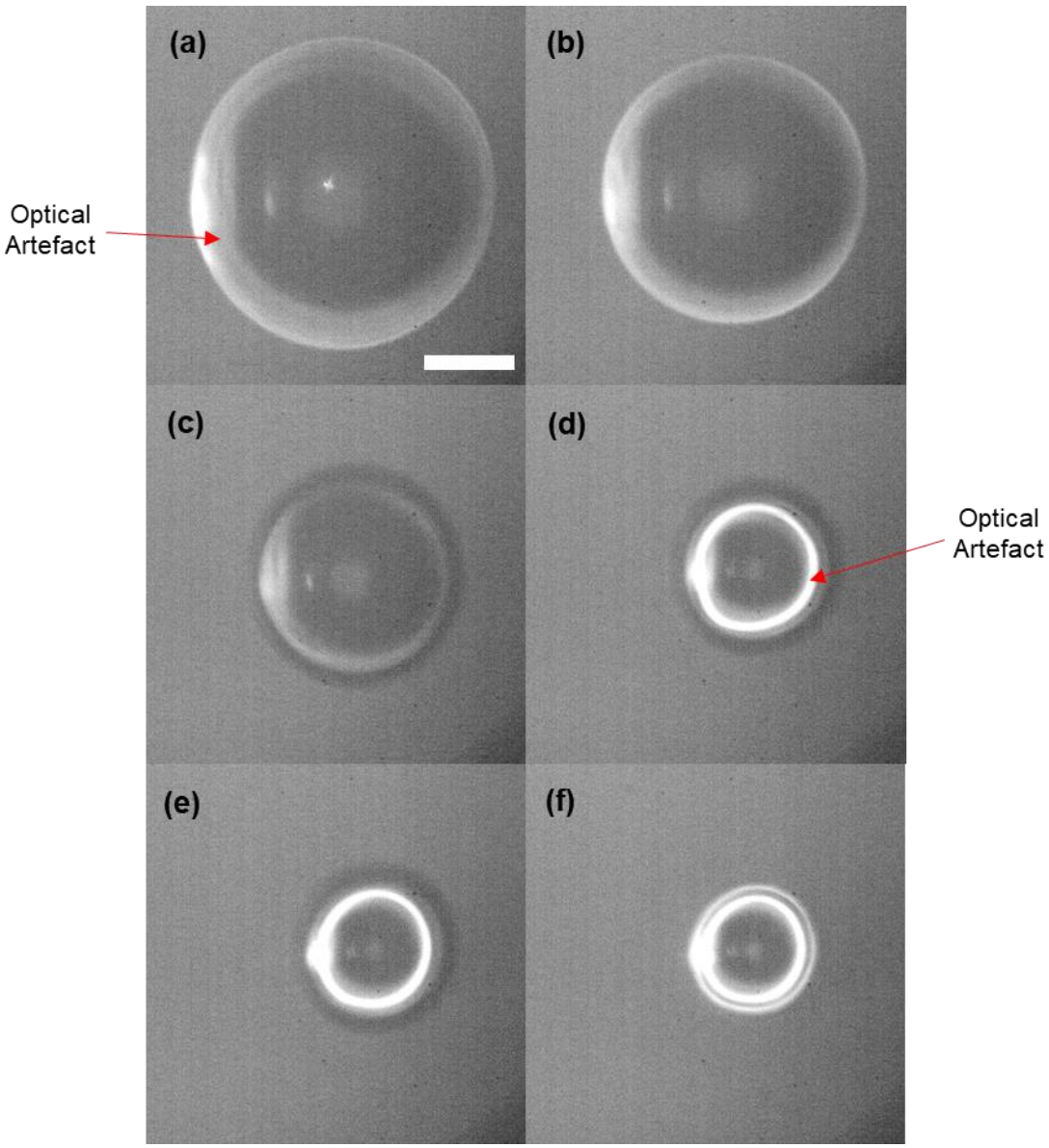

Figure 3.27. A drop of an aqueous solution containing 2.0 %wt glucose and 1.2 %wt DPGMEA viewed from underneath. Images were captured (a) 8 ms, (b) 0.4 s, (c) 0.8 s, (d) 1.2 s, (e) 1.6 s and (f) 4.0 s after deposition onto a hydrophobised substrate. The drop was jetted with a symmetrical bipolar waveform with a drive voltage of 30 V. The scale bar is 30 μm.

The failure of the glucose-DPGMEA-water formulations to precipitate glucose and to proceed to complete evaporation may be explained by considering the chemical potential of the water in the system. The discussion will be based on the simpler aqueous glucose solution (in the absence of DPGMEA) which showed the same behaviour. For a drop of pure water and air at equilibrium, the gas phase is saturated with water vapour ($RH = 1$) and the chemical potentials of water $\mu_{water,\ liq}$ (pure water) and water vapour $\mu_{water,\ vap}$ ($RH = 1$) are equal. If the relative humidity is reduced to $RH = a$, the chemical potential of the vapour is reduced to $\mu_{water,\ vap}$ ($RH = a$). For a drop of pure water in an open

atmosphere with $RH < 1$, $\mu_{water,\,liq}$ (pure water) > $\mu_{water,\,vap}$ ($RH = a$) and the drop evaporates completely (Fig. 3.28a).

If glucose is introduced into the water drop, the chemical potential is reduced to $\mu_{water,\,liq}$ (glucose solution). Fig. 3.28b corresponds to a drop of pure water in an open atmosphere with $RH < 1$. The drop is able to evaporate so long as $\mu_{water,\,liq}$ (glucose solution) > $\mu_{water,\,vap}$($RH = a$). Glucose is involatile so its mole fraction increases as water evaporates; $\mu_{water,\,liq}$ (glucose solution) therefore reduces over time. Evaporation of the glucose solution ceases when $\mu_{water,\,liq}$ (glucose solution) = $\mu_{water,\,vap}$($RH = a$). A solute is therefore able to inhibit the evaporation of the drop if the solute reduces the vapour pressure so that it becomes equal to the relative humidity. The vapour pressure of the saturated solution must therefore be greater than the relative humidity for precipitation of the solute from solution.

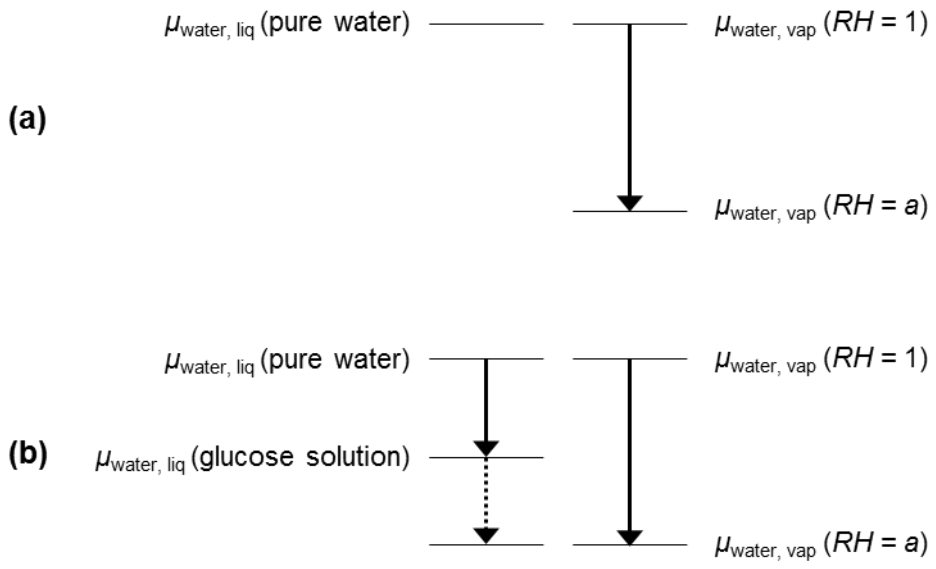

Figure 3.28. The chemical potential μ of (a) water and (b) aqueous glucose solutions compared with the chemical potential of water vapour at relative humidity $RH = a$, which is reduced from $RH = 1$.

3.8.2 Sodium Oxalate as the Solute

The suitability of sodium oxalate, NaOx, as a species that would partition preferentially into the water-rich phase was investigated. The structure of NaOx is given in Figure 3.19c. Water was added to a fixed mass of NaOx (*Aldrich*, 99.5+%) at 293 K until all the solid dissolved; in water the solubility limit was 3.5 %wt. When the same exercise was repeated with DPGMEA as solvent, NaOx did not fully dissolve at 0.03 %wt. Based on the individual solubilities in DPGMEA and water, NaOx appears to have the right properties for selective patterning with phase-separating DPGMEA-water formulations.

Printing trials were carried out with an aqueous formulation containing 1.5 %wt NaOx and 1.5 %wt DPGMEA on a hydrophobised substrate; micrographs are displayed

in Figure 3.29. As the drop evaporates, the loss of volume is reflected in a decreasing contact area (Figs. 3.29a−d) and the DPGMEA-rich phase separates at the contact line (red dots in Figs. 3.29c, d). The early drying dynamics match those found for DPGMEA-water mixtures in the absence of a solute (*cf.* Fig. 3.24). Just after t = 2.1 s, the central water-rich phase, supersaturated in NaOx, nucleates and crystals are deposited (Fig 3.29e). Unlike for the glucose formulations, the NaOx formulation fully evaporates to leave crystals in a central spot (Figs. 3.29f), though the remaining DPGMEA infiltrated the NaOx deposit to leave the substrate free from stagnant oil.

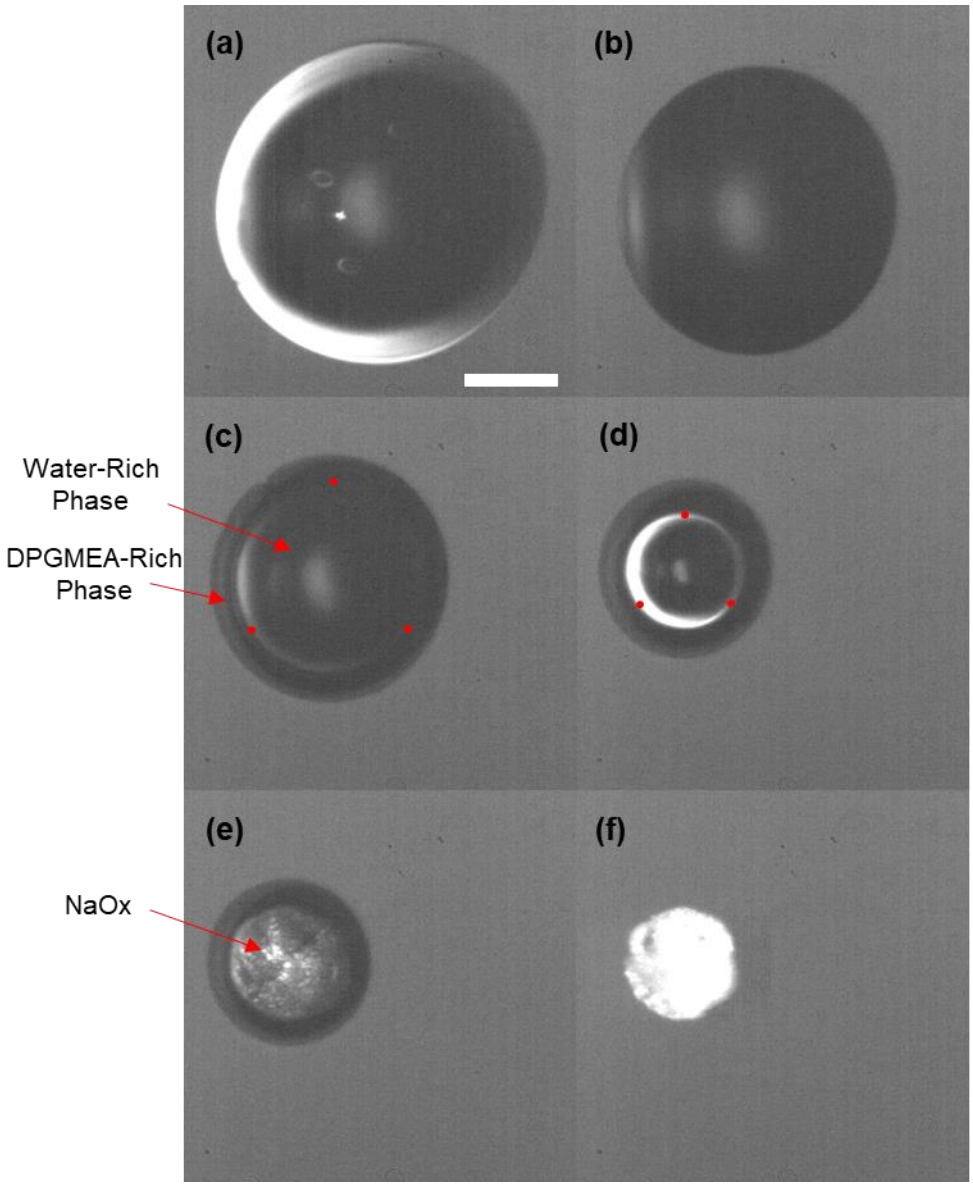

Figure 3.29. An ink-jet printed drop of an aqueous solution containing 1.5 %wt sodium oxalate and 1.5 %wt DPGMEA viewed from underneath. Images were captured (a) 8 ms, (b) 0.80 s, (c) 1.40 s, (d) 2.00 s, (e) 2.14 s and (f) 2.40 s after deposition onto a hydrophobic substrate. The drop was jetted with a symmetrical bipolar waveform with a drive voltage of 30 V. Red dots mark the interfacial boundary between the water-rich and DPGMEA-rich phases. The scale bar is 30 μm.

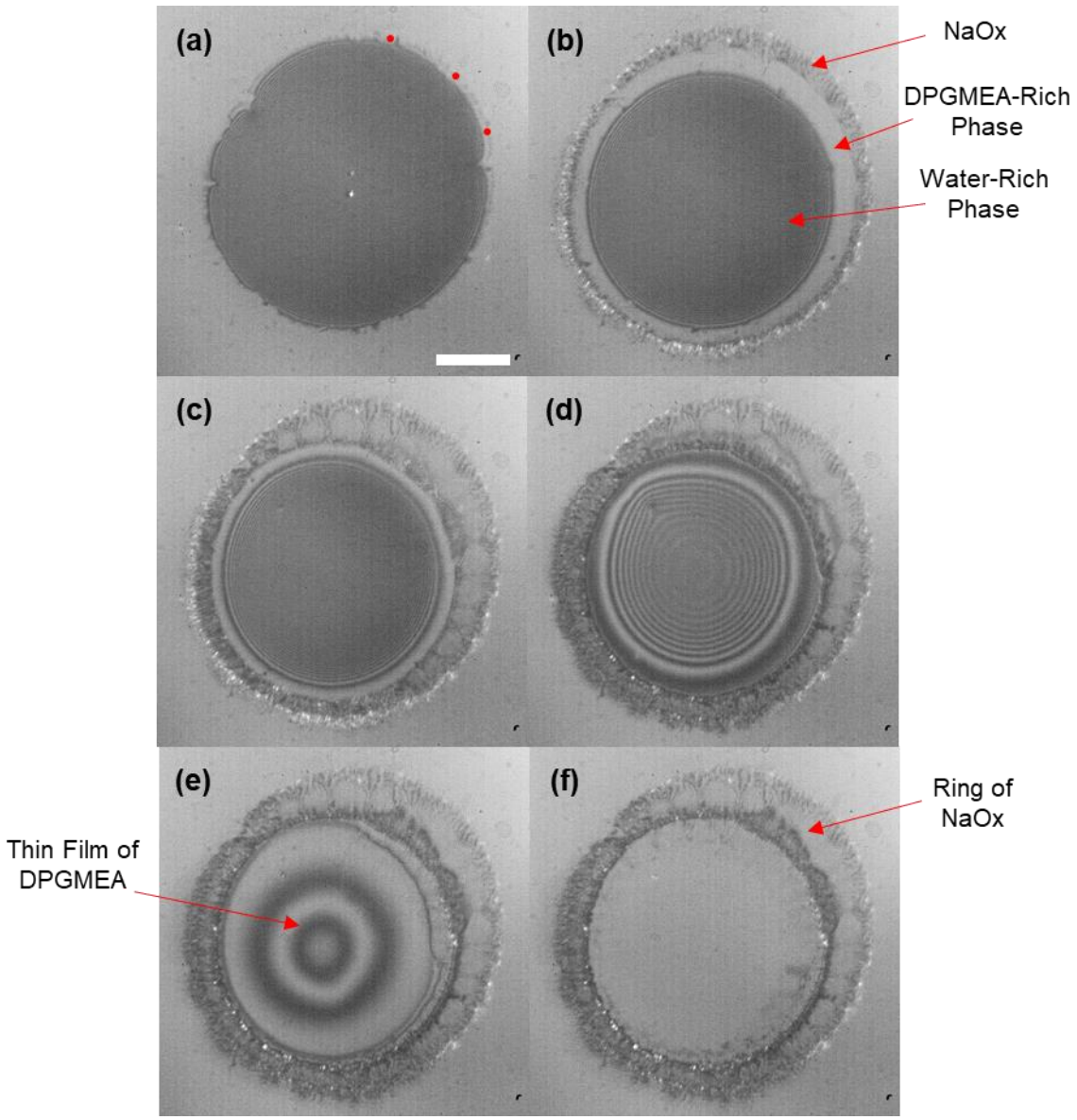

Figure 3.30. An ink-jet printed drop of an aqueous solution containing 1.5 %wt sodium oxalate and 1.5 %wt DPGMEA viewed from underneath. Images were captured (a) 30 ms, (b) 0.30 s, (c) 0.80 s, (d) 0.80 s, (e) 0.95 s and (f) 1.00 s after deposition onto a substrate cleaned in *iso*-propyl alcohol. The drop was jetted with a symmetrical bipolar waveform with a drive voltage of 30 V. Red dots mark a small amount of the DPGMEA-rich phase that wets the substrate beyond the main drop. The scale bar is 50 μm.

The drying dynamics and the NaOx deposit morphology was different when the formulation was jetted onto a glass substrate that had only been bath sonicated in *iso*-propyl alcohol; Figure 3.30 shows a series of micrographs. The drop adopted a spherical cap upon impact, and just visible in Figure 3.30a (marked by red dots) is a small amount of the oil-rich phase that wets the substrate beyond the contact area of the major phase. The contact line of the aqueous phase did not pin and receded as water evaporated (Figs. 3.30b−d); a thin film of the oil-rich phase surrounded the water phase and receded in tandem. NaOx deposition began within 100 ms of deposition and a small amount was

washed outwards by the initial spreading of the oil-rich phase (Fig. 3.30b). When t = 0.8 s, most of the water had evaporated and the outer ring of the oil-rich phase pins at a more substantial ring of NaOx (Fig. 3.30d). After complete water evaporation, the remaining thin film of DPGMEA de-pins and dries (Fig. 3.30e−f); no NaOx crystallised from the oil-rich film at late times (Fig. 3.30f).

3.8.3 Sodium Oxalate and Benzoic Acid as the Solutes

Having demonstrated that a solute can be partitioned into the water-rich phase and subsequently crystallised, formulations that additionally contained a solute which would preferentially partition into the DPGMEA-rich phase were investigated. The species must be soluble in a NaOx-DPGMEA-water mixture so that the original formulation is a single phase. Benzoic acid, BA, (*Fluka Chemika*, >99.5%) was identified as potentially possessing the correct molecular properties to meet the criteria. The structure of BA is given in Figure 3.19d. DPGMEA was added to a fixed mass of benzoic acid at 295 K until complete solvation was achieved; the solubility limit was ~20 %wt. The reported solubility limit of benzoic acid in water is 3.7 g L^{-1} at 295 K.[87] Benzoic acid thus appears to have the right properties for selective patterning with phase-separating DPGMEA-water formulations.

In order to realise phase-selective patterning, the four components water, DPGMEA, NaOx and benzoic acid need to be mixed in proportions such that the system occupies a single water-rich phase. The challenge is that the one-phase region of the phase diagram is a function of all four mass fractions φ_m. In designing a formulation, a few initial criteria were considered: the aqueous 1.5 %wt NaOx and 1.5 %wt DPGMEA formulation printed well; DPGMEA has a lower solubility in water as a result of the presence of NaOx; the maximum ratio of the mass fractions of benzoic acid and DPGMEA is fixed at 20:80 due to the solubility of the former in the latter. A number of formulations were prepared in order to optimise the ratios of the four components: compositions and observations are recorded in Table 3.5 for formulations A – G. Formulations A – C demonstrated that the four components can be included in proportions that form a single phase. Formulations D – F have the proportion of NaOx fixed at the desired level and increasing amounts of an 18 %wt benzoic acid solution in DPGMEA added; formulation E is a single phase but some benzoic acid precipitated from Formulation F. Formulation G indicates that the amount of benzoic acid cannot be increased at the expense of NaOx. Formulation E represents the formulation with the

highest proportions of the solutes; printing trials were carried out on both hydrophobic and hydrophilic substrates.

TABLE 3.5. Formulation compositions by mass fraction for mixtures of water, DPGMEA, benzoic acid (BA) and sodium oxalate (NaOx).

Formulation	φ_m^{DPGMEA}/(%wt)	φ_m^{BA}/(%wt)	φ_m^{NaOx}/(%wt)	Notes
A	7.5	0.34	0.0	Single Phase
B	7.5	0.34	1.0	Single Phase
C	6.2	0.70	0.9	Single Phase
D	2.5	0.45	1.4	Single Phase
E	3.8	0.69	1.4	Single Phase
F	4.8	0.85	1.4	BA Crystals
G	5.1	0.93	0.9	BA Crystals

3.8.3.1 Jetting onto Hydrophobic Substrates

Typical results of printing Formulation E onto hydrophobic substrates (Section 2.1) are presented in Figure 3.31. The drop arrives having already begun phase separation (boundary marked by red dots in Fig. 3.31a): a likely explanation is that the formulation is close to the binodal and phase separation occurs due to evaporation of water either at the nozzle orifice just before jetting or during flight. At $0.1 < t < 1.0$ s a lens of the DPGMEA rich phase was present at the apex (marked by yellow dots in Fig 3.31b). Unlike the other trials with DPGMEA-water mixtures on hydrophobic substrates, the DPGMEA phase remained pinned (Fig. 3.31c *cf.* Figs 3.22, 3.24 and 3.29). The difference from prior experiments could be explained by precipitation of benzoic acid crystals at the contact line having the effect of significantly depressing the receding contact angle. The interfacial boundary moved radially inwards as evaporation continued until loss of the aqueous phase revealed the NaOx deposit (Fig. 3.31d). As observed in Figure 3.29e, the NaOx precipitated only from the water-rich phase. At $t = 15.2$ s, the film of the DPGMEA-rich phase ruptured with the majority of the liquid receding to the central deposit; some liquid remained at the former contact line position. The evaporation of the DPGMEA caused benzoic acid to crystallise on top of the NaOx deposit: linear crystals were visible around the edge of the deposit (Fig. 3.31f). Though Formulation E indicates the solutes are partitioning as desired, no phase-selective patterning control was observed since the second solute ended up crystallising on the first.

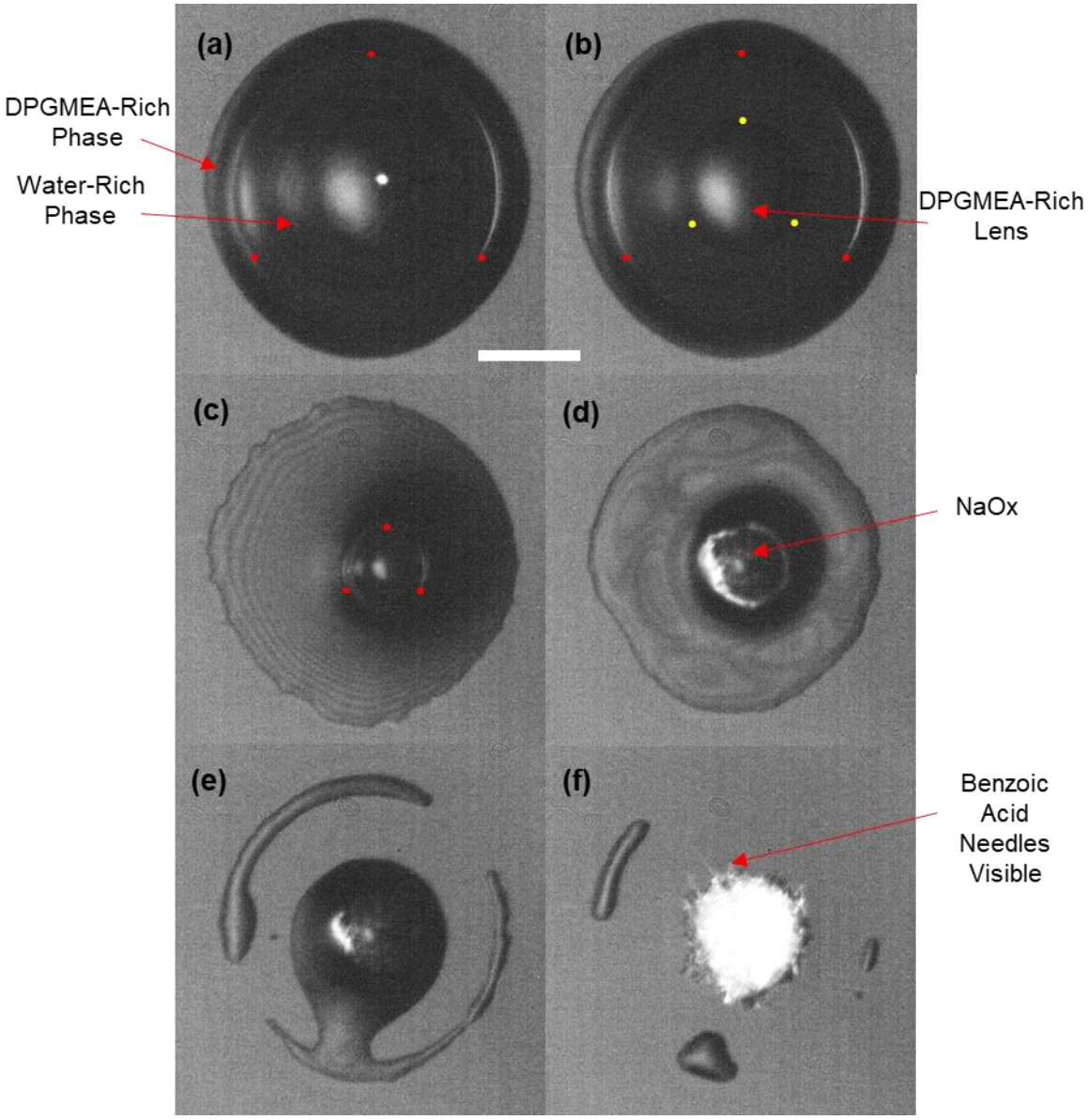

Figure 3.31. A drop of an aqueous solution containing 1.4 %wt sodium oxalate, 0.7 %wt benzoic acid and 3.8 %wt DPGMEA (Formulation E) viewed from underneath. Images were captured (a) 30 ms, (b) 0.2 s, (c) 1.6 s, (d) 14.4 s, (e) 16.0 s and (f) 36.5 s after deposition onto a hydrophobised substrate. The drop was jetted with a symmetrical bipolar waveform with a drive voltage of 20 V. Red dots mark the interfacial boundary between the water-rich and DPGMEA-rich phases and yellow dots mark the edges of the DPGMEA-rich lens. The scale bar is 30 μm.

Several facts support the interpretation of how, where and when NaOx and benzoic acid is deposited: first, it was established experimentally that NaOx is not soluble in DPGMEA and that the solubility of benzoic acid in DPGMEA is ~20 %wt (see Section 3.8.3). In Figure 3.31d, water has already fully evaporated, leaving DPGMEA as the only solvent. The crystals visible in Figure 3.31d must therefore be NaOx, in keeping with the evaporation dynamics displayed in Figure 3.29, for a drop containing only water,

DPGMEA and NaOx. Additionally, the presence of benzoic acid at this stage is not likely given the high solubility in DPGMEA. Second, the drop contains a 2:1 ratio of NaOx to benzoic acid. If the crystals in Figure 3.31d must be NaOx due to the absence of water and no NaOx can remain in the DPGMEA-rich phase due to its poor solubility therein, the increase in size of the deposit in Figure 3.31f from that in Figure 3.31d must be due to benzoic acid that is deposited at late times after significant DPGMEA evaporation. Third, the crystals at the edge of the deposit in Figure 3.31f have the form of needles, in contrast to Figure 3.29f where no benzoic acid was included in the formulation. As benzoic acid is known to crystallise as needles or leaflets,[88–90] benzoic acid must have been deposited on top of the NaOx at late times.

3.8.3.2 Jetting onto Hydrophilic Substrates

The drying dynamics of Formulation E on a substrate cleaned in acetone showed much more complex drying dynamics than for the hydrophobic substrate described above. Typical phase separation dynamics are displayed at early times in Figure 3.32 and at late times in Figure 3.34. Initially, drops adopted a low contact angle and a thin film of the DPGMEA-rich phase is visible on the drop surface (Fig. 3.32a); separation possibly occurred to a small degree at the print head orifice. Within 30 ms of deposition, the second phase was also visible at the contact line (red dots in Fig. 3.32b) and began to spread over the substrate (Fig. 3.32c). A thin film of the DPGMEA phase on the surface of the aqueous phase (Fig. 3.32a, b) contracted into a lens that remained at the apex (yellow dots in Fig. 3.32c−e); a sketch of the arrangement of phases is shown in Figure 3.33a. As water continued to evaporate, regions of DPGMEA-rich phase at the contact line were swept towards the apex, with some coalescing with the lens and others returning to the contact line (Fig. 3.32d). The driving force of the material transfer is a Marangoni flow radially along the surface from the contact line to the apex: the water concentration, and hence surface tension, is expected to be lowest at the contact line. In Figure 3.32e, most of the water has evaporated and the drop is still a water-rich phase with an oil-rich lens at the surface and the contact line. Close to the time of complete water loss, however, the lens migrated to the contact line and coalesced with the DPGMEA-rich phase located there. The system therefore became a water-rich phase surrounded by a DPGMEA phase (Fig. 3.32f, see Fig. 3.33b).

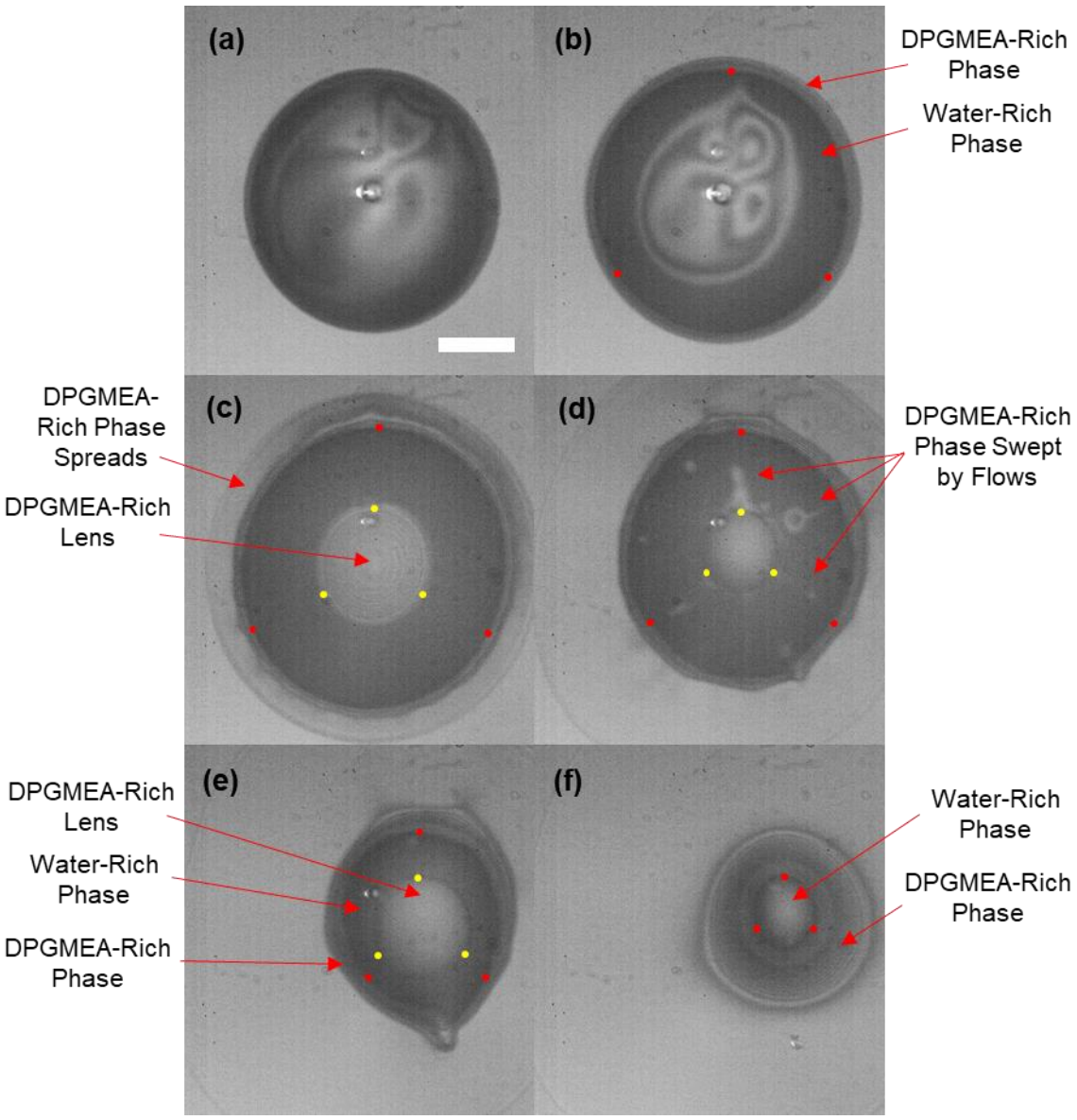

Figure 3.32. A drop of an aqueous solution containing 1.4 %wt sodium oxalate, 0.7 %wt benzoic acid and 3.8 %wt DPGMEA (Formulation E) viewed from underneath. Images were captured (a) 14 ms, (b) 28 ms, (c) 0.10 s, (d) 0.24 s, (e) 0.42 s and (f) 0.68 s after deposition onto a substrate cleaned in acetone. The drop was jetted with a symmetrical bipolar waveform with a drive voltage of 30 V. Red dots mark the interfacial boundary between the water-rich and DPGMEA-rich phases and yellow dots mark the edges of the DPGMEA-rich lens. The scale bar is 40 μm.

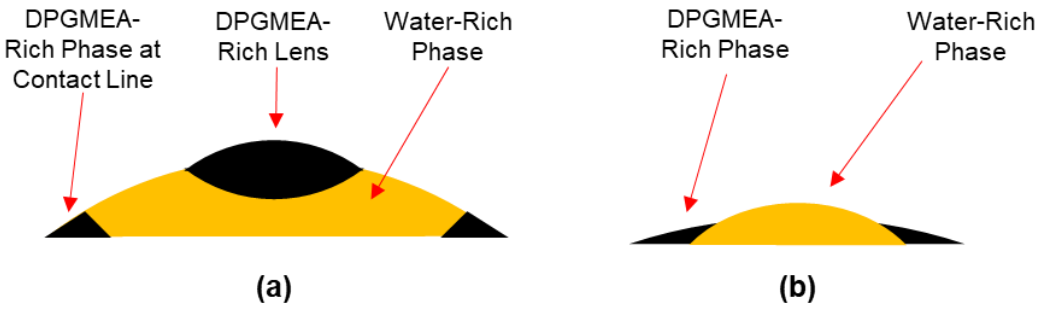

Figure 3.33. Sketch of the arrangement of phases observed for Formulation E at earlier times (see Fig. 3.32d, e) and at later times (see Fig. 3.32f).

The behaviour of Formulation E at late times is given in Figure 3.34 for a different drop. As discussed above, when the majority of the water has evaporated the drop is characterised by a water-rich phase with DPGMEA-rich phases present as a lens and around the contact line (Fig. 3.34a, see Fig. 3.33a). After the lens coalesced with the contact line (arrangement of phases as in Fig. 3.33b), the DPGMEA-rich phase began to spread over a large area (Fig. 3.34b). As on the hydrophobic substrate, the loss of the water-rich phase leaves a localised NaOx deposit (Fig. 3.34c *cf*. Fig 3.29e). The spreading DPGMEA film ruptures to leave benzoic acid crystals (Fig. 3.34d). The film rupture was not always observed and a different oil-partitioning solute might crystallise more reliably. The final deposit was therefore a localised spot of the water-partitioning solute, surrounded by an even layer of the oil-partitioning solute; formulation E on a hydrophilic substrate is therefore an example of how phase-selective patterning from a single fluid can be achieved.

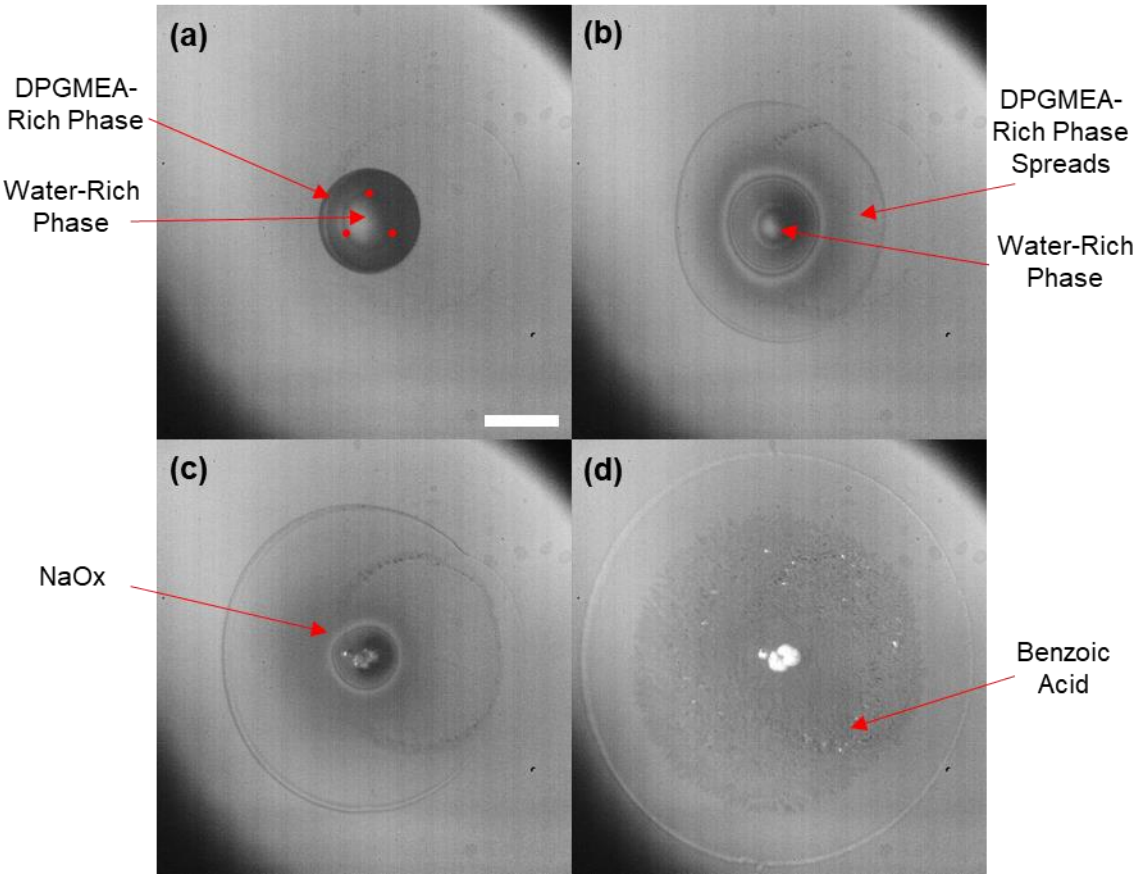

Figure 3.34. A drop of an aqueous solution containing 1.4 %wt sodium oxalate, 0.7 %wt benzoic acid and 3.8 %wt DPGMEA (Formulation E) viewed from underneath. Images were captured (a) 0.23 s, (b) 0.35 s, (c) 0.47 s and (d) 3.9 s after deposition onto a substrate cleaned in acetone. The drop was jetted with a symmetrical bipolar waveform with a drive voltage of 20 V. Red dots mark the interfacial boundary between the water-rich and DPGMEA-rich phases. The scale bar is 60 μm.

The facts that support the above interpretation of Figure 3.34 as to how, where and when NaOx and benzoic acid is deposited closely matches those given in support of the interpretation of the same formulation behaves on the hydrophobic substrate (see Section 3.8.3.1): first, the insolubility of NaOx in DPGMEA means that upon complete water evaporation between Figures 3.34b and 3.34c, means that it must be entirely deposited at this stage. This is in keeping with dynamics in the absence of benzoic acid (Fig 3.29e) and the behaviour on the hydrophobic substrate (Fig. 3.31d). Second, the high solubility of benzoic acid in DPGMEA means that it will remain in solution after complete evaporation. As the DPGMEA-rich phase spreads to occupy an area much larger than the original drop (Figs. 3.34b, c), benzoic acid will be carried to parts of the substrate that made no contact with the water-rich phase at any point. The crystals that are deposited after rupture of the DPGMEA film (Fig. 3.34d) can therefore only be NaOx if they were transported by being dragged as the DPGMEA film advanced. This is unlikely since the layer of crystals is so even. A more compelling explanation is that benzoic acid was distributed throughout the DPGMEA-rich phase and crystallised suddenly at late times. Third, the large thin layer of crystals have the appearance of fine platelets or needles which is characteristic of benzoic acid.[88–90]

3.8.4 Discussion

The jetting experiments with glucose-DPGMEA-water mixtures did not produce deposits: glucose did not begin to crystallise before the solvent vapour pressure became equal to the relative humidity. The experiments demonstrated that phase-selective patterning cannot be achieved if the solute has a high solubility.

The deposits from the NaOx-BA-DPGMEA-water formulations on the hydrophobic substrate also did not lead to selective patterning: the wetting of the NaOx deposit by the oil-rich phase after evaporation of the water-rich phase led to both solutes being deposited at the same location. On a hydrophilic substrate, however, the oil-rich phase did not collect at the NaOx deposit, but spread into a thin layer over the glass. When the benzoic acid crystallised, the deposit had the form of a large circle of benzoic acid, with a concentrated spot of NaOx in the centre; thus phase-selective patterning was realised.

Some of the characteristics of the phase-selective patterning displayed by the NaOx-BA-DPGMEA-water formulations, however, were unfavourable. First the oil had a low volatility so the benzoic acid reached saturation slowly. Second, benzoic acid crystallisation was not always observed and a solute that crystallised more rapidly would

be preferable. The deliberate inclusion of nanoparticles at very low concentration could act as nucleation centres and facilitate more rapid crystallisation. Third, the contact line receded asymmetrically as water evaporated and at late times the oil-rich phase spread over large areas of the substrate. Such significant mobility of the contact line is undesirable for ink-jet formulations: one of the major advantages of ink-jet printing as a patterning tool is the fine control over drop placement and uncontrolled wetting lowers pattern resolution. Substrate patterning might inhibit contact line movement.

In order to achieve phase-selective patterning, a formulation requires a number of characteristics. First, the solute with the preference for partitioning into the water-rich phase cannot be too soluble else it will fail to crystallise before evaporation is retarded by the lowering of the solvent chemical potential; glucose, for example, did not crystallise. Second, the solute with the preference for partitioning into the oleic phase must have a high solubility in the oleic co-solvent else it is unlikely to dissolve in sufficient quantities in water; the maximum concentration of the oleic solute is limited by the amount of the oleic solvent included in the formulation. Third, all components must be soluble in the major solvent simultaneously; the presence of each solute limits the miscibility of the others. Fourth, an optimised formulation should have $\theta_a > 0$ and $\theta_r = 0$ for all phases on the target substrate so that well-defined arrays may be deposited.

Phase-selective patterning was one of the major goals of this investigation and a number of different types of formulation have been surveyed. The other hypothesised impact of phase separation on the substrate was a disruption of the coffee-ring effect due to enhanced evaporative flux at the contact line for drops with $\theta < 90°$. This avenue of investigation was not pursued to the same degree as phase-selective patterning. Aqueous solutions of DPGMEA of concentration 15.1 %wt and 1.2 %wt were seeded with 1-μm diameter polystyrene spheres and were printed. Phase separation was observed in both cases in the form of a DPGMEA-rich ring at the contact line that moved radially inwards as water was lost. The positions of the tracer particles were difficult to track since they were not clearly visible in the DPGMEA-rich phase. It also appeared that the particles dissolved in DPGMEA since the 1.2 %wt solution left a continuous polymer film when the last of the oil evaporated. The impact of phase separation on outward radial flow was therefore inconclusive. In order to investigate the internal flows, obtaining tracer particles visible in both phases is desirable. If the particles are not visible in both phases but are insoluble, the final deposit can still be examined for evidence of internal flows. It would also be advantageous to try tracking the internal flows in a modified formulation where the oil evaporated more quickly and did not form a long-lived pool.

3.9 Alkanes in Methanol

Sections 3.5 − 3.8 explored the design of water-based phase-separating formulations. The phase separation phenomenon is general and, in principle, any liquid may be selected as the major component, provided a partially miscible co-solvent having appropriate evaporation characteristics can be identified. In this section, an account of research into designing phase-separating formulations based on methanol-alkane mixtures is presented. First, methanol-alkane pairs are examined quantitatively to identify which are expected to phase separate. Second, printing results are reported on hydrophilic and hydrophobic substrates.

As before, the following nomenclature will be used to describe a phase separating alkane-water mixture: *alkane-rich phase* for a methanol solution in alkane, comprising > 50 %vol alkane; *methanol-rich phase* for an alkane solution in methanol, comprising > 50 %vol methanol; *saturated* to indicate the minor component is present at its miscibility limit.

3.9.1 Rationale

Physical data relating to aqueous solutions are abundant and are regularly included in reference volumes. In contrast, the sheer number of possible liquid-liquid pairings when the major component is non-aqueous makes it likely that physical data is not readily available for a given system. Pairs of liquids that show the potential for phase separation may be screened quantitatively using the criterion κ (Section 3.4.1) using the mole fractions, vapour pressures and diffusion coefficients of the components. In Section 3.7, it was demonstrated that κ^{henry}, where vapour pressures are estimated from Henry's law, Equation (3.44), correctly indicates whether a pair of liquids has the propensity to separate during evaporation. For alkane-methanol mixtures, values of the Henry constant have not been measured, but the vapour pressures of the pure components are well known. Assuming the pure vapour pressure of each component is a close approximation to the value in a two-phase mixture, Equation (3.29) may be re-written to define κ^{pure}:

$$\kappa^{\text{pure}} = \frac{{p_{\text{A}}}^* D_{\text{A}} x_{\text{B}}}{{p_{\text{B}}}^* D_{\text{B}} x_{\text{A}}}, \tag{3.49}$$

where components A and B are the major and minor components respectively; if $\kappa^{\text{pure}} > 1$, separation is expected.

TABLE 3.6. Physical data relating to a series of potential components for formulating MeOH-in-alkane phase-separating fluids under evaporation and an assessment of their viability.

	A	T/K	$x_{\mathrm{MeOH,lim}}$ [a]	p_{A}*/kPa [b]	D_{A}/ (10^{-5} m^2 s^{-1}) [c]	κ^{pure}	Viable?
1	Hexane	295	0.215	17.9	0.753	0.162	N
2	Heptane	295	0.147	5.26	0.693	0.028	N
3	Octane	290	0.093	1.17	0.626	0.003	N
4	Nonane	295	0.102	0.50	0.606	0.002	N
5	Decane	290	0.066	0.11	0.556	0.0002	N

a: [1−5].[47] *b*: [1−5].[91] *c*: [1−5].[76,77]

TABLE 3.7. Physical data relating to a series of potential components for formulating alkane-in-MeOH phase-separating fluids under evaporation and an assessment of their viability.

	A	T/K	$x_{\mathrm{A,lim}}$ [a]	p_{A}*/kPa [b]	D_{A}/ (10^{-5} m^2 s^{-1}) [c]	κ^{pure}	Viable?
1	Hexane	295	0.189	17.9	0.753	0.39	N
2	Heptane	295	0.095	5.26	0.693	0.66	N
3	Octane	290	0.053	1.17	0.626	1.28	Y
4	Nonane	295	0.038	0.50	0.606	2.95	Y
5	Decane	290	0.022	0.11	0.556	6.05	Y

a: [1−5].[47] *b*: [1−5].[91] *c*: [1−5].[76,77]

For methanol at 290 K, p = 11.0 kPa and $D = 1.54 \times 10^{-5}$ m^2 s^{-1}, whilst at 295 K, p = 14.4 kPa and $D = 1.58 \times 10^{-5}$ m^2 s^{-1}.[76,77,91] Values for κ^{pure} alkane-in-methanol solutions and methanol-in-alkane solutions are recorded in Tables 3.6 and 3.7. Hexane is the first of the alkanes not to be fully miscible with methanol at room temperature but the decreasing mutual solubilities mean that undecane and heavier alkanes are too insoluble; the C_6–C_{10} alkanes have appropriate miscibility ranges.[47] None of the formulations that use methanol as the solute would produce a formulation that phase separates under evaporation (Table 3.6). The high vapour pressure and diffusion coefficient of methanol ensures that it has a shorter lifetime on the substrate than the alkane; supersaturation would therefore not be observed. The rapidity of methanol evaporation does mean, however, that alkane-in-methanol formulations are likely to phase separate (Table 3.7), with the data suggesting that solutions of octane, nonane and decane would show the correct behaviour.

3.9.2 Experimental Details

The solubilities of the minor components in methanol-alkane mixtures recorded in Tables 3.6 and 3.7 are for a mix of temperatures that straddle typical ambient conditions in the lab. The solubility limits, $\varphi_{m,max}$, were re-measured for two reasons: first, in order to measure surface and interfacial tensions across the full range of miscibility, the miscibility limits should be well known. Second, when considering the initial alkane concentration in printing fluids, it is useful to know the solubility under ambient conditions. The results are displayed in Table 3.8. The solubilities of alkanes in methanol were determined by adding methanol to fixed volumes of alkane until that alkane dissolved completely in the methanol-rich phase. The solubilities of methanol in alkanes were determined by adding methanol to fixed volumes of alkane until markings on paper were fully obscured due to the cloudiness of the mixtures (path length ~3 cm); samples were bath sonicated between methanol additions. The results agree with the reference values within 1.5 %wt for the alkane-in-methanol solutions. For the methanol-in-alkane solutions, the agreement is within 0.2 %wt when octane and decane are the solvents; when nonane is the solvent the disagreement is larger, but the discrepancy matches the expected trend in solubility with temperature. Overall the solubilities are lower than the published values, given the temperatures for the nonane-methanol mixtures are close.

TABLE 3.8. The solubility limits, $\varphi_{m,max}$, for the minor components of alkane-methanol mixtures measured at 294 K compared against reference values.

Major Component A	Minor Component B	$\varphi_{m,max}{}^{B}$ / (%wt)	Ref. $\varphi_{m,max}{}^{B}$ / (%wt)[a]
Methanol	Octane	18.0 ± 0.2	16.6[b]
Methanol	Nonane	12.65 ± 0.08	13.5[c]
Methanol	Decane	9.68 ± 0.03	8.9[b]
Octane	Methanol	2.6 ± 0.1	2.8[b]
Nonane	Methanol	1.82 ± 0.04	2.8[c]
Decane	Methanol	1.48 ± 0.07	1.6[b]

a: reference data.[47] *b*: T = 290 K. *c*: T = 295 K.

Printing trials for decane-in-methanol solutions are described in particular detail in the following section, so density, surface/interfacial tension and contact angle measurements are reported here. The densities of decane-in-methanol solutions across the miscibility range were measured at 294 K and were found to be linear in composition; the

constants associated with Equation (3.32) are recorded in Table 3.9. The density of pure decane was 0.7229 g mL^{-1} and the density of a 1.6 %wt methanol solution was 0.7231 g mL^{-1}. Surface and interfacial tensions were measured by pendent drop tensiometry using the equipment and procedures described in Section 2.4. Contact angles of the saturated solutions were measured on glass substrates made hydrophobic with hexamethyldisilazane (Section 2.1).

TABLE 3.9. The constants and standard errors obtained from a linear least-squares fitting routine for the densities of decane-in-methanol solutions as a function of composition at 294 K.

Major Component A	Minor Component B	ρ_A^* / (g mL^{-1})	k / [g mL^{-1} (%wt)$^{-1}$]
MeOH	Decane	0.7843 ± 0.0004	−0.00096 ± 0.00006

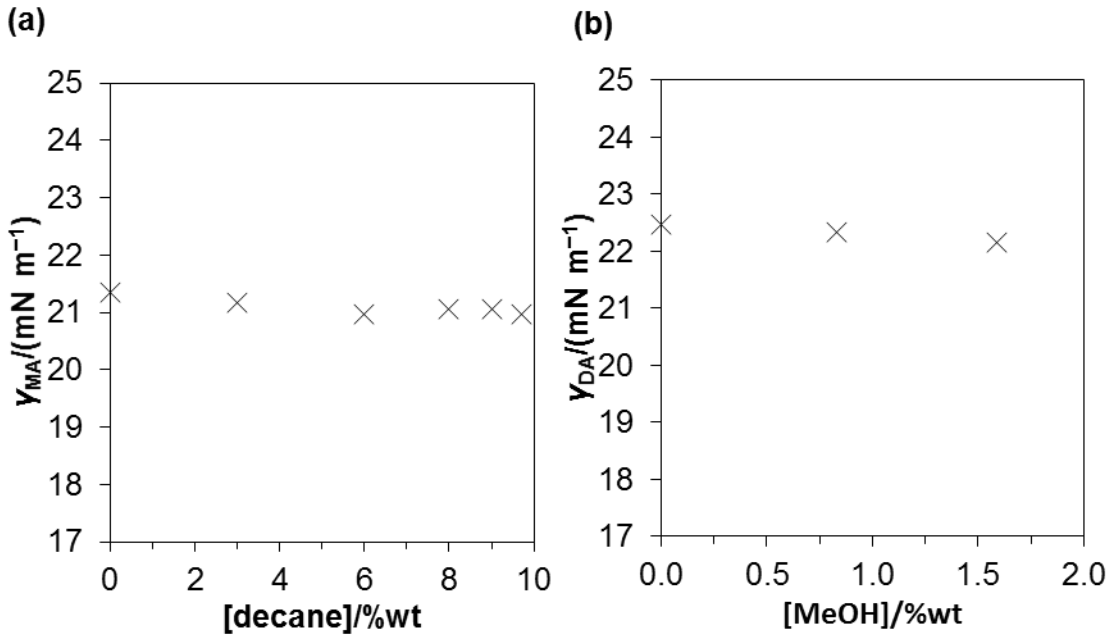

Figure 3.35. (a) The surface tension in air of decane solutions in methanol, γ_{MA}, up to the miscibility limit, at 295 K. (b) The surface tension in air of methanol solutions in decane, γ_{DA}, up to the miscibility limit, at 295 K.

The surface tensions of decane-in-methanol solutions and methanol-in-decane solutions are displayed in Figure 3.35 across the full range of miscibility and were invariant with composition. A saturated methanol-rich liquid had a surface tension, γ_{MA}^{sat}, of 20.9 ± 0.1 mN m^{-1} and formed a zero contact angle on hydrophobic substrates. A saturated decane-rich liquid had a surface tension, γ_{DA}^{sat} of 22.1 ± 0.1 mN m^{-1} and formed a contact angle of 5 ± 1° on hydrophobic substrates. The interfacial tension recorded

between the saturated liquids, γ_{MD}^{sat}, was 2.19 ± 0.02 mN m^{-1} and the contact angle for a drop of the saturated decane-rich liquid on a hydrophobic substrate submerged in the methanol-rich liquid was 63 ± 4°.

3.9.3 Expected Separation Behaviour for Decane-in Methanol Solutions

The behaviour of a phase-separating decane-methanol mixture is considered using the principles that guided the evaluation of the butanol-water system in Section 3.5.3; separation is expected first at the contact line. For the saturated decane-rich phase on the saturated methanol-rich phase the spreading ratio $S_{D/M} = -3.40 \pm 0.01$ mN m^{-1}, based on the values of the surface/interfacial tensions reported in Section 3.9.2. The decane-rich phase is therefore not expected to wet the surface of the saturated methanol-rich phase thermodynamically, but instead to form lenses.

As was carried out for butanol-water mixtures (see Section 3.5.3), the angles at the three-phase contact line (Fig. 3.36a) may be found using a Neumann triangle (Fig. 3.36b). The angles for a lens of the saturated decane-rich phase on a saturated methanol-rich phase in air are shown in Fig 3.36c.

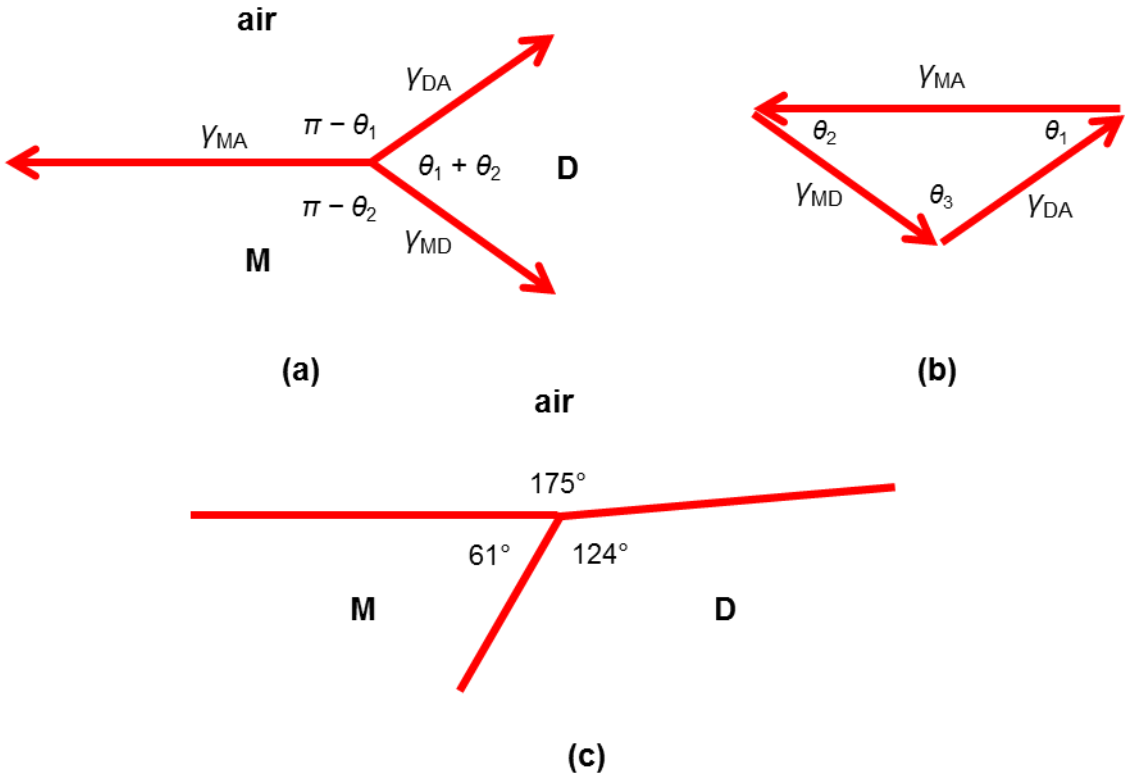

Figure 3.36. (a) The force balance at the three-phase contact line for a lens of methanol-saturated decane (D) on decane-saturated methanol (M) in air. The arrow lengths are not to scale to aid clarity. (b) Neumann triangle. (c) The equilibrium angles at 295 K. The angles do not sum to 360° due to rounding.

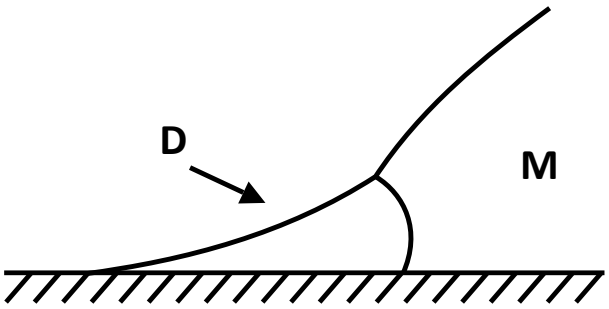

Figure 3.37. Geometry of a drop of decane-saturated methanol (M) with methanol-saturated decane (D) at the contact line. The model is based on measured surface and interfacial tensions (T = 295 K) and contact angles on a hydrophobized substrate (T = 294 K).

Assuming the Laplace pressure of the major phase can be neglected when determining the shape of the annular ring of the decane-rich phase (see Section 3.5.3), the Laplace pressures across the DA and MD interfaces are equal:

$$\frac{\gamma_{\mathrm{AD}}{}^{\mathrm{sat}}}{R_{\mathrm{AD}}{}^{\mathrm{sat}}} = \frac{\gamma_{\mathrm{DM}}{}^{\mathrm{sat}}}{R_{\mathrm{DM}}{}^{\mathrm{sat}}}. \tag{3.50}$$

The ratio between the two radii of curvature, $R_{\mathrm{AD}}{}^{\mathrm{sat}} : R_{\mathrm{DM}}{}^{\mathrm{sat}}$, is 10.0 : 1 and would appear as in Figure 3.37. The methanol-rich phase is expected to undercut partially the decane-rich phase.

3.9.4 Printing Trials

Half-saturated solutions of octane (9.1 %wt), nonane (6.3 %wt) and decane (4.8 %wt) in methanol each phase separated when printed. Printed drops of the nonane and decane solutions commonly arrived at the substrate with well-developed alkane-rich phases; phase separation was occurring at the print head orifice due to rapid methanol evaporation. The impact of phase separation, however, for the octane solutions was less pronounced, with alkane-rich phases developing only to a small extent. The lower degree of separation observed for the octane solution is expected since $\kappa^{\mathrm{pure}} \sim 1$, meaning the propensity to separate during evaporation is borderline.

Variable drying dynamics were observed for the half-saturated alkane solutions in methanol due to the variable numbers and volumes of the alkane-rich phases present when the drops were deposited. Printing the solutions continuously should prevent separation occurring at the print head orifice if the ejection frequency was sufficiently high. Alternatively, more consistent printing results should be achieved if the initial fraction of alkane is lower, so that a greater proportion of the methanol must evaporate before supersaturation is achieved. Lowering the proportion of the alkane, however, might cause the volume of the new phase to become very low. The decane formulations

have a greater propensity to phase separate than the nonane formulations and were thus investigated further.

Printing trials were carried out with 2.0 %wt, 3.1 %wt and 4.7 %wt solutions of decane in methanol onto hydrophobic substrates (Section 2.1). All three concentrations showed phase separation. The higher the concentration of decane the more likely separation had begun to occur at the print head orifice, resulting in decane-rich phases on arrival at the substrate. The decane-rich phases were better developed for the 4.7 %wt solution and consequently drying dynamics were not repeatable: drops became highly radially unsymmetrical when large decane-rich phases reached the contact line (Fig 3.38). In contrast, the 2.0 %wt and 3.1 %wt solutions tended to arrive at the substrate as a single phase or with a small number of small drops of decane-rich phase; axisymmetric drying dynamics were therefore more often observed than for the 4.7 %wt solutions.

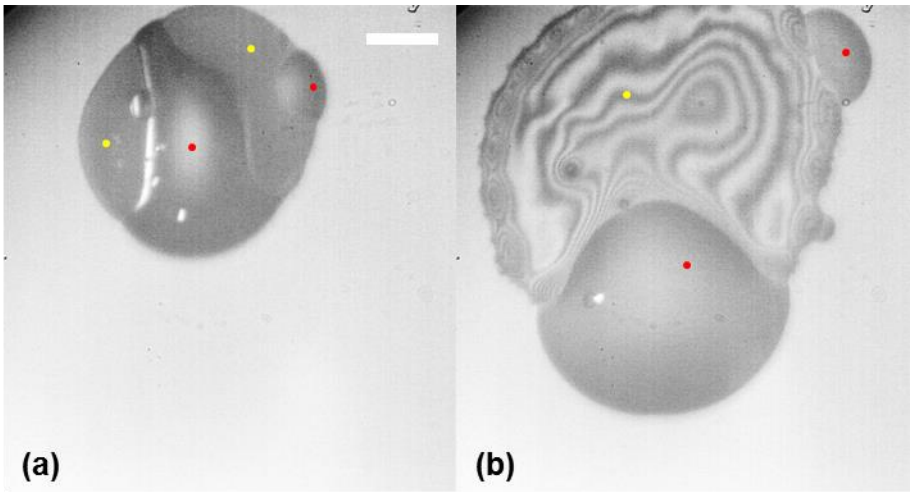

Figure 3.38. A drop of a 4.7 %wt decane solution in methanol viewed from underneath. Images were captured (a) 3 ms and (b) 15 ms after deposition onto a hydrophobic substrate. Red spots mark the decane-rich phases and yellow spots mark the methanol-rich phases. The drop was jetted with a symmetrical bipolar waveform with a drive voltage of 30 V. The scale bar is 40 μm.

The drying dynamics of a 3.1 %wt decane in methanol solution are exemplified in Figure 3.39. The drop arrives as a single phase (Fig. 3.39a). By t = 14 ms the drop has spread over a much larger area (Fig. 3.39b) and the Newton rings in the image indicate that the methanol-rich phase has become a thin film. During spreading, the contact line does not maintain an annular structure, but displays fingering (Fig. 3.39b); the fingers grow over time and reach their maximum size at t = 24 ms (Fig. 3.39c). Fingering occurs due to Marangoni instabilities and can occur for surface tension gradients caused by temperature,[92] composition[93] and surfactant.[94] Here, the instability is driven by surface

tension gradients caused by composition: since the decane-rich phase has a higher surface tension than the methanol-rich phase (Fig. 3.35), the latter spreads faster than the former.

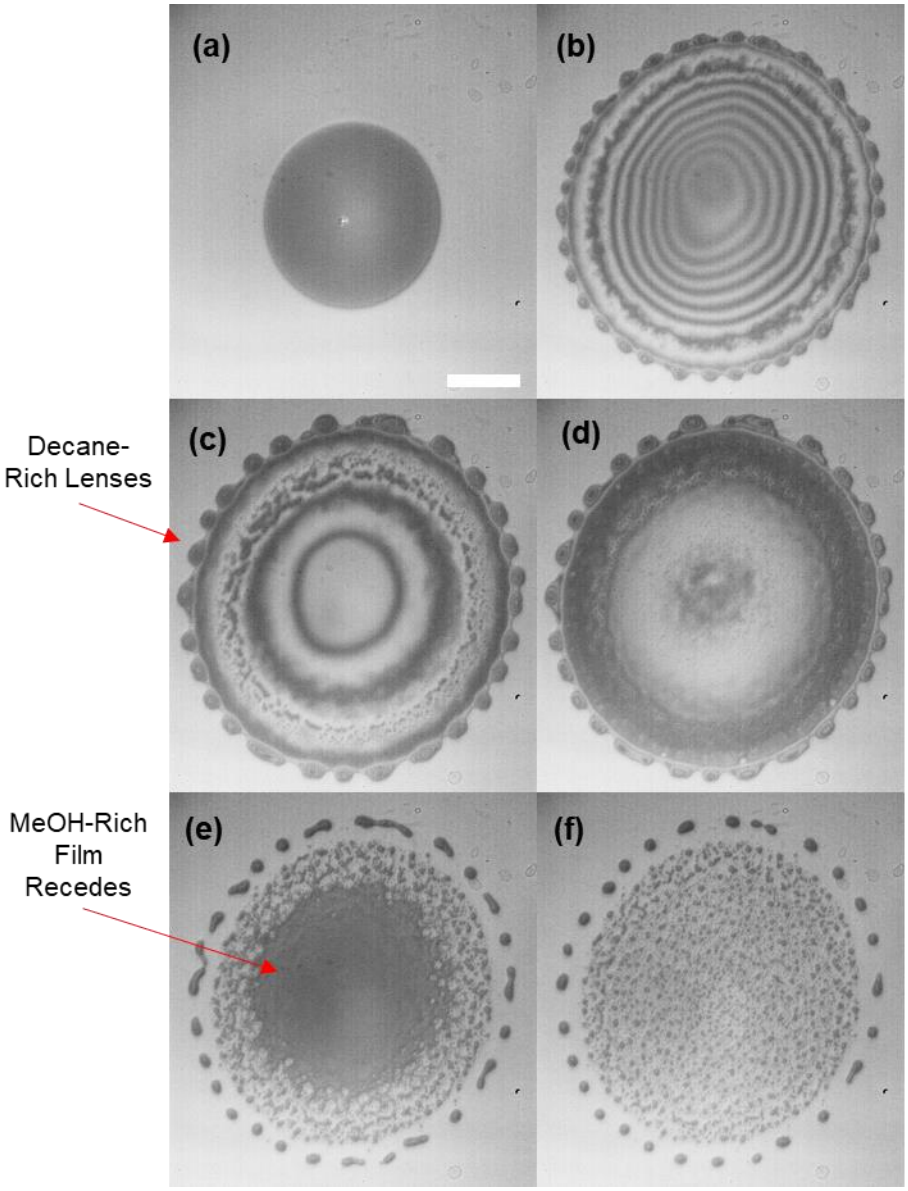

Figure 3.39. A drop of a 3.1 %wt decane solution in methanol viewed from underneath. Images were captured (a) 4 ms, (b) 14 ms, (c) 24 ms, (d) 30 ms, (e) 36 ms and (f) 38 ms after deposition onto a hydrophobic substrate. The drop was jetted with a symmetrical bipolar waveform with a drive voltage of 25 V. The scale bar is 60 μm.

The Newton rings in the methanol-rich phase become more widely spaced with time indicating the thinning of the film under evaporation (Figs. 3.39b−d). At t = 29 ms, the methanol-rich film ruptures at the contact line and recedes radially inwards (Fig. 3.39e); a ring of decane-rich droplets remain at the contact line. The receding methanol film also leaves an even layer of decane-rich droplets of approximate diameter 4 μm (Fig. 3.39f), which evaporate completely by t = 75 ms; the drops formed early in the drying

process and are visible in Figure 3.39c in the outer region of constructive interference. The layer of decane-rich droplets are likely to form by a different mechanism to those formed at the contact line: a distribution of droplets of a new phase throughout a supersaturated solution is consistent with spinodal decomposition.

The observations from the printing trials with the 3.1 %wt decane-in-methanol solutions are in agreement with the expected spreading behaviour: the regions of decane-rich phase formed discrete lenses in contact with the methanol-rich film, apparent in Figure 3.39c. The observation of a zero contact angle by the saturated methanol-rich liquid on the hydrophobic substrates explains the initial rapid spreading of the single-phase droplet at deposition from the print head (Fig. 3.39b). In contrast, the decane-rich liquid formed a low, but finite angle.

3.9.5 Discussion

Using only the diffusion coefficients, pure vapour pressures and the solubility limit, κ^{pure} was defined. Observations during jetting trials matched the indications given by κ^{pure}: phase separation in methanol solutions of octane was borderline, whilst clear cut for methanol solutions of nonane and decane. The criterion κ is thus effective even using the assumption that both components in the two-phase binary mixture have vapour pressures that match those of the pure fluids. κ^{pure} is widely applicable: it can be used for non-aqueous mixtures where physical data was less readily available than for aqueous systems.

The drying dynamics observed during the decane-in-methanol trials tended to be less repeatable than the aqueous formulations unless the initial decane concentration was low. The high volatility of methanol (at T = 295 K, p = 14.4 kPa; $D = 1.58 \times 10^{-5}$ m^2 s^{-1})[76,77,91] produced drying times that were < 40 ms. Assuming a drop radius $r_0 \sim 1 \times 10^{-4}$ m, the velocity of the interface $v \sim 1 \times 10^{-3}$ m s^{-1}. Binary liquid diffusion coefficients[74] D_{AB} are of the order 10^{-9} m^2 s^{-1}, so that $Pe \sim 100$ (see Section 3.4.2). Printed drops of decane-methanol mixtures therefore cannot be expected to attain equilibrium geometries and compositions. Non-uniform composition at the contact line was observed through the fingering instability in Figure 3.39. The large Péclet number also indicates that solutes would not have time to partition into different phases before evaporation is complete: phase-selective patterning is therefore not possible with alkane-methanol mixtures under room temperature and pressure.

The demonstration of phase separation in a non-aqueous fluid widens the range of solutes that could be patterned selectively. The use of all-organic fluids presents

additional opportunities for formulation design: the wide range of functionalities and the ability to alter solvation and evaporative properties by moving along a particular homologous series allows the fine tuning of formulation characteristics. Non-aqueous formulations, however, do have disadvantages versus their aqueous counterpart; for example, the former produce hazardous vapours that require capturing and processing.

Non-aqueous formulations that give repeatable drying dynamics, attain equilibrium geometries and compositions and have sufficient time for partitioning of solutes into opposite phases will have a major solvent that was not as volatile as methanol. A solvent like ethylene glycol has the correct characteristics to be the minor component. With a vapour-phase diffusion coefficient $D = 1.1 \times 10^{-5}$ m^2 s^{-1} and vapour pressure p = 0.012 kPa at 298 K,[64,76,77] it has a much lower evaporation rate than decane. Ethylene glycol is polar and is miscible in all proportions with water. It should therefore be not too difficult to find a co-solvent in which it is partially miscible and from which it phase separates during evaporation.

3.10 Phase Separation in Aqueous Solutions of Salt and Polymer

Sections 3.5 − 3.9 explored fluids that phase separated as a result of partial miscibility of arbitrary solvent mixtures. In contrast, this section explores systems where pairs of solutes in a single solvent give rise to phase separation resulting from the interaction between the solutes. When two polymers are dissolved in the same solvent a number of possible outcomes exist: first the polymers could be completely miscible and the solution is homogenous. Second the polymers could be incompatible and phase separation occurs, with each polymer partitioning into opposite phases. Third, the polymers could form a coacervate and phase separation occurs, with both polymers partitioning into the same phase.[95]

Incompatibility can be observed for aqueous solutions of two non-ionic polymers like poly(vinyl alcohol) with dextran, poly(vinyl pyrrolidone) with methyl cellulose and poly(ethylene glycol) with poly(propylene glycol). Phase separation is also possible with aqueous solutions of a polyelectrolyte and a non-ionic polymer (sodium dextran sulphate with dextran, with the addition of NaCl) and pairs of polyelectrolytes (sodium carboxymethyl dextran and sodium carboxymethyl cellulose, with the addition of NaCl). Incompatibility is not limited to solutions containing two polymers, but has been observed for solutions containing a polymer and a low-molecular-weight component; an example is an aqueous solution containing poly(ethylene glycol), PEG, and potassium phosphate.[95]

The time required for a pair of incompatible polymers in solution to separate should be considered relative to the lifetime of ink-jet printed drops. PEG with MW = 8000 g mol^{-1} has $D \sim 3 \times 10^{-11}$ m^2 s^{-1} in 2% aqueous solution at 295 K.[96] The time t to diffuse the radius r_0 of a printed drop is $\sim (r_0)^2/D$. For PEG8000, $t \sim 200$ s in a drop with $r_0 = 80$ μm, neglecting any migration due to composition gradients. A 300 pL water drop dries in ~5 s. A pair of incompatible polymers cannot therefore be expected to form well-developed domains before a volatile solvent completely evaporates; a solvent with a low volatility would be required. Polymer-salt incompatibility should, however, yield well-developed domains from an aqueous formulation, according to the partitioning analysis for small molecules given in Section 3.4.2. This section explores the potential for formulating phase-separating ink-jet fluids using polymer-salt incompatibility. First, the phase diagram of the PEG-K_3PO_4 system is presented and second, an account of experimental formulation trials is given.

3.10.1 Phase Diagram for the Aqueous PEG-K_3PO_4 system

The phase diagram for aqueous solutions of PEG and potassium phosphate, K_3PO_4, is given in Figure 3.40 for a number of different PEG molecular masses.[95] For each binodal, the critical point is marked with a cross and tie lines may be constructed between the n^{th} circles on each side of the critical point. As discussed in Section 3.1.1, a composition within a two-phase region exists as two phases with compositions corresponding to the

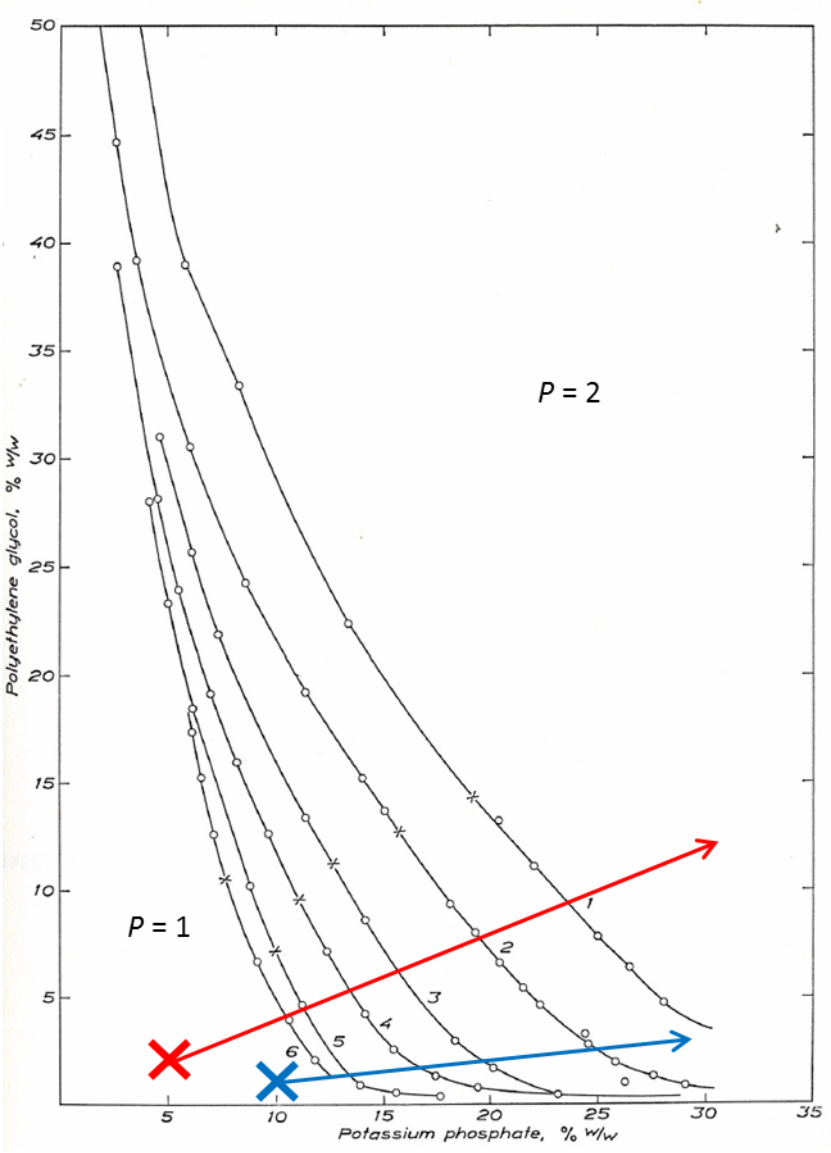

Figure 3.40. Phase diagram for aqueous solutions of K_3PO_4 and polyethylene glycol (PEG) of various molecular weights. Binodals are marked for (1) 300 g mol^{-1}, (2) 600 g mol^{-1}, (3) 1540 g mol^{-1}, (4) 4000 g mol^{-1}, (5) 6000 g mol^{-1} and (6) 20000 g mol^{-1} PEG. Critical points are marked with black crosses (×) and tie lines may be constructed between the n^{th} circles on each side of the critical points. The large blue cross marks a solution containing 1 %wt PEG and 10 %wt K_3PO_4 and the blue arrow marks the change in composition as water is lost to evaporation. The large red cross marks a solution containing 2 %wt PEG and 5 %wt K_3PO_4 and the red arrow marks the change in composition as water is lost to evaporation. Reproduced with permission.[95] Copyright 1960, John Wiley & Sons

termini of the tie line at the binodal; the relative proportions of the two phases may be estimated using the lever rule. The range of compositions over which the PEG-K_3PO_4 system is stable as a single phase decreases with increasing PEG molecular mass. Knowledge of the binodals allows ink-jet formulations to be designed that exist as one phase at manufacture but phase separate during evaporation on the substrate.

3.10.2 Experimental Results

Before printing trials were conducted, aqueous mixtures of poly(ethylene glycol) with a molecular mass of 8000 g mol^{-1}, PEG8000, (*Acros Organics*) and K_3PO_4 (*Sigma-Aldrich*, ≥98%) were prepared. The structure of PEG is given in Figure 3.41. The number of phases present at selected compositions are recorded in Table 3.10. The formulation containing 1 %wt PEG8000 and 10 %wt K_3PO_4 existed as a single phase, whilst the other three formed two phases. The PEG8000:K_3PO_4 ratio in all four solutions is fixed so that if the first entry were to be left to evaporate the solution would pass through the compositions recorded on the subsequent rows (see the blue arrow in Figure 3.40). An ink-jet printed drop of a solution containing 1 %wt PEG8000 and 10 %wt K_3PO_4 would therefore be expected to display phase separation during evaporation.

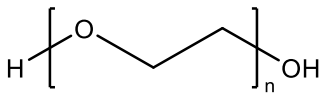

Figure 3.41. The chemical structure of poly(ethylene glycol).

TABLE 3.10. The number of phases formed by solutions containing both PEG8000 and K_3PO_4, at various concentrations.

[PEG8000]/ (%wt)	[K_3PO_4]/ (%wt)	Observations
1.0	10	1 Phase
1.5	15	2 Phases
2.0	20	2 Phases
2.5	25	2 Phases

A solution containing 2.0 %wt PEG8000 and 5.0 %wt K_3PO_4 was also found to be one phase. Increasing the PEG8000 concentration by a factor of two from the solution containing 1.0 %wt PEG8000 and 10 %wt K_3PO_4, and halving the concentration of K_3PO_4, should mean that when phase separation occurs each phase should be of more equal mass: the composition trajectory during evaporation indicated by the red arrow in

Figure 3.40 crosses the binodal closer to the critical point than the trajectory indicated by the blue arrow.

Typical drying dynamics for a solution containing 2.0 %wt PEG8000 and 5.0 %wt K_3PO_4 when ink-jet printed onto a hydrophobic substrate are displayed in Figure 3.42. The fluid arrived at the substrate as a single phase (Fig 3.42a) and the contact line receded initially due to water evaporation; at t = 1.0 s the contact line became pinned (Fig. 3.42b). Phase separation is apparent in Figure 3.42c (phase boundary marked by red dots), where a spherical cap of liquid has continued to recede as water evaporates but is surrounded by a thin film of a second fluid. Based on the observation of the polymer-rich phase being the less massive of the two in the trials for the 1.0 %wt PEG8000 and 10 %wt K_3PO_4, it is likely that the thin film surrounding the spherical cap is polymer-rich. The thin film is dry round the outer edge as indicated by the fine irregular structure (Fig. 3.42c); the region between the contact line and the water-rich phase may have a smooth surface and may also be dry. The central phase stops evaporating once the solutes become sufficiently concentrated (Figs. 3.42e−f). Incomplete evaporation of the central phase can be explained by the same reasoning invoked for the incomplete evaporation of the glucose solutions (Section 3.8.1): solvent evaporation is retarded due to the low solvent chemical potential imparted by the presence of the highly soluble K_3PO_4.

The high solubility of K_3PO_4 (900 g L^{-1} at 293 K)[97] retarded the evaporation of the water so that drops of solutions of PEG8000 and K_3PO_4 incompletely evaporated. Magnesium sulphate has a lower solubility limit in water, at 360 g L^{-1} at 293 K,[98] so it might precipitate from the phase-separating fluid rather than retard evaporation at late times. A solution containing 9.9 %wt $MgSO_4$ (*Aldrich*, 97+%) and 2.0 %wt PEG8000 formed a single phase at formulation and was printed onto a hydrophobic substrate; the drops were a single phase when the salt concentration inhibited solvent evaporation. However, printed drops of a solution containing 5.0 %wt $MgSO_4$ and 2.0 %wt PEG8000 did phase separate: the drying dynamics were analogous to those pictured in Figure 3.42, with the solute failing to precipitate from the central phase.

Solute precipitation could be induced if the salt had more limited solubility in water. NaOx successfully crystallised from the DPGMEA-water mixtures (Section 3.8.2) so might not retard evaporation in the same manner as K_3PO_4 and $MgSO_4$. However, when excess PEG8000 was added to a saturated aqueous NaOx solution, no separation was observed; phase separation would therefore not be observed on the substrate.

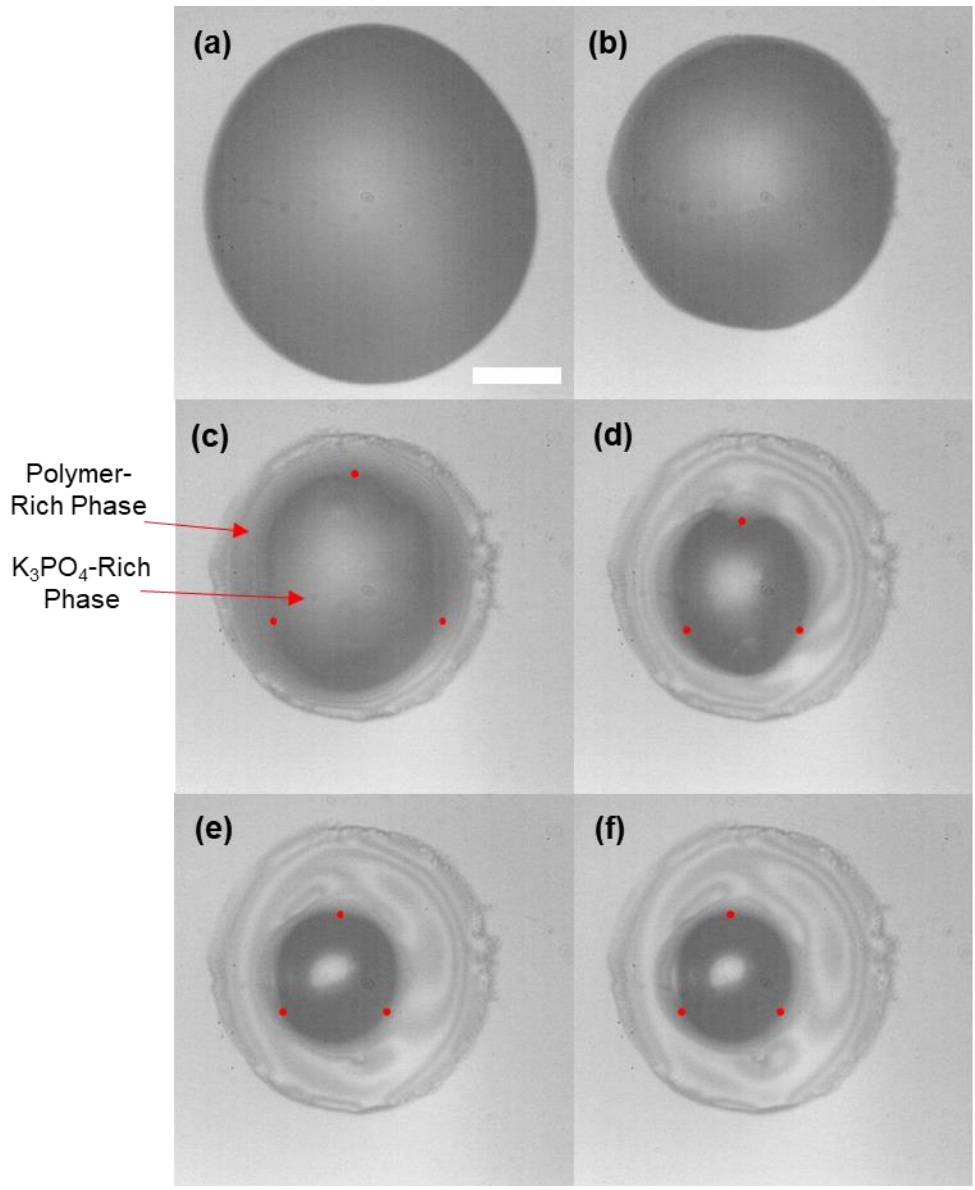

Figure 3.42. A drop of an aqueous solution containing 2.0 %wt PEG8000 and 5.0 %wt K_3PO_4 viewed from underneath. Images were captured (a) 0.20 s, (b) 1.00 s, (c) 1.70 s, (d) 2.40 s, (e) 3.00 s and (f) 3.90 s after deposition onto a hydrophobic substrate. The drop was jetted with a symmetrical bipolar waveform with a drive voltage of 30 V. Red dots mark the interfacial boundary between the phases. The scale bar is 40 μm.

3.10.3 Discussion

Solutions of PEG8000 and K_3PO_4 phase separated during printing trials: a thin polymer-rich film formed that surrounded a central phase containing K_3PO_4; the central phase did not evaporate completely due to the high solubility of the salt. Passing the deposit under a heating element or operating in an atmosphere with $RH = 0$ could drive off the remaining solvent.

The system has advantageous characteristics: water-based formulations are inexpensive and the vapour is non-hazardous. Additionally, the contact line pinned early during the drying process, preventing recession at late times. Were a central salt deposit

produced, it would not be wetted by the second phase to the same extent as was observed for the water-DPGMEA-NaOx-Ba system on a hydrophobic substrate (see Fig. 3.31).

Formulations that separate due to incompatible solvated species have already been demonstrated in ink-jet scenarios. Parry *et al.*[99] showed that a formulation containing a polymeric initiator and a non-initiating polymer can be used to manufacture sub-micron patterns of polymer brushes. Here, the phase-rich in the initiator formed at the contact line, whilst the central phase was rich in the non-initiating polymer; thus when polymer brushes were grown, they were much narrower than the original drop size. The solvent was a 1:1 v/v mixture of water and ethylene glycol and the authors do not quote a drop drying time. Given that ethylene glycol has a vapour-phase diffusion coefficient $D = 1.1 \times 10^{-5}$ m^2 s^{-1} and vapour pressure $p = 0.012$ kPa at 298 K,[64,76,77] the total drying time of the drop will be much longer than for pure water, allowing sufficient time for the polymers to phase separate. This strategy could be used for other solutions of incompatible polymers to attain phase-selective patterning.

3.11 Summary

Fluids that can be ink-jet printed as a single phase but then undergo phase separation on the substrate during evaporation have been investigated. A quantitative criterion κ was developed to identify if a formulation had the propensity to phase separate; the criterion made use of only readily available physical data (solubility limit, component vapour pressures and gas-phase diffusion coefficients). Modelling the component vapour pressures according to Raoult's law led to the false indication that butanol-water mixtures would phase separate upon jetting; the vapour pressures in partially miscible mixtures are highly non-ideal and significantly underestimated the butanol vapour pressure at saturation in aqueous solution. However, modelling the minor component vapour pressure according to Henry's law is a better approximation and allowed a wide range of aqueous mixtures to be screened; aqueous glycol ether solutions were identified as suitable candidates. The criterion κ was also shown to be effective when the components were assumed to maintain pure vapour pressures in binary mixture, making the analysis useful for non-aqueous mixtures where physical data is less abundant.

When jetted, DPGMEA-water mixtures formed an oil-rich phase as a ring at the contact line, in keeping with the local enhanced evaporative flux versus the apex; the low volatility of DPGMEA resulted in stagnant oil on the substrate after complete water evaporation. Selective patterning was observed on a hydrophilic substrate when sodium oxalate and benzoic acid were included in the formulation, with the former partitioning into the water-rich phase and the latter into the oil-rich phase; the deposit comprised a central spot of sodium oxalate surrounded by benzoic acid. Requirements for designing formulations that give phase-selective deposition and guidelines for selecting appropriate solutes were suggested.

Phase separation was also observed for non-aqueous mixtures: nonane-in-methanol and decane-in-methanol solutions were printed and were observed to separate during evaporation, as expected from the associated κ values. The high volatility of the methanol made separation behaviour irreproducible unless the alkane was included at low concentrations. Analysis showed that evaporation was too rapid for uniform geometries and compositions to be attained. A major component with a lower volatility would improve the applicability of non-aqueous formulations. Ethylene glycol has the correct properties for the minor component.

Separation in ink-jet formulations was additionally investigated using aqueous solutions of a poly(ethylene glycol) and K_3PO_4, where separation proceeds due to solute incompatibility. When jetted, a thin film of polymer formed around a central phase rich

in K_3PO_4, but complete loss of water was not observed due to the high solubility of the salt. Patterning where phase separation is driven by a pair of incompatible polymers requires a solvent that is less volatile than water.

Phase-separating formulations were hypothesised as able to disrupt coffee-ring flow owing to production of a new phase at the contact line where evaporative flux is greatest. The strategy requires diffusion of the major component through the new phase could become rate limiting, instead of diffusion in the vapour. Brief trials were inconclusive.

4 Ink-Jet Printing of High-Molecular-Weight Polymers via Emulsions

The ink-jet printing of solutions of high-molecular-weight polymers is non-trivial owing to complex rheological behaviour under high strain conditions.[42] The inclusion of polymers, even in small quantities, radically alters the dynamics of fluids emerging from an orifice: long-lived elastic filaments between the main drop body and the nozzle develop that decelerate the drop and may even prevent detachment entirely.[100] Consequently, there is a limit in the weight fraction of polymer that may be included in printing fluids; for a high-MW sample, the limit is much less than 1 %wt.[101] The aim of this chapter is to present an investigation into using emulsions to facilitate the jetting of inks with a much higher polymer content than is possible in binary solution.

The structure of this chapter is as follows: first, the filamentation and detachment dynamics of polymer solutions under high strain conditions is discussed in the context of experiments at millimetre-sized orifices and filament-thinning rheometers (Section 4.1). Second, investigations into the ink-jet printing of polymer solutions are reviewed (Section 4.2). Third, an outline of the mechanisms by which emulsions facilitate the printing of high-molecular-weight polymers is given (Section 4.3), along with a demonstration of the feasibility of the strategy (Section 4.4). Fourth, a brief overview of emulsion science is presented (Section 4.5). Fifth, an account of the practical investigation is provided from Section 4.6 onwards, including emulsification studies (Sections 4.7 and 4.8) and printing trials (Sections 4.9 and 4.10). Sixth, the success of the using emulsions to print high-molecular-weight polymers is evaluated and important formulation considerations are discussed (Section 4.11). Seventh, a summary is given (Section 4.12).

4.1 The behaviour of Polymer Solutions under Elongational Strain

This section outlines the behaviour of polymer solutions under elongational strain. Hereafter, observations of detachment dynamics are presented, along with a description of the coil-stretch transition, which causes the departure from Newtonian dynamics. Additionally, a model describing the balance of forces during filamentation is presented and the factors that determine the filament relaxation time are discussed.

4.1.1 Characteristics of Drop Detachment for Polymer Solutions

Investigations into the behaviour of polymer solutions during drop formation and detachment have been carried out on fluids in liquid-bridge rheometers[102–106] and drops emerging from an orifice.[107–111] Amarouchene *et al.*[107] compared the detachment dynamics for pure water and dilute aqueous polymer solutions from a capillary (Fig 4.1a). In the pure water case, the authors observed that $h_{min} \propto (t_p - t)^{2/3}$, in keeping with the expected potential flow regime. A 250 ppm solution of PEO (molecular weight ~4000 kDa) initially followed the same Newtonian dynamics. Cooper-White *et al.*[110] also observed Newtonian necking dynamics with dilute solutions of PEO with molecular weights in the range 8 – 1000 kDa early in the drop formation process. Polymer solutions are viscoelastic and respond as a Newtonian fluid at low strain rates. The strain rates

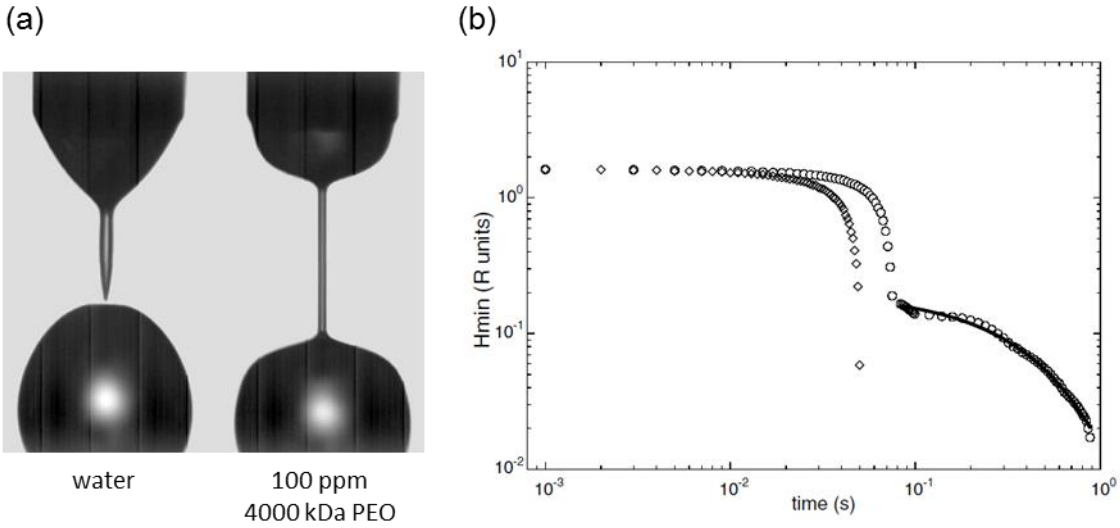

Figure 4.1. (a) Detachment if a water drop (left) and a 100 ppm solution of 4000 kDa PEO (right) from a 4-mm diameter capillary. (b) The variation in minimum neck radius h_{min} over time for the water (diamonds) and the PEO solution (circles). Part of the PEO curve has been fitted with an exponential function. The *y*-axis has been normalised with the capillary radius (2 mm). Reprinted with permission from Y. Amarouchene, D. Bonn, J. Meunier and H. Kellay, *Phys. Rev. Lett.*, 2001, **86**, 3558–3561. Copyright 2001, by the American Physical Society.

experienced by the fluid become large as a pendent drop approaches the pinch point, particularly where the neck radius is smallest. Amarouchene *et al.*[107] observed long cylindrical filaments abruptly form between the fluid in the orifice and the main drop body above a critical strain rate $\dot{\varepsilon}_{crit}$ as the neck rapidly thinned towards detachment (Fig 4.1a). The filament reduced in thickness exponentially and significantly delayed drop breakoff (Fig 4.1b). The formation of filaments by polymer solutions is a well-known phenomenon.[104–111]

4.1.2 The Coil-Stretch Transition

The departure from Newtonian behaviour for polymer solutions is caused by the impact of high strain rates on polymer conformation. An ideal polymer chain in dilute solution in a good solvent exists in a conformation that is slightly expanded from a random walk conformation and may be approximated to a sphere of radius R_g. Under high strain rates, a polymer undergoes the coil-stretch transition. Physically, the coil-stretch transition corresponds to a polymer chain being stretched out into an extended state as a result of the strain rate being faster than that of diffusive relaxation back to equilibrium conformation.[112] Under Zimm dynamics, segments in a coiled polymer hydrodynamically interact with one-another and reduce the overall drag experienced by the polymer. The polymer is therefore treated as sphere of radius R_g and solvent does not freely flow through the pervaded chain volume. The relaxation time for a polymer is given by the Zimm relaxation time τ_Z in the undistorted state.

The Weissenberg number *Wi* is the product of the strain rate $\dot{\varepsilon}$ and the relaxation time τ:

$$Wi = \dot{\varepsilon}\tau \,. \tag{4.1}$$

The coil-stretch transition occurs over a narrow range of strain rates[112] and is complete when

$$Wi = \dot{\varepsilon}\tau_Z = \frac{1}{2}. \tag{4.2}$$

Thus the coil-stretch transition occurs at a critical strain rate $\dot{\varepsilon}_{crit}$, corresponding to a critical Weissenberg number Wi_{crit}.

The coil-stretch transition increases $\langle R^2 \rangle$ and therefore reduces the number of possible chain conformations: the number of conformations is maximised for $\langle R^2 \rangle = 0$, whilst only one conformation is possible when fully extended. The reduction in conformational freedom comes at an entropic cost and the associated restoring force f_E

introduces elastic character to the polymer solution. For small extensions ($R << R_{max}$), an ideal polymer chain obeys Hooke's law and is linear in R:

$$f_E = \frac{3kT}{Nb^2} R \,. \tag{4.3}$$

The entropic force becomes non-linear as R approaches R_{max}.[113]

4.1.3 The Dynamics of Drop Detachment for a Viscous Polymer Solution

A mathematical description of a thinning capillary of an elastic fluid has been produced by Entov and Hinch.[114] The analysis is based on the uniform cylindrical filaments that can be produced by liquid filament rheometers and makes no attempt to describe the dynamics of filament formation process. The polymers are modelled as finitely-extensible nonlinearly-elastic (FENE) dumbbells with N uncoupled relaxation modes, each with elastic modulus G_i and relaxation time τ_i; each mode has a finite maximum extension L_i. The cylindrical filament has radius h and is modelled as subject to uniform surface tension γ. The elongational strain $\dot{\varepsilon}$ is therefore given by

$$\dot{\varepsilon} = \frac{2}{h}\frac{\mathrm{d}h}{\mathrm{d}t} \,. \tag{4.4}$$

The liquid in the study is assumed viscous so that initially the filament thinning dynamics are controlled by the balance between the capillary pressure acting to thin the filament and the viscosity acting in opposition. The filament radius thins in this regime according to

$$h = h_0 - \frac{\gamma}{6\eta} t \,, \tag{4.5}$$

where t is time, h_0 is the filament radius at $t = 0$ and η is the solvent viscosity. The polymer solution is therefore following the same necking dynamics as a viscous Newtonian liquid in the viscous thread regime where $h_{min} \propto (t_p - t)$.

During viscous thinning of the filament, elastic stress in the fluid increases. The elastic stress, however, cannot exceed the capillary pressure. When the elastic stress is significant, the strain rate must reduce in order that the elastic stress does not exceed the capillary pressure (illustrated in Figure 4.2). A reduction in the strain rate correlates with a reduction in the viscous stress so that elastic and capillary forces are the dominant forces acting on the thinning filament. In the elasto-capillary thinning regime, the radius of the filament decreases exponentially according to

$$h = h_0 \left(\frac{h_0 G(t)}{\gamma} \right)^{1/3} \,, \tag{4.6}$$

where

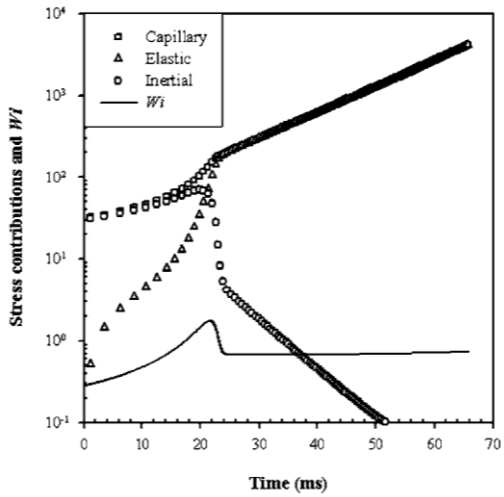

Figure 4.2. Modelled variation of the Weissenberg number *Wi* over time in a thinning capillary of a polymer solution. The contributions to the stress are also shown. In this case, after 10 ms, *Wi* = 0.5 and elastic stress in the filament becomes significant, increasing to equal the capillary stress. The inertial stress decreases as the elastic stress increases. Reprinted from V. Tirtaatmadja, G. H. McKinley and J. J. Cooper-White, *Phys. Fluids*, 2006, **18**, 43101, with the permission of AIP Publishing.

$$G(t) = \sum_{i}^{N} g_i \exp\left(-\frac{t}{\tau_i}\right) ; \tag{4.7}$$

g_i and τ_i are the elastic modulus and relaxation time of mode i, respectively.

As the radius of the filament decreases, the capillary pressure increases. The elasto-capillary balance is maintained by extension of the filament occurring at a strain rate corresponding to $Wi = 2/3$, just larger than Wi_{crit}. Polymers therefore continue to stretch and elastic stress continues to build in the filament. The elastic stress at time t is dominated by the mode with the closest relaxation time τ_i to t. As the strain rate reduces with increasing elastic stress, the fastest-relaxing modes decay quickly and the rate of filament thinning is determined by the slowest-relaxing mode. The exponential reduction in filament radius was observed experimentally by Bazilevskii *et al.*[104] for filaments of aqueous solutions of poly(acrylamide) thinning on a liquid filament rheometer.

Once the FENE dumbbells reach their maximum extension L_i, they act as a suspension of rigid rods. Consequently, the solution can be approximated to viscous fluid of viscosity η^*. The filament thinning regime thus returns to Newtonian dynamics for a viscous liquid and the radius is described by

$$h = \frac{\gamma}{6\eta^*}\left(t_p - t\right). \tag{4.8}$$

The filament radius reduces to zero in this regime and breakoff is observed. Bazilevskii et al.[104] also observed the effects of finite extensibility during filament thinning.

4.1.4 Filament Relaxation Times

In the analysis of Entov and Hinch,[114] the relaxation times τ_i of the FENE dumbbell modes determines the rate of exponential reduction in the filament radius over time. During the elastocapillary thinning regime for a dilute PEO solution, Amarouchene *et al.*[107] observed that the exponential reduction in minimum neck thickness $h_{\min}$ was in good agreement with

$$h_{\min} = h^* \exp\left(-\frac{t}{\tau_{\text{fil}}}\right), \tag{4.9}$$

where h^* and τ_{fil} are constants. An investigation by Cooper-White *et al.*[110] using dilute PEO solutions over a range of molecular weights found that the length of the filament at break-off and the lifetime of the filament increased with increasing polymer molecular weight, and hence relaxation time.

The transition of polymers from coiled to stretched conformations close to the Newtonian pinch point leads to the elastocapillary force balance and the generation of filaments. It might therefore be expected that τ_{fil} is equal to the Zimm relaxation time τ_{Z} since the fluids used by Amarouchene *et al.*[107] are dilute and should obey unentangled dynamics. Christanti and Walker[115] found, however, that the time constant τ_{fil} for the exponential reduction in the filament radius was greater than the Zimm relaxation time when dilute PEO solutions were jetted from a nozzle, though the discrepancy was less than an order of magnitude. Other studies have also indicated a departure from dilute unentangled polymer dynamics in filaments. Amarouchene *et al.*[107] observed that τ_{fil} increased, and therefore the rate of filament thinning decreased, with increasing polymer concentration. Tirtaatmadja *et al.*[111] investigated the deformation and drop breakup of solutions of PEO below the overlap concentration c^* when flowing out of a millimetre-sized orifice. For $c/c^* \sim 0.5$, τ_{fil} was larger than τ_{Z} by about an order of magnitude, in agreement with Christanti and Walker.[115]

Tirtaatmadja *et al.*[111] also found that τ_{fil} was proportional to the molecular weight of the polymer and to its concentration. The ratio $\tau_{\text{fil}}/\tau_{\text{Z}}$ effectively normalises the time constant for filament thinning by the solvent viscosity and the polymer molecular weight. A plot of $\tau_{\text{fil}}/\tau_{\text{Z}}$ against c/c^* was linear for the trials carried out by Tirtaatmadja *et al.*[111] and the results from studies by Amarouchene *et al.*[107] and Christanti and Walker[115] were all described well by the same line of best fit (Fig. 4.3). For $0.01 \leq (c/c^*) \leq 1$, the trend obeyed

$$\tau_{\text{fil}} = 0.463\tau_{\text{Z}}\left(\frac{c}{c^*}\right)^{0.65}. \tag{4.10}$$

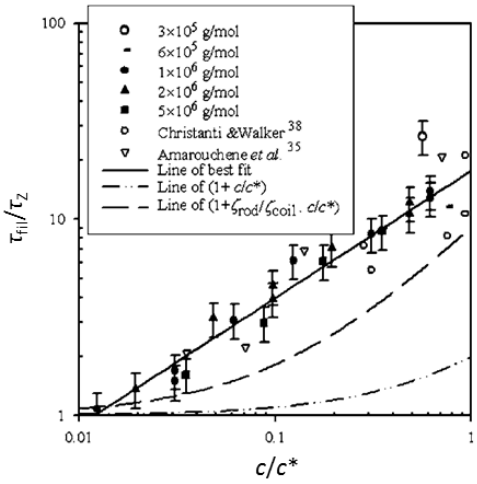

Figure 4.3. The observed filament relaxation time τ_{fil} scaled by the Zimm relaxation time τ_Z against solution concentration c scaled by the overlap concentration c^* for PEO solutions. The figure also contains results from Amarouchene *et al.*[107] and Christanti and Walker.[115] Reprinted from V. Tirtaatmadja, G. H. McKinley and J. J. Cooper-White, *Phys. Fluids*, 2006, **18**, 43101, with the permission of AIP Publishing.

Tirtaatmadja *et al.*[111] concluded that the relaxation times observed in filaments between the main drop and the liquid in the orifice is a result of polymer-polymer interactions. The dependence of relaxation time in filaments upon reduced concentration is consistent with semidilute polymer behaviour, since increasing concentrations increases the extent to which inter-chain interactions occur and raises the relaxation time strongly. The elastocapillary regime is established during the drop formation of a polymer solution once $Wi = 0.5$, so that the polymers undergo the coil-stretch transition and the solution develops an elastic character. The surface area of a polymer coil under equilibrium conditions is given by the surface area of a sphere of radius R_g. In an extended state, however, the polymer approximates more closely to a cylinder and the surface area is much increased. Consequently, in an extended conformation, the onset of semidilute polymer dynamics occurs at a lower concentration than seen for polymers under low shear conditions where coils still approximate to spheres.[116] Dilute polymer solutions therefore cease to exhibit Zimm dynamics in the filament and $\tau_{fil} > \tau_Z$.

The results of Tirtaatmadja *et al.*[111] indicate that τ_{fil}/τ_Z approaches unity as c/c^* decreases towards ~0.01 (Fig. 4.3), suggesting that at very low polymer concentrations, Zimm relaxation dynamics are observed in elongating filaments. A concentration therefore exists below which polymer chains do not interact with each other when in extended conformations, giving rise to unentangled polymer dynamics.[117] Polymer solutions that remain unentangled even at maximum extension are termed ultradilute.

4.2 The Behaviour of Polymer Solutions under Ink-Jet Conditions

In Section 4.1, the behaviour of polymer solutions under elongational strain was discussed. In this section, factors relating to the printability of polymer solutions are explored, including jetting dynamics, concentration limits and strain-induced degradation of polymers.

4.2.1 General Printability of Polymer Solutions

A fluid with the correct balance of physical properties for ink-jet printing generally obeys the criterion $0.1 < Oh < 1$.[17] If $Oh > 1$, viscous dissipation in the fluid prevents drops from achieving sufficient velocity to overcome surface forces, causing a failure to detach. In contrast, if $Oh < 0.1$, detachment does not result in the production of a single drop, but several. Any unfavourable printing behaviour by a fluid can only be managed to a limited degree by adjusting formulation since three of the four properties in the Ohnesorge number are largely fixed:[42] for typical oleic and aqueous systems, densities vary between $0.8 – 1.2$ g mL^{-1} and surface tensions vary over the range $20 – 70$ mN m^{-1}, whilst the size of the drop is largely determined by the size of the orifice. The viscosity of a fluid, however, is easily manipulated by the addition of additives and varies over a much larger range of values.

The printability, then, of a polymer solution is first considered in terms of its low-shear viscosity.[42] The inclusion of polymers into a formulation at low concentrations raises the viscosity, and the rate of increase with concentration greatly increases above the overlap concentration. The low-shear viscosity of a concentrated polymer solution can cause the fluid to have $Oh > 1$ and thus be unsuitable for printing.

The inclusion of small quantities of polymer into an ink-jet formulation can be beneficial for improving formulation performance. In the simplest case, the addition of polymers can allow the viscosity, and hence the value of *Oh*, to be optimised for a particular print process.[6] Block co-polymers have been shown to confer greater stability upon pigment dispersions.[118] Polymers with low molecular masses can be added to act as binders to improve the water fastness of images on a substrate.[119] At certain concentrations, the addition of polymers to ink-jet formulations reduce the prevalence of satellite drops formation during printing, leading to an increase in pattern resolution.[120,121]

Representative drop ejection velocity from an industrial print head is of the order $10 – 20$ m s^{-1}. Assuming the drop height is similar to that of the orifice, which may typically be ~20 μm, the elongational strain, as given in Equation (4.4), is ~10^6 s^{-1}. In contrast, Christanti and Walker[115] ejected drops from an orifice of diameter 0.5 mm at a

speed of 2 m s^{-1}, corresponding to an elongational strain rate of 10^4 s^{-1}. The strain rates, then, encountered by polymer solutions during ink-jet printing are about two orders of magnitude higher than those from millimetre-sized orifices and filament rheometers. The qualitative necking and detachment behaviour of dilute polymer solutions at the lower strain rates have also been observed during ink-jet printing.[101,120–123] The printability of a polymer solution is ultimately determined by the severity of non-Newtonian behaviour manifested at high shear. It is therefore insufficient to ensure that the fluid possesses an Ohnesorge number corresponding to low-shear conditions in the correct range for ink-jet printing.[122]

4.2.2 Jetting Dynamics of Polymer Solutions

Hoath *et al.*[122] jetted a series of solutions containing linear polystyrenes, each having equivalent low-shear viscosity and $c/c^* < 1$. The 110-kDa polystyrene solution formed a filament between the main drop body and the orifice which necked in several locations along the structure to form satellite droplets. At higher molecular weight (210 kDa < M < 488 kDa) the filaments were punctuated with small drops after ~150 μs, known as a beads-on-a-string structure (Fig 4.4). The beads were sometimes observed to merge with the main drop body so that satellites were not generated.

Bazilevskii *et al.*[120] printed a series of aqueous-glycerin solutions of polyacrylamide from a thermal ink-jet device. Polymers had molecular weights in the range 500 – 6000 kDa and were included at concentrations 10 – 200 ppm by weight. They found that jetting and breakoff behaviour could be described according to three broad regimes (Fig. 4.5a): (1) the jet tail disintegrates into several satellites; (2) the tail is completely drawn into the main drop and no satellites are produced; (3) the drop fails to detach and is withdrawn back into the nozzle. For a pure water-glycerin solution the first regime was observed: detachment from the nozzle occurred after ~80 μs and the tail disintegrated into satellite drops after ~150 μs. Qualitatively, the same regime was followed by dilute polymer solutions, though the addition of polyacrylamide at concentrations as low as 10 ppm caused long-lived filaments to form between the main drop body and the orifice. Drop breakoff was delayed relative to that observed for the pure solvent and satellites were produced from the disintegrating filament. Upon increasing the concentration or molecular weight the jets transitioned into the second behaviour regime, and upon further increase, into the third. The concentrations at which the transitions occurred decreased as polymer molecular weight increased (Fig. 4.5a).

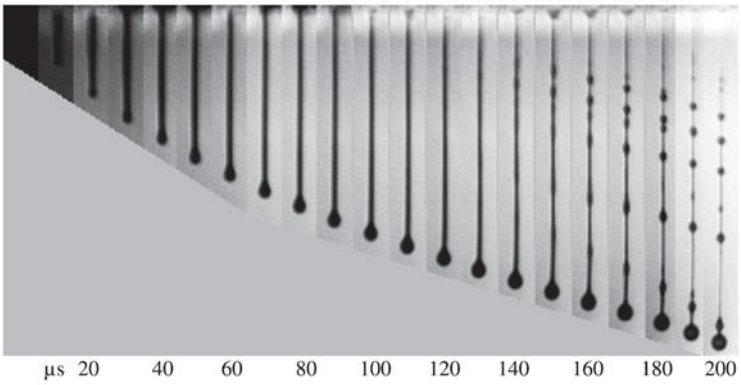

Figure 4.4. The evolution of a drop of a 0.4-%wt polystyrene solution in diethyl phthalate (M_w = 210 g mol^{-1}) over time. Jetted from a MicroFab print head (30-μm orifice diameter) with a waveform amplitude of 35 V. The figure height represents 0.92 mm. Reproduced with permission.[122]

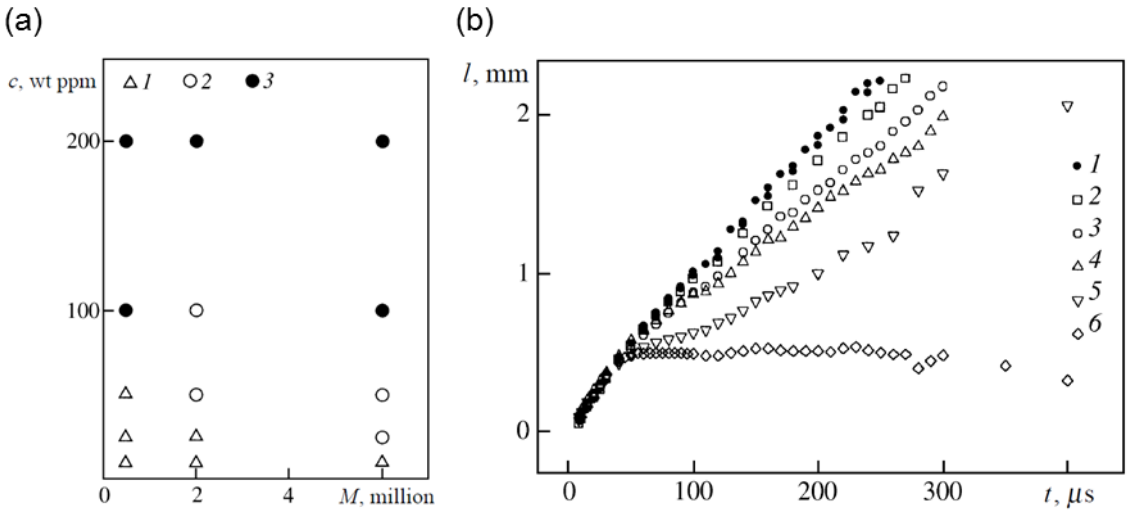

Figure 4.5. (a) "Dependence of the polymer solution jet ejection regimes on the polymer molecular weight M and the polymer concentration c in a water-glycerin (50/50) mixture: 1 corresponds to ejection with separation of several secondary droplets from the leading drop, 2 to formation of a single drop without loss of liquid in secondary drops, and 3 to the braking and stopping of the jet in flight." (b) "Displacement of the leading point of the jet as a function of time for jets polyacrylamide solution (M = 2 million), c = 0, 10, 25, 50, 100, and 200 wt ppm (points 1–6, respectively)." *Fluid Dynamics*, 2005, **40**, 376–392, A. V. Bazilevskii, J. D. Meyer and A. N. Rozhkov, Copyright 2005, Springer Science+Business Media, Inc.. With permission of Springer.

Bazilevskii *et al.*[120] also monitored the displacement of the main drop as a function of time and found that though the polymer solutions initially followed the same displacement dynamics as the Newtonian pure solvent, the polymer-containing jets were subject to a deceleration after ~50 μs (Fig. 4.5b). The deceleration was more severe at higher concentrations and polymer molecular weights, with some decelerating to a complete halt (third regime behaviour). The development of long-lived filaments, delayed breakoff and decelerating main drops are consistent with the non-Newtonian behaviour

of polymer solutions emerging from orifices and in filament rheometers, as discussed in Sections 4.1.1 and 4.1.4.

Xu *et al.*[121] conducted printing experiments on cellulose ester polymer solutions both above and below the overlap concentration c^*. The polymers had molecular masses in the range 10 – 50 kDa. The jetting dynamics were dependent on concentration: at lower concentrations, $0.3 \leq (c/c^*) \leq 2.5$, filaments disintegrated into satellites, whilst at a higher concentration, $(c/c^*) = 3.8$, the filament was drawn into the main drop and no satellites were generated. The filaments decelerated the main drop body, with greater deceleration observed for higher concentrations, and the breakoff time increased with concentration. Both trends continued above $(c/c^*) = 1$ and are consistent with increasing elasticity in the solutions.

4.2.3 Concentration Printing Limits for Polymer Solutions

de Gans *et al.*[100] investigated acetophenone solutions of polystyrene dispensed from micropipettes. The micropipettes had orifice diameters of 70 μm and drops were ejected with velocities of the order 2 m s^{-1}, placing the results outside of industrially relevant length and time scales, but in a similar regime to that employed in this thesis. With a fixed dispenser drive voltage, the maximum printable weight fraction of polymer decreased as molecular weight increased (Fig. 4.6a). The maximum printable concentration was 5

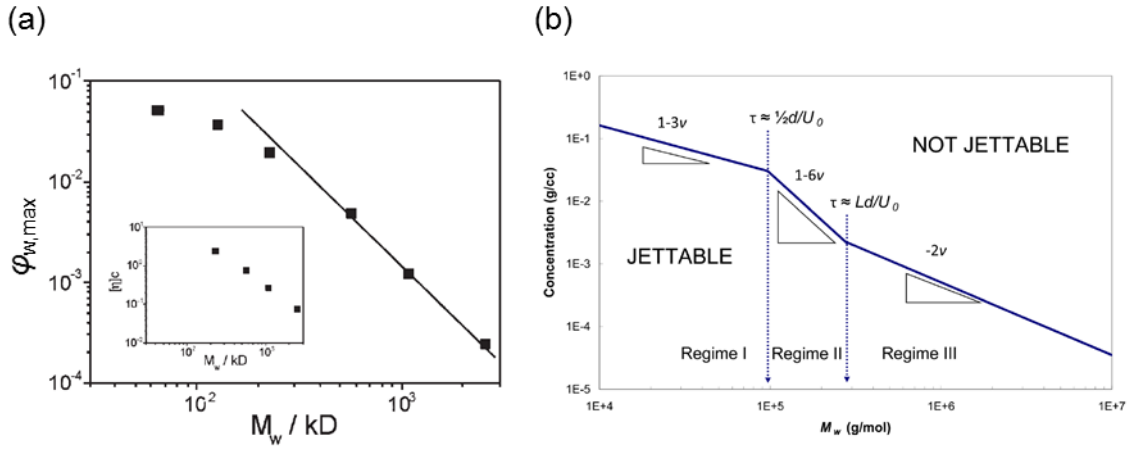

Figure 4.6. (a) The maximum printable weight fraction $\varphi_{w,max}$ against molecular weight M_w for polystyrene solutions in acetophenone from a micropipette with an orifice diameter of 70 μm. The line is a power law with exponent −2.14. Reproduced with permission.[124] Copyright 2004 WILEY-VCH Verlag GmbH & Co. KGaA, Weinheim (b) The trend in the maximum printable concentration of polystyrene solutions in DEP as a function of molecular weight when using a FENE model of the polymers. The three regimes discussed in the text are marked, along with the power law exponent, which is a function of solvent quality ν. Reprinted with permission from S. D. Hoath, O. G. Harlen and I. M. Hutchings, J. Rheol., 2012, 56, 1109–1127. Copyright 2012, The Society of Rheology.

%wt for M_w = 64 kDa, decreasing to 0.5 %wt for M_w = 564 kDa, decreasing to 0.1 %wt for M_w = 2530 kDa. For polymers with M_w > 564 kDa, the maximum printable weight fraction corresponded to solutions below the overlap concentration and the maximum printable weight fraction, $\varphi_{w,max}$, scaled according to the power law

$$\varphi_{w,max} \propto {M_w}^{-2.14} . \quad (4.11)$$

Hoath *et al.*[101] qualitatively observed the same reduction in $\varphi_{w,max}$ with polymer molecular weight when jetting diethyl phthalate solutions of polystyrene (24 kDa ≤ M_w ≤ 488 kDa) below c^*. The authors also observed that the print head drive voltage required to achieve a jet with velocity ~6 m s^{-1} increased with both concentration and polymer molecular weight. A number of different printing regimes were identified in the $\varphi_{w,max}$ – M_w data by modelling the polymers in solution as FENE dumbbells and considering the factors that decelerate the main drop as a function of the initial Weissenberg number (Fig. 4.6b). The values of $\varphi_{w,max}$ in each regime scaled as a power law of the form

$$\varphi_{w,max} \propto {M_w}^{p}, \quad (4.12)$$

where p is a function of solvent quality ν. The first regime covered jetting conditions where initially Wi < 0.5, so that elongational strain was insufficient to trigger the coil-stretch transition in the polymers and the solution behaved as a viscous fluid, displaying no elasticity. The second regime corresponded to initial jetting conditions where 0.5 < Wi < L, where L is the extensibility defined in terms of maximum polymer length l and the equilibrium diameter:

$$L = \frac{l}{2R_g}. \quad (4.13)$$

In the second regime, the polymers in solution underwent the coil-stretch transition and elastic character was introduced, but did not reach their extensibility limit. In the third regime, Wi > L initially so that polymers were stretched into their fully extended state. The impact of polymer conformation on the deceleration of the main drop in the different regimes bears strong resemblance those discussed by Entov and Hinch[114] in their analysis of the regimes of filament thinning dynamics (Section 4.1.3). Hoath *et al.*[101] identified that the expressions for p in the scaling law for $\varphi_{w,max}$ as $(1 - 3\nu)$, $(1 - 6\nu)$ and (-2ν) for the first, second and third regimes respectively.

McIlroy *et al.*[125] noted that the transition from the first to the second regime should occur at a slightly higher initial Weissenberg number than Wi = 0.5 since the strain rate decreases in the ligament as it increases in length. Jetting conditions where initially Wi = 0.5 would therefore not have strain rates above the critical value for sufficient time for

elastic forces to become significant. Modelling by McIlroy *et al.*[125] agreed with the $\varphi_{w,max}$ – M_w data from Hoath *et al.*[101]

4.2.4 Degradation of Polymers During Ink-Jet Processes

Polymers are susceptible to scission when exposed to high strain rates. The factors affecting degradation have been investigated for dilute and semidilute polymer solutions emerging from opposing jets.[126,127] A polymer in dilute solution undergoes the coil-stretch transition at a critical strain rate $\dot{\varepsilon}_{crit}$. In an extended state, a chain experiences greater viscous friction from solvent molecules than when in an equilibrium conformation.[112] At strain rates greater than $\dot{\varepsilon}_{crit}$, the enhanced hydrodynamic drag continues to stretch the polymer.[126] Polymer scission is a result of the stress in the polymer backbone exceeding the strength of the covalent bonds in the chain (Fig. 4.7a). For fracture to occur the polymer must reside in a flow with strain rate greater than the degradation strain rate $\dot{\varepsilon}_{deg}$ for a sufficient amount of time for the critical stress to be achieved.[128] An isolated polymer undergoes central scission into two almost equal halves since the stress is largest on the central bonds in an extended chain.[126] Keller *et al.*[126] established that the degradation strain rate varies with molecular weight M according to

$$\dot{\varepsilon}_{deg} \propto M^{-2}, \tag{4.14}$$

whilst for $\dot{\varepsilon}_{crit}$ the equivalent relationship is

$$\dot{\varepsilon}_{crit} \propto M^{-1.5}. \tag{4.15}$$

The latter result is in agreement with the functional dependence of the inverse Zimm relaxation time $(\tau_Z)^{-1}$ for an ideal polymer. For a low-molecular-weight polymer, $\dot{\varepsilon}_{deg} >> \dot{\varepsilon}_{crit}$, but the indices in Equations (4.14) and (4.15) show that $\dot{\varepsilon}_{deg}$ and $\dot{\varepsilon}_{crit}$ converge as

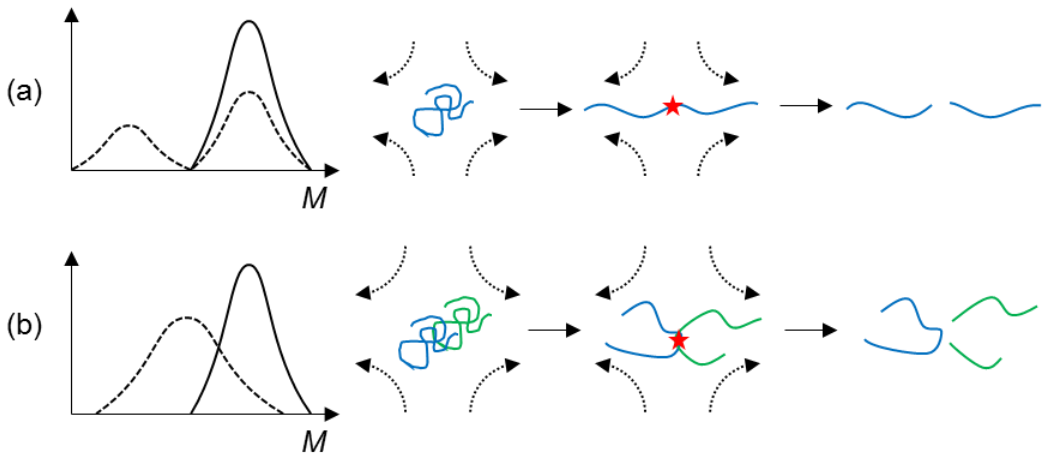

Figure 4.7. Schematic diagrams showing the mechanisms of (a) central scission and (b) random scission. Stars indicate the point of breakage. Also depicted are the mass distributions before (solid lines) and after breakage (dashed lines).

molecular weight increases. Above a certain molecular weight, $\dot{\varepsilon}_{deg} \leq \dot{\varepsilon}_{crit}$ and the polymer fractures without undergoing the coil-stretch transition.

Müller *et al.*[127] observed the semidilute polymer solutions had a different degradation mechanism from dilute solutions. A clear peak at half the original molecular weight in the mass distribution corresponding to central scission was not present, suggesting fracture was not a result of polymer-solvent frictional interactions. The semidilute polymer solutions formed transient networks at high shear rates when passing through opposed jets and the peak in the molecular weight distribution decreased, whilst the whole distribution broadened. The results were consistent with almost random scission caused by chain entanglements which are able to occur at a wide range of points along a particular backbone (Fig. 4.7b). The restrictions caused by junction points between chains at high shear rates produce localised stress at non-central backbone locations, giving rise to scission at other locations.

Degradation of high-molecular-weight polymers has been observed in drop-on-demand ink-jet printing systems. A-Alamry *et al.*[129] found that the severity and type of polymer scission depended on concentration, polydispersity and print head geometry for polystyrene and PMMA solutions. When jetting from a Dimatix DMP-2800 print head with an orifice diameter of 23 μm and drop velocities ~10 m s^{-1}, the elongational strain rate was ~3×10^5 s^{-1}. Polymers of low polydispersity with M_w < 100 kDa did not degrade when printed on account of $\dot{\varepsilon}_{deg}$ being larger than the strain rates experienced. Polymers of low polydispersity with M_w > 1000 kDa also remained intact upon printing since chains did not experience high strain rates for the critical residence time for sufficient stress to build up in the backbone.[125,129] At intermediate molecular weights, 100 kDa < M_w < 1000 kDa, polymers of low polydispersity displayed concentration-dependent degradation.[129] Above (c/c^*) = 0.5, no degradation was observed, whilst below (c/c^*) = 0.5, central scission occurred. The latter result is consistent with the behaviour of dilute polymer solutions in elongational flows that fracture as a result of polymer-solvent hydrodynamic drag in an extended conformation.[126]

Solutions of polydisperse polymers (PDI > 1.3) showed different degradation behaviour when printed than when samples had lower dispersity.[129] Polymers did not undergo central scission, but instead the molecular weight distribution broadened and shifted to lower molecular weight upon printing. The results are indicative of almost random fracture caused by entanglements, as observed for semidilute polymer solutions in elongational flows.[127] A solution containing a more polydisperse polymer sample has a wider range of constituent molecular masses, so that polymers relax over different

timescales and generate potentially strained inter-chain overlap.[42] Thus polymers fracture at various points along the backbone.

A-Alamry *et al*.[129] also conducted printing trials with a MicroFab print head with a nozzle orifice of diameter 50 μm and ejected drops at ~5 m s^{-1}, corresponding to strain rates of ~1×10^5 s^{-1}. The solutions containing polymers of low polydispersity showed no change in molecular weight distribution. With polydisperse polymers (PDI > 1.3), however, the molecular weight distribution shifted to lower molecular weight and broadened indicating random scission, as found for trials with the Dimatix print head.

Further insight into the factors affecting the degradation of polymers in solution when printed from a drop-on-demand ink-jet print head was supplied by McIlroy *et al*.[125], who modelled the polymers as FENE dumbbells. Values for $\dot{\varepsilon}_{crit}$ and $\dot{\varepsilon}_{deg}$ were calculated for a wide range of molecular weights and the fluid velocity was assumed to be three times larger than that of the ejected drops. For the Dimatix print head, polystyrene with M > 256 kDa would be expected to form fully extended conformations under the strain rates associated with the ligament. Crucially, however, the strain rates in the ligament were found to be less than $\dot{\varepsilon}_{deg}$ for molecular weights in the range trialled by A-Alamry *et al*.[129] The Dimatix print head features a sudden contraction and simulations by McIlroy *et al*.[125] found that such a geometry causes significant stretching of polymers at the nozzle exit. The strain rate at the nozzle exit $\dot{\varepsilon}_{noz}$ was compared against $\dot{\varepsilon}_{deg}$ to reveal that $\dot{\varepsilon}_{noz} > \dot{\varepsilon}_{deg}$ for M > ~250 kDa coinciding with the range of lower polydispersity samples printed by A-Alamry *et al*.[129] Central scission of chains is therefore a result of high strain rates inside the nozzle. Similar analysis for the MicroFab print head found that $\dot{\varepsilon}_{noz} > \dot{\varepsilon}_{deg}$ for M > ~500 kDa. McIlroy *et al*.[125] suggested the reason that A-Alamry *et al*.[129] did not observe central scission above this value was that the MicroFab print head does not feature a sudden contraction so that polymers do not become fully extended inside the nozzle.

A study into the response of polymers in a continuous ink-jet printing environment was carried out by Wheeler *et al*.[130] on a Domino A-series *plus* instrument using samples of polydisperse PMMA (PDI > 2) in solution. When the printer was run continuously with a semidilute PMMA solution with M_w = 468 kDa, the solids content increased over time, whilst polymer molecular weight decreased and PDI increased. However, no change in M_z was observed for a 90-kDa PMMA solution, indicating that a lower mass limit exists below which no degradation occurs, as seen in DOD apparatus.[129] Polymer scission for the 468-kDa PMMA solution was isolated as occurring in the pump, as opposed to at the print head.

4.3 A New Strategy: Emulsion Formulations

In Sections 4.1 and 4.2, the impact of polymers upon fluid dynamics under high-strain conditions was discussed. This section summarises the factors that make polymer solutions non-trivial to print and outlines how emulsion formulations provide the mechanisms to overcome the associated problems.

4.3.1 A Summary of the Problems with Printing Polymer Solutions

The ink-jet printing of solutions containing high-molecular-weight polymers is non-trivial (Section 4.2) with complex detachment behaviour even observed for drops emerging from millimetre-sized orifices (Section 4.1). A target application may require a large amount of a high-molecular-weight polymer to be printed onto a substrate and a number of considerations would need to be taken into account when designing the formulation: first, the optimum fluid properties for ink-jet printing are those for which $0.1 < Oh < 1$, placing limitations on the formulation viscosity and therefore polymer concentration (Section 4.2.1): polymers raise the solution viscosity in proportion to their concentration when dilute, with the rate of increase becoming larger above c^*.

Second, polymer solutions display a departure from Newtonian dynamics during drop detachment. Whilst a Newtonian fluid rapidly necks under capillary pressure and detaches (Section 4.1.1), long-lived filaments develop between the main drop body and the fluid in the orifice for polymer solutions in the dilute regime (Sections 4.1.1 and 4.2.2). The high strain rates that develop close to the Newtonian pinch point are sufficient to deform polymers from their equilibrium conformations into an extended conformation. The coil-stretch transition (Sections 4.1.2) for an unentangled polymer in solution is expected over a narrow range of strain rates calculable from the Zimm relaxation time. The unravelling of polymer chains introduces elastic character to the fluid which causes the rate of necking to become exponential (Section 4.1.3), delaying break off. The elastic filament also decelerates the main drop body (Section 4.2.2). The non-Newtonian behaviour becomes more severe with increasing molecular weight and concentration (Section 4.1.4), placing upper limits on the printability of polymer solutions (Section 4.2.3).

Third, the high strain rates experienced by polymers in the print head orifice or in associated pumps can cause polymer scission (Section 4.2.4). Fracture can either occur centrally as a result of polymers stretched at a critical rate in an extended conformation or randomly due to localised stress as a result of inter-chain entanglements. Degradation is unfavourable where control over the molecular weight is important for application.

4.3.2 Emulsions as a Strategy to Avoid the Coil-Stretch Transition

One strategy for depositing polymers would be to print very dilute solutions in order that significant non-Newtonian character is avoided. Whilst simple from a formulation perspective, multiple print head passes would be required in order to build up a significant layer of polymer, costing time and lowering efficiency. Additionally there is no protection against polymer scission. A better strategy involves dispersing solutions of high-MW polymers as the discontinuous phase of an emulsion in order to shield polymers from high strain rates, thus avoiding the coil-stretch transition, non-Newtonian detachment dynamics and polymer scission (Fig. 4.8). An investigation into the feasibility of using emulsion formulations to overcome the limitations of printing polymers in binary solution is presented hereafter.

The basic formulation of a polymer-containing emulsion requires dissolving the polymer in a good solvent and dispersing it into an aqueous surfactant solution. At equilibrium, surfactant molecules are present at the oil-water interface of the emulsified droplets. Any deformation of an emulsified droplet away from sphericity under strain leads to an increase in surface area and a concurrent decrease in surfactant surface excess Γ. If the deformation were held constant for sufficient time, surfactant would diffuse from the bulk and return the surface excess to its equilibrium value. The time τ_{dep} for a surfactant molecule to diffuse the depletion length Γ/c, where c is the bulk concentration is

$$\tau_{\mathrm{dep}} = \frac{\pi}{4D}\left(\frac{\Gamma}{c}\right)^2 , \tag{4.16}$$

where D is the diffusion coefficient.[131] For a typical surfactant like SDS at the c.m.c.,[132–134] $c \sim 8$ mM, $\Gamma \sim 3\times10^{-6}$ mol m^{-2} and $D \sim 0.4\times10^{-9}$ m^2 s^{-1}, giving $\tau_{\mathrm{dep}} \sim 10^{-4}$ s. In contrast, drop detachment at an ink-jet print head takes place on a much faster timescale at ~10^{-5} s. An emulsified droplet would therefore not be expected achieve equilibrium surface coverage by diffusion of surfactant from the bulk when deformed during the printing process. Given the timescales for diffusion and deformation, the number of surfactant molecules present at the oil-water interface can be assumed constant.

Emulsified droplets resist deformation when exposed to strain and the underlying physical mechanism is provided by the free energy, G, of the oil-water interface. The interfacial free energy can be simply expressed as

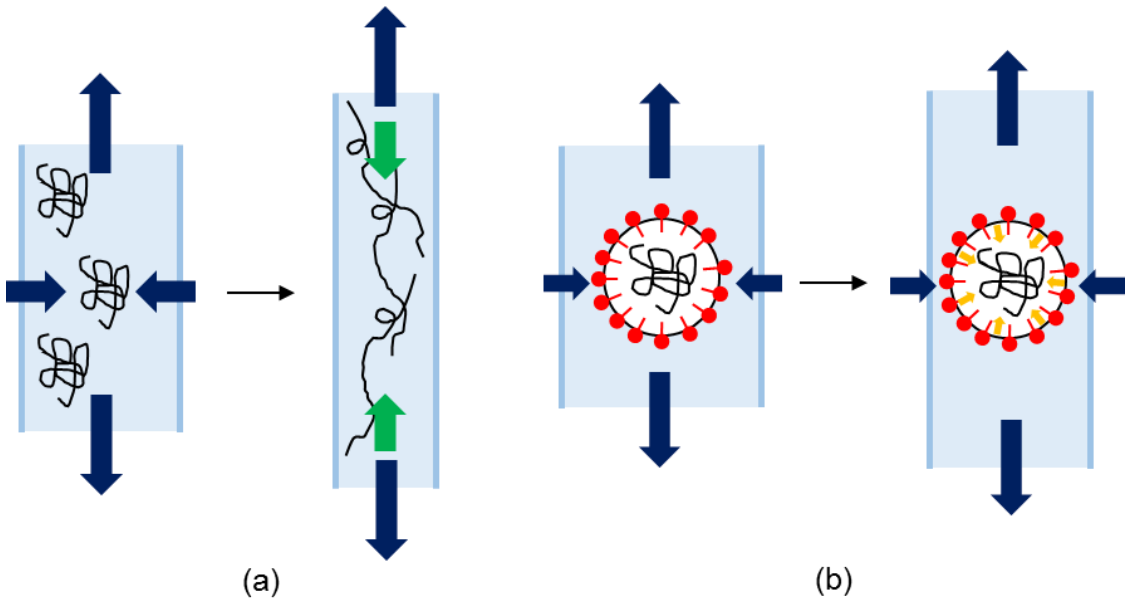

Figure 4.8. (a) Polymers in solution undergo the coil-stretch transition close to the Newtonian pinch point for a droplet emerging from an orifice; blue arrows show fluid motion. The fluid develops elasticity (green arrows) that causes an exponential reduction in radius. (b) Proposed behaviour of polymers encapsulated in emulsified droplets; the interfacial forces (orange arrows) prevent the coil-stretch transition and the drop detaches from the orifice as normal.

$$G = \gamma A, \tag{4.17}$$

where γ is the interfacial tension and A is the area of the interface. At constant temperature T and pressure p, the change in interfacial free energy when the dispersed droplet is deformed is then

$$\left(\frac{\partial G}{\partial A}\right)_{T,p,n} = \gamma + A\left(\frac{\partial \gamma}{\partial A}\right)_{T,p,n}, \tag{4.18}$$

assuming the number of surfactant molecules at the interface, n, is constant. The first term on the right-hand side of Eq. (4.18) is simply the interfacial tension. Creating new interface always comes at an energy penalty and the free energy is minimised when interfacial area is minimised. The interfacial tension therefore hinders the deformation of an emulsified droplet under strain and acts to return it to sphericity, where curvature is minimised.

The second term on the right-hand side of Equation (4.18) is known as the Gibbs elasticity, or alternatively as the surface dilational modulus. The interfacial tension between the oil and water phases is lowered by the presence of surfactant molecules. Upon deformation of an emulsified droplet, the surface area increases which lowers the surfactant surface excess. The timescales involved in ink-jet printing means that surfactant is unable to diffuse from the bulk and return the interface to equilibrium coverage whilst strain is active. The reduction in surface excess is concurrent with a rise

in the interfacial tension, giving the interface an “elastic” character. The Gibbs elasticity is a second energy penalty incurred upon increasing the surface area of an emulsified droplet on a short timescale and enhances the degree to which the interfacial tension is able to limit droplet deformation under strain. If the resistance to deformation exceeds the viscous stresses on the droplet then the droplet does not deform, the polymers experience little strain and the rheology of the fluid as it approaches pinch off is determined by the Newtonian character of the continuous phase. The ink can therefore be successfully printed.

4.4 Deformation of Drops under Straining Flows in the Fluid Matrix

Limiting the extent of discontinuous phase deformation during print processes is central to the success of using emulsions to facilitate the ink-jet printing of high-molecular-weight polymers. This section outlines models for the deformation of drops under the straining flow of a fluid matrix, discusses the impact of surfactant and viscoelasticity, and demonstrates the feasibility of using the interfacial forces of emulsified droplets to facilitate the printing of high-molecular weight polymers.

4.4.1 Deformation of Newtonian Drops under Weak Flow

Experimental and theoretical investigations into the deformation of spherical droplets have mainly focussed on two types of straining flow in the surrounding fluid matrix: plane hyperbolic flow and simple shear.[135,136] Plane hyperbolic flow corresponds to a stretching motion in the *x*-*y* plane and can be described by

$$u_x = \dot{\varepsilon}x, \quad u_y = -\dot{\varepsilon}y, \tag{4.19}$$

where $\dot{\varepsilon}$ is the strain rate and u_x and u_y are the velocity components along the *x*- and *y*-directions respectively. Simple shear is a stretch principally along the diagonal of the *x*-*y* plane with an additional rotation about the origin and can be described by

$$u_x = Gy, \quad u_y = 0. \tag{4.20}$$

Quantitative analysis of drop deformation behaviour was conducted by Taylor,[137,138] solving the steady-state balance of viscous and interfacial forces on the deformed droplet. The additional variables that are required to characterise the system comprise the viscosity of the fluid matrix, η, the viscosity of the drop, η', the undistorted radius of the drop, *r*, and the surface tension between the drop and the matrix, γ. The parameters are grouped into viscosity ratio λ, defined as

$$\lambda = \frac{\eta'}{\eta}, \tag{4.21}$$

and the capillary number *C*, defined as

$$C = \frac{\dot{\varepsilon}\eta r}{\gamma}. \tag{4.22}$$

Physically, the capillary number quantifies the relative magnitudes of viscous and interfacial forces. At low distortions the drop shape, *D*, is characterised through its half-length, L, and half breadth, B, according to

$$D = \frac{L - B}{L + B}. \tag{4.23}$$

A drop retains an almost spherical shape when $C << 1$ because the flow is weak compared with the surface tension. In this limit, Taylor[138] showed that *D* is linear in *C* according to

$$D = \frac{19\lambda + 16}{16\lambda + 16} C. \tag{4.24}$$

To test the validity of Equation (4.24), Taylor[138] designed and constructed instruments to generate model flows: for extensional flow, four cylinders were placed on the corners of a square and for simple shear flow, two parallel bands of cinema film were mounted on rollers (Fig. 4.9). The instruments were adjusted manually in order to keep drops at the correct position in the flows and images were captured after drops attained a steady state. Drops were observed to deform as prolate spheroids along the principle axis of strain. For neutrally-buoyant Newtonian drops in Newtonian suspending fluids (λ = 0.0003, 0.9 and 20) drop deformation was linear in both weak extensional and shearing flows. Deviations from linearity were manifested when $0.1 < D < 0.5$, depending on λ and flow type. Taylor also observed that in some flows the drop shape was not stable beyond a critical deformation D_c, corresponding to a critical capillary number C_c and strain rate $\dot{\varepsilon}_c$, resulting in the drop bursting. Drops with λ = 0.0003 were stable in highly deformed shapes in both extensional and shear flows and had large values of C_c. Upon increasing the drop viscosity to λ = 0.9, drops broke at lower degrees of deformation, corresponding to lower C_c. At λ = 20, the flow-dependent breakup was observed: in plane-hyperbolic flow, C_c was lower again, whilst in simple shear, C_c had increased and the drop deformed little. The stability of highly viscous drops to shear is a result of the greatest elongation taking place at 45° to the bands, after which material is swept back towards the line parallel to the bands, where there is no extension. In contrast, plane-hyperbolic flow only sweeps material in the direction of the greatest elongation, until eventually viscous forces overcome interfacial forces and the drop ruptures. Of the systems investigated by Taylor,

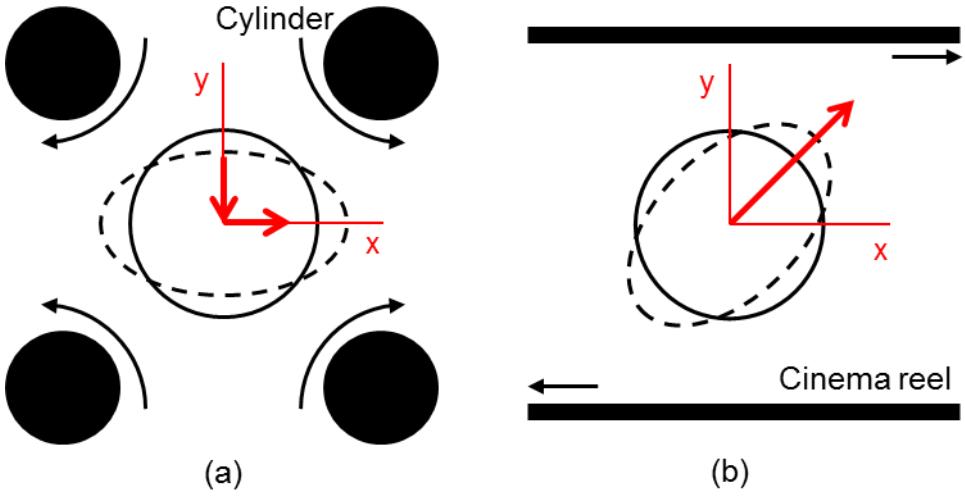

Figure 4.9. Schematic diagrams of the experimental apparatus implemented by Taylor[138] showing the coordinate systems and the drop deformation. (a) Extensional flow. (b) Shear flow.

the one for which $\lambda = 20$ is most relevant to printing polymer-containing emulsions, since $\lambda > 50$.

Bentley and Leal[139] designed a computer-controlled four-roll mill which allowed the drop position to be maintained far more reliably than for manual control, allowing much longer for the drop shape to equilibrate. The greater control also allowed flows with vorticity intermediate to plane-hyperbolic flow and simple shear to be investigated; increasing vorticity corresponds to increasing rotational character of the flow. Experiments[140] with the mill confirmed that D is linear in C for $C << 1$, as predicted by Eq. (4.24). Tretheway and Leal[141] demonstrated that Newtonian fluids with higher λ in extensional flow deviate from the linear C-D relationship at lower C, displaying higher D for a given C than fluids with lower λ (Fig 4.10). Bentley and Leal[140] found that the critical deformation D_c and critical capillary number C_c decreased with increasing λ in extensional flow for $\lambda < 1$ and was approximately constant for $\lambda > 1$ (Fig. 4.11); in shear flow C_c decreased with increasing λ for $\lambda < 1$, but increased with λ for $\lambda > 1$. The critical capillary number was always larger for simple shear than for plane-hyperbolic flow. Marked on Figure 4.11 is the range of λ relevant to printing polymer-containing emulsions. Under extensional flow, these droplets ($\lambda > 50$) have $C_c \sim 0.1$.

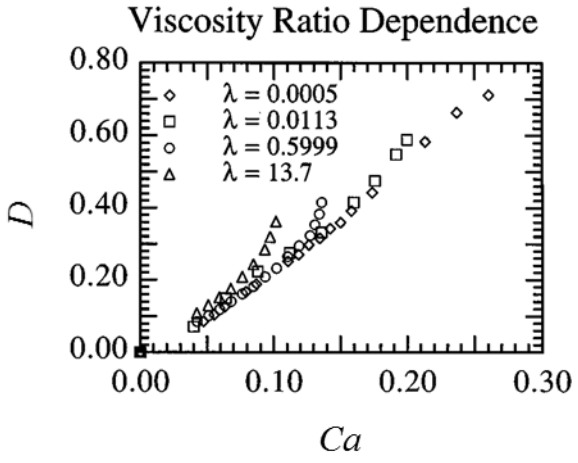

Figure 4.10. The drop deformation D as a function of capillary number Ca in extensional flow for Newtonian liquids suspended in a hydrophobic polymerised castor oil; λ is the ratio of the drop to the surrounding fluid. Reproduced with permission.[141] Copyright 1999, American Institute of Chemical Engineers (AIChE).

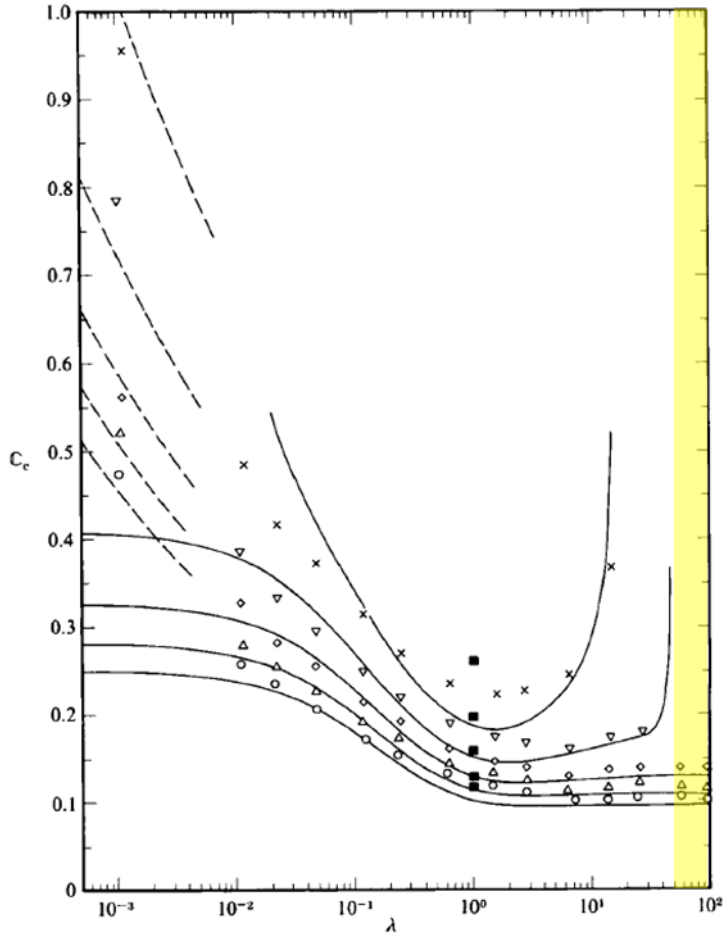

Figure 4.11. The critical capillary number C_c as a function of viscosity ratio λ for different flow types. Circles mark extensional flow and crosses mark near shear flow; the other data relates to flows that smoothly vary between these two limits. Marked in yellow is the range of λ for polymer-containing emulsions. B. J. Bentley and L. G. Leal, *J. Fluid Mech.*, 1986, **167**, 241, reproduced with permission.

For a concentrated polymer solution dispersed in an aqueous surfactant solution, $\lambda >> 1$, so that $D \sim C$. The elongational strain rate $\dot{\varepsilon}$ in a MicroFab print head with a nozzle orifice of 50 μm and a drop velocity of 2 m s^{-1} is ~10^5 s^{-1}. Assuming $\eta \sim 10^{-3}$ Pa s, $\gamma \sim 10^{-2}$ N m^{-1}, $r \sim 10^{-6}$ m and $\dot{\varepsilon} \sim 10^5$ s^{-1}, $C \sim 10^{-2}$ and the extent of deformation is small. For an industrial print head the strain rate is higher: $\dot{\varepsilon} \sim 10^6$ s^{-1}. The degree of deformation is therefore larger, with $C \sim 10^{-1}$. In both cases, the degree of deformation is modest and the interfacial forces will prevent encapsulated polymer molecules from undergoing the coil-stretch transition. As stated earlier, the Gibbs elasticity will reduce the degree of deformation further.

For the industrial print head, the capillary number under jetting conditions is similar to C_c. The model of deformation produced by Taylor, Eq. (4.24), gives the steady-state deformation of a droplet in a straining fluid matrix. The model therefore does not incorporate the effect of the Gibbs elasticity, which only appears in the time-dependent

problem. The Gibbs elasticity has the effect of reducing the degree of deformation, so that Eq. (4.24) will overestimate the departure from sphericity. Consequently, droplets are expected to have higher C_c than observed in the steady-state case.

4.4.2 Drop Deformation in the Presence of Surfactants

The deformation of a drop suspended in a straining fluid is modified by the presence of surfactant at the interface: first, surfactants change the mean interfacial tension, thus altering the stresses normal to the interface. Second, variations in interfacial concentration of surfactant give rise to Marangoni stresses that act tangentially to the interface.

Stone and Leal[142] considered theoretically the impact of surfactant on the deformation of a neutrally-buoyant Newtonian drop in an extensional flow of an immiscible Newtonian fluid. The surfactant was assumed insoluble in either phase so that it resided exclusively at the interface and was not subject to transfer to or from the bulk. The reduction of the interfacial tension by surfactant was modelled using a linear equation of state, which hold in the limit of very low Γ:

$$\gamma = \gamma^* - \Gamma RT, \tag{4.25}$$

where γ* is the interfacial tension between the pure fluids. The dimensionless parameter β gives a measure of the impact of the degree of surface coverage on the interfacial tension:

$$\beta = \frac{\mathrm{d}\gamma}{\mathrm{d}\Gamma}\left(\frac{\Gamma_0}{\gamma^*}\right) = \frac{RT\Gamma_0}{\gamma^*}. \tag{4.26}$$

where Γ_0 is the uniform surface excess in the absence of flow. The balance between convection of surfactant towards the drop extremes and surface diffusion is given by δ, which is the ratio of the surface Péclet number, Pe_s to the capillary number:

$$\delta = \frac{Pe_s}{C} = \frac{\gamma^* r}{\eta D_s}. \tag{4.27}$$

where D_s is the surface diffusivity. Assuming small deformation and nearly uniform surfactant concentration over the interface,

$$D \approx \frac{3C_0 b_r}{4 + C_0 b_r}, \tag{4.28}$$

where C_0 is the capillary number in the absence of surfactant and

$$b_r = \frac{5}{4}\frac{(16 + 19\lambda) + 4\beta\delta/(1-\beta)}{10(1+\lambda) + 2\beta\delta/(1-\beta)}. \tag{4.29}$$

Numerical studies by Stone and Leal[142] where $\lambda = 1$ and C_0, δ and β were varied found that the surfactant convection and dilution altered the steady-state deformation of the drops compared with drops of uniform surfactant concentration at the initial

equilibrium level (Fig. 4.12a). In the limit of large δ convection dominates: surfactant is swept towards the tips of the drop, lowering the interfacial tension and increasing the deformation (Fig. 4.12b). In the limit of low δ dilution dominates: the surfactant maintains uniform coverage, but any deformation reduces the number of molecules per unit area, raising the interfacial tension and lowering the degree of deformation (Fig. 4.12c). Convection and dilution effects are inherently coupled: surfactant dilution and diffusion retards the reduction in interfacial tension produced by convection, reducing drop deformation. Milliken *et al.*[143] found theoretically that surfactant convection and dilution had the greatest impact on deformation for low λ and that the effects are difficult to resolve at $\lambda > 10$. Thus were surfactant dilution or convection to occur during the ejection of an emulsion formulation ($\lambda > 50$) from an ink-jet print head, the impact would be negligible.

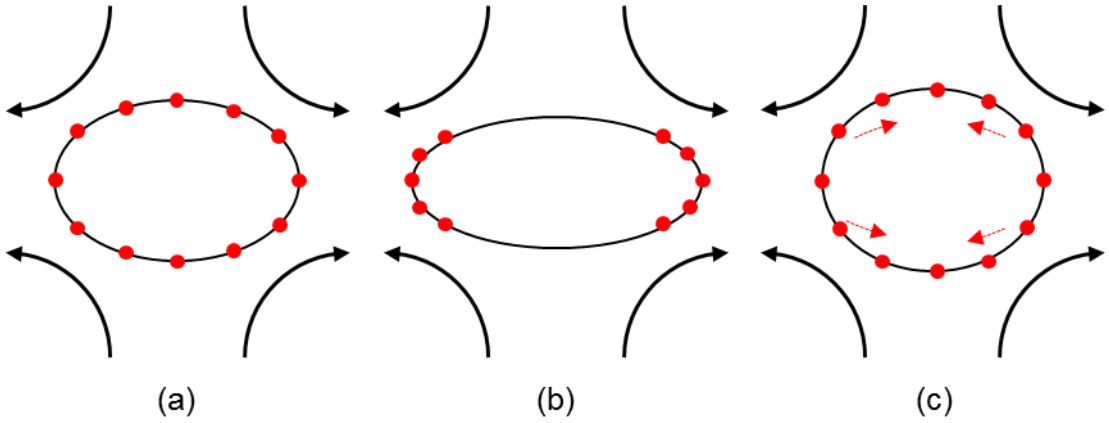

Figure 4.12. Schematic diagrams of the impact of surfactant upon the degree of deformation under flow. (a) Assuming surfactant is evenly distributed. (b) When surfactant convection is dominant, showing enhanced deformation versus the case of even surfactant distribution. (c) When surfactant dilution is dominant, showing reduced deformation versus the case of even surfactant distribution.

4.4.3 Drop Deformation of Non-Newtonian Fluids

Tretheway and Leal[141] carried out a study on the effects of introducing viscoelastic character to the drops being deformed by the extensional flow of castor oil. Drops of ethylene-glycol solutions of polyacrylamide PAM (MW = 15000 kDa) displayed similar behaviour at low shear rate to Newtonian fluids of equivalent low-shear viscosity (Fig. 4.13). At higher shear rates, however, the polymer solution deformed to a larger extent at a given C than the Newtonian drop. The polymer solution also exhibited larger C_c and D_c than the Newtonian drop. The deviation in behaviour of the two systems occurred when C corresponded to Wi ~ 1: the point at which viscoelastic character becomes manifested. The deformation response with rising capillary number for different PAM solutions was the same regardless of concentration, and showed little deviation from that of pure

ethylene glycol. The impact of an increase in λ with the addition of polymer, which tends to increase D at a particular C, was therefore almost exactly cancelled by viscoelastic effects, which tends to reduce D with increasing drop viscoelasticity.

Tretheway and Leal[141] also investigated the behaviour of aqueous PAM solutions. The PAM solutions and pure water displayed tip streaming at elevated strain rates suggesting the presence of a surfactant, though the authors were not able to suggest the source of the impurity. The deformation behaviour was compared against Newtonian fluids with the same low-shear viscosity. Pure water showed enhanced D at a given C versus the Newtonian fluid. A PAM solution at low polymer concentration (c = 0.05 %wt) showed the same trend with smaller deviations suggesting that the surfactant enhancement to deformation was overcoming the viscoelastic reduction. At increased polymer concentration (c = 0.25 %wt and 1 %wt) the reverse was observed, with the drop showing lower D at a given C than the equivalent Newtonian fluids, indicating the dominance of polymer effects over surfactant effects. The impact of the polymers was observed once the strain rate corresponded $Wi > 1$.

During the jetting of a polymer-containing emulsion, the viscoelasticity of the dispersed drops reduces the deformation versus a Newtonian drops when $Wi > 1$. Therefore, Eq. (4.24) is an overestimate.

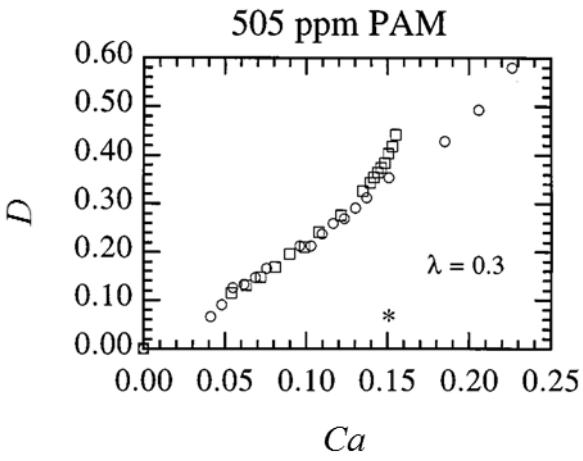

Figure 4.13. The deformation D as a function of capillary number Ca for drops suspended in a hydrophobic polymerised castor oil and subjected to extensional flow. (squares) 505 ppm polyacrylamide solution (MW = 15000 kDa) in ethylene glycol. (circles) a Newtonian liquid of equivalent viscosity ratio. The asterisk marks Wi = 1 for the polymer. Reproduced with permission.[141] Copyright 1999, American Institute of Chemical Engineers (AIChE).

4.5 Fundamentals of Emulsion Science

Having demonstrated that the interfacial forces of emulsified drops are able to shield encapsulated polymers from the high strain rates involved in ink-jet printing, this section outlines the fundamentals of emulsion science.

4.5.1 An Introduction to Emulsions

An emulsion is defined as a system comprising two immiscible fluids, with one dispersed inside the continuous matrix of the other.[144] Typically in a macroemulsion (hereafter "emulsion"), one of the fluids has an aqueous character (the "water" phase) and the other has an oleic character (the "oil" phase). Emulsions are therefore commonly designated oil-in-water (O/W) or water-in-oil (W/O) systems depending on which fluid forms the continuous phase. The length scale of emulsified droplets ($>10^{-6}$ m) is larger than the wavelength of light so that light scatters on passing through samples, leading to optical opacity at high concentrations or a cloudy appearance at low concentrations.[145] The dispersion of one phase inside the other comes at an energy penalty, as shown by Eq. (4.17), since it is facilitated by a vast increase in surface area and an increase in the number of the relatively unfavourable surface interactions. Consequently, an emulsion resulting from the agitation of two pure immiscible liquids is unstable and the droplets rapidly coalesce since in the phase-separated state interfacial area is minimised.[144]

Long-term stability may be conferred to emulsions by the inclusion of emulsifiers and stabilisers in the formulation.[145] An emulsifier modifies the properties of the oil-water interface, thus facilitating emulsion formation and stabilisation, whilst a stabiliser imparts long-term stability. Low-molecular-weight amphiphiles are effective emulsifiers and high-molecular-weight hydrocolloids are effective stabilisers. Finely divided particles can also be used to stabilise emulsions.[146] Emulsions are only kinetically stable since the most thermodynamically stable state is given when phase-separated.[145]

The same oil-water-surfactant system may form an O/W or a W/O emulsion depending upon the relative proportions of each component and the temperature. Bancroft's rule states that the emulsion phase in which the surfactant is more soluble forms the continuous phase, following from general observations. The rule, however, is not universally true, with an example being the aerosol-OT-water-heptane system at room temperature: despite higher solubility in heptane than water, an O/W emulsion is observed for a 50:50 water-heptane emulsion by volume. The rule fails to take into account the difference between the solubility of the surfactant in binary solution with each phase individually and the partitioning of surfactant in the oil-water-surfactant system.

Additionally, the differing solubilities of surfactant monomer and aggregates in the each phase is neglected. The phase that forms the continuous phase is given by the phase into which the aggregates spontaneously partition.[144]

Microemulsions are distinct from macroemulsions because the former are thermodynamically stable. Consequently, the dispersions form spontaneously and will not phase separate over time. Microemulsion droplets have diameters of the order 10^{-8} m so that formulations appear transparent. The surfactant has a distinct monomer solubility limit in each of the aqueous and oleic phases, above which additional surfactant forms aggregates (the critical micelle concentration). A number of different equilibrium microemulsion states are possible depending on the particular oil, water and surfactant chosen, and their relative ratios: an aqueous continuous phase containing O/W droplets in equilibrium with an excess oleic phase containing monomeric surfactant (Winsor I); an oleic continuous phase containing W/O droplets equilibrium with an excess aqueous phase containing monomeric surfactant (Winsor II); a surfactant-rich phase in equilibrium with both an aqueous and an oleic phase (Winsor III). The type of microemulsion formed additionally depends on the temperature and by raising or lowering the temperature, the formulation can move between the Winsor I and II states, via the Winsor III state.[144]

4.5.2 Principles of Emulsion Formation

Emulsion manufacture fundamentally requires the disruption of two immiscible fluids in contact such that micrometre-scale droplets of one become suspended in the other. The process has a large free energy cost due to the large increase in interfacial area compared with the equilibrium phase-separated state. Fine emulsified droplets are produced by the successive breakdown of larger-scale drops. The Laplace pressure, Δp, (Eq. (2.4)) quantifies the difference in pressure that exists between the inside and outside of a droplet. For a sphere, the radii of curvature are equal to the droplet radius r, so that Eq. (2.4) simplifies to

$$\Delta p = \frac{2\gamma}{r}. \tag{4.30}$$

The deformation of droplets away from sphericity under agitation and the division of droplets into smaller species is accompanied by an increase in curvature, and hence Δp. Further, the successive division of droplets requires progressively more stress as the length-scale decreases since the Laplace pressure depends inversely upon the droplet radius. The sample must therefore be exposed to highly vigorous agitation in order to impart sufficient energy to produce very fine emulsified drops.[147]

The stresses that divide the discontinuous phase are generated externally to the sample and act upon suspended droplets via the continuous phase. In unbounded flow, disruption occurs under the movement of the continuous phase through viscous and inertial forces; apparatus boundaries have little effect. Viscous forces act parallel to the interface to deform drops and cause shear stresses to develop between the two phases. Viscous deformation occurs under laminar flow, or turbulent flow if eddies in the fluid are larger than the drop size. If the eddies are of a similar size to the drops, inertial forces can cause the dispersed phase to divide. Inertial deformation occurs through pressure fluctuations parallel to the surface. Lower intensity emulsification methods like static mixers, stirrers and rotor-stator mixers (*e.g.* "Ultra-Turrax") emulsify using viscous-laminar, viscous-turbulent and inertial-turbulent flows. Several higher intensity emulsification strategies exist: colloid mills work on the rotor-stator principle and disrupt through viscous forces; high-pressure homogenisers produce turbulent flow when a pressurised system is decompressed; ultrasonic processing produces pressure fluctuations that result from cavitation.[147]

Other emulsification methods take place in bounded flow, where apparatus dimensions are similar to size of the discontinuous phase. Membrane emulsification is the process by which the discontinuous phase is injected into the continuous phase.[147]

Drops with clean interfaces tend to coalesce when in contact so that interfacial area, and thus free energy, is minimised. An emulsification processes must therefore impart significant amounts of energy over a time period that is fast relative to coalescence such that there is a net decrease in the size of dispersed particles. The addition of surfactant is conducive to emulsification because it lowers the interfacial tension between the phases and imparts stability against immediate coalescence. Lowering the interfacial tension is advantageous for two reasons: first, the amount of free energy required to produce additional interfacial area is reduced, making emulsification more efficient. Second, the Laplace pressure is reduced so that the stresses required to deform the dispersed phase are lower. Consequently, smaller emulsified drops can be produced using the limiting agitation strength of a particular piece of equipment.[147] A surfactant should help generate emulsified droplets that are smaller than the print head orifice.

Surfactant provides stability against coalescence: the approach of two droplets partially covered with surfactant induces a flow of the continuous phase from the intervening volume, exerting shear on the droplet interfaces (Fig. 4.14). The shear acts to sweep surfactant at the interfaces, generating an opposing stress that acts to slow the rate of droplet approach. If the rate of approach is sufficiently slow and the opposing stress

acts for sufficient time, the driving force bringing the drops together might abate and the drops can move apart. Thus coalescence is avoided.[147]

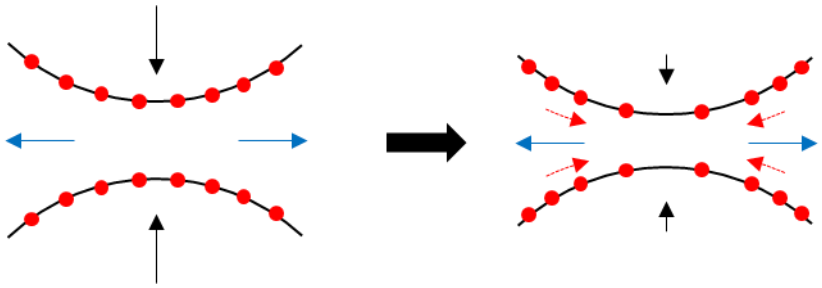

Figure 4.14. Schematic diagram of surfactant-imparted stability to coalescence in emulsions. Outward flow of fluid between the droplets sweeps surfactant and induces Marangoni flows at the drop surfaces that slows the rate of approach.

4.5.3 Emulsion Stability and Degradation

Thermodynamically unstable emulsions proceed via a number of mechanisms towards the phase-separated state, where the interfacial area is minimised. The processes have in common the generation of larger dispersed phase drops at the expense of smaller ones. The main forms of emulsion degradation include (1) flocculation and coalescence, where interaction potentials can bring drops into closer proximity, (2) creaming and sedimentation, where a phase density difference causes collection under gravity, and (3) Ostwald ripening, where large drops grow and small drops contract.[144]

4.5.3.1 Flocculation and Coalescence

The stability of an emulsion towards degradation by flocculation and coalescence is controlled by the balance of attractive and repulsive interactions between droplets.[148] The attractive forces experienced derive from dipoles across drops that arise from transient fluctuations in electron distribution, known as dispersion forces.[52] The oscillating dipole on one droplet has an associated electric field and is able to polarize a neighbouring droplet. The attractive interaction acts to draw the two droplets together. The two-body additive dispersion energy W_{disp} for a pair of planar surfaces is given by

$$W_{\text{disp}}(D) = -\frac{A}{12\pi D^2}, \tag{4.31}$$

where A is the Hamaker constant and D is the distance between the surfaces.

If ions are adsorbed to the interfaces of the emulsified droplets, a repulsive interaction exists between them resulting from the formation of an electric double layer. The counterions to the ions adsorbed at the interface are distributed in the continuous phase and have a concentration that decays exponentially with distance from the interface. When two drops approach, counterions are moved closer to the surfaces which, whilst

electrostatically favourable, increases ion concentration at entropic cost. An osmotic pressure acts to dilute the counterions in response. The electric double layer interaction energy W_{dl} between two planar surfaces is given by

$$W_{\mathrm{dl}}(D) = -\frac{2\sigma^2}{\varepsilon_0 \varepsilon_r \kappa} e^{-\kappa D}, \tag{4.32}$$

where σ is the surface charge, ε_0 is the permittivity of free space, ε_r is the relative permittivity of the continuous phase and κ is the inverse Debye length, r_D. The inverse Debye length is defined as

$$\kappa = (r_D)^{-1} = \left(\frac{2e^2 \sum_i n_i {z_i}^2}{\varepsilon_0 \varepsilon_r kT}\right)^{\frac{1}{2}}, \tag{4.33}$$

where *e* is the fundamental charge and *n* is the molar concentration of the i^{th} ion of charge *z*. The Debye length r_D defines the length over which drops interact electrostatically.[52]

The model of colloidal stability given by the sums of Eqs. (4.31) and (4.32) is named DLVO theory, after Derjaguin and Landau,[149] and Verwey and Overbeek.[150] The two-body potential energy for a pair of emulsified droplets is dominated by W_{disp} at short and long separations, giving rise to a primary and secondary minima respectively (Fig. 4.15).[148] A droplet residing in the primary minimum is able to coalesce, whilst the secondary minimum corresponds to a flocculated state. At intermediate separations a primary maximum exists, resulting from W_{dl}.

A droplet on the approach to another will possess translational energy of the order *kT* and the relative size of the peaks and troughs in the interaction potential dictates emulsion stability towards flocculation and coalescence. If the secondary minimum is small compared with *kT* and the primary maximum large then the emulsion is stable as osmotic pressure keeps the drops apart and thermal energy is sufficient to prevent flocculation. If the secondary minimum has a depth of a few multiples of *kT*, the thermal energy might be insufficient to overcome the attractive forces, preventing the drops from moving apart again. The drop aggregates are termed "flocs" and are associated drops separated by a layer of fluid with osmotic pressure preventing close contact and coalescence. If the primary maximum is a few multiples of *kT* or non-existent, the drops approach each other irreversibly and coalesce.

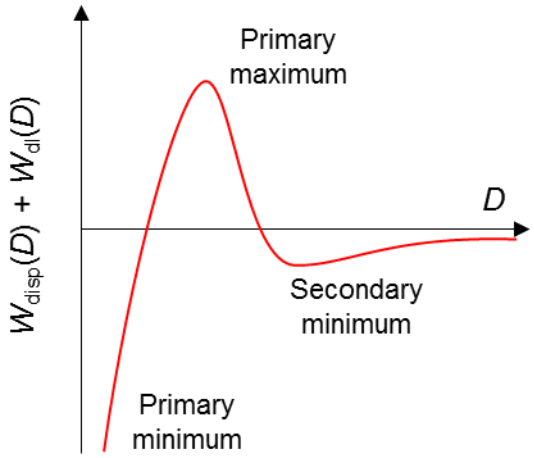

Figure 4.15. Schematic diagram of the interaction potential according to the DVLO model of colloidal stability. $W_{disp}(D)$ is the dispersion energy, $W_{dl}(D)$ is the double-layer repulsion energy and D is the separation of the two bodies.

A simple strategy for improving the stability of an emulsion ink towards flocculation and coalescence is to increase the strength of W_{dl}, by increasing the droplet surface charge, reducing the ionic strength of the continuous phase or by reducing the relative permittivity of the continuous phase.[148] A charged surfactant is therefore advantageous for the stability of emulsion inks against coalescence.

Flocculation may also be induced under different mechanisms by polymers in the formulation. The first mechanism is bridging flocculation (Fig. 4.16a) and occurs when polymers are able to adsorb to the emulsified droplet interface. When two droplets approach each other closely, polymer adsorbed on one of the bodies may also adsorb to the interface of the other, forming a bridge and binding the centres together. For bridging flocculation to occur a number of conditions must be met: first, the interfaces must not be completely covered by adsorbed polymer so that sites are available for binding. Second, the polymer must be sufficiently surface active to displace adsorbed surfactant. Third, the polymer radius of gyration must be long enough to allow binding at distances greater than the electric double layer.[148]

The second mechanism is depletion flocculation (Fig. 4.16a) and is active for polymers that do not adsorb at the droplet interface. A polymer in dilute solution approximates to a sphere of radius R_g, placing a geometrical constraint on how close it may approach emulsified droplets. Consequently an excluded volume exists around droplets in which polymer does not reside. Depletion flocculation is driven by the fact that the overlap of excluded volumes by different emulsified droplets releases solvent to dilute the polymer.[148]

The addition of a polymer to the continuous phase of an emulsion ink to optimise the viscosity for jetting, could cause flocculation.

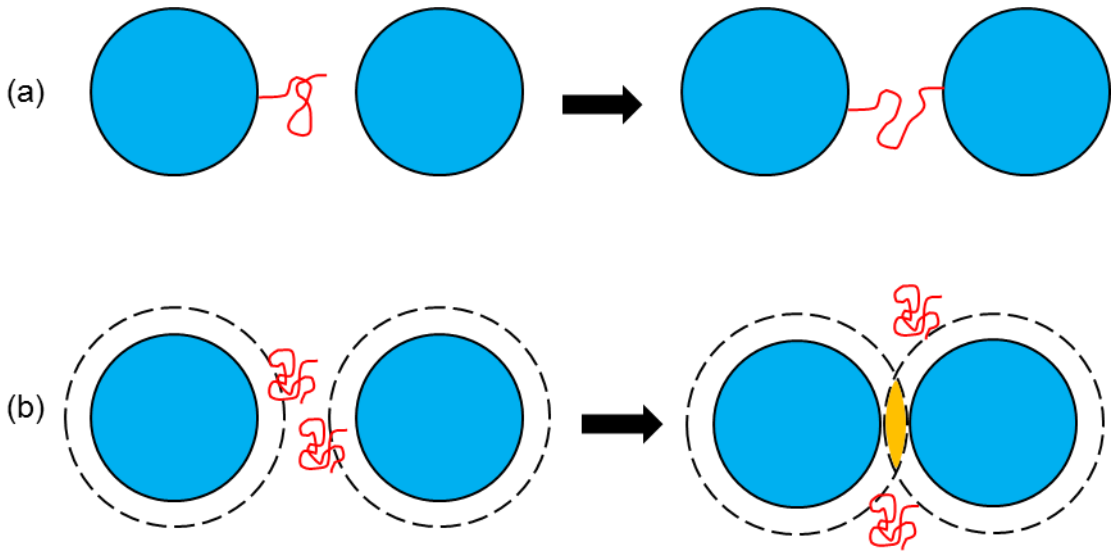

Figure 4.16. Schematic diagrams of polymer-induced flocculation. (a) Bridging flocculation. (b) Depletion flocculation.

4.5.3.2 Creaming and Sedimentation

A difference in density between the continuous and discontinuous phases produces a buoyancy force F_{buoy} on the emulsified droplets:

$$F_{buoy} = \frac{4}{3}\pi r^3(\rho_c - \rho_d)g, \tag{4.34}$$

where g is acceleration due to gravity, r is the drop radius, ρ_c is the density of the continuous phase and ρ_d is the density of the discontinuous phase. If $\rho_c > \rho_d$, $F_{\text{buoy}} > 0$ and droplets migrate towards the top of the container in a process known as creaming. In contrast, if $\rho_c < \rho_d$, F_{buoy} is < 0 and drops tend to aggregate or "sediment" at the bottom of the container. Typically, creaming is observed in O/W emulsions whilst sedimentation is observed for W/O emulsions, though it depends on which phase is the more dense. Emulsions appear opaque due to the scattering of light by the micrometre-sized droplets. A creaming formulation develops a transparent layer at the bottom of the container corresponding to a severe depletion of the discontinuous phase. The boundary between the opaque and transparent layers moves upwards over time as the droplets collect at top of the container. A sedimenting sample shows the same behaviour, except the clear phase develops at the top of the container and the boundary moves down over time. The speed v of migration of an isolated hard sphere is given by Stokes' Law:

$$v = \frac{2(\rho_c - \rho_d)gr^2}{9\eta_c}, \quad (4.35)$$

where η_c is the viscosity of the continuous phase.[144]

Creaming and sedimentation do not alter the droplet size distribution and can be reversed by agitation[144] but the collection of the dispersed phase into a layer at the top or bottom of the container impacts the rate at which other degradation processes occur.[148] The increased droplet concentration in the layer reduces the average droplet separation so that droplets encounter one-another more frequently. The speed at which flocculation and coalescence occurs will therefore be higher than if the droplets were dispersed uniformly. Similarly, Ostwald ripening can occur on a faster scale since molecules that make up the discontinuous phase have to travel less far through the continuous phase in order to collect in larger droplets.

Considering Eq. (4.35), the strategies for reducing the rate of creaming or sedimentation in an emulsion ink are several: first, reduce the size of the dispersed phase. Since $v \propto r^2$, a smaller scale discontinuous phase has a large impact upon the creaming/sedimentation rate.[148] Second, reduce the difference in density between the phases. Co-solvents can be included in the formulation so that the emulsified droplets are neutrally buoyant. Third, increase the viscosity of the continuous phase through viscosity modifiers such as polymers. A disadvantage of the inclusion of polymers is the potential for generating flocs through depletion flocculation, increasing effective r and enhancing the creaming or sedimentation rate.

4.5.3.3 Ostwald Ripening

Ostwald ripening is the process whereby larger emulsified droplets grow over time, whilst smaller species shrink.[144] The Kelvin equation[151] states that the solubility of the material in a dispersed drop c_r in the continuous phase is a function of the droplet radius r:

$$c_r = c_\infty \exp\left(\frac{2\gamma V_m}{rRT}\right), \quad (4.36)$$

where c_∞ is the solubility in a system containing only a planar surface, γ is the interfacial tension of the droplet and V_m is the molar volume of the dispersed fluid. The solubility of material in small emulsified drops in the continuous phase is thus larger than that of larger droplets and material from the former tends to diffuse through the continuous fluid and condense at the latter, decreasing the overall surface area.

Lifshitz and Slyozov[152] produced a model to describe the rate of Ostwald ripening over time t:

$$\frac{\mathrm{d}(r_c{}^3)}{\mathrm{d}t} = \frac{8c_\infty \gamma V_\mathrm{m} D}{9RT}, \tag{4.37}$$

where D is the diffusion coefficient of the dispersed phase molecules in the continuous phase and r_c is the critical radius: the radius at a given time above which droplets grow and below which droplets shrink. Aspects of the theory were validated experimentally by Kabalnov and co-workers,[153] who were able to observe the change in drop size as oil condensed from a saturated solution. The cube of the average drop radius $\bar{r}$ increased linearly with time and the growth rate of individual drops was followed to show that r_c coincides with $\bar{r}$. The dispersed phase size distribution, when plotted as a function of $r/\bar{r}$, was independent of time.

The addition of a species that is insoluble in the continuous phase into the dispersed phase provides a way for emulsions to become stabilised to Ostwald ripening.[154] The insoluble component is unable to diffuse through the continuous phase which, in the absence of coalescence, fixes the number of droplets in the system.[144] Consequently, the transfer of the more soluble component from small to large droplets under Ostwald ripening raises the concentration of the insoluble species in the smaller drops, lowering the local chemical potential of the discontinuous solvent. Ostwald ripening ceases when the Laplace pressure difference between the smaller and larger droplets is balanced by the difference in chemical potential of the discontinuous solvent therein.

Kabal'nov *et al.*[155] showed that if the initial concentration of the insoluble component is high, the size distribution of droplets undergoes little change before equilibrium is reached (Fig. 4.17a). If, however, the insoluble species is of low initial concentration, the drops are unable to achieve equilibrium. Initially Ostwald ripening proceeds as if the insoluble species were not present but the fine particles are unable to disappear, resulting in a bimodal size distribution developing. The coarser particles then continue to grow under regular Ostwald ripening dynamics, whilst the fine particles grow at the expense of the coarse particles.

Evidence of Ostwald ripening was observed for emulsion inks. As the polymer was not soluble in the continuous phase, the number of centres was fixed. The smallest drops (~1 μm) attained a stable size, whilst the larger drops grew over time to 10s of microns in diameter (see Section 4.8).

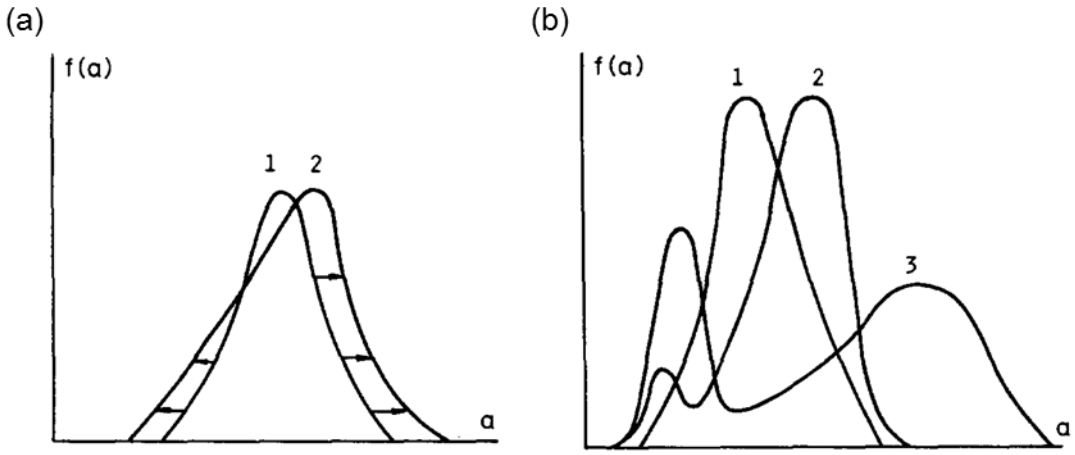

Figure 4.17. The evolution over time of the size distribution for a dispersion of emulsified drops containing an insoluble component. (a) The insoluble component is present at high concentration, leading to an equilibrium distribution. (b) The insoluble component is present at low concentration, leading to a bimodal distribution the does not attain equilibrium. Reprinted from A. S. Kabal'nov, A. V. Pertzov and E. D. Shchukin, *Colloids and Surfaces*, 1987, **24**, 19–32. Copyright 1987, with permission from Elsevier.

4.6 Materials and Procedures

Polystyrene kindly supplied by Dr. L. Hutchings (Durham University, UK). Particulate material was removed by dissolving the polystyrene in toluene and filtering the solution. The polymer was recovered through dropwise addition to methanol (Fisher, AR), followed by filtration. Residual solvent was removed under vacuum at 70°C until the mass no longer changed. The polystyrene was characterised by gel-permeation chromatography (GPC) as having M_n = 549 kDa and polydispersity index, PDI = 1.06. GPC experiments were run on a Viscotek TDA 302 (Malvern) using samples of concentration 1 mg mL^{-1} in THF (Fisher, Chromatography GPC grade) and calibrated against linear polystyrene standards.

The discontinuous phase precursors were polymer solutions in toluene (*Fisher*, AR grade), anisole (*Sigma-Aldrich*, 99%), methyl benzoate (*Acros Organics*, 99%) or diethyl phthalate, DEP (*Sigma-Aldrich*, 99.5%); the structures are given in Figure 4.18. Whilst all are good solvents for polystyrene, they differ significantly in density ρ, gas-phase diffusivity D and vapour pressure p (Table 4.1). Polymer solutions were prepared by mass and equilibration was ensured by gentle agitation overnight.

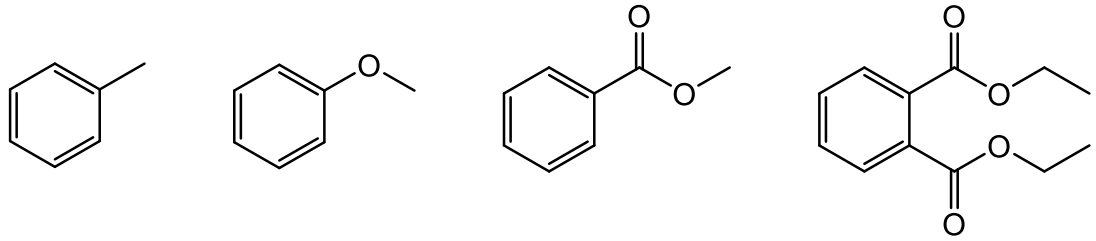

Figure 4.18. The chemical structures of (a) toluene, (b) anisole, (c) methyl benzoate and (d) diethyl phthalate.

TABLE 4.1. The vapour pressure, *p*,[64] the vapour diffusion coefficient in air, *D*,[76,77] and the liquid density of the fluids used to formulate emulsions at 293 K.

	p / kPa	D / (10^{-5} m^2 s^{-1})	ρ / (g mL^{-1})
Water	2.3	2.43	1.00
Toluene	2.9	0.78	0.87
Anisole	0.34	0.75	1.00
Methyl Benzoate	0.034	0.69	1.08
Diethyl Phthalate	4×10^{-5}	0.53	1.12

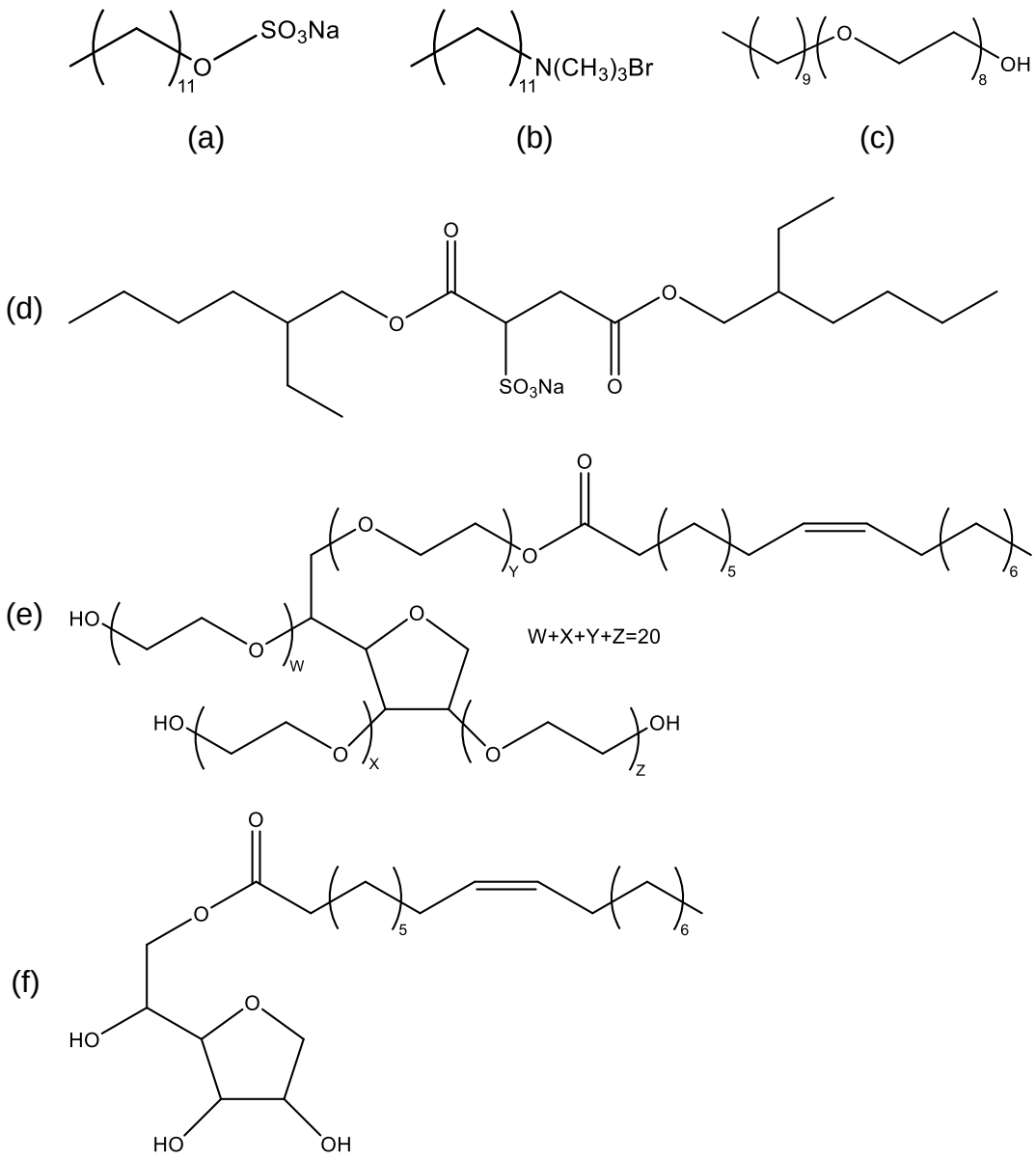

Figure 4.19. The chemical structures of (a) SDS, (b) C_{12}TAB, (c) $C_{10}E_8$, (d) AOT, (e) Tween 80 and (f) Span 80.

In most cases, the continuous phase was an aqueous surfactant solution. The surfactants trialled were sodium dodecylsulphate SDS (*Sigma-Aldrich*, >99.0%), sodium dioctyl sulphosuccinate, AOT (*Acros Organics*, 96%), dodecyltrimethylammonium bromide, C_{12}TAB (*Alfa Aesar*, 99%) and octaethylene glycol monodecyl ether, $C_{10}E_8$ (Nikko Chemicals); the structures are given in Figure 4.19. Mixtures of PEG-20 sorbitan monooleate, Tween 80 (*Sigma-Aldrich*) and sorbitan monooleate, Span 80, (*Fluka Analytical*) were also trialled as emulsion stabilisers (see Fig. 4.19), with the former administered in the aqueous phase and the latter administered in the oleic phase.

Emulsions were prepared by adding the continuous and discontinuous phase precursors to a 6-mL PTFE beaker. For polymer-free emulsions, formulations were

readily prepared by volume. For polymer-containing formulations, however, compositions were determined by mass since polymer solutions tended to cling to container walls as a result of viscosity, making the transfer of a specific volume difficult. Compositions are reported in terms of the concentrations of polymer and surfactant in the appropriate emulsion precursors and in terms of the total mass fraction φ_w or volume fraction φ_v of discontinuous phase. A coarse initial mixing of the two phases was achieved by magnetic stirring, so that the oil phase was suspended in the surfactant solution. Emulsification was then carried out with the ultrasonic horn USH (*Sonics*, VC505) equipped with a 3-mm stepped microtip. The USH resonates at 20 kHz and can be operated with a minimum amplitude of 22%. The use of a microtip limits the maximum amplitude to 40%. Typically for polymer-free emulsions, processing at 25% amplitude for < 30 s was sufficient. For polymer-containing emulsions, however, sequential processing at 25% and 40% amplitude was often required to give a discontinuous phase sufficiently smaller than the print head orifice. The USH was used in bursts of up to a minute and the formulation was stirred and recovered from the beaker walls in the intervening periods. To measure the size of the dispersed phase drops in the emulsions, aliquots were sandwiched between two coverslips and imaged on the printing rig under illumination from LED 1 (see Fig. 2.5). Emulsions were printed onto hydrophobised substrates produced in the manner described in Section 2.1.

Ultrasound is known to lead to polymer degradation[156] so the effect of preparing emulsions with the USH was investigated. A formulation comprising 9.5-%wt polystyrene solution in methyl benzoate (φ_w = 0.4) and 14.8 mM SDS was emulsified using the USH for 2 min at 25% amplitude, followed by 1 min at 40% amplitude. The polymer extracted from the formulation had a reduced M_n at 419 kDa and an increased polydispersity at 1.21.

Rheological measurements were made on an AR 2000 (TA Instruments) using a cone-and-plate geometry with a 60-mm-diameter cone. The 4-wt% PS emulsion had a constant viscosity of 5 ± 1 mPa s at strain rates of 1 – 1000 s^{-1}. A 4-%wt PS solution had a constant viscosity of 45 ± 1 mPa s at strain rates of 1 – 2000 s^{-1}.

4.7 Emulsification in the Absence of Polymer

A practical investigation into the viability of using emulsion formulations to enhance the printing of high-molecular-weight polymers was conducted and the results are presented hereafter. The investigation focussed upon formulating a model system with a high-molecular-weight polystyrene as the target polymer. First, emulsification experiments in the absence of polymer were carried out in order to select viable emulsion stabilisers for the formulation (see below). Second, formulations that included polymer were manufactured to optimise emulsification process (Section 4.8). Third, printing trials were carried out with a number of different discontinuous phase fluids to investigate the impact on ease of printing and deposit morphology (Section 4.9). Fourth, the jetting, drying and deposit characteristics for the optimised formulation were investigated (Section 4.10).

A series of polymer-free emulsions were produced in order to explore which surfactants would be appropriate for polymer-containing emulsions; the results are present below. Methyl benzoate was one of several candidates for the dispersed phase fluid and was present in each formulation at $\varphi_v = 0.3$. The surfactants were trialled over a range of concentrations and observations on dispersed phase size, stability and dispersity were noted.

SDS is an anionic surfactant with a hydrophilic sulphate head group and a hydrophobic dodecyl tail group. Formulations with 10 mM SDS (Fig. 4.20a) and 1 mM SDS (Fig. 4.20b) fully emulsified the oil phase, whilst with 0.1 mM SDS (Fig. 4.20c) a negligible second phase remained on top of the emulsion after production. All three formulations were homogenous and had low dispersity in emulsified drop diameter *d*. The dispersed phase size increases with decreasing surfactant but, in all three cases, all droplet diameters are in the range 2 – 4 μm. A formulation made using a 0.01 mM SDS solution did not emulsify fully, with an immiscible layer present on top of the emulsion and a dispersed phase droplets visible to the naked eye.

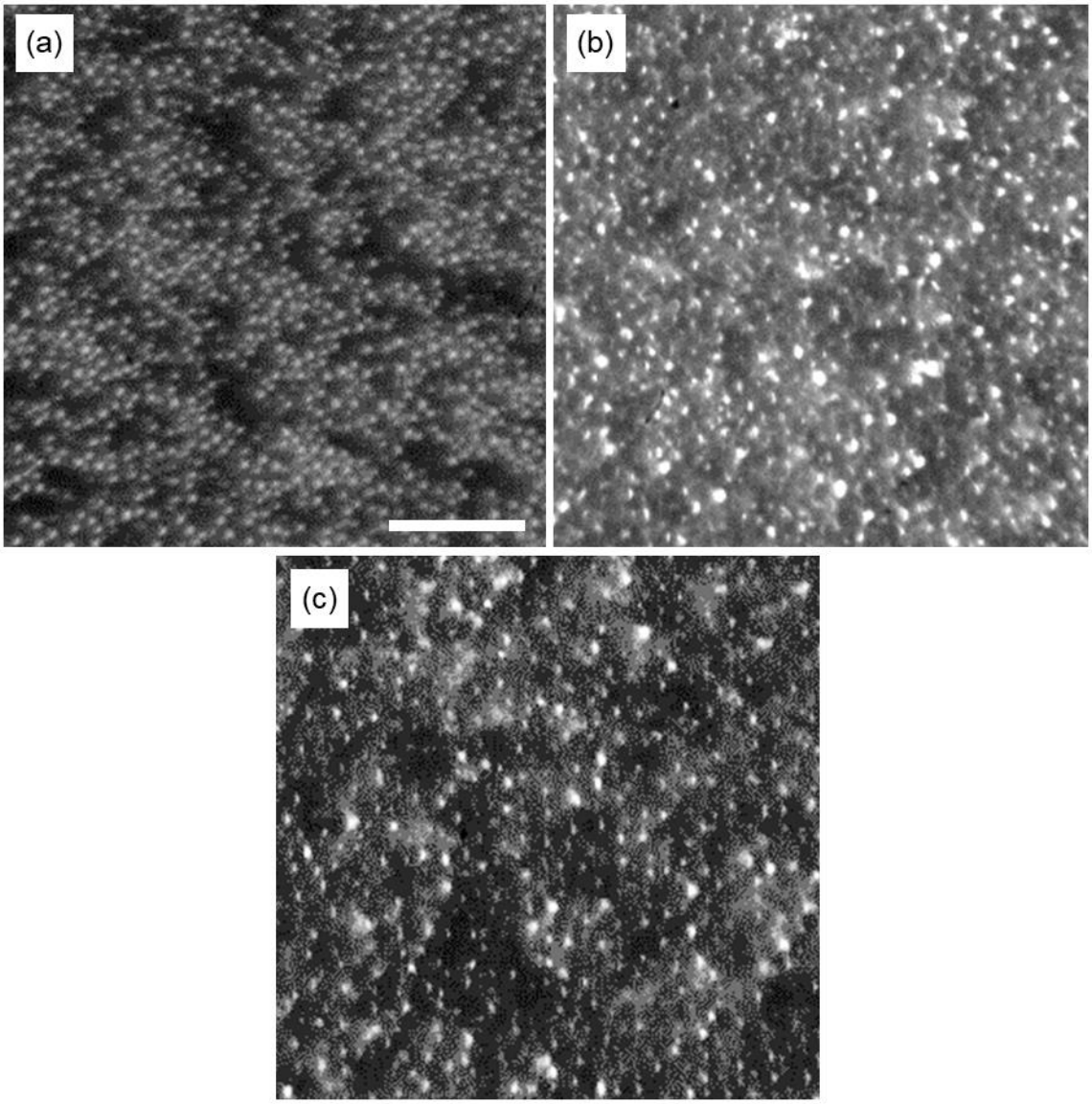

Figure 4.20. Images of emulsions of methyl benzoate (φ_v = 0.3) and SDS solutions of concentration (a) 10 mM, (b) 1 mM and (c) 0.1 mM. Emulsified by USH: 25% amplitude, 20 s. The scale bar is 30 μm.

AOT is an anionic surfactant with two hydrophobic octyl tails that are bonded to a central hydrophilic region comprising two ester groups and a charge-bearing sulphate group. AOT is a more efficient emulsifier than SDS because AOT occupies a larger area at an interface than SDS, so that fewer moles are required to achieve the same interfacial coverage. Formulations made with 10 mM AOT (Fig. 4.21a) and 1 mM AOT (Fig. 4.21b) both emulsified all the methyl benzoate, though a negligible amount of oil was not emulsified when 0.1 mM AOT (Fig. 4.21c) was used. All three of the emulsions were homogenous and had low apparent dispersity. The emulsion drop diameters increase from ~1 μm with 10 mM AOT, to ~2 μm for 1 mM AOT, to ~4 μm for 0.1 mM AOT. A formulation with 0.01 mM AOT did not completely emulsify, giving an upper immiscible layer and emulsified drops visible to the naked eye.

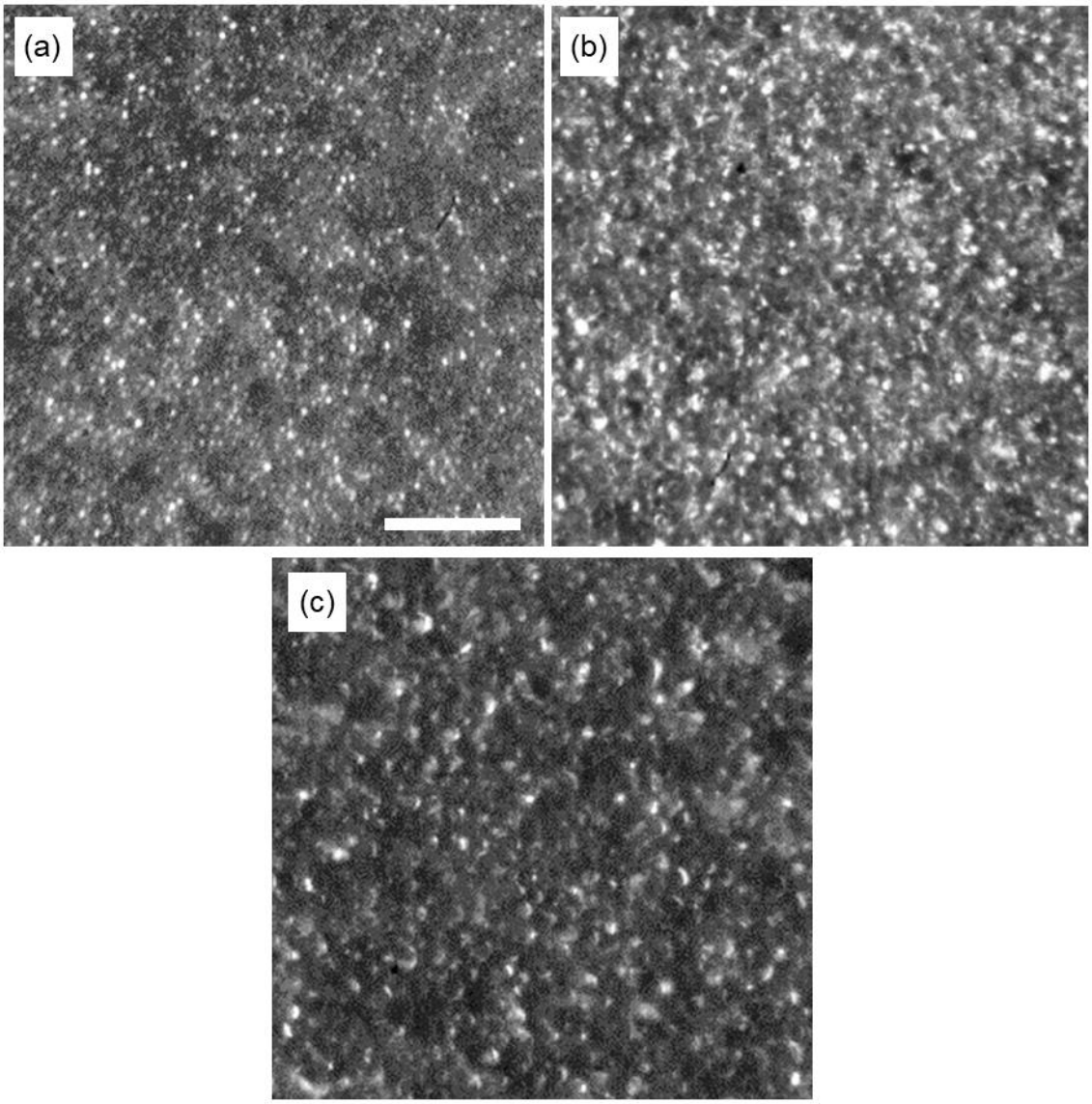

Figure 4.21. Images of emulsions of methyl benzoate (φ_v = 0.3) and AOT solutions of concentration (a) 10 mM, (b) 1 mM and (c) 0.1 mM. Emulsified by USH: 25% amplitude, 20 s. The scale bar is 30 μm.

C_{12}TAB is a cationic surfactant, with a hydrophilic ammonium head group and a hydrophobic dodecyl tail group. Formulations produced with 10 mM C_{12}TAB (Fig. 4.22a) gave emulsified droplets with $d < 2$ μm, whilst 1 mM C_{12}TAB (Fig. 4.22b) gave slightly larger droplets at approximately 3 μm. Though these formulations have a dispersed phase of the correct scale, several factors make them unattractive. The emulsion made with 1 mM C_{12}TAB had a second phase still present after manufacture and thus did not completely emulsify. Additionally, the formulation appeared to cling to the glass container. These attributes were much less pronounced when 10 mM surfactant was used, but were clearly present at 5 mM surfactant.

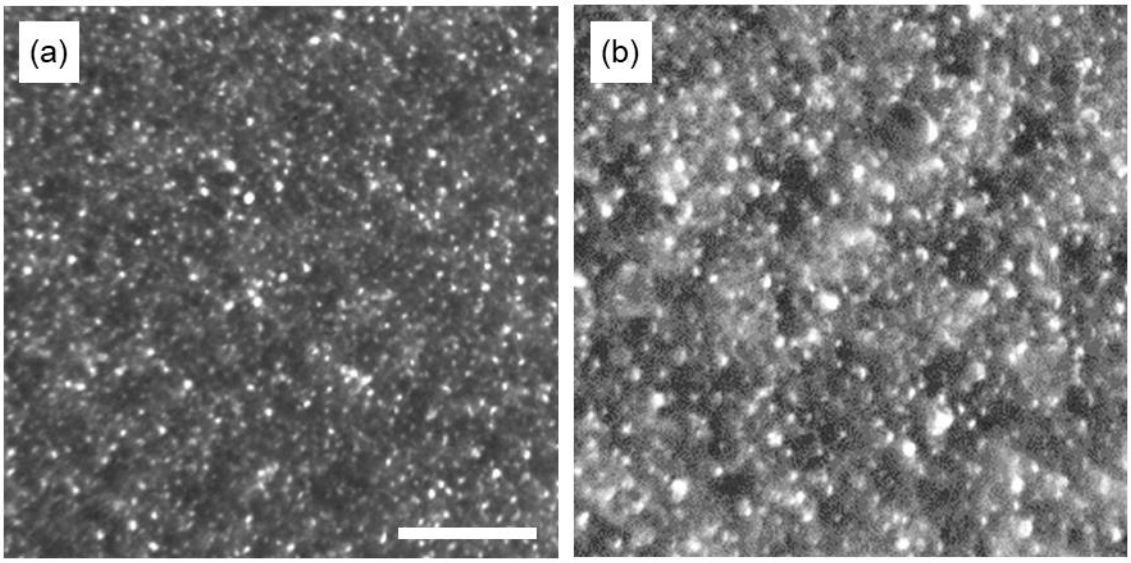

Figure 4.22. Images of emulsions of methyl benzoate (φ_v = 0.3) and C_{12}TAB solutions of concentration (a) 10 mM and (b) 1 mM. Emulsified by USH: 25% amplitude, 20 s. The scale bar is 30 μm.

$C_{10}E_8$ is a non-ionic surfactant comprising a short hydrophilic polyethylene oxide chain linked to a short polyethylene chain. As a small diblock copolymer, $C_{10}E_8$ should occupy more interfacial area than a small ionic surfactants like SDS, and so should be more efficient. Formulations, however, made using 10 mM $C_{10}E_8$ (Fig. 4.23a) and 1 mM $C_{10}E_8$ (Fig. 4.23b) did not produce a dispersed phase with characteristic diameters of a few microns as for SDS, AOT and C_{12}TAB. Instead, emulsified drops with diameters of 10^1 – 10^2 μm were produced. Emulsified drops such as these are larger than the nozzle orifice and would be problematic to jet.

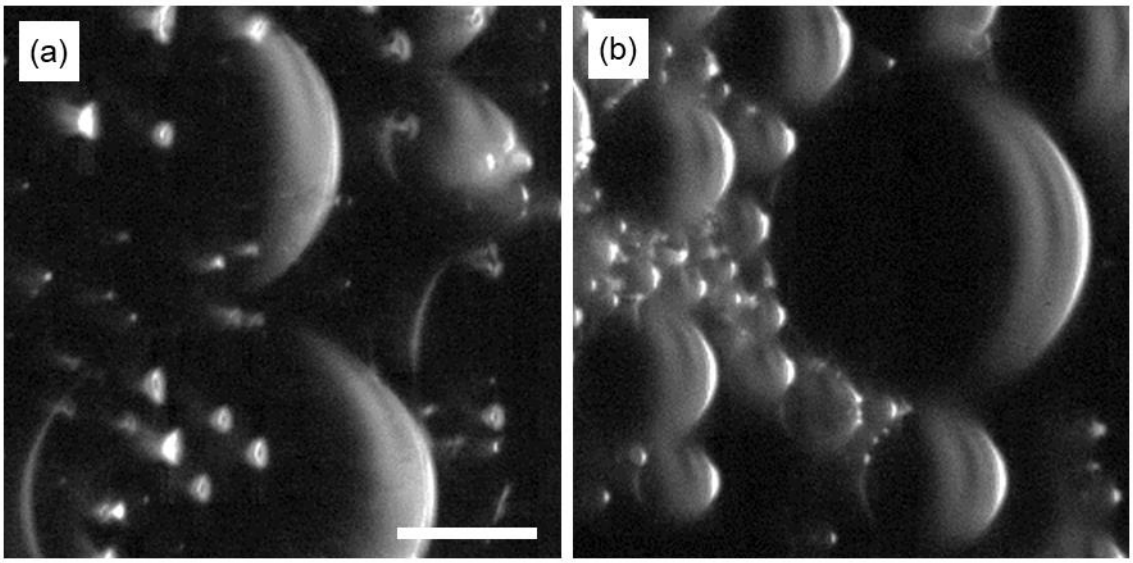

Figure 4.23. Images of emulsions of methyl benzoate (φ_v = 0.3) and $C_{10}E_8$ solutions of concentration (a) 10 mM and (b) 1 mM. Emulsified by USH: 25% amplitude, 30 s. The scale bar is 30 μm.

The last system trialled was a pair of non-ionic co-surfactants: Tween 80 and Span 80. The advantage of using co-surfactants is that they can be added to the formulation in different ratios to optimise emulsion stability. Each ratio can be characterised according to its hydrophilic-lipophilic balance (HLB) value and, by trialling a range of HLB values, the optimum ratio of surfactants can be identified.[157,158] The concentration or identity of the surfactants are then varied, whilst maintaining the optimum HLB value, to produce the emulsion with the desired characteristics and stability. The HLB value for a particular formulation is calculated by taking a weighted average of the component surfactant HLB values according to their concentration. For Tween 80, $HLB = 15.0$ and, for Span 80, $HLB = 4.3$.[159]

A range of emulsion formulations were formulated at 1 mM surfactant over the HLB range 15.0 – 12.5 at increments of 0.5 using the Tween 80 – Span 80 system (Fig 4.24). In all cases, the emulsified drop diameters appear in the 5 – 20 μm range, and no particular HLB value appears superior to the other. The dispersed phase produced with 1 mM surfactant is less than half the diameter of the nozzle orifice (50 μm) but Ostwald ripening would quickly render these formulations difficult to print. Repeating the trials across the same HLB range with 10 mM surfactant (Fig 4.25) yields much reduced dispersed phase diameters. Most emulsified drops have $d < 10$ μm, with the vast majority being only a few microns. Though some drops are still present with $d > 10$ μm, their number are few, especially compared with the 1 mM surfactant formulations (Fig 4.24).

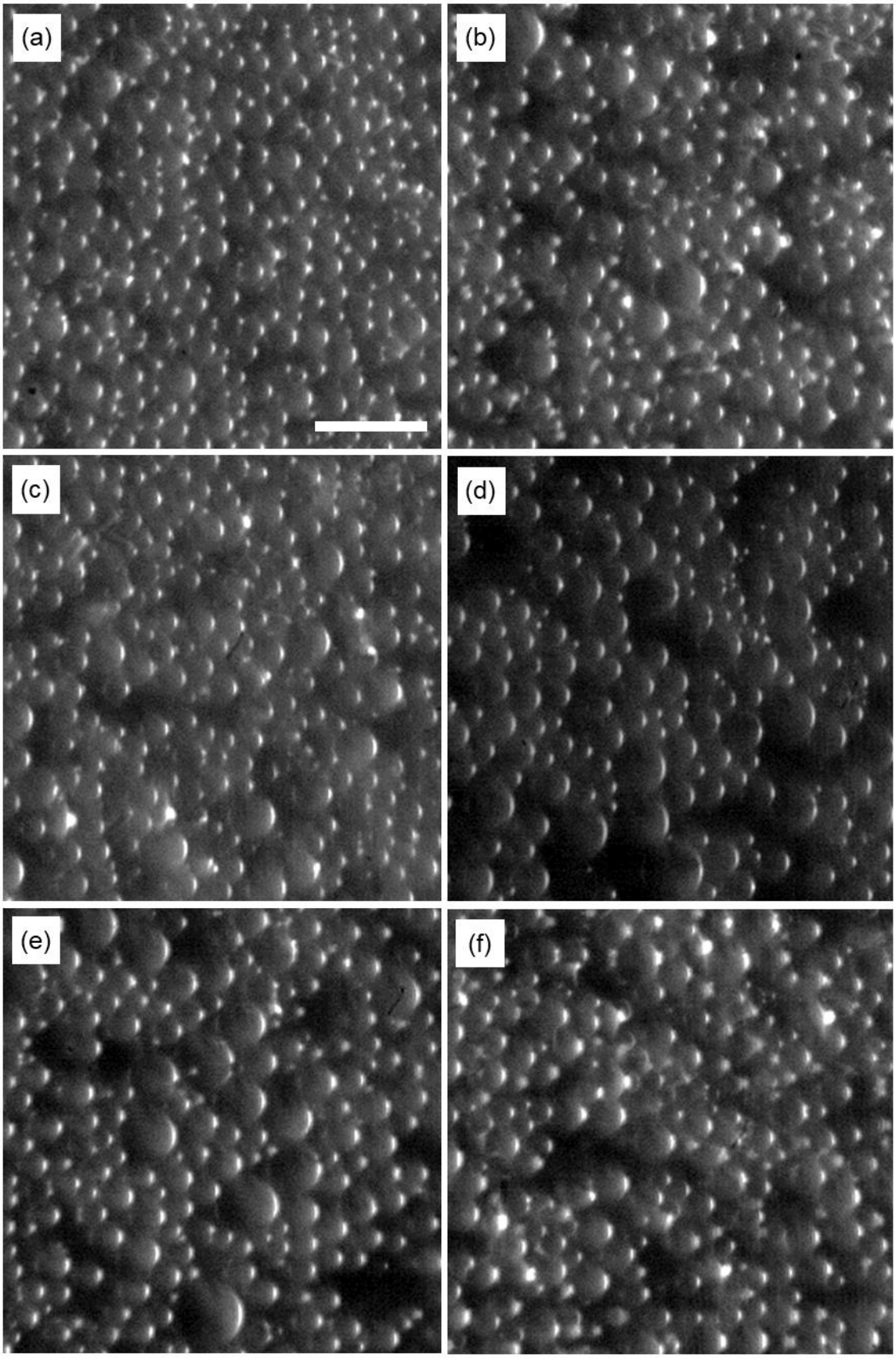

Figure 4.24. (a) An emulsion of methyl benzoate (φ_v = 0.3) and 1-mM Tween 80 (HLB = 15.0). The HLB was varied in other formulations to (b) 14.5, (c) 14.0, (d) 13.5, (e) 13.0 and (f) 12.5 by reducing the concentration of Tween 80 in the continuous phase precursor and introducing Span 80 to the discontinuous phase precursor. Emulsified by USH: 25% amplitude, 20 s. The scale bar is 30 μm.

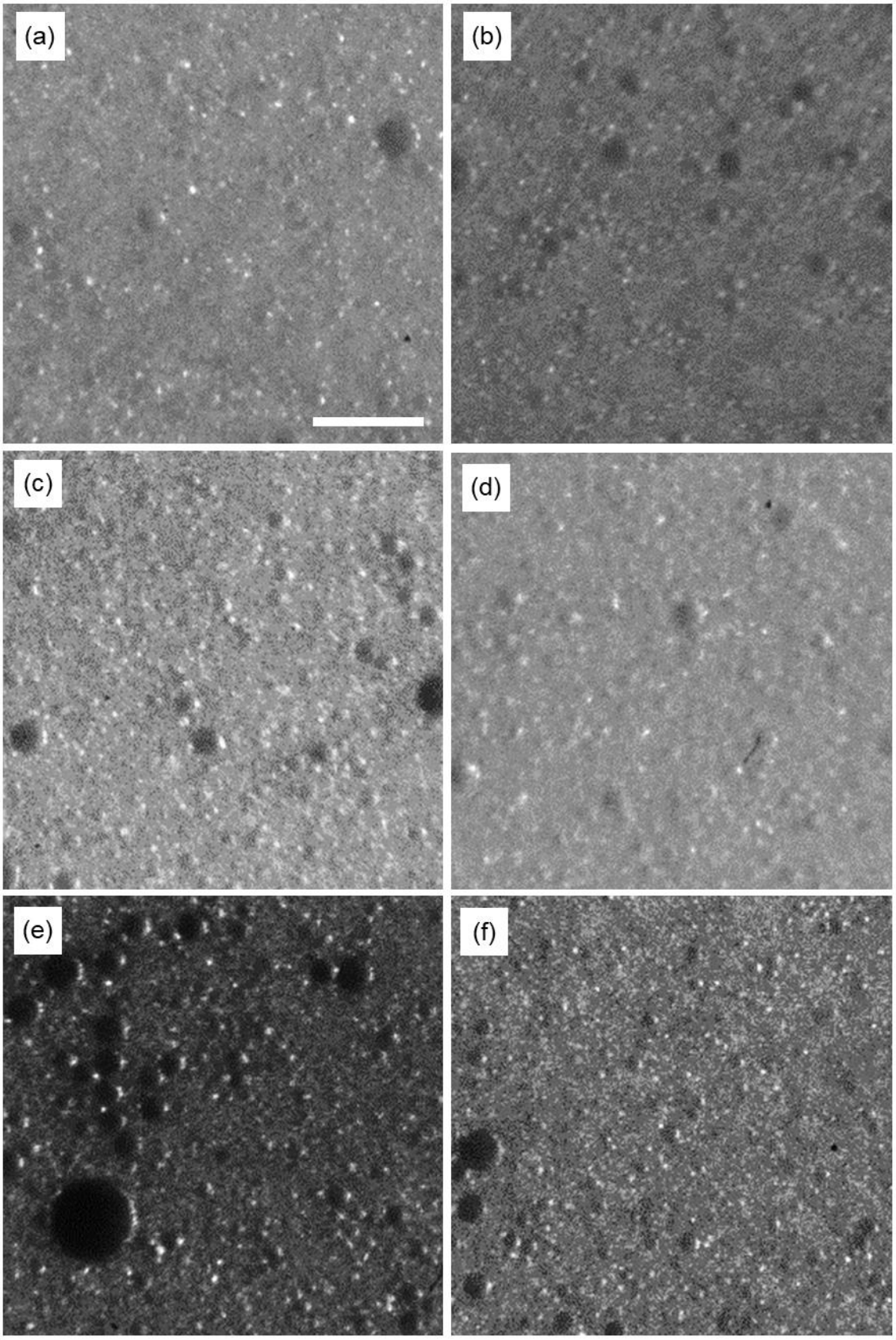

Figure 4.25. (a) An emulsion of methyl benzoate (φ_v = 0.3) and 10-mM Tween 80 (HLB = 15.0). The HLB was varied in other formulations to (b) 14.5, (c) 14.0, (d) 13.5, (e) 13.0 and (f) 12.5 by reducing the concentration of Tween 80 in the continuous phase precursor and introducing Span 80 to the discontinuous phase precursor. Emulsified by USH: 25% amplitude, 20 s. The scale bar is 30 μm.

The trials described above show that, for water and methyl benzoate, a wide variety of surfactants may be used to produce emulsions that have a dispersed phase of the correct size for printing. Formulations made with SDS (0.1 mM), AOT (0.1 mM), C_{12}TAB (0.1 mM) and Tween 80/Span 80 (10 mM) over a range of HLB values had dispersed phases of diameters below a tenth of the nozzle orifice diameter. For SDS, AOT and C_{12}TAB, increasing the concentration improved emulsion stability and further reduced the size of the emulsified drops. $C_{10}E_8$ did not yield suitable emulsions: perhaps the surfactant diffuses to the interface too slowly or imparts lower stability to small droplets on account of its charge neutrality.

The major instability observed in the trials was sedimentation caused by the density difference between water (ρ = 1.00 g mL^{-1}) and methyl benzoate (ρ = 1.08 g mL^{-1}). The largest dispersed phase species are not self-dispersing and collect at the bottom of the container. Smaller droplets also tend to sediment, but much more slowly (Section 4.5.3.2). Ostwald ripening increases the size of the largest species over time, which compounds the problem. Sedimentation was manifested in samples as a layer that formed at the bottom of vials after they had been allowed to stand for several hours and gentle agitation would re-disperse the droplets. One strategy for slowing creaming or sedimentation is to increase the continuous phase viscosity. Water remains attractive as the continuous phase solvent since the majority of vapour that would be produced on the evaporation of formulations would be non-hazardous.

The simplest way to increase continuous phase viscosity is to introduce a water-soluble polymer. The viability of the strategy was trialled using 2-hydroxyethyl cellulose, HEC, (*Sigma-Aldrich*, M_w = 250 kDa). An emulsion produced with toluene and 10-mM SDS (Fig 4.26a) had dispersed droplets with diameters of ~2 μm. Formulations produced that additionally contained 0.50 %wt HEC (Fig 4.26b) and 1.0 %wt HEC (Fig 4.26c) flocculated rapidly under depletion flocculation (Section 4.5.3.1): depletion flocculation is more likely than bridging flocculation as HEC is not active at the emulsion interface. Flocculation enhanced the creaming rate versus the formulation without a modified continuous phase. The black regions of the images in Figures 4.26b and c are aqueous phase without oil droplets. The HEC concentration was not raised further because the addition of large amounts of polymer to the continuous phase to stabilise the emulsion would introduce the unfavourable non-Newtonian printing characteristics that the formulations are seeking to mitigate for the target polymer.

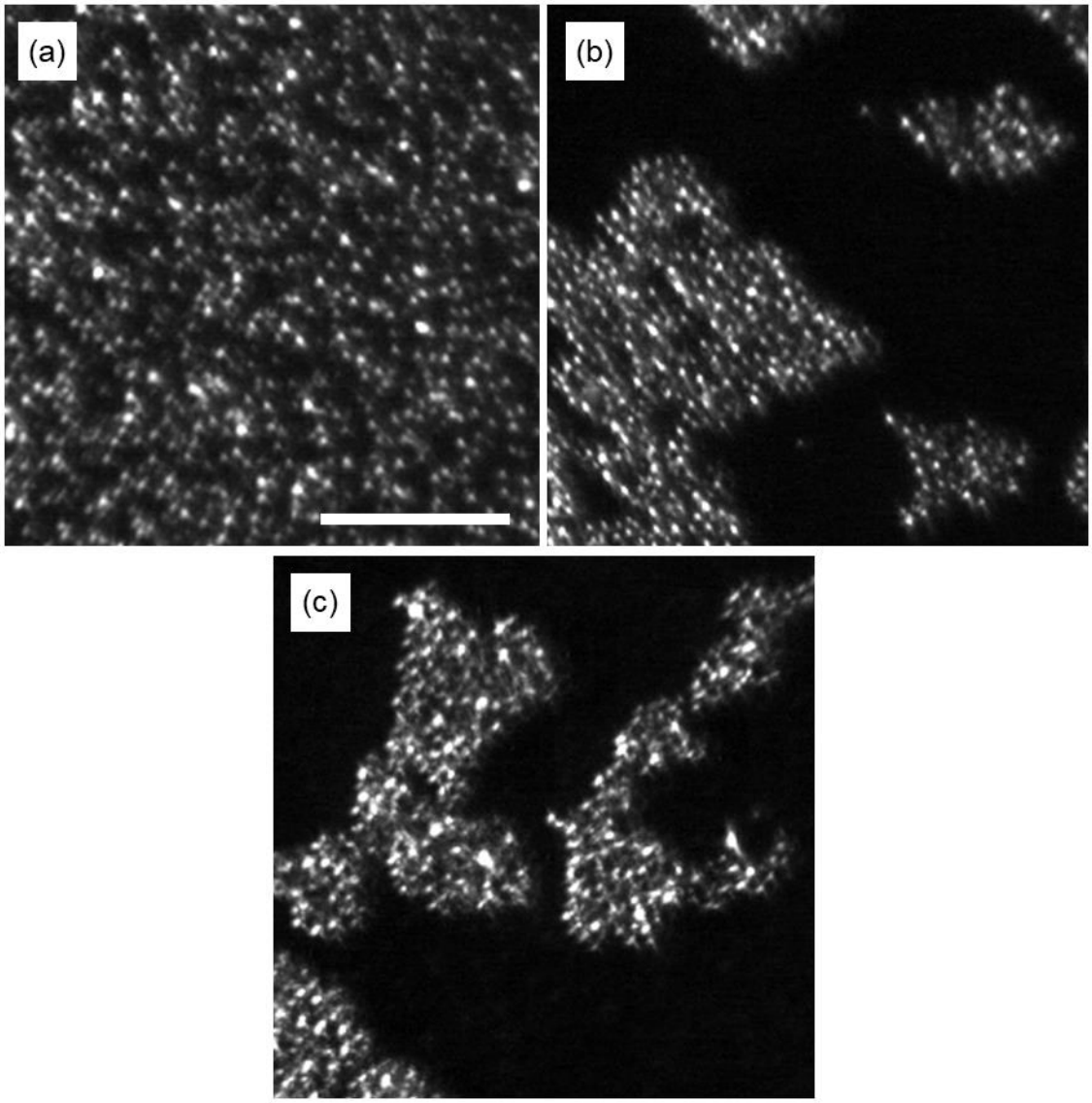

Figure 4.26. (a) An emulsion of toluene (φ_v = 0.1) and a solution containing 10-mM SDS. (b) An emulsion of toluene (φ_v = 0.1) and a solution containing 8-mM SDS and 0.50 %wt HEC. (c) An emulsion of toluene (φ_v = 0.1) and a solution containing 8-mM SDS and 1.0 %wt HEC. Emulsified by USH: 40% amplitude, 20 s. Aliquots were extracted from the formulations less than 30 min after emulsification. The scale bar is 30 μm.

4.8 Emulsification in the Presence of Polymer

In Section 4.7, it was shown that emulsions with the correct emulsified drop characteristics can be produced with the ultrasonic horn in the presence of a range of surfactants, but in the absence of the target polymer in the discontinuous phase. The impact of including a high-molecular-weight polystyrene in the discontinuous phase precursor is shown in Figure 4.27 for a series of formulations with a dispersed phase based upon methyl benzoate ($\varphi_w = 0.3$) and SDS as the surfactant stabiliser. In the absence of polymer (Fig. 4.27a), the formulation had a low dispersity with $d \sim 1$ μm. When the high-molecular-weight polystyrene was introduced to the discontinuous phase precursor at 4 %wt (Fig. 4.27b) or 8 %wt (Fig. 4.27c), the oil droplets were polydisperse. In both cases, emulsified drops with $d \leq 1$ μm were still present, but in addition drops larger in diameter than 3 μm were visible. The dispersity was more pronounced for the formulation manufactured with 8-%wt polystyrene in the discontinuous phase, with larger coarse emulsified drops. Though the inclusion of polymer in the formulations led to an overall coarsening of the discontinuous phase versus the polymer-free formulation, the emulsified drops were still small relative to the 50-μm nozzle orifice diameter, making them feasible to print.

Polymer-containing emulsions were formulated with the surfactants trialled in Section 4.7 in order to see if a different surfactant performed better than SDS. The overall goal of printing emulsions is to deposit as much polymer as possible. Formulations containing an increased polystyrene content, at 3 %wt overall, were produced (Fig. 4.28). When SDS was used as the surfactant (Fig. 4.28a) the same behaviour was observed as in Figure 4.27c, but the discontinuous emulsified drops were larger, at up to 10 μm. Emulsions produced with C_{12}TAB (Fig. 4.28b) appeared to perform much better when an aliquot was viewed on the printing rig, with the vast majority of visible species having $d \sim 1$ μm and with only a very few being larger at up to 6 μm. The major disadvantage of using C_{12}TAB instead of SDS, however, was that a sediment was visible in the vial within hours of production. Formulations made using AOT as the surfactant stabiliser (Fig. 4.28c) featured large emulsified drops with diameters in the 10s and 100s of microns and were thus much larger than the nozzle orifice ($d = 50$ μm), making them unsuitable for printing. Similar behaviour was observed in when attempting to produce an emulsion with $C_{10}E_8$ as the surfactant stabiliser (Fig. 4.28d). When Tween 80/Span 80 mixtures were tested in formulations containing polymer, a slightly lower overall polystyrene concentration (2.6 %wt) was attempted over an HLB range of 15.0 – 12.5. The emulsions

produced (Fig. 4.29), however, did not appear printable either, with droplet diameters in the 10s and 100s of microns.

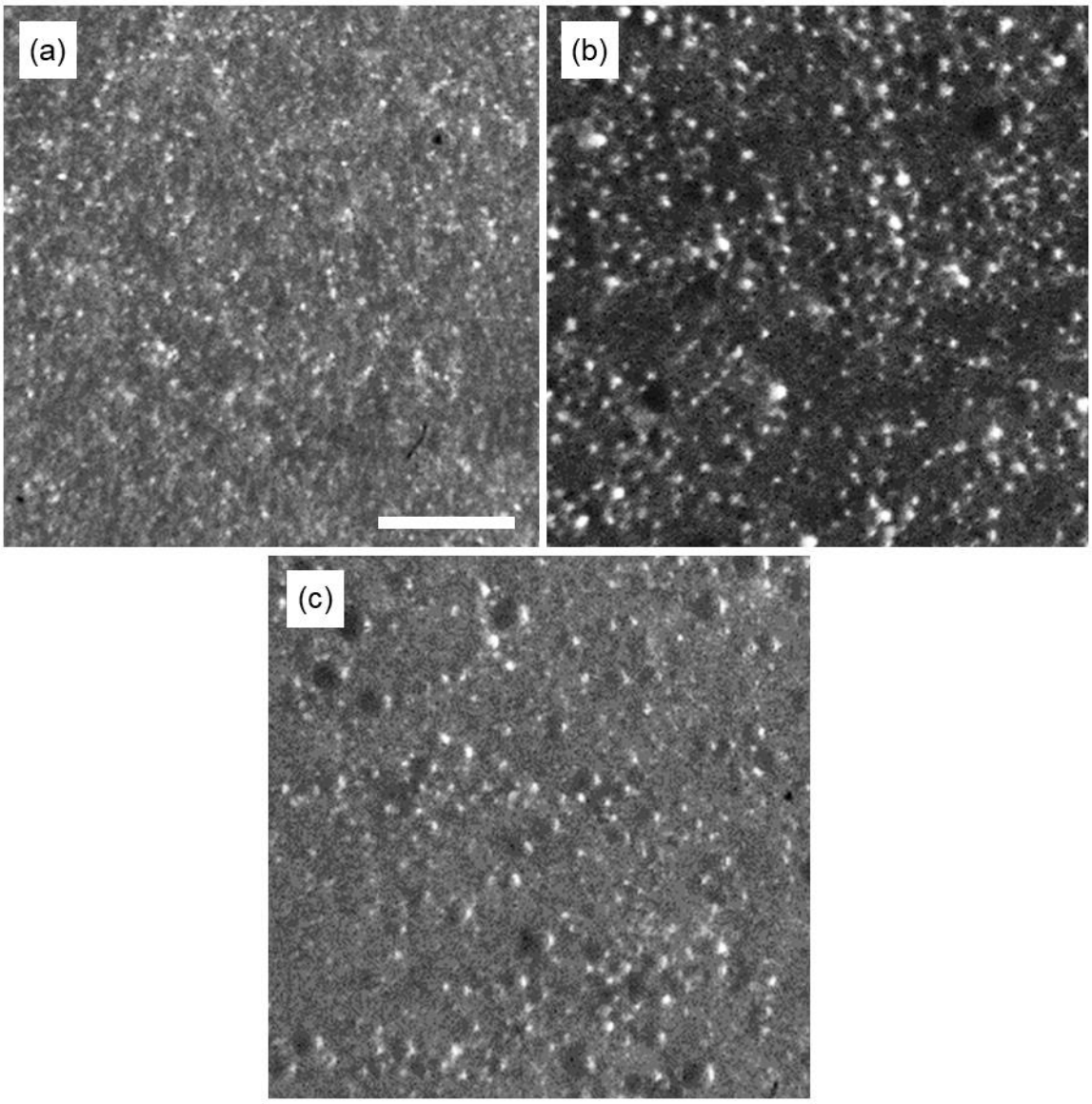

Figure 4.27. Images of emulsions containing different amounts of polymer. (a) An emulsion of methyl benzoate (φ_w = 0.3) and a 10-mM SDS solution. Emulsified by USH: 25% amplitude, 1 min. (b) An emulsion of 4-%wt polystyrene in methyl benzoate (φ_w = 0.3) and a 10-mM SDS solution. Emulsified by USH: 25% amplitude, 1 min; 40 % amplitude, 1 min. (c) An emulsion of 8-%wt polystyrene in methyl benzoate (φ_w = 0.3) and a 10-mM SDS solution. Emulsified by USH: 25% amplitude, 1 min; 40 % amplitude, 1 min. The scale bar is 30 μm.

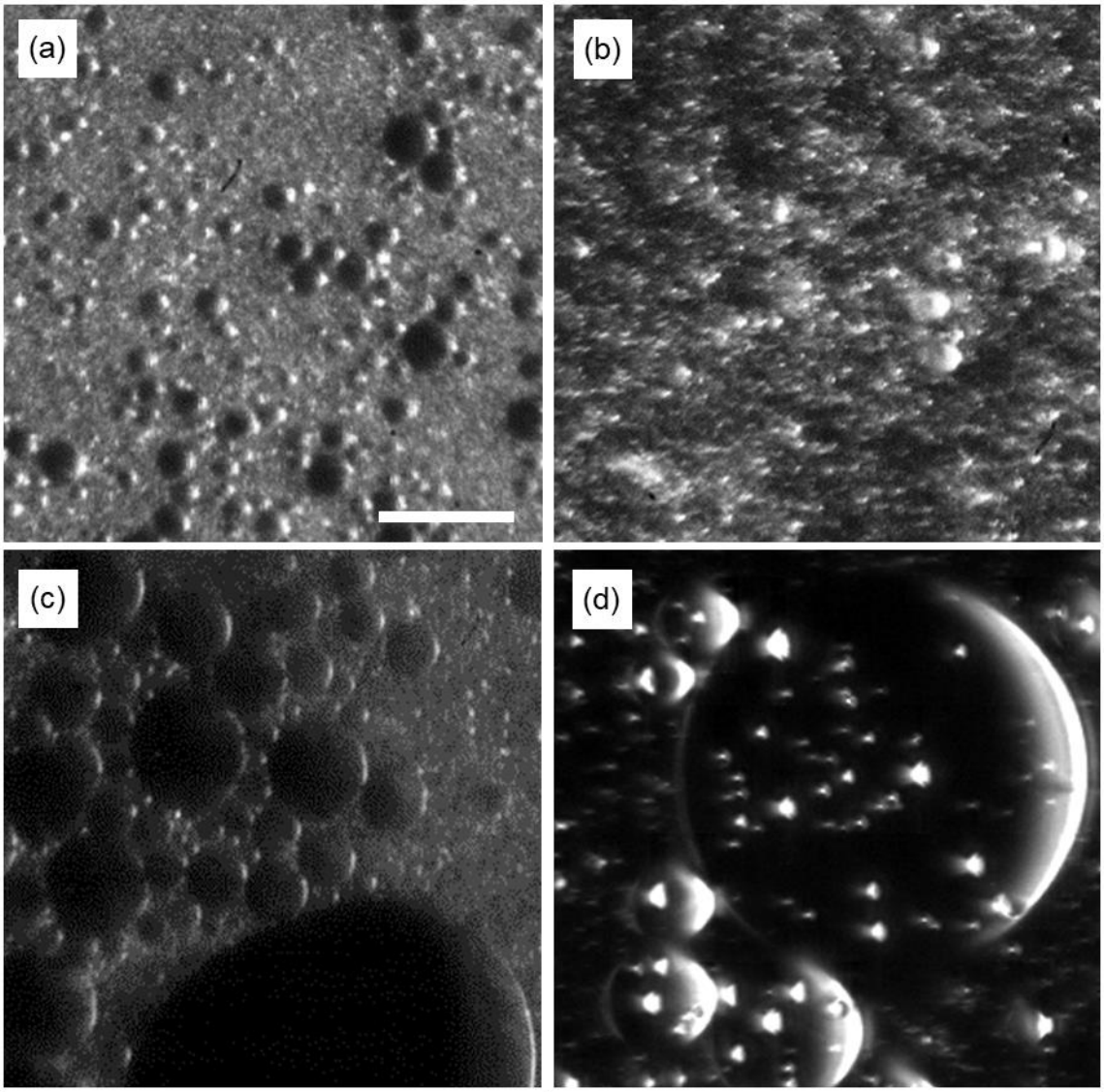

Figure 4.28. Images emulsions manufactured with different surfactants. (a) An emulsion of 10-%wt polystyrene in methyl benzoate (φ_w = 0.3) and a 10-mM SDS solution. Emulsified by USH: 25% amplitude, 10 min. (b) An emulsion of 15-%wt polystyrene in anisole (φ_w = 0.2) and a 9-mM C_{12}TAB solution. Emulsified by USH: 25% amplitude, 1 min. (c) An emulsion of 10-%wt polystyrene in methyl benzoate (φ_w = 0.3) and a 5-mM AOT solution. Emulsified by USH: 25% amplitude, 4 min. (d) An emulsion of 10-%wt polystyrene in anisole (φ_w = 0.2) and a 9-mM $C_{10}E_8$ solution. Emulsified by USH: 25% amplitude, 1 min; 40 % amplitude, 40 s. The scale bar is 30 μm.

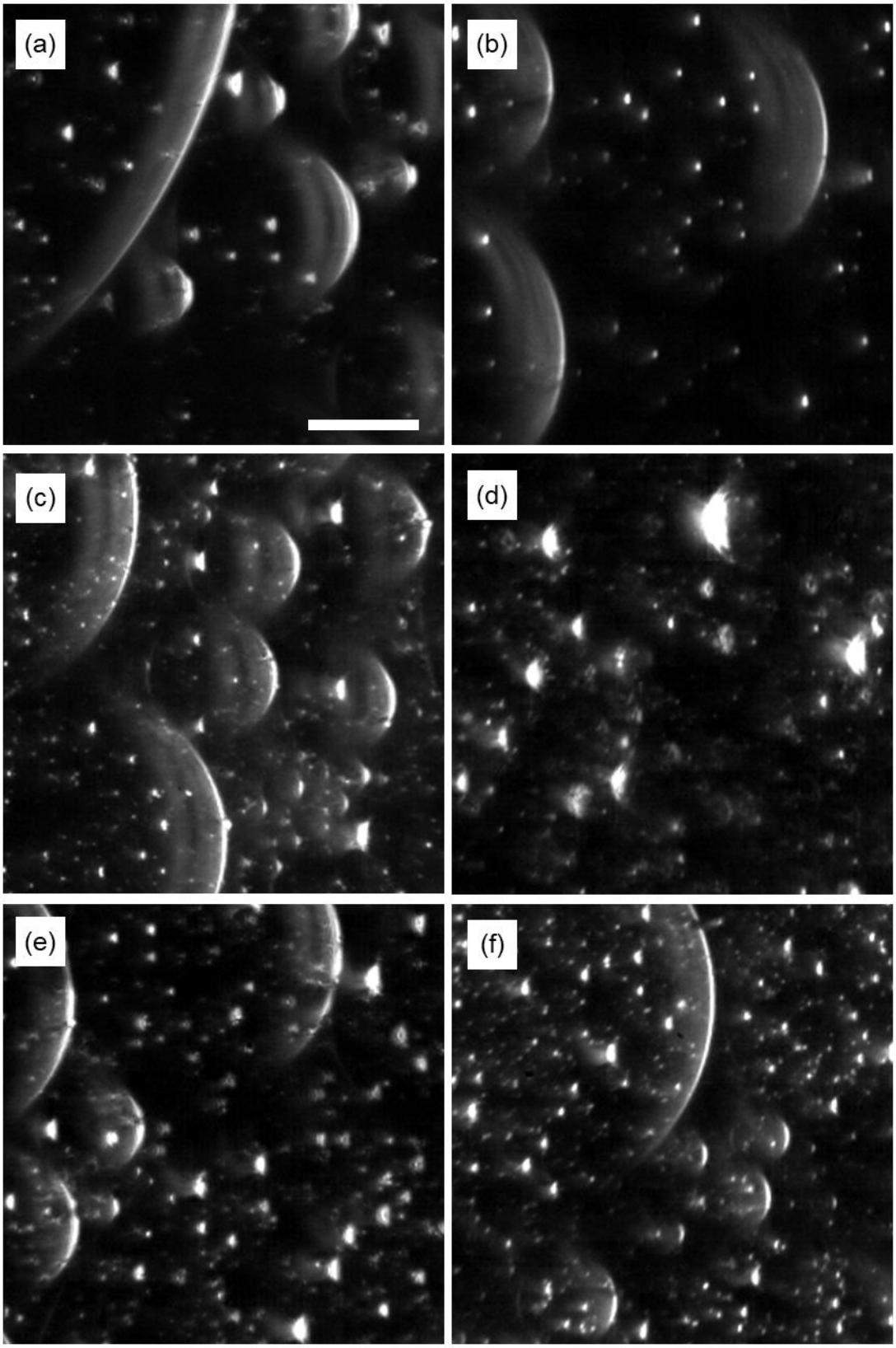

Figure 4.29. (a) An emulsion of 6.5-%wt polystyrene in methyl benzoate (φ_v = 0.4) and 10-mM Tween 80 (HLB = 15.0). The HLB was varied in other formulations to (b) 14.5, (c) 14.0, (d) 13.5, (e) 13.0 and (f) 12.5 by reducing the concentration of Tween 80 in the continuous phase precursor and introducing Span 80 to the discontinuous phase precursor. (a) and (b) Emulsified by USH: 25% amplitude, 1 min; 40 % amplitude, 1 min. (c), (e) and (f) Emulsified by USH: 25% amplitude, 1 min. (d) Emulsified by USH: 25% amplitude, 2 min. The scale bar is 30 μm.

The emulsions that were produced in the absence of polymer in the discontinuous phase in Section 4.7 with SDS, C_{12}TAB, AOT and Tween 80/Span 80 mixtures appeared monodisperse and had discontinuous phases with diameters of only a few microns (Figs. 4.20 – 4.25), making them suitable for printing. For SDS, C_{12}TAB and AOT, this was true at surfactant concentrations of 1 mM, though for Tween 80/Span 80 mixtures this was true at 10 mM. The ultrasonic horn was also therefore shown to be a suitable emulsification method. Upon including the high-molecular-weight polystyrene in the oil phase, markedly different behaviour was observed, with emulsions possessing droplets of different sizes, some with $d > 10$ μm. This is because the polymer solution properties that inhibit printing also inhibit emulsification, since high strain rates are involved in the division of emulsified droplets. For formulations using AOT and Tween 80/Span 80 mixtures, the emulsified drops were too coarse for printing. Whilst for SDS and C_{12}TAB formulations the largest species were still much smaller than the print head orifice, other emulsification methods were trialled to see if the formulations can be further improved.

One alternative to the ultrasonic horn was a bath sonicator, which should additionally cause less damage to the polymer than the ultrasonic horn. A formulation comprising a 10-%wt polystyrene solution in methyl benzoate ($\varphi_w = 0.3$) and a 10 mM SDS solution was initially subjected to agitation by hand and then was bath sonicated for 70 min. The resulting emulsion was not finely divided, with dispersed phase drops visible to the naked eye. Another alternative was to use a vortex mixer (*Stuart*, SA8) with a maximum agitation speed of 2500 rpm. A formulation comprising a 9-%wt polystyrene solution in methyl benzoate ($\varphi_w = 0.3$) and a 10 mM SDS solution was mixed at 2500 rpm for 2 min. After the emulsion was allowed to stand, a layer of emulsified drops visible to the naked eye sedimented. The failure of the bath sonicator and the vortex mixer indicates that significant disruptive forces are required to break down drops of polymer solution.

The disruptive forces of a high-shear homogeniser (*IKA*, T10 Ultra Turrax) are intermediate between those of gentle agitation and the ultrasonic horn. A formulation comprising a 9-%wt polystyrene solution in methyl benzoate ($\varphi_w = 0.4$) and a 15 mM SDS solution was processed at speeds between 8000 and 20500 rpm. The emulsified drops produced were frequently much larger than the print head orifice, with some visible at $d > 240$ μm (Fig 4.30a). Repeating the trial with the homogeniser, but with pre-agitation from the ultrasonic horn, did not eradicate the presence of emulsified droplets with $d >$ 10 μm (Fig 4.30b, *cf.* Fig. 4.28a). Overall, the performance of the ultrasonic horn in combination with formulations using SDS as surfactant produced the best emulsions:

emulsification of all the oil, small dispersed phase species relative to the print head orifice and lower propensity to separate or form layers than other surfactants.

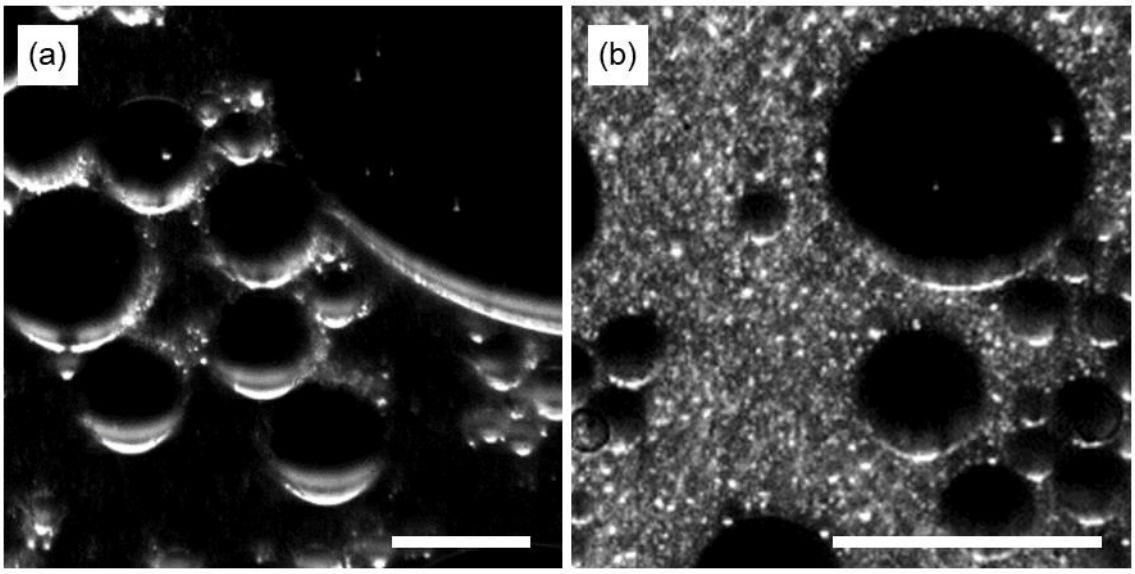

Figure 4.30. Images of emulsions manufactured with the Ultra Turrax. Emulsions were sequentially processed at 8000, 9500, 11500, 14500 and 20500 rpm for a minute at each setting. Formulations are emulsions of 9.4-%wt polystyrene in methyl benzoate (φ_w = 0.4) and a 14.8-mM SDS solution. (a) Pre-agitated by stirring only. (b) Pre-agitated by stirring and by USH: 25% amplitude, 1 min. The scale bars are 40 μm.

Finally the amplitude of the ultrasonic horn was varied between 25% and 40% and the impact upon the emulsified drop sizes was investigated. A formulation comprising a 10%-wt polystyrene solution in methyl benzoate (φ_w = 0.4) was emulsified with an 11.5 mM SDS solution using the ultrasonic horn for 2 min at 25% amplitude. The resulting emulsion (Fig. 4.31a) has large numbers of oil drops with d ~ 1 μm and several with diameters in the range 5 – 20 μm. When the formulation was processed for a further minute using the ultrasonic horn at an increased amplitude of 40% (Fig. 4.31b), the larger emulsified drops reduced in size and drops with d > 15 μm became significantly rarer. The general reduction in the scale of the discontinuous phase is advantageous since it reduces the chance of a large emulsified drop becoming lodged at the print head orifice. Emulsifying the formulation at a lower amplitude before using a higher amplitude also reduced the chances of the horn tip becoming exposed to air during emulsification and causing air bubbles to be distributed through the formulation. The limitations of the ultrasonic horn microtip mean that it cannot be operated above 40% amplitude and that further reductions in emulsified drop size cannot be achieved with the ultrasonic horn. The ultrasonic horn routine and amplitudes required to achieve a printable emulsions

depended on the identity of the oil and the concentration of the polymer solution. In the printing trials recorded later, some emulsions were printable after only being subjected to the ultrasonic horn at 25% amplitude.

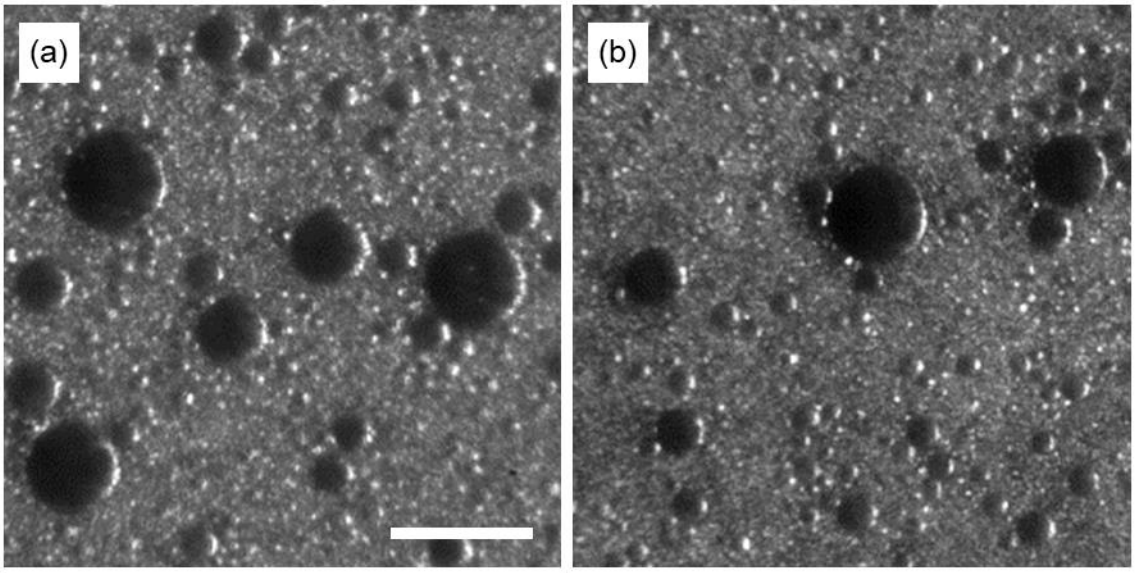

Figure 4.31. Images of emulsions manufactured under different ultrasonic horn conditions. Formulations are emulsions of 10-%wt polystyrene in methyl benzoate (φ_w = 0.4) and a 11.5-mM SDS solution. (a) Emulsified by USH: 25% amplitude, 2 min. (b) Emulsified by USH: 25% amplitude, 2 min; 40% amplitude, 1 min. The scale bar is 30 μm.

A key parameter in the formulations is the surfactant concentration. The emulsions were designed to deposit more high-molecular-weight polymer than is possible in solution, so the overall amount of surfactant included should be small relative to the amount of polymer. It would be a false victory if the formulation cost of using emulsions to print polymers is that a significant proportion of the final deposit originated from the stabilising species. A series of emulsions were therefore prepared with a 15-%wt polystyrene solution in anisole (φ_w = 0.3) and SDS solutions of concentration 15 mM, 12 mM, 8 mM and 4 mM (Fig. 4.32). The formulation produced using 15 mM SDS (0.30 %wt overall) had the familiar high numbers of drop with d ~1 μm and the smaller numbers of larger drops with diameters commonly 5 – 15 μm (Fig. 4.32a). Upon reducing the surfactant concentration (Figs. 4.32b−d), the larger species became progressively more numerous and greater in diameter. The formulation prepared with 4 mM SDS (Fig. 4.32d) had 0.10 %wt surfactant overall and emulsified drops with d > 15 μm were much more common than when 15 mM SDS was used. In all four emulsions the polymer is present at 4.5 %wt overall, so that if an emulsion drop were to dry, the surfactant would make up 2 – 6 %wt of the deposit, depending on the concentration of SDS used. Although the

polymer mass fraction in the deposit increases as the surfactant concentration decreases, the smaller droplets produced at higher SDS concentrations are advantageous for printing. The effects of dispersed phase buoyancy and Ostwald ripening also take longer to become problematic for smaller drops.

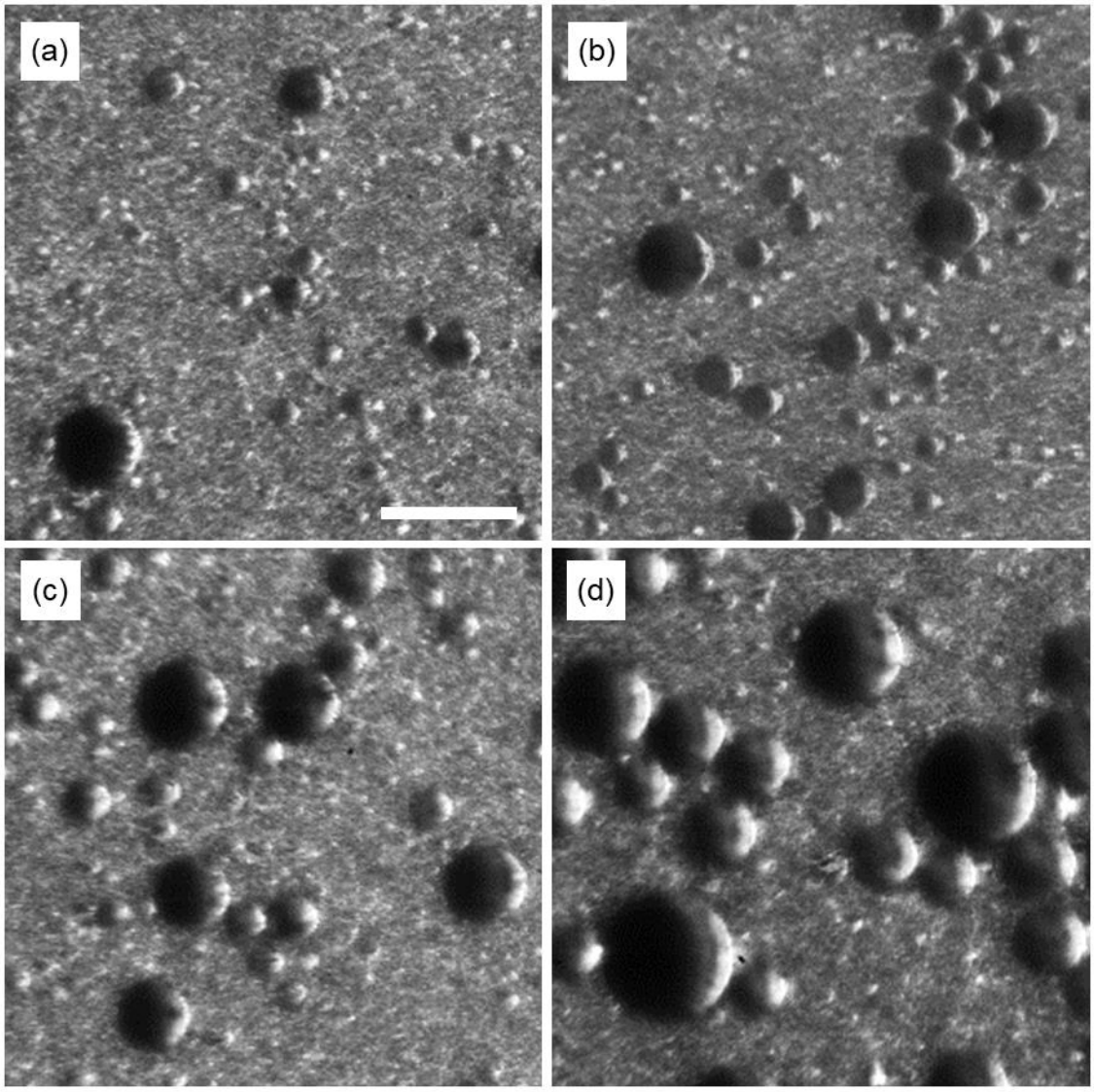

Figure 4.32. Images of emulsions manufactured with different amounts of surfactant. Formulations are emulsions of 15-%wt polystyrene in anisole (φ_w = 0.3) and SDS solutions of concentrations (a) 15 mM, (b) 12 mM, (c) 8 mM and (d) 4 mM. Emulsified by USH: 25% amplitude, 1 min; 40 % amplitude, 1 min. Aliquots were extracted 2 hrs after manufacture. The scale bar is 30 μm.

Trials were also carried out to assess the stability and homogeneity of the emulsions. After formulation, the size distribution of the emulsified drops did not remain constant (Fig. 4.33). The largest species present in an emulsion of 10-%wt polystyrene in methyl benzoate (φ_w = 0.4) and 15-mM SDS grew from ~10 μm at manufacture to up to 40 μm after 5.5 hours, though the large numbers of 1-μm droplets appeared unchanged. The growth of the larger droplets whilst the smallest ones remain a constant size is

consistent with Ostwald ripening in the presence of a non-soluble component (Section 4.5.3.3). Blockages as a result of large emulsified drops is therefore more likely as a formulation ages and emulsions may become unprintable after a few hours.

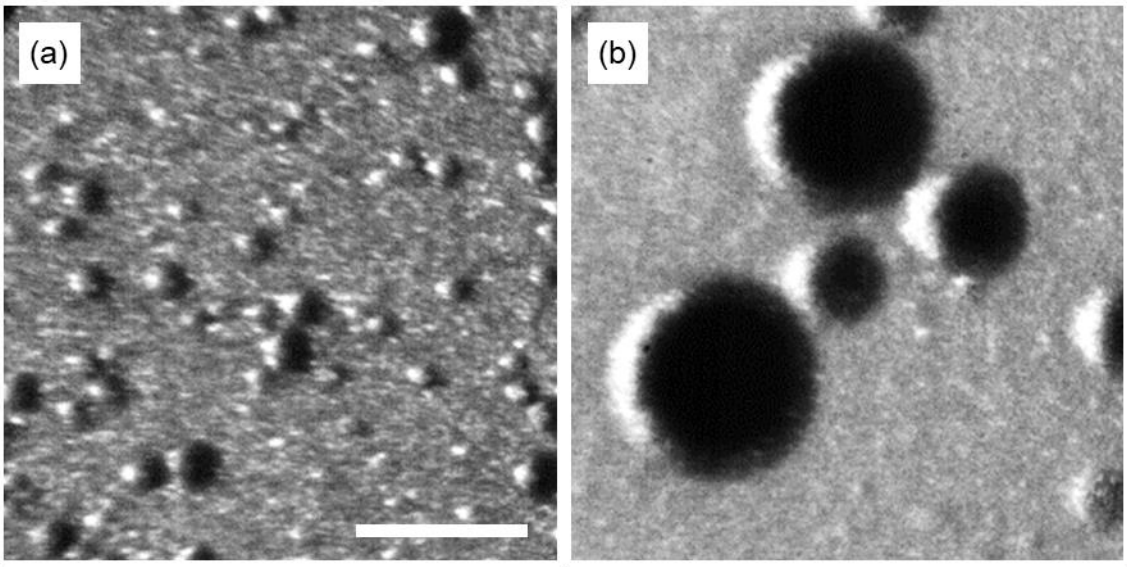

Figure 4.33. Images of an emulsion (a) after manufacture and (b) 5.5 hrs after manufacture. The formulation is an emulsion of 10-%wt polystyrene in methyl benzoate (φ_w = 0.4) and a 15-mM SDS solutions. Emulsified by USH: 25% amplitude, 2 min; 40 % amplitude, 1 min. The scale bar is 30 μm.

The production of large emulsified drops that would block the print orifice under Ostwald ripening is one unfavourable instability characteristic. Another has to do with the associated Stokes velocity of the largest drops. As the radius of an emulsified drop increases, the larger is its Stokes velocity and the faster the effects of sedimentation and creaming are manifested (Section 4.5.3.2). Figure 4.34 shows an emulsion 3.3 hr after manufacture that was formulated using a 10-%wt polystyrene solution in methyl benzoate (φ_w = 0.3) and a 10 mM SDS solution. When the emulsion had been allowed to stand, an aliquot contained few dispersed droplets with $d > 2$ μm, though micron-sized droplets are abundant (Fig. 4.34a). After agitating the formulation, a number of dispersed drops with diameters 10 − 45 μm were present in an aliquot (Fig. 4.34b). The re-dispersion of large emulsified drops under gentle agitation is consistent with creaming/sedimentation and will need to be managed during printing. A dispersed phase with a propensity to sediment will accumulate at the print head orifice, raising the effective proportion of dispersed phase and potentially causing misfire. A creaming dispersed phase will see decreasing masses of polymer deposited per drop over time as emulsified drops move away from the nozzle.

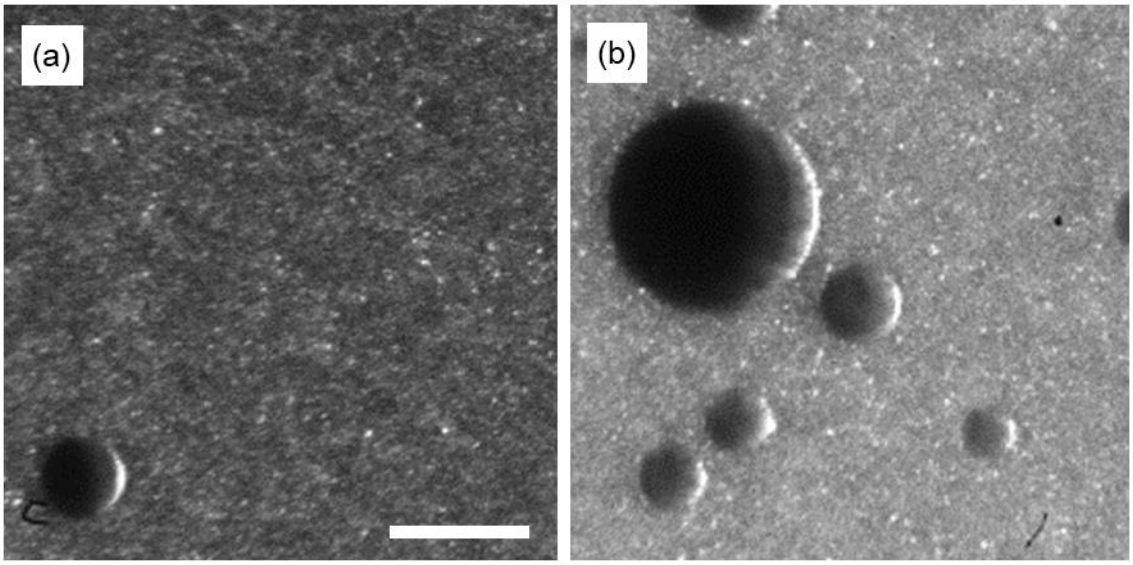

Figure 4.34. Images of an emulsion 3.3 hrs after manufacture (a) after being allowed to settle and (b) after being agitated. The formulation is an emulsion of 10-%wt polystyrene in methyl benzoate (φ_w = 0.3) and a 10-mM SDS solutions. Emulsified by USH: 25% amplitude, 1 min; 40 % amplitude, 1 min. The scale bar is 30 μm.

4.9 The Effect of Varying the Discontinuous Phase Oil upon Printing Trials

In Section 4.8, it was established that emulsions containing 0.25 %wt SDS overall and had oil phase fractions φ_w = 0.3 possessed the correct characteristics for the ink-jet printing of high-molecular-weight polymers. All polymer-containing emulsions were characterised by large numbers of small micron-sized emulsified drops present alongside a much smaller number of drops with diameters up to 10 μm (Fig. 4.28a). Long-term stability was not observed with significant Ostwald ripening in the larger emulsified drops over the course of a few hours risking print head blockages and discontinuous phase buoyancy reducing formulation homogeneity over time.

An investigation into how the identity of the discontinuous phase influences the dynamics of the drying process and the nature of the deposit is presented in this section for toluene, diethyl phthalate, anisole and methyl benzoate. The key characteristics of the organic solvent that influenced overall formulation performance were density and vapour pressure relative to water, affecting emulsion stability, likelihood of nozzle blockages and the manner in which polymer is deposited on the substrate.

4.9.1 A Toluene Discontinuous Phase

Figure 4.35 shows images of an emulsion comprising a 10.0-%wt toluene solution of polystyrene (φ_w = 0.3) and 14.5-mM SDS at various times *t* after printing of a droplet. Initially a large number of micron-sized emulsified drops can be seen, each appearing as a white spot (Fig 4.35a). They migrate towards the contact line.[43] Radial convection occurs at low Capillary and Bond numbers (i.e. surface tension dominates over viscosity and gravity) and with pinned contact lines, where the droplet always maintains the shape of a spherical cap during evaporation. As the drop dries, the dispersed phase collects and coalesces at the contact line, reducing overall drop brightness (compare Figs. 4.35a – c). Polystyrene begins to be deposited before evaporation of the continuous phase is complete and when *t* = 2.6 s a polymer ring starts to develop (Fig. 4.35c). The drop remains pinned on the inside of the deposit as the polystyrene dries radially inwards, so that the contact line recedes slightly (Figs. 4.35d – e). Evaporation is completed at *t* = 6.4 s (Fig. 4.35f) and the deposit is characterised by a continuous polystyrene ring, with very little material in the centre. The nature of the deposit is determined by the fact that toluene and water have similar evaporation rates at ambient conditions, so that the dispersed phase does not coalesce before drying is completed.

The tendency of the toluene (ρ = 0.87 g mL^{-1}) droplets to cream within the feed to the print head also presented practical challenges during jetting because the volume

fraction of dispersed phase in printed drops fell over time. The impact of creaming is manifested in Figure 4.35a, where larger dispersed phase drops always present alongside the micron-sized drops after emulsification are entirely absent. The reduction in volume fraction of the discontinuous phase at the print head orifice leads directly to a lower overall effective polymer concentration in drops and therefore a smaller amount of polystyrene deposited per drop.

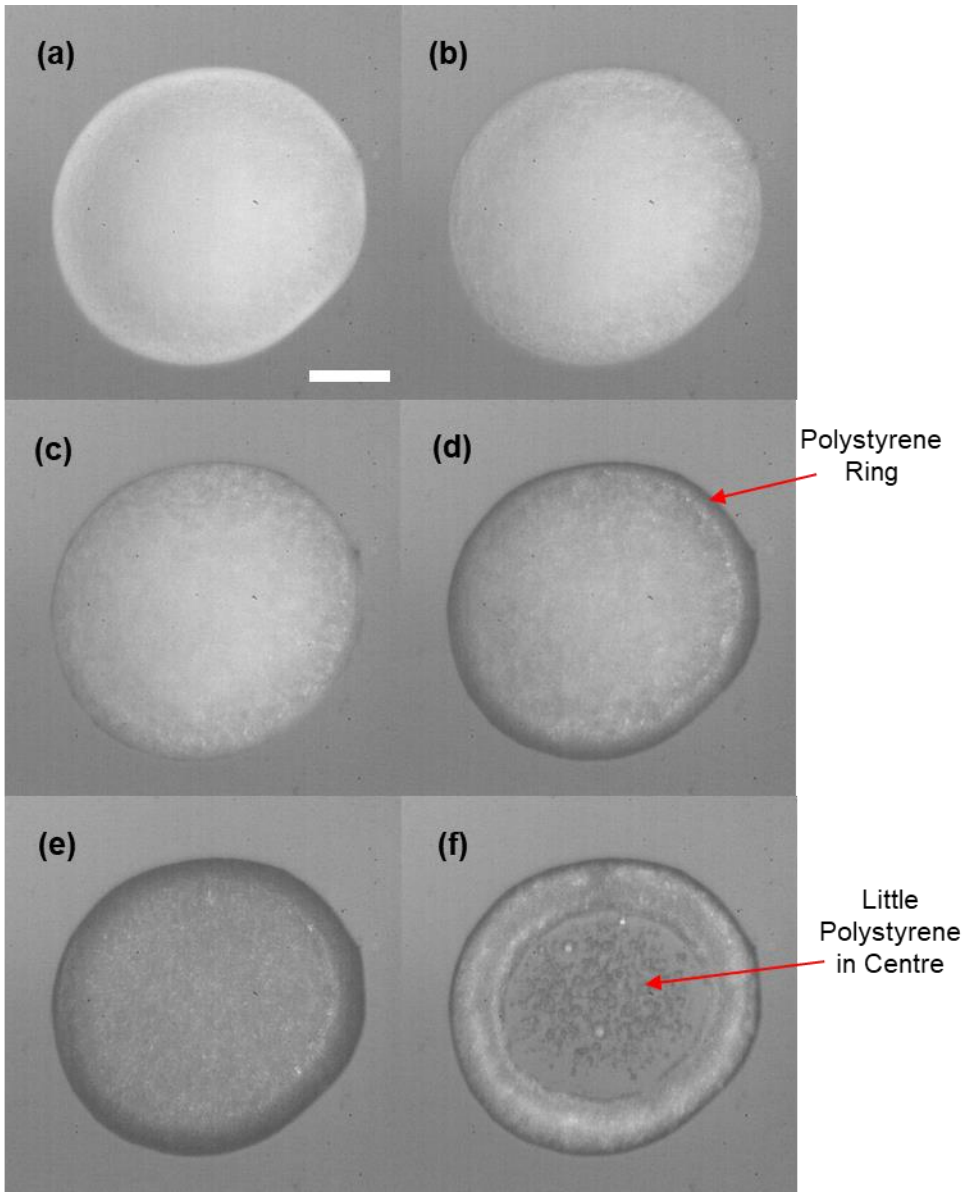

Figure 4.35. The drying process of an emulsion comprising a 10.0-%wt toluene solution of polystyrene (φ_w = 0.3) and 14.5-mM SDS. Images were captured (a) 0.1 s, (b) 1.3 s, (c) 2.6 s, (d) 3.8 s, (e) 5.1 s and (f) 6.4 s after the drop impacted the substrate. Emulsified by USH: 25% amplitude, 2 min. Jetted with a bipolar waveform of amplitude 100 V onto a slide hydrophobised with hexamethyldisilazane. The scale bar is 40 μm.

4.9.2 An Anisole Discontinuous Phase

Figure 4.36 displays images of an ink-jet printed emulsion formulated from a 9.9-%wt anisole solution of polystyrene (φ_w = 0.3) and a 14.5-mM SDS solution as it dries. The overall behaviour is markedly different to when toluene was used in the oil phase (Fig. 4.35). Initially, the printed drop looks much the same with brightness corresponding to the number of oil phase drops (Fig 4.36a). The discontinuous phase moves radially outwards under convective flow and begins to coalesce, as is visible at t = 0.8 s (Fig 4.36b). Anisole has a vapour pressure about ten times lower than water and the evaporation of the latter is almost complete by t = 1.6 s (Fig 4.36c). The loss of the continuous phase occurs before the discontinuous phase has dried significantly so that only polymer solution remains at t = 2.4 s (Fig 4.36d). The result is a continuous, filled polystyrene deposit (Fig 4.36c) since the discontinuous phase coalesces just before complete water evaporation.

The continuous, filled deposit resulting from evaporation of the anisole-based formulation may be advantageous for application. The main advantage of anisole (ρ = 0.995 g mL^{-1}) as the discontinuous phase is that it is neutrally buoyant; the concentration of the dispersed phase remained far more consistent from drop to drop than was observed with toluene.

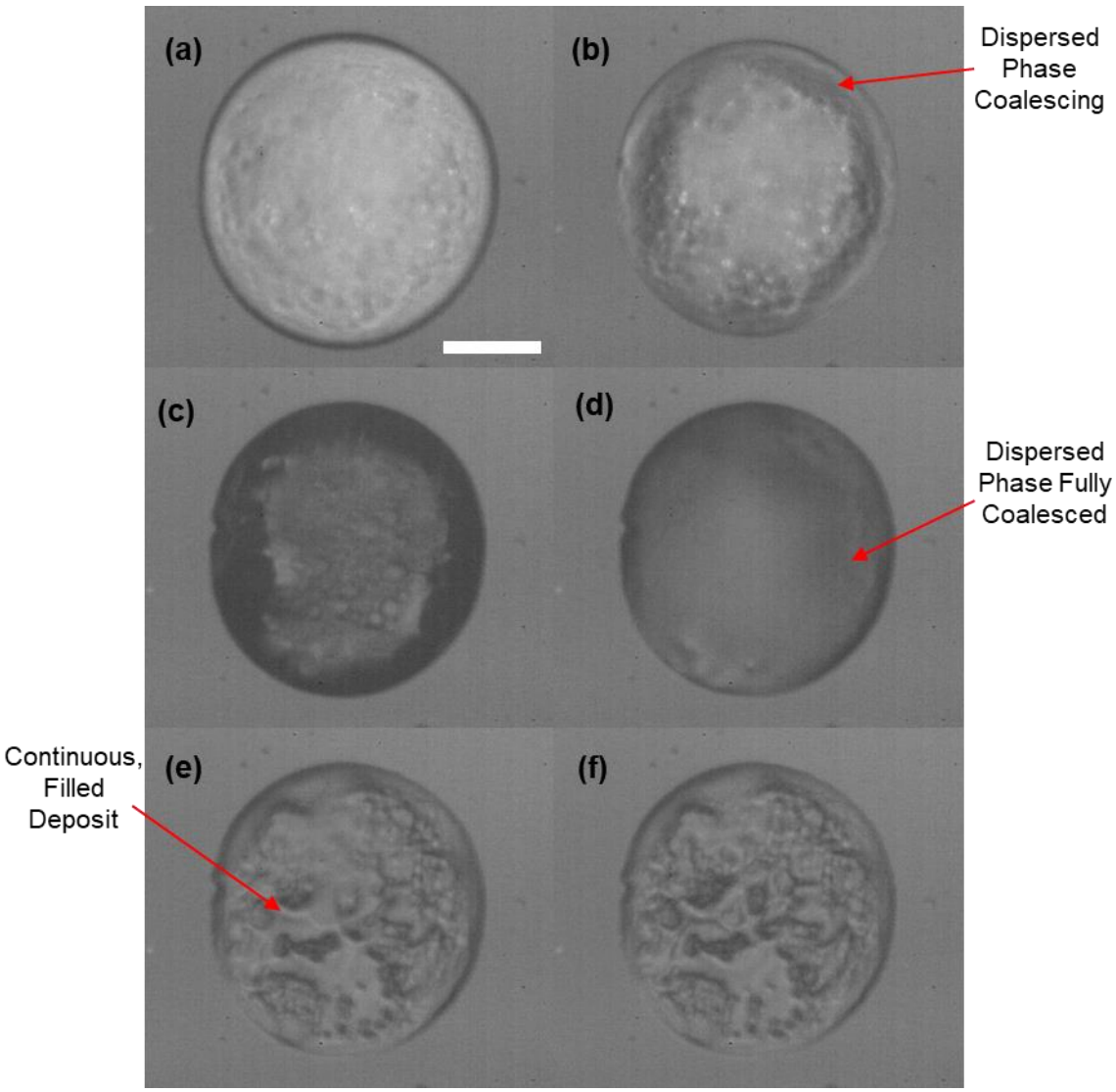

Figure 4.36. The drying process of an emulsion comprising a 9.9-%wt anisole solution of polystyrene (φ_w = 0.3) and 14.5-mM SDS. Images were captured (a) 0.1 s, (b) 0.8 s, (c) 1.6 s, (d) 2.4 s, (e) 3.2 s and (f) 4.1 s after the drop impacted the substrate. Emulsified by USH: 25% amplitude, 2 min; 40% amplitude for 1 min. Jetted with a bipolar waveform of amplitude 100 V onto a slide hydrophobised with hexamethyldisilazane. The scale bar is 40 μm.

4.9.3 A Diethyl Phthalate Discontinuous Phase

Figure 4.37 shows how an emulsion formulated with 4.8-%wt diethyl phthalate solution (φ_w = 0.3) and 14.5-mM SDS behaved when printed. After deposition, emulsified drops with diameters in the range 5 – 10 μm sedimented across entire base of the printed drop (Fig. 4.37a). Evaporation of the water induces coalescence of the discontinuous phase from the contract line radially inwards (Fig. 4.37c – d). After complete loss of water at t = 2.6 s (Fig. 4.37e), the discontinuous phase fully coalesces to produce a continuous film of polymer solution that shows no sign of drying even after t = 5 min (Fig. 4.37f).

The vapour pressure of DEP is 4×10^{-5} kPa. The printing behaviour with DEP as the discontinuous phase is characteristic of organic solvents with a very low vapour

pressure at ambient temperatures. A very low vapour pressure is advantageous because nozzle clogging as a result of polystyrene deposited at the print head orifice during printing trials was more infrequent, as compared with toluene and anisole formulations. The vapour pressure of DEP is of the order 10^5 times lower than water (Table 4.1) which means that it did not evaporate concurrently with the continuous phase in printed drops at all. Whilst this allows for greater deposit control compared with toluene and anisole, formulations with DEP did not yield a solid deposit within a minute of deposition. They would therefore be impractical for printing polymer films, unless a separate heating step were introduced. Another disadvantage with using DEP is that it has a density of 1.12 g mL^{-1} resulting in sedimentation of dispersed phase drops. Over time the discontinuous phase sinks towards the nozzle orifice so that the volume fraction of discontinuous phase in a printed drop progressively increases.

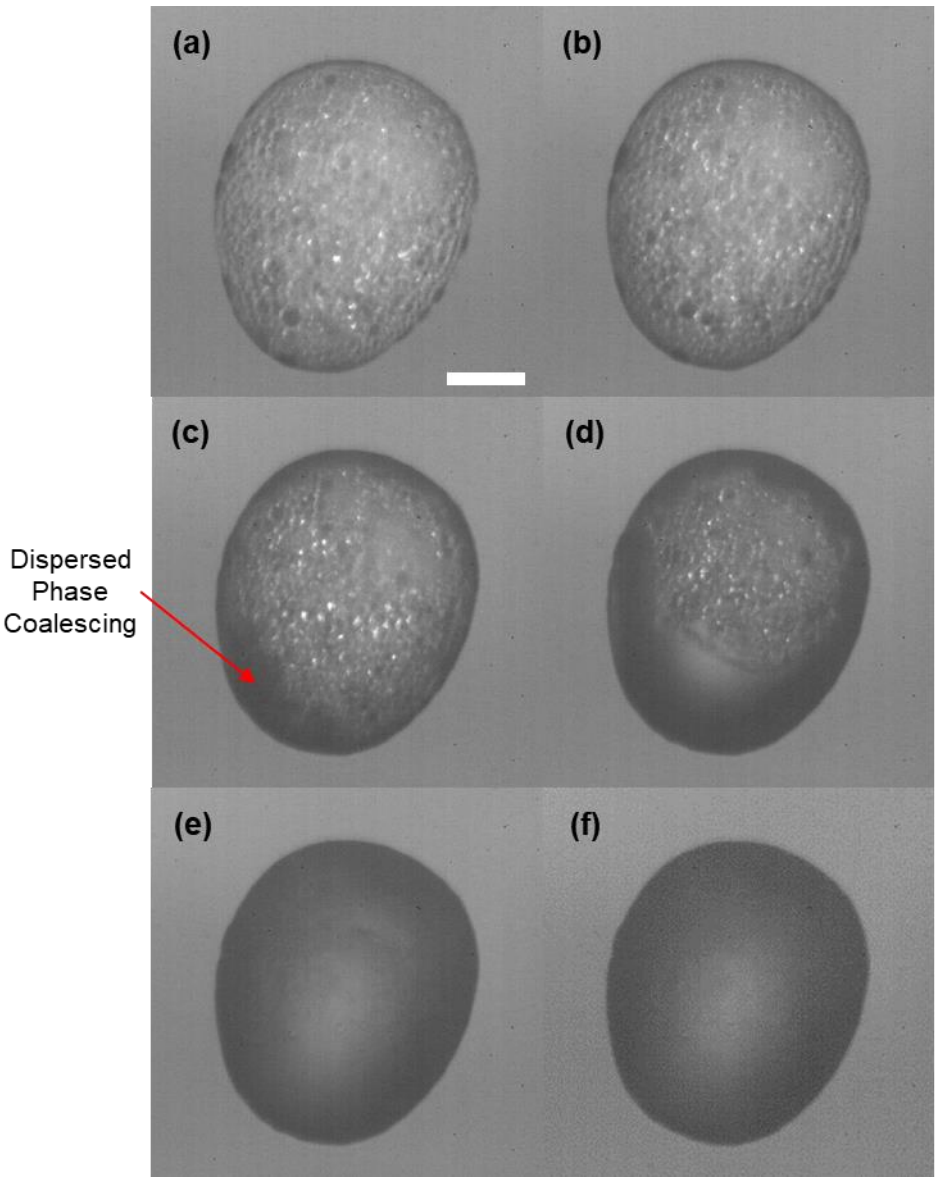

Figure 4.37. The drying process of an emulsion comprising a 4.8-%wt DEP solution of polystyrene (φ_w = 0.3) and 14.5-mM SDS. Images were captured (a) 0.2 s, (b) 0.6 s, (c) 1.2 s, (d) 1.8 s, (e) 2.6 s and (f) > 5 min after the drop impacted the substrate. Emulsified by USH: 25% amplitude, 2 min. Jetted with a bipolar waveform of amplitude 60 V onto a slide hydrophobised with hexamethyldisilazane. The scale bar is 40 μm.

4.9.4 A Methyl Benzoate Discontinuous Phase

The formulation that gave the best overall printing behaviour and drying dynamics contained methyl benzoate solutions of polystyrene as the discontinuous phase. Nozzle clogging was less frequent than when anisole was the dispersed phase and it was possible to print polymer at a higher overall concentration (3.8 %wt). Methyl benzoate (ρ = 1.08 g mL^{-1}) has a tendency to sediment in water, though less severely than DEP. Its vapour pressure is about 100 times smaller than water, giving printing dynamics that are intermediate between anisole and DEP. Images of a drying emulsion drop formulated

with a 9.5-%wt methyl benzoate solution of polystyrene (φ_w = 0.4) and a 14.8-mM SDS solution are shown in Figure 4.38 (imaged from below) and Figure 4.39 (imaged from the side). The total drying time was of the order 25 s. Evaporation of drops of this size has been shown to be diffusion limited,[60] so the drying dynamics were controlled by the difference in vapour pressure and diffusion coefficient between the continuous and discontinuous phases. The predicted ratio of the evaporation rate of water to methyl benzoate at a typical *RH* of 0.4 is 140. There were, therefore, two distinct stages to the drying process: (1) rapid evaporation of the aqueous phase over the first 1.3 s after drop impact, with associated coalescence of the discontinuous phase into a single continuous oleic phase, and (2) slow evaporation of methyl benzoate over the subsequent 25 s.

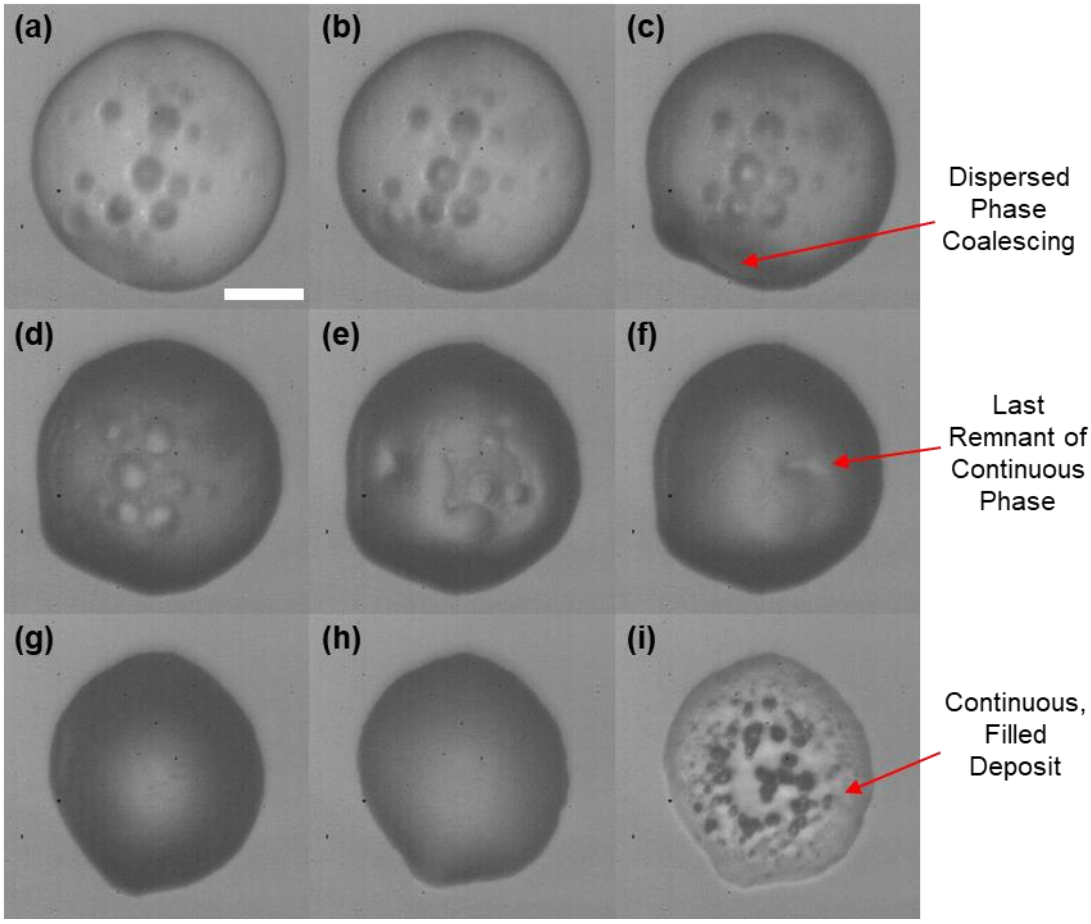

Figure 4.38. The drying process of an emulsion comprising a 9.5-%wt methyl benzoate solution of polystyrene (φ_w = 0.4) and 14.8-mM SDS. Images were captured (a) 0.1 s, (b) 0.3 s, (c) 0.6 s, (d) 0.9 s, (e) 1.2 s, (f) 1.3 s, (g) 1.8 s, (h) 12.0 s and (i) 24.0 s after the drop impacted the substrate. Emulsified by USH: 25% amplitude, 2 min. Jetted with a bipolar waveform of amplitude 100 V onto a slide hydrophobised with hexamethyldisilazane. The scale bar is 40 μm.

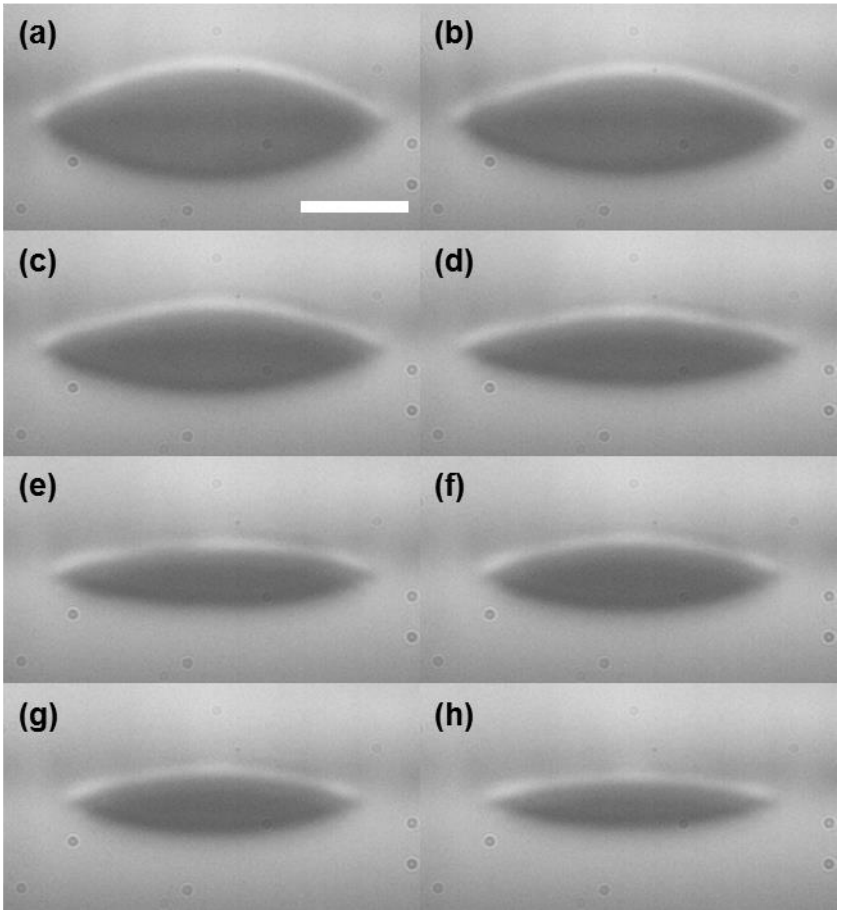

Figure 4.39. Side views of the same drop as in Figure 4.38. Images were captured (a) 0.1 s, (b) 0.3 s, (c) 0.6 s, (d) 0.9 s, (e) 1.2 s, (f) 1.8 s, (g) 5.0 s and (h) 10.0 s after the drop impacted the substrate. Jetted with a bipolar waveform of amplitude 100 V onto a slide hydrophobised with hexamethyldisilazane. The scale bar is 40 μm.

Within 0.1 s of impact, the drop adopted a spherical cap with a diameter of about 130 μm (Figs. 4.38a and 4.39a). Initially the contents of the drop appeared bright, due to scattering from a large number of micron-sized emulsified droplets (Fig. 4.38a). Larger droplets of dispersed phase were also visible as dark circles at diameters of 5 – 20 μm. Enhanced evaporation near the contact line induced convective transport of emulsion droplets towards the contact line (the so-called coffee-ring effect) and an increased local concentration of oil droplets led to coalescence. At time t = 0.3 s, a continuous ring of polymer solution began to form at the contact line (Fig. 4.38b). Coalescence of the dispersed phase proceeded radially inwards (visible Figs. 4.38c − e) and the brightness of the drop reduced as more and more particles coalesced and there were fewer scattering centres (compare Figs. 4.38a − e). A continuous polymer solution remained once the aqueous phase had evaporated entirely; visually only a single phase remained after 1.3 s (Fig. 4.38f).

Figure 4.39 shows that the drop shape was a reasonable approximation to a spherical cap, with small deviations as the drop evolved from water-continuous to oil-continuous (Figs. 4.39d − e). The diameter and volume of the drop extracted from the footage is plotted against time in Figure 4.40. The diameter decreased by only 7 μm over the first 1.3 s, so that the loss of water was reflected in the decreasing height of the drop (Figs. 4.39a − e) whilst the contact line remained largely pinned (Figs. 4.38a − e). After complete evaporation of the aqueous phase, the remaining polymer solution adjusted its shape under surface tension and the contact line receded to reduce the diameter to 110 μm by t = 1.8 s (Figs. 4.38g, 4.39f, 4.40), after which time the contact line stabilised. Evaporation continued to be reflected by decreasing drop height (Figs. 4.39f − h) until a continuous polystyrene deposit was left upon complete loss of solvent at t = 24 s (Fig. 4.38i).

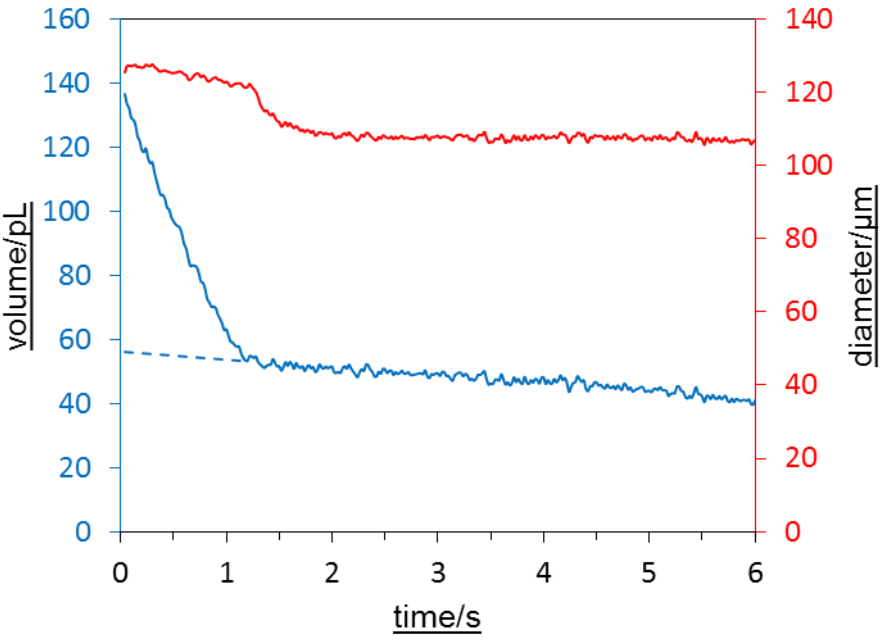

Figure 4.40. The volume change of an ink-jet printed drop of an emulsion containing polymer in the discontinuous phase over the first six seconds of drying (solid line). This is the same drop as in Figures 4.38 and 4.39. Volumes were determined by fitting a spherical cap to images of the drop obtained from the side. The initial volume of the discontinuous phase can be estimated by using linear regression to extrapolate the trend observed after 1.3 s back to time = 0 s (dashed line).

The rate volume loss was initially high at 74 ± 7 pL s^{-1}, corresponding mainly to water evaporation (Fig. 4.40). At t = 1.3 s there was a sharp change in the rate of volume loss and evaporation proceeded at a much slower rate (2.1 ± 0.2 pL s^{-1}). The knee in the evaporation rate coincides approximately with the disappearance of two discrete phases in the images in Figure 4.38. After 1.3 s, only methyl benzoate remained and, as noted earlier, it had a much lower evaporation rate than water. The observed ratio of the rate of

evaporation of water to that of methyl benzoate was 30, which is substantially lower than the expected ratio of 140.

If evaporation is diffusion controlled, then the rate of evaporation of methyl benzoate will depend only on the contact angle and drop diameter[61] and not on the presence of the aqueous phase. Hence, to estimate the initial volume of the oleic phase, the volume in Figure 4.40 at $t > 1.3$ s was extrapolated back to $t = 0$ s, to yield a value of 55 ± 5 pL. The initial drop volume was 140 ± 10 pL. The volume fraction of the discontinuous phase was thus 41 %vol, or 45 %wt, and the overall PS concentration was 4.3 %wt, assuming that polystyrene had a uniform concentration (9.5 %wt) across all dispersed phase species. The formulation was prepared with a discontinuous phase that comprised 40 %wt of the emulsion. The increase in the amount of discontinuous phase in the printed drop can be attributed to the tendency of the larger methyl benzoate droplets to sediment in water such that emulsified droplets collect at the nozzle. Thus in this single drop, the discontinuous phase had a proportion by weight about 12 % higher than the formulation average. In continuous printing applications, this segregation would not occur.

4.10 Jetting and Deposit Studies with the Optimised Formulation

In Section 4.9 it was established that methyl benzoate is a better discontinuous phase solvent than toluene, anisole and DEP: print head orifice clogging was less frequent than with anisole formulations; a clear two-stage drying process gave continuous filled polystyrene deposits unlike for toluene and anisole deposits; drying was complete in an acceptable timeframe unlike for DEP formulations. An investigation into the jetting dynamics of formulations based upon methyl benzoate and the topography of the deposit will now be presented. The formulated used was a 9.5-wt% methyl benzoate solution of polystyrene (φ_w = 0.4) dispersed in a 14.8-mM SDS solution, matching that used in Section 4.9.4 and Figures 4.38 and 4.39.

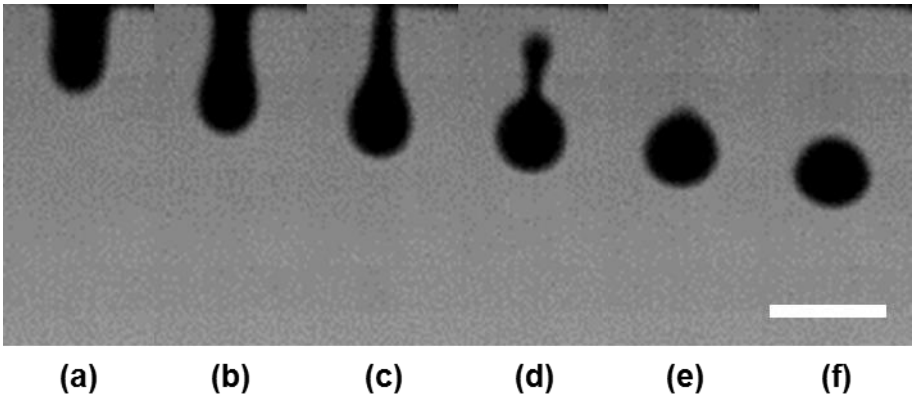

Figure 4.41. The printing dynamics of an emulsion containing 3.8-%wt polystyrene (M_n = 419 kDa) overall. The emulsion consists of a 9.5-wt% methyl benzoate solution of polystyrene (φ_w = 0.4) dispersed in a 14.8-mM SDS solution. The images were captured (a) 18, (b) 36, (c) 53, (d) 71, (e) 89 and (f) 107 μs after the fluid first became visible. The nozzle orifice diameter was 50 μm and the print head was actuated with a symmetrical bipolar waveform of amplitude 50 V. The scale bar is 100 μm.

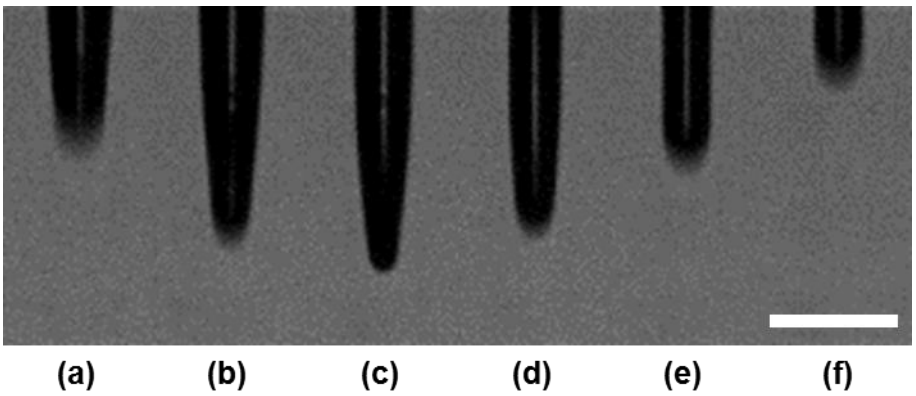

Figure 4.42. The printing dynamics of a 4.0-%wt solution of polystyrene (M_n = 549 kDa) in methyl benzoate. The images were captured (a) 9, (b) 18, (c) 27, (d) 36, (e) 44 and (f) 53 μs after the fluid first became visible. The nozzle orifice diameter was 50 μm and the print head was actuated with a symmetrical bipolar waveform of amplitude 100 V. The scale bar is 100 μm.

4.10.1.1 Jetting Dynamics

The jetting dynamics of the emulsion are shown in Figure 4.41. As fluid emerged from the nozzle, the drop necked under capillary pressure in keeping with its expected Newtonian character (Figs. 4.41a − c). Detachment took place at the orifice (Fig. 4.41d) and the remainder of the neck was drawn into the main drop body (Fig. 4.41e). The drop did not show the long-lived filament and elasticity commonly associated with printing polymer solutions, even though the overall concentration of polymer in the emulsion was 3.8 %wt.

In contrast, Figure 4.42 shows how a 4.0-%wt PS solution in methyl benzoate behaved when printed. The PS implemented here had a slightly higher number-average molecular mass (M_n = 549 kDa) than the emulsion (M_n = 419 kDa) on account of the fact that it had not been exposed to ultrasound. Attempts were made to print the polystyrene solution with a symmetrical bipolar waveform with drive voltages up to 100 V. Under no conditions was drop detachment observed. Instead, a column of fluid proceeded from the orifice (Figs. 4.42a−c), decelerated without any sign of necking, and was then drawn back inside the nozzle (Figs. 4.42d−f).

One explanation for the difference in behaviour between the emulsion and the polymer solution with the same overall wt% of polymer is the difference in viscosity. The emulsion has a viscosity of 5 mPa s (at strain rates up to 10^3 s^{-1}), which is a typical value for inks for drop-on-demand print heads. Conversely, the 4-%wt polymer solution has a low shear viscosity of 45 mPa s, which exceeds the recommended operational range of the MicroFab print head (< 20 mPa s). That elasticity also plays a role in the non-printability of the polymer solutions can be seen both from an estimate of the polymer relaxation time and from the behaviour of more dilute (and less viscous) polystyrene solutions (see Figure 4.43).

The Zimm relaxation time, τ_Z, of the PS used in this study solvated in methyl benzoate may be estimated from the published value of τ_Z of polystyrene with a similar molecular weight in chemically similar solvent. Vadillo *et al.*[160] reported τ_Z = 84 μs for a PS sample with mass-average molecular weight M_w = 488 kDa in DEP. The Zimm relaxation time scales as $\tau_Z \propto \mu N^{3\nu}$, where μ is the solvent viscosity, N is the number of Kuhn monomers in the polymer and ν is the solvent quality.[113] At 298 K, the viscosity of DEP is 11 mPa s and that of methyl benzoate is 2 mPa s.[64] Taking both DEP and methyl benzoate to be good solvents ($\nu \sim 0.6$), the Zimm relaxation time for PS in dilute solution in methyl benzoate is ~20 μs. The coil-stretch transition in dilute solution is thus expected at strain rates of ~2×10^4 s^{-1}. The 4-%wt PS solution is semidilute so the characteristic

relaxation time will be longer and the coil-stretch transition will occur at lower strain rates. The extensional strain rates in the ligament between the main drop and the fluid in the orifice may be estimated from the images in Figures 4.41b and c: between the images, 17 μs has elapsed, but the radius of the ligament has approximately halved. For a cylinder of constant volume, a reduction in radius by factor of 2 must lead to an increase in length by a factor of 4. A value of ~2×10^5 s^{-1} is thus obtained, which is at least an order of magnitude higher than that required to cause a coil-stretch transition in the polymer.

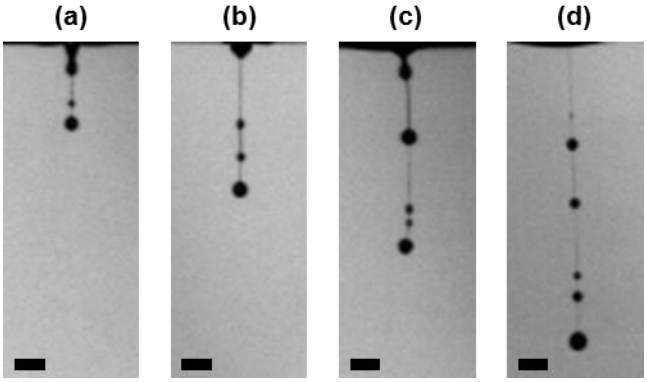

Figure 4.43. The effect of concentration upon the jetting behaviour of solutions of PS (M_n = 549 kDa) in methyl benzoate. Fluids were jetted from a print head with a 50-μm orifice that was actuated with symmetrical bipolar waveforms. The amplitude of the drive pulse was tuned to optimize jetting. (a) A 0.25-%wt solution, captured 150 μs after the fluid first emerged from the nozzle. The waveform was of amplitude 15 V. (b) A 0.50-%wt solution, captured 200 μs after the fluid first emerged from the nozzle. The waveform was of amplitude 22 V. (c) A 0.75-%wt solution, captured 260 μs after the fluid first emerged from the nozzle. The waveform was of amplitude 27 V. (d) A 1.00-%wt solution, captured 370 μs after the fluid first emerged from the nozzle. The waveform was of amplitude 53 V. The scale bars are 100 μm.

The elasticity expected of the polymer solutions can be seen clearly in more dilute solutions. A 2 wt% PS solution in methyl benzoate would not jet with any of the waveforms explored, but for lower concentrations of 0.25 – 1.00 wt% drop detachment was achieved, with drops speeds after detachment in the range 0.8 – 1.3 m s^{-1}. Figure 4.43 displays images of solutions with polymer concentrations of 0.25, 0.50, 0.75 and 1.00 %wt close to the point where the drop breaks off. Each formed long-lived filaments between the main drop body and the orifice; the ligament length at detachment and the time to detachment increased with concentration. The non-Newtonian jetting dynamics are consistent with polymers undergoing the coil-stretch transition and introducing elasticity to the fluid, as discussed above. Additionally, the print head drive voltage required for detachment increased with concentration, from 15 V for 0.25-%wt PS to 53 V for 1.00-%wt PS.

The characteristics of jetting for the 0.75- and 1.00-%wt solutions were poor, with the filament disintegrating into multiple satellites (Fig. 4.43c and d). The filament for the 0.50-%wt solution (Fig. 4.43b) led to the production of a single satellite that did not coalesce with the main droplet within 500 μm of the point of detachment. The 0.25 %wt solution detached comparatively quickly after emerging from the orifice (Fig. 4.43a) and produced a single satellite that coalesced when the main drop had travelled a further 35 μm. Thus only the 0.25 %wt PS solution showed acceptable jetting performance. Conversely, the emulsion with a 15-times higher polymer concentration shows Newtonian jetting dynamics. Oil-in-water emulsions thus provide a viable strategy for printing high-MW polymers both through a reduction in low-shear viscosity and through the elimination of non-Newtonian dynamics arising from the coil-stretch transition of the polymer chains.

4.10.1.2 Deposit Topography

The polystyrene deposit displayed in Figure 4.38i possessed a non-uniform distribution of features that are irregular in shape and appeared dark relative to the lighter coloured, smoother surface surrounding them. The image of another dry deposit in Figure 4.44a shows even more pronounced irregularities. The illumination in the rig in Figure 2.5 is optimised to highlight interfaces in the evaporating droplets and does not provide a quantitative measure of the irregularities in the surfaces. Consequently, an interferogram (*Taylor Hobson*, Talysurf CCI 6000) was taken to profile the height of the deposit in Figure 4.44a and is displayed in Figure 4.45a. The deposit was dome shaped with a mean maximum height near the centre of around 2.5 μm. Figures 4.45b and c represent orthogonal slices through the deposit and are overlaid by circular arcs fitted by a least-squares fitting routine. The circular arcs describe the overall cross-sections well, with the fits characterised by standard deviations of 0.25 and 0.21 μm in Figures 4.45b and c respectively. The deposit can therefore be described as a spherical cap. The very large majority of the irregularities had lateral dimensions below 10 μm so that deviations from the smoothly varying arcs are in fact small.

The deposit comprises both PS (~4 %wt in the initial formulation) and SDS (~0.25 %wt initially), since the latter is non-volatile. A possible origin of the surface irregularities in the dry deposits is the presence of SDS crystallised on the surface of the polystyrene. Washing with water for 30 mins did not, however, change the image (Fig. 4.44b) so if the irregularities are due to residual surfactant then the surfactant must be

buried within the polymer deposit. They may also arise from buckling of the polymer film in the later stages of drying.

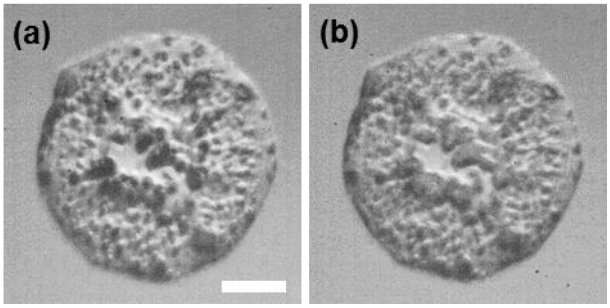

Figure 4.44. (a) An image of a dry polystyrene deposit left by a printed emulsion drop. (b) An image of the same deposit after it had been soaked in water for 30 min. The emulsion had comprised a 9.5-%wt methyl benzoate solution of polystyrene (φ_w = 0.4) and 14.8-mM SDS. Images were captured using the printing rig. The scale bar is 30 μm.

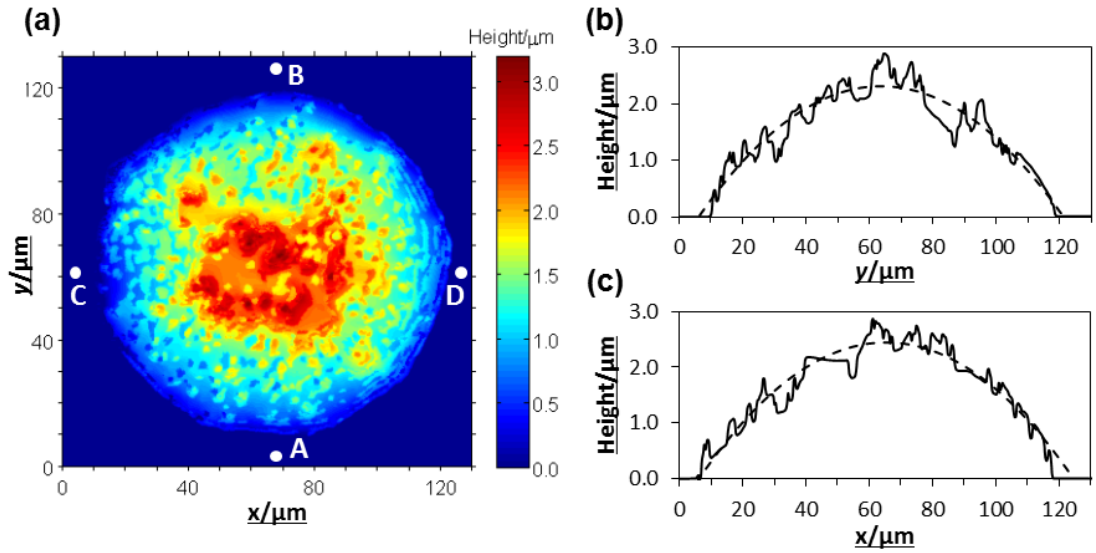

Figure 4.45. (a) A colour map displaying the deposit topography of an ink-jet printed emulsion drop containing polymer in the discontinuous phase. The emulsion formulation was a 9.5-%wt methyl benzoate solution of polystyrene (φ_w = 0.4) dispersed in a 14.8-mM SDS solution. Polystyrene made up 3.8 %wt of the total formulation. The deposit surface was profiled using coherence correlation interferometry. (b) The surface profile along the vector AB. (c) The surface profile along the vector CD.

4.11 Discussion

The jetting experiments show that polymers can be printed at higher concentrations than is possible in solution. An emulsion containing PS of M_n = 419 kDa at an overall concentration of 3.8 %wt (Fig. 4.41) was successfully printed. Conversely, solutions of PS in methyl benzoate could not be printed at all at concentrations of 4 wt% (Fig. 4.42) and 2 wt% (Fig. 4.43d). At concentrations of 0.25 – 1.00 %wt, drop detachment was observed but the elastic properties of the solutions led to long-lived filaments that delayed drop breakoff and disintegrated into satellites (Fig. 4.43a−c). The highest concentration that could be tuned to give satellite-free jetting contained 0.25-%wt PS, though even this solution produced long ligaments (Fig. 4.43a). The observations are consistent with a previous study[101] that reported an ink-jet printing limit of 0.25 %wt for a polystyrene (M_n = 488 kDa) solution in DEP at 6 m s^{-1}. We have therefore demonstrated that emulsions increase the amount of polymer that can be delivered to a substrate in a single drop by an order of magnitude.

Emulsion formulations present a clear advantage in manufacturing since a layer of a certain thickness can be deposited in fewer passes, reducing process complexity. The formulations that included a methyl-benzoate oleic phase exhibited a two-stage drying regime which left a spherical cap of concentrated polymer solution after complete evaporation of the continuous phase. The resulting deposits were continuous and dome shaped: the ring stains commonly encountered for dispersed particulates were not observed.[43] A uniform deposit is beneficial for most applications.

One disadvantage of the emulsion approach is the necessity to include a surfactant in the formulation, which may be undesirable for the functional properties of the deposited film. Trials were conducted with a range of surfactants including well-known emulsifiers such as AOT and Tween80 as well as a cationic surfactant C_{12}TAB, but SDS gave the best emulsions. An SDS homologue with a lower cmc might permit a lower surfactant loading, but one will invariably need sufficient surfactant to form a substantial fraction of a monolayer at the oil-water interface; for micron-sized droplets a surfactant loading of less than 0.1 %wt is unlikely to be achieved. An alternative approach would be to use a lower molecular weight surfactant that is sufficiently volatile to be removed during an annealing step, or possibly a photo- or thermally-degradable surfactant.

A challenge in using emulsions to print high-MW polymers is the manufacture of the emulsion itself. The ultrasonic preparation method leads to highly polydisperse emulsions with small numbers of large droplets and large numbers of sub-micron droplets, which consume a lot of surfactant on account of their high collective surface

area. The polydispersity has its origin in Ostwald ripening.[155] PS is insoluble in water so it is unable to pass through the continuous phase under Ostwald ripening dynamics. The number of centres is then fixed, leading to a dispersity governed by Laplace pressure and polymer chemical potential. It is possible that a different processing procedure would yield better formulations. Low-shear emulsification methods, such as bath sonication and shaking by hand, were attempted to avoid polymer scission but found that emulsification was very poor; a high-shear homogeniser offered no improvement. The SDS concentration was deliberately kept low (0.25 %wt) so that the major component of the deposit would be polystyrene.

The data in Section 4.9.4 represent the highest PS loading achieved in a printable emulsion. The polymer solution properties that inhibit printing also inhibit emulsification, since high strain rates are involved in the division of emulsified droplets. Increasing the polymer concentration in the fluid to be dispersed increases its non-Newtonian character and resulted in formulations with larger droplets of dispersed phase. Large droplets become problematic when they approach the size of the print head orifice since they impact jetting behaviour. They are also not as effective at shielding polymers from high strain rates since deformation under shear is linear with radius, as in Equation (4.24). The other way of increasing the polymer loading is to increase the volume fraction, φ_v, of the dispersed phase. The upper limit on φ_v is determined by the viscosity which is printable, which limits φ_v in practice to about 0.6.[161]

A number of solvents were explored in developing the optimised system. The factors that require consideration when selecting the oleic solvent are threefold: first, the dispersed phase should be a good solvent for the polymer in order to achieve a high polymer loading. Second, the solvent should be significantly less volatile than water so that the drop evaporates in two discrete stages: evaporation of water and coalescence of the oleic phase into a uniform spherical cap, followed by evaporation of the organic solvent. The solvent, however, should be sufficiently volatile that it dries within an acceptable processing time. For example, toluene (p_A = 2.9 kPa at 293 K) is too volatile and DEP ($p_A = 4 \times 10^{-5}$ kPa at 293 K) is too involatile. Third, neutrally buoyant solvents such as anisole (ρ = 0.995 g mL^{-1}) give more uniform drop compositions than dispersed phases that cream (such as toluene, ρ = 0.865 g mL^{-1}) or sediment (such as DEP, ρ = 1.12 g mL^{-1}). Although methyl benzoate is denser than water, the density difference is small enough to allow successful printing but can lead, as shown in Figure 4.40, to droplets whose composition varies from the mean composition.

In principle, the strategy for printing high-molecular-weight polymers in emulsions could be used to print water-soluble polymers in a W/O emulsion. The continuous phase, however, would need to be highly volatile (heptane, for example) which may lead to difficulties with clogging of the ink-jet nozzles. The primary purpose of the strategy is to shield the contents of the emulsified droplets from exposure to high strain rates. The strategy could therefore prove useful for protecting sensitive samples from the demanding environments in ink-jet print heads and any associated pump apparatus. Emulsions might be useful for delivering living cells to substrates, for example.

4.12 Summary

Oil-in-water emulsions provide a means for ink-jet printing high-MW polymers at a concentration much higher than is possible in a binary solution. The model formulation described in this investigation comprised a 9.5-%wt polystyrene (PS: M_n = 419 kDa, PDI = 1.21) solution in methyl benzoate (40 %wt overall) dispersed in a 14.8-mM SDS solution. This emulsion could readily be jetted from a MicroFab nozzle (diameter 50 μm) at 50 V to produce a single drop, without any sign of the filaments and non-Newtonian behaviour commonly associated with polymer solutions. In contrast, it was not possible to print a binary solution in the same solvent with a similar overall concentration (~4 %wt) at any drive voltage, with emerging fluid always being drawn back into the nozzle. The emulsions function by shielding the polymer chains from extensional flow, which occurs solely in the continuous, aqueous medium. For typical jetting parameters and micron-sized droplets, capillary forces dominate viscous forces and the droplets of the dispersed phase, containing the polymer, remain close to spherical.

The drying of printed emulsion drops on a hydrophobised surface was observed with two high-speed cameras which capture images from underneath and from the side. A two-stage drying process was observed. Initially, drop behaviour was dominated by water evaporation and emulsified droplets coalesced first at the contact line. Complete evaporation of the continuous phase left a spherical cap of the polymer dissolved in the organic solvent. A second, slower stage involved the evaporation of the organic solvent to leave a continuous deposit of the dry polymer. The PS deposits were profiled by interferometry and were found to have a dome shape with a central thickness of around 2.5 μm and a diameter around 110 μm. Cross sections through the deposit showed a roughness with a standard deviation around one tenth of the height of the deposit. The topography may arise from embedding of crystals of surfactant within the polymer deposit or from buckling of the polymer film in the later stages of drying.

The strengths of using emulsions to print high-MW polymer are that they allow an order-of-magnitude increase in the polymer loading compared to a binary solution and that they give a continuous deposit with approximately uniform coverage. The emulsification of the polymer solutions, however, was not trivial and monodisperse emulsions were not produced. The viscoelastic characteristics of polymer solutions that inhibit jetting are also likely to hinder the breaking of larger drops into smaller ones. Involatile surfactants, such as SDS, used to stabilize the emulsion remain in the dry deposit, which may be undesirable for functional materials. Selection of solvents with appropriate volatility and density is important for printing of uniform polymer films.

5 Concluding Remarks

Multi-phase formulations are a useful design tool for ink-jet fluids. The formulations described in this thesis are only model systems but they demonstrate the principles of how formulations of multiple phases might be exploited in the application of ink-jet technology. Both studies explored some of the parameter space for different combinations of solvents and lessons may be drawn from the successful and unsuccessful aspects of each formulation trialled. As indicated in the introduction, ink-jet formulations are highly tailored for their application. Consequently, once the formulation designer has isolated the target materials for deposition, he may select the appropriate carrier solvents to optimise jetting and drying characteristics, as well as tune the multi-phase behaviour. The dynamics of the multiple phases during evaporation adds additional complexity to design and the trials in this thesis showed diverse behaviour depending on the contact angle on the substrate, solvent volatility, surface tensions and densities. Knowledge of the physical chemistry of a system allows control over all aspects of ink-jet printing and increases the chances of successful innovation.

Whilst phase-selective patterning and polymer delivery via emulsions have been demonstrated in principle, challenges remain. For the phase-separating formulations, the investigation represents early steps towards applications, but much more research is required for a robust and useful process to be developed. Further work is required to identify aqueous mixtures where the oil-rich phase dries more rapidly and to identify non-aqueous mixtures that evaporate sufficiently slowly for equilibrium compositions to be attained. Contact line motion needs to be addressed through the addition of additives or modification of the substrate to better realise phase-selective patterning. The impact of phase separation on internal flows was not pursued, but remains a valid line of inquiry.

For the polymer-containing emulsions, more research is required to enable the manufacture of commercially viable formulations. The larger dispersed drops should be eradicated and the rate of Ostwald ripening should be slowed to improve printing reliability over longer periods and formulation shelf life. The ideal emulsification method would avoid high strain rates to prevent polymer degradation, but that may be unavoidable. Neutral buoyancy should be attained for the dispersed phase to further enhance the shelf-life of formulations. Despite the challenges, polymer delivery via emulsions may be broadly applied across polymer classes and a working model system has been thoroughly investigated.

6 References

1 I. M. Hutchings and G. D. Martin, in *Inkjet Technology for Digital Fabrication*, eds. I. M. Hutchings and G. D. Martin, John Wiley & Sons, Ltd., Chichester, U.K., 2013.

2 W. Thompson, *US Pat. 109,688*, 1870.

3 R. G. Sweet, *Rev. Sci. Instrum.*, 1965, **36**, 131–136.

4 U.S. Patent 3,683,212, *US Pat. 3,683,212*, 1972.

5 U.S. Patent 3,946,398, *US Pat. 3,946,398*, 1976.

6 O. A. Basaran, H. Gao and P. P. Bhat, *Annu. Rev. Fluid Mech.*, 2013, **45**, 85–113.

7 N. Morita, A. A. Khalate, A. M. van Buul and H. Wijshoff, in *Fundamentals of Inkjet Printing: The Science of Inkjet and Droplets*, ed. S. D. Hoath, Wiley-VCH, Weinheim, Germany, 2016.

8 C. H. Hertz, *US Pat. 3,416,153*, 1968.

9 E. P. Furlani, B. G. Price, G. Hawkins and A. G. Lopez, *Proc. NSTI Nanotechnol. Conf.*, 2006, **2**, 534–537.

10 J. M. Chwalek, D. P. Trauernicht, C. N. Delametter, R. Sharma, D. L. Jeanmaire, C. N. Anagnostopoulos, G. A. Hawkins, B. Ambravaneswaran, J. C. Panditaratne and O. A. Basaran, *Phys. Fluids*, 2002, **14**, 37–40.

11 T. Hara, Y. Sato, Y. Shirato and Y. Takatori, *US Pat. 4,296,421*, 1981.

12 T. Hara, Y. Sato, Y. Shirato and Y. Takatori, *US Pat. 4,251,824*, 1981.

13 H. Kobayashi, N. Koumura and S. Ohno, *US Pat. 4,243,994*, 1981.

14 A. U. Chen and O. A. Basaran, *Phys. Fluids*, 2002, **14**, 1–4.

15 H. Y. Gan, X. Shan, T. Eriksson, B. K. Lok and Y. C. Lam, *J. Micromechanics Microengineering*, 2009, **19**, 55010.

16 N. Riefler and T. Wriedt, *Part. Part. Syst. Charact.*, 2008, **25**, 176–182.

17 N. Reis and B. Derby, *Ink jet deposition of ceramic suspensions: Modeling and experiments of droplet formation*, 2000, vol. 625.

18 D. Jang, D. Kim and J. Moon, *Langmuir*, 2009, **25**, 2629–2635.

19 P. C. Duineveld, M. M. de Kok, M. Buechel, A. H. Sempel, K. A. H. Mutsaers, P. van de Weijer, I. G. J. Camps, T. J. M. van de Biggelaar, J.-E. J. M. Rubingh and E. I. Haskal, in *Organic Light-Emitting Materials and Devices V*, ed. Z. H. Kafafi, 2002, vol. 4464, pp. 59–67.

20 B. Derby, *Annu. Rev. Mater. Res.*, 2010, **40**, 395–414.

21 S. G. Yeates, D. Xu, M.-B. Madec, D. Caras-Quintero, K. A. Alamry, A.

Malandraki and V. Sanchez-Romaguera, in *Inkjet Technology for Digital Fabrication*, eds. I. M. Hutchings and G. D. Martin, John Wiley & Sons, Ltd., Chichester, U.K., 2013.

22 M. Singh, H. M. Haverinen, P. Dhagat and G. E. Jabbour, *Adv. Mater.*, 2010, **22**, 673–685.

23 B.-J. de Gans, P. C. Duineveld and U. S. Schubert, *Adv. Mater.*, 2004, **16**, 203–213.

24 Q. Liu and M. Orme, *J. Mater. Process. Technol.*, 2001, **115**, 271–283.

25 J. Perelaer, B.-J. de Gans and U. S. Schubert, *Adv. Mater.*, 2006, **18**, 2101–2104.

26 P. J. Smith, D. Y. Shin, J. E. Stringer, B. Derby and N. Reis, *J. Mater. Sci.*, 2006, **41**, 4153–4158.

27 S. B. Fuller, E. J. Wilhelm and J. M. Jacobson, *J. Microelectromechanical Syst.*, 2002, **11**, 54–60.

28 P. Calvert, *Chem. Mater.*, 2001, **13**, 3299–3305.

29 T. R. Hebner, C. C. Wu, D. Marcy, M. H. Lu and J. C. Sturm, *Appl. Phys. Lett.*, 1998, **72**, 519–521.

30 C. N. Hoth, S. A. Choulis, P. Schilinsky and C. J. Brabec, *Adv. Mater.*, 2007, **19**, 3973–3978.

31 M. Mott, J.-H. Song and J. R. G. Evans, *J. Am. Ceram. Soc.*, 1999, **82**, 1653–1658.

32 H. L. Costa and I. M. Hutchings, in *Proceedings of NIP24: International Conference on Digital Printing Technologies*, Society for Imaging Science and Technology, Springfield, VA, 2008, pp. 256–259.

33 B. J. De Gans, S. Hoeppener and U. S. Schubert, *Adv. Mater.*, 2006, **18**, 910–914.

34 S. F. Jahn, L. Engisch, R. R. Baumann, S. Ebert and W. A. Goedel, *Langmuir*, 2009, **25**, 606–610.

35 E. L. Talbot, *PhD Thesis*, Durham University, 2014.

36 MicroFab Technologies Inc., *Low Temperature Dispensing Devices*, Plano, TX, U.S.A.

37 MicroFab Technologies Inc., *Ink-Jet Microdispensing Basic Set-up*, Plano, TX, U.S.A, 2012.

38 MicroFab Technologies Inc., *MicroFab Technote 99-03: Drive Waveform Effects on Ink-Jet Device Performance*, Plano, TX, U.S.A, 1999.

39 First Ten Ångstroms, *Laplace-Young and Bashforth-Adams Equations*, Portsmouth, VA, U.S.A., 2000.

40 R. P. Woodward, *FTÅ200 Measurement Capabilities*, First Ten Ångstoms,

Portsmouth, VA, U.S.A.

41 J. F. Padday, *Surface and Colloid Science, Vol. 1*, Wiley, New York, U.S.A., 1969.

42 J. S. . Wheeler and S. G. Yeates, in *Fundamentals of Inkjet Printing: The Science of Inkjet and Droplets*, ed. S. D. Hoath, Wiley-VCH, Weinheim, Germany, 2016.

43 R. D. Deegan, O. Bakajin, T. F. Dupont, G. Huber, S. R. Nagel and T. A. Witten, *Nature*, 1997, **389**, 827–829.

44 T. Still, P. J. Yunker and A. G. Yodh, *Langmuir*, 2012, **28**, 4984–4988.

45 E. L. Talbot, L. Yang, A. Berson and C. D. Bain, *ACS Appl. Mater. Interfaces*, 2014, **6**, 9572–9583.

46 P. W. Atkins and J. de Paula, *Atkins' Physical Chemistry*, Oxford University Press, Oxford, U.K., 8th edn., 2006.

47 D. Shaw, A. Skrzecz, J. W. Lorimer and A. Maczynski, Eds., *IUPAC Solubility Data Series: Alcohols with Hydrocarbons*, Oxford University Press, Oxford, 1994, vol. 56.

48 J. E. Shelby, *Introduction to Glass Science and Technology*, Royal Society of Chemistry, Cambridge, U.K., 2nd edn., 2005.

49 F. Brochard-Wyart, J. M. Di Meglio, D. Quere and P. G. De Gennes, *Langmuir*, 1991, **7**, 335–338.

50 K. M. Wilkinson, C. D. Bain, H. Matsubara and M. Aratono, *ChemPhysChem*, 2005, **6**, 547–555.

51 A. W. Adamson and A. P. Gast, *Physical Chemistry of Surfaces*, John Wiley & Sons, Inc., New York, U.S.A., 6th edn., 1997.

52 J. N. Israelachvili, *Intermolecular and Surface Forces*, Academic Press, London, UK, 2nd edn., 1991.

53 A. Amirfazli and A. W. Neumann, *Adv. Colloid Interface Sci.*, 2004, **110**, 121–141.

54 J. Stringer and B. Derby, in *Inkjet Technology for Digital Fabrication*, eds. I. M. Hutchings and G. D. Martin, John Wiley & Sons, Ltd., Chichester, U.K., 2013.

55 J. Drelich, E. Chibowski, D. D. Meng and K. Terpilowski, *Soft Matter*, 2011, **7**, 9804.

56 P. S. Brown, A. Berson, E. L. Talbot, T. J. Wood, W. C. E. Schofield, C. D. Bain and J. P. S. Badyal, *Langmuir*, 2011, **27**, 13897–13903.

57 E. Talbot, C. Bain, R. De Dier, W. Sempels and J. Vermant, in *Fundamentals of Inkjet Printing: The Science of Inkjet and Droplets*, ed. S. D. Hoath, Wiley-VCH, Weinheim, Germany, 2016.

58 J. D. Smith, C. D. Cappa, W. S. Drisdell, R. C. Cohen and R. J. Saykally, *J. Am. Chem. Soc.*, 2006, **128**, 12892–12898.

59 Y. O. Popov, *Phys. Rev. E*, 2005, **71**, 36313.

60 E. L. Talbot, A. Berson, P. S. Brown and C. D. Bain, *Phys. Rev. E*, 2012, **85**, 61604.

61 H. Hu and R. G. Larson, *J. Phys. Chem. B*, 2002, **106**, 1334–1344.

62 R. G. Larson, *AIChE J.*, 2014, **60**, 1538–1571.

63 G. J. Dunn, S. K. Wilson, B. R. Duffy, S. David and K. Sefiane, *J. Fluid Mech.*, 2009, **623**, 329–351.

64 C. L. Yaws, Ed., *Chemical Properties Handbook: Physical, Thermodynamic, Environmental, Transport, Safety, and Health Related Properties for Organic and Inorganic Chemicals*, McGraw-Hill, New York, U.S.A., 1999.

65 S. David, K. Sefiane and L. Tadrist, *Colloids Surfaces A Physicochem. Eng. Asp.*, 2007, **298**, 108–114.

66 H. Hu and R. G. Larson, *Langmuir*, 2005, **21**, 3972–3980.

67 W. D. Ristenpart, P. G. Kim, C. Domingues, J. Wan and H. A. Stone, *Phys. Rev. Lett.*, 2007, **99**, 234502.

68 E. L. Talbot, A. Berson and C. D. Bain, in *Proceedings of NIP28: The 28th International Conference on Digital Printing Technologies and Digital Fabrication Conference 2012*, Society for Imaging Science and Technology, Springfield, VA, 2012, pp. 420–423.

69 H. B. Eral, D. M. Augustine, M. H. G. Duits and F. Mugele, *Soft Matter*, 2011, **7**, 4954–4958.

70 R. D. Deegan, O. Bakajin, T. F. Dupont, G. Huber, S. R. Nagel and T. A. Witten, *Phys. Rev. E*, 2000, **62**, 756–765.

71 H. Hu and R. G. Larson, *J. Phys. Chem. B*, 2006, **110**, 7090–7094.

72 E. L. Talbot, H. N. Yow, L. Yang, A. Berson, S. R. Biggs and C. D. Bain, *ACS Appl. Mater. Interfaces*, 2015, **7**, 3782–3790.

73 J. Park and J. Moon, *Langmuir*, 2006, **22**, 3506–3513.

74 R. C. Reid, J. M. Prausnitz and B. E. Poling, *The Properties of Gases and Liquids*, McGraw-Hill, Inc., New York, U.S.A., 4th edn., 1987.

75 M. Góral, B. Wiśniewska-Gocłowska and A. Mączyński, *J. Phys. Chem. Ref. Data*, 2006, **35**, 1391–1414.

76 E. N. Fuller, P. D. Schettler and J. C. Giddings, *Ind. Eng. Chem.*, 1966, **58**, 18–27.

77 E. N. Fuller, K. Ensley and J. C. Giddings, *J. Phys. Chem.*, 1969, **73**, 3679–3685.

78 S. Karpitschka, F. Liebig and H. Riegler, *Langmuir*, 2017, acs.langmuir.7b00740.

79 J. A. V. Butler, D. W. Thomson and W. H. Maclennan, *J. Chem. Soc.*, 1933, 674–686.

80 *Product Information: DOW P-Series Glycol Ethers and DOW E-Series Glycol Ethers*, DOW Chemical.

81 R. Sander, *Atmos. Chem. Phys.*, 2015, **15**, 4399–4981.

82 *Product Information: Ecological and Toxicological Data of DOW Glycol Ethers*, Dow Chemical.

83 ParaChem, http://www.parchem.com, (accessed 21 June 2017).

84 H. Tan, C. Diddens, P. Lv, J. G. M. Kuerten, X. Zhang and D. Lohse, *Proc. Natl. Acad. Sci.*, 2016, **113**, 8642–8647.

85 A. S. Johns and C. D. Bain, in *Proceedings of NIP32: The 32nd International Conference on Digital Printing Technologies and Printing for Fabrication 2016*, Society for Imaging Science and Technology, Springfield, VA, 2016, pp. 275–280.

86 M. Windholz, S. Budavari, R. F. Blumetti and E. S. Otterbein, Eds., *The Merck Index*, Merck & Co., Inc., Rahway, NJ, U.S.A., 10th edn., 1983.

87 A. Apelblat, E. Manzurola and N. Abo Balal, *J. Chem. Thermodyn.*, 2006, **38**, 565–571.

88 G. A. Sim, J. M. Robertson and T. H. Goodwin, *Acta Crystallogr.*, 1955, **8**, 157–164.

89 X. Holmbäck and Å. C. Rasmuson, *J. Cryst. Growth*, 1999, **198**–**199**, 780–788.

90 M. Eagleson, Ed., *Concise Encyclopedia Chemistry*, W. de Gruyter, Berlin, Germany, 1994.

91 *Cheric*, http:\\www.cheric.org/research/kdb, (accessed December 2015).

92 a. M. Cazabat, F. Heslot, S. M. Troian and P. Carles, *Nature*, 1990, **346**, 824–826.

93 D. Pesach and A. Marmur, *Langmuir*, 1987, **3**, 519–524.

94 S. M. Troian, X. L. Wu and S. A. Safran, *Phys. Rev. Lett.*, 1989, **62**, 1496.

95 P.-Å. Albertsson, *Partition of Cell Particles and Macromolecules*, Almqvist & Wiksell, Stockholm, Sweden, 1960.

96 R. A. Waggoner, F. D. Blum and J. C. Lang, *Macromolecules*, 1995, **28**, 2658–2664.

97 D. R. Lide, Ed., *CRC Handbook of Chemistry and Physics*, CRC Press, Inc., Boca Raton, USA, 74th edn., 1993.

98 R. D. Ashford, *Ashford's Dictionary of Industrial Chemicals*, Wavelength Publications, Saltash, U.K., 3rd edn., 2011.

99 A. V. S. Parry, A. J. Straub, E. M. Villar-Alvarez, T. Phuengphol, J. E. R. Nicoll,

W. K. X. Lim, L. M. Jordan, K. L. Moore, P. Taboada, S. G. Yeates and S. Edmondson, *J. Am. Chem. Soc.*, 2016, **138**, 9009–9012.

100 B.-J. de Gans, E. Kazancioglu, W. Meyer and U. S. Schubert, *Macromol. Rapid Commun.*, 2004, **25**, 292–296.

101 S. D. Hoath, O. G. Harlen and I. M. Hutchings, *J. Rheol.*, 2012, **56**, 1109–1127.

102 M. Stelter, T. Wunderlich, S. K. Rath, G. Brenn, A. L. Yarin, R. P. Singh and F. Durst, *J. Appl. Polym. Sci.*, 1999, **74**, 2773–2782.

103 M. Stelter, G. Brenn, A. L. Yarin, R. P. Singh and F. Durst, *J. Rheol.*, 2002, **46**, 507.

104 A. Bazilevskii, V. Entov and A. Rozhkov, *Polym. Sci. Ser. A*, 2001, **43**, 716–726.

105 S. L. Anna and G. H. McKinley, *J. Rheol.*, 2001, **45**, 115.

106 C. Clasen, J. Eggers, M. A. Fontelos, J. Li and G. H. McKinley, *J. Fluid Mech*, 2003, **556**, 283–308.

107 Y. Amarouchene, D. Bonn, J. Meunier and H. Kellay, *Phys. Rev. Lett.*, 2001, **86**, 3558–3561.

108 Y. Christanti and L. M. Walker, *J. Nonnewton. Fluid Mech.*, 2001, **100**, 9–26.

109 R. P. Mun, J. A. Byars and D. V Boger, *J. Nonnewton. Fluid Mech.*, 1998, **74**, 285–297.

110 J. J. Cooper-White, J. E. Fagan, V. Tirtaatmadja, D. R. Lester and D. V. Boger, *J. Nonnewton. Fluid Mech.*, 2002, **106**, 29–59.

111 V. Tirtaatmadja, G. H. McKinley and J. J. Cooper-White, *Phys. Fluids*, 2006, **18**, 43101.

112 R. G. Larson and J. J. Magda, *Macromolecules*, 1989, **22**, 3004–3010.

113 M. Rubenstein and R. H. Colby, *Polymer Physics*, Oxford University Press Inc., New York, U.S.A., 2003.

114 V. M. Entov and E. J. Hinch, *J. Nonnewton. Fluid Mech.*, 1997, **72**, 31–53.

115 Y. Christanti and L. M. Walker, *J. Rheol.*, 2002, **46**, 733–748.

116 G. M. Harrison, J. Remmelgas and L. G. Leal, *J. Rheol.*, 1999, **43**, 197–218.

117 G. M. Harrison, J. Remmelgas and L. G. Leal, *J. Rheol.*, 1998, **42**, 1039–1058.

118 H. J. Spinelli, *Adv. Mater.*, 1998, **10**, 1215–1218.

119 GB2351292, 2000.

120 A. V. Bazilevskii, J. D. Meyer and A. N. Rozhkov, *Fluid Dyn.*, 2005, **40**, 376–392.

121 D. Xu, V. Sanchez-Romaguera, S. Barbosa, W. Travis, J. de Wit, P. Swan and S. G. Yeates, *J. Mater. Chem.*, 2007, **17**, 4902–4907.

122 S. D. Hoath, D. C. Vadillo, O. G. Harlen, C. McIlroy, N. F. Morrison, W.-K. Hsiao,

T. R. Tuladhar, S. Jung, G. D. Martin and I. M. Hutchings, *J. Nonnewton. Fluid Mech.*, 2014, **205**, 1–10.

123 B.-J. de Gans, L. Xue, U. S. Agarwal and U. S. Schubert, *Macromol. Rapid Commun.*, 2005, **26**, 310–314.

124 B.-J. de Gans, E. Kazancioglu, W. Meyer and U. S. Schubert, *Macromol. Rapid Commun.*, 2004, **25**, 292–296.

125 C. McIlroy, O. G. Harlen and N. F. Morrison, *J. Nonnewton. Fluid Mech.*, 2013, **201**, 17–28.

126 A. Keller and J. A. Odell, *Colloid Polym. Sci.*, 1985, **263**, 181–201.

127 A. . Müller, J. . Odell and S. Carrington, *Polymer*, 1992, **33**, 2598–2604.

128 G. Marrucci, *Polym. Eng. Sci.*, 1975, **15**, 229–233.

129 K. A-Alamry, K. Nixon, R. Hindley, J. A. Odel and S. G. Yeates, *Macromol. Rapid Commun.*, 2011, **32**, 316–320.

130 J. S. R. Wheeler, S. W. Reynolds, S. Lancaster, V. S. Romanguera and S. G. Yeates, *Polym. Degrad. Stab.*, 2014, **105**, 116–121.

131 C. D. Taylor, D. S. Valkovska and C. D. Bain, *Phys. Chem. Chem. Phys.*, 2003, **5**, 4885–4891.

132 K. J. Mysels, *Langmuir*, 1986, **2**, 423–428.

133 J. C. Conboy, M. C. Messmer and G. L. Richmond, *J. Phys. Chem. B*, 1997, **101**, 6724–6733.

134 A. Siderius, S. K. Kehl and D. G. Leaist, *J. Solution Chem.*, 2002, **31**, 607–625.

135 J. M. Rallison, *Annu. Rev. Fluid Mech.*, 1984, **16**, 45–66.

136 H. A. Stone, *Annu. Rev. Fluid Mech.*, 1994, **26**, 65–102.

137 G. I. Taylor, *Proc. R. Soc. A Math. Phys. Eng. Sci.*, 1932, **138**, 41–48.

138 G. I. Taylor, *Proc. R. Soc. A Math. Phys. Eng. Sci.*, 1934, **146**, 501–523.

139 B. J. Bentley and L. G. Leal, *J. Fluid Mech.*, 1986, **167**, 219.

140 B. J. Bentley and L. G. Leal, *J. Fluid Mech.*, 1986, **167**, 241.

141 D. C. Tretheway and L. G. Leal, *AIChE J.*, 1999, **45**, 929–937.

142 H. A. Stone and L. G. Leal, *J. Fluid Mech.*, 1990, **220**, 161.

143 W. J. Milliken, H. A. Stone and L. G. Leal, *Phys. Fluids A Fluid Dyn.*, 1993, **5**, 69–79.

144 B. P. Binks, in *Modern Aspects of Emulsion Science*, ed. B. P. Binks, Royal Society of Chemistry, Cambridge, 1998.

145 E. Dickinson, *Annu. Reports Sect. 'C' (Physical Chem.)*, 1986, **83**, 31.

146 S. U. Pickering, *J. Chem. Soc., Trans.*, 1907, **91**, 2001–2021.

147 P. Walstra and P. E. A. Smulders, in *Modern Aspects of Emulsion Science*, ed. B. P. Binks, Royal Society of Chemistry, Cambridge, 1998.

148 M. M. Robins and D. J. Hibberd, in *Modern Aspects of Emulsion Science*, ed. B. P. Binks, Royal Society of Chemistry, Cambridge, 1998.

149 B. Derjaguin and L. Landau, *Acta Physicochim.*, 1941, **14**, 633–662.

150 E. J. W. Verwey and J. T. . Overbeek, *Theory of the Stability of Lyophobic Colloids*, Elsevier, Amsterdam, 1948.

151 W. Thomson, *Proc. R. Soc. Edinburgh*, 1872, **7**, 63–68.

152 I. M. Lifshitz and V. V. Slyozov, *J. Phys. Chem. Solids*, 1961, **19**, 35–50.

153 A. S. Kabalnov, A. V Pertzov and E. D. Shchukin, *J. Colloid Interface Sci.*, 1987, **118**, 590–597.

154 W. I. Higuchi and J. Misra, *J. Pharm. Sci.*, 1962, **51**, 459–466.

155 A. S. Kabal'nov, A. V. Pertzov and E. D. Shchukin, *Colloids and Surfaces*, 1987, **24**, 19–32.

156 A. M. Basedow and K. H. Ebert, in *Physical Chemistry. Advances in Polymer Science, vol 22*, Springer, Berlin, Heidelberg, 1977.

157 ICI Americas Inc., *The HLB System; a Time Saving Guide to Emulsifier Selection*, 1980.

158 Akzo Nobel, *HLB & Emulsification*, 2011.

159 Croda Europe Ltd, *Span and Tween*, Snaith, U.K.

160 D. C. Vadillo, W. Mathues and C. Clasen, *Rheol. Acta*, 2012, **51**, 755–769.

161 R. Pal, *J. Rheol.*, 2001, **45**, 509–520.